DEFENSE TECHNICAL INFORMATION CENTER

Information for the Defense Community

DTIC® has determined on __1 /OCT/2010__ that this Technical Document has the Distribution Statement checked below. The current distribution for this document can be found in the DTIC® Technical Report Database.

☒ **DISTRIBUTION STATEMENT A.** Approved for public release; distribution is unlimited.

☐ **© COPYRIGHTED**; U.S. Government or Federal Rights License. All other rights and uses except those permitted by copyright law are reserved by the copyright owner.

☐ **DISTRIBUTION STATEMENT B.** Distribution authorized to U.S. Government agencies only (fill in reason) (date of determination). Other requests for this document shall be referred to (insert controlling DoD office)

☐ **DISTRIBUTION STATEMENT C.** Distribution authorized to U.S. Government Agencies and their contractors (fill in reason) (date of determination). Other requests for this document shall be referred to (insert controlling DoD office)

☐ **DISTRIBUTION STATEMENT D.** Distribution authorized to the Department of Defense and U.S. DoD contractors only (fill in reason) (date of determination). Other requests shall be referred to (insert controlling DoD office).

☐ **DISTRIBUTION STATEMENT E.** Distribution authorized to DoD Components only (fill in reason) (date of determination). Other requests shall be referred to (insert controlling DoD office).

☐ **DISTRIBUTION STATEMENT F.** Further dissemination only as directed by (inserting controlling DoD office) (date of determination) or higher DoD authority.

Distribution Statement F is also used when a document does not contain a distribution statement and no distribution statement can be determined.

☐ **DISTRIBUTION STATEMENT X.** Distribution authorized to U.S. Government Agencies and private individuals or enterprises eligible to obtain export-controlled technical data in accordance with DoDD 5230.25; (date of determination). DoD Controlling Office is (insert controlling DoD office).

REPORT DOCUMENTATION PAGE

1. REPORT DATE (DD-MM-YYYY)	2. REPORT TYPE	3. DATES COVERED (From - To)
09/27/2010	Final Technical Report	August 01, 2008 to July 31, 2010

4. TITLE AND SUBTITLE
Investigation of ELF Signals Associated With Mine Warfare: A University of Idaho and ARD Collaboration, Phase II

5a. CONTRACT NUMBER

5b. GRANT NUMBER
N00014-08-1-1170

5c. PROGRAM ELEMENT NUMBER

6. AUTHOR(S)
Young, Jeffrey L.

5d. PROJECT NUMBER
08PR08992-00

5e. TASK NUMBER

5f. WORK UNIT NUMBER

7. PERFORMING ORGANIZATION NAME(S) AND ADDRESS(ES)
University of Idaho, Office of Sponsored Programs
Morrill Hall Room 414
PO Box 443020
Moscow, ID   83844-3020

8. PERFORMING ORGANIZATION REPORT NUMBER

9. SPONSORING/MONITORING AGENCY NAME(S) AND ADDRESS(ES)
Office of Naval Research
One Liberty Center
875 N. Randolph Street, Suite 1425
Arlington, VA   22203-1995

10. SPONSOR/MONITOR'S ACRONYM(S)
ONR

11. SPONSORING/MONITORING AGENCY REPORT NUMBER
PR# 08PR08992-00

12. DISTRIBUTION AVAILABILITY STATEMENT
Unlimited

13. SUPPLEMENTARY NOTES

14. ABSTRACT
Extremely low frequency (ELF) electromagnetic signals are used by enemy combatants to detect and, subsequently, to incapacitate, by means of surface and subsurface mines, naval vessels. The questions that are being asked in this investigation are: 1) once an ELF signal is generated, how far will it propagate and still be detectable and 2) how can such signals be modeled, excited and measured? To this end, the scenario considered is one in which an ELF source of the electric or magnetic kind is located in or above water, such as a lake or ocean. This source stimulates an ELF signal that is free to propagate in the water and air, and is reflected by various material interfaces. For purposes of experimental demonstration, the investigation focuses on the scenario of ELF sources and signals in the context of Lake Pend Oreille, where the Acoustic Research Detachment (ARD, Bayview, Idaho) is located. The research program was designed with two major thrusts: Modeling and experimentation. The modeling thrust was coordinated and executed by the University of Idaho (UI), Moscow, Idaho; the experimentation thrust was coordinated and executed by ARD.

15. SUBJECT TERMS
ELF signals, electric fleet

16. SECURITY CLASSIFICATION OF:			17. LIMITATION OF ABSTRACT	18. NUMBER OF PAGES	19a. NAME OF RESPONSIBLE PERSON
			UU	68	Jeffrey L. Young
a. REPORT	b. ABSTRACT	c. THIS PAGE			19b. TELEPONE NUMBER (Include area code)
U	U	U			208-885-6829

Final Report

Investigation of ELF Signals Associated with Mine Warfare: A University of Idaho and Acoustic Research Detachment Collaboration, Phase Two

by

Jeffrey L. Young, Dennis M. Sullivan, Robert G. Olsen and Christopher L. Wagner

Primary Contact:
Jeffrey L. Young
MRC Institute/Electrical and Computer Engineering
University of Idaho
Moscow, ID 83844-1024
208-885-6829
jyoung@uidaho.edu

for

Mr. Leroy Sverduk, PE
Office of Naval Research
One Liberty Center
875 N. Randolph St., Rm 1016
Arlington, VA 22203-1995

NSWCCD-753 / ONR-321
Cell: (240) 507-7910
Carderock Office: (301) 227-3163
ONR Office: (703) 696-8557

July 31, 2010

Supporting Information:

Introduction

Described herein are the key findings and results associated with the project entitled "Investigation of ELF Signals Associated with Mine Warfare, A University of Idaho and Acoustic Research Detachment Collaboration, Phase Two." Phase Two is a continuation of the Phase One effort under the same title. The scope, objectives and outcomes of Phase Two are similar to those described in the report and proposal of Phase One. Some of the following text is also found in the Phase One report.

Extremely low frequency (ELF) electromagnetic signals are used by enemy combatants to detect and, subsequently, to incapacitate, by means of surface and subsurface mines, naval vessels. This program is of high importance to the Navy – particularly since ELF signals are one of the primary signature emissions of the Navy's proposed electric ship fleet.

The questions that are being asked in this investigation are: 1) once an ELF signal is generated, how far will it propagate and still be detectable and 2) how can such signals be modeled, excited and measured? To this end, the scenario considered is one in which an ELF source of the electric or magnetic kind is located in or above water, such as a lake or ocean. This source stimulates an ELF signal that is free to propagate in the water and air, and is reflected by various material interfaces, say between the water and air, or between the water and the floor. For purposes of experimental demonstration, the investigation focuses on the scenario of ELF sources and signals in the context of Lake Pend Oreille, where the Acoustic Research Detachment (ARD, Bayview, Idaho) is located and entrusted with the necessary assets to perform validation measurements.

The research program was designed with two major thrusts: Modeling and experimentation. The modeling thrust was coordinated and executed by the University of Idaho (UI), Moscow, Idaho; the experimentation thrust was coordinated and executed by ARD. This report focuses primarily on the modeling thrust. A separate report from ARD has been issued that addresses the experimentation thrust (See "ELF Phase Three Test 1," complied by Frank Jurenka, Chris Burgy and Vicki Pfeifer, July 15, 2010. Note: ARD expensed Phase Three funds while UI was still expensing Phase Two funds.).

Both students and faculty of the University of Idaho and of Washington State University were involved in this project. Team members include:

Prof. Jeffrey L. Young (UI), Lead PI:
- Dr. Christopher L. Wagner, Research Engineer, FDTD code development
- Mr. Robert Rebich, MSEE RA, Quasi-static code development
- Mr. Christopher Johnson, MSEE RA, Data analysis and code development

- Mr. Das Butherus, MSEE RA, Data analysis and code development
- Mr. Chenchen "Jimmy" Li, BSEE RA, Topographical data translation
- Ms. Neelima Dahal, BSEE RA, Data analysis
- Mr. Markus Geiger, BSEE RA, Data analysis

Prof. Dennis Sullivan (UI):
- Mr. Yang Xia, Research engineer, FDTD parallelization code development
- Mr. Alireza Mansoori, MSEE RA, FDTD parallelization code development

Prof. Robert Olsen (WSU):
- Mr. Zhi Li, MSEE RA, Layered media modeling

ELF Modeling

The activities pursued during Phase Two continue those pursued during Phase One, with particular emphasis on the refinement and validation of the numerical models. Portions of the following text summarize the modeling effort undertaken by the University of Idaho and are also found in the Phase One report. Some of that text has been updated to reflect new knowledge gained since the Phase One report was issued. In subsequent sections, unique results and findings associated with Phase Two activities will be presented.

Modeling of ELF electromagnetic signals in water environments can be accomplished either by means of direct, analytical solution of Maxwell's equations or by numerical solutions of the same. The former is attractive for purposes of gaining insights into the physical mechanisms that hinder or aid the propagation of ELF signals. The disadvantage is found in the number of simplifying assumptions that are made to bring about a closed-form solution. A numerical solution has no such simplifying assumptions, but does suffer from discretization errors. In principle, it can model all of the physical and geometrical features of the domain of consideration. The price paid for doing so, however, is the required time and the CPU/memory resources needed to accomplish the task. Data visualization and management are other issues that need to be addressed when working with large data sets produced by numerical solvers. The positive and negative tradeoffs between these two approaches (i.e. analytical vs. numerical) suggest that no one method is superior. For that reason the UI team adopted a diverse strategy that encompasses many different approaches in order to assure a positive outcome and to provide deliverable modeling methodologies.

The five principle techniques or tools that were considered during the Phase One and Phase Two efforts were the a) Sommerfeld Half-Space (SHS) method, b) Finite-difference, time-domain method (FDTD), c) High Frequency Structural Simulator (HFSS), finite-element code, d) Maxwell code and e) quasi-static method (QES). A summary of these methods is provided next. Detailed technical information on the SHS, FDTD and quasi-static methods are provided in the attached appendices.

Sommerfeld Half-Space (SHS) Method

The SHS method is an analytical approach that assumes that all interfaces (say between water and air, or between water and floor) are planar and infinitely extended. This assumption is reasonably valid for the water-air interface, particularly in open water regions where the source is located near the surface. For the littoral zones, the method may fail, particularly when electric sources are used to excite the ELF signals. By assuming that the interfaces are flat, a closed-form solution can be devised that is cast in terms of Fourier-Bessel integrals. These integrals can be evaluated numerically and rapidly in a matter of seconds on any desktop machine. Even with the potential deficiency of treating all interfaces as planar, the SHS method is attractive as a validation tool for the other numerical modeling approaches. For example, the team used the SHS method to validate the data produced by the FDTD or HFSS methods (described next) when these numerical methods consider the same layered media problem statement. The SHS method is also attractive in quantifying the up-over-down effect. This effect is associated with a low signal loss path through the air and a high signal loss path up and down through the water. If the path through the water is short, then the up-over-down signal loss can be low relative to a direct path between a source and sensor in the water. Professor Robert Olsen of Washington State University (WSU) is the lead investigator of the SHS method.

Finite Difference, Time-Domain Method (FDTD)

The FDTD method is a numerical approach that discretizes Maxwell's equations in their fundamental form using a staggered grid and leap-frog integrator. This method has been fully vetted in the open literature and has been established as a robust way of obtaining accurate simulation data. In principle, the FDTD method accounts for all material interfaces and inhomogeneities by assigning permittivity, permeability and conductivity values along edges of the grid elements. Curvilinear boundaries are approximated by straight line, stair-stepped boundaries. For geometrical features that are significantly less than a wavelength, such stair-stepping causes no appreciable errors in the computed data. Note that the domain of interest at Lake Pend Oreille does not exceed 8 km on a side; the lake floor at its deepest point is about 335 m. Assuming an operating frequency of 100 Hz and a water conductivity of 0.018 S/m, we note that the corresponding skin depth is 375 m and the wavelength is 2.356 km; for air, the wavelength is 3,000 km. Thus the domain spans a fraction of a wavelength in air but about 3.4 wavelengths (or 21.3 skin depths) in water. The significant disparity between these two relative sizes potentially introduces computational complexities. One area of concern is the proper design of an absorbing boundary condition (ABC) or perfectly matched layer (PML) that will allow an open physical domain to be truncated into a finite computational domain. Placement of this

4

ABC/PML in terms of wavelengths is critical if non-spurious reflections are to be avoided. Significant time and effort was expended to figure out a way to design an optimal PML. The outcome of this effort is described in the paper by Wagner and Young, "FDTD numerical tests of the convolutional-PML at extremely low frequencies," *IEEE Antennas and Wireless Propagation Letters,* vol. 8, pp. 1398-1401, 2009. This paper is attached to this report. Dr. Christopher Wagner of the University of Idaho is the lead researcher of the FDTD and PML effort.

Given the amount of computing time that is required to run an FDTD simulation for domain sizes contemplated in this project (domains are on the order of kilometers), simulation times can be excessive (i.e. hours to days). For this reason, an effort in computational parallelization was undertaken using message passing interface (MPI) protocols and specialized graphics hardware. As shown in Appendix C, simulation times can be reduced by over a factor 16 using these kinds of parallelization techniques. Professor Dennis Sullivan of the University of Idaho is the lead researcher of this activity.

High Frequency Structural Simulator (HFSS)

HFSS is a commercially available electromagnetic, finite-element, frequency-domain, numerical solver that has been designed by Ansoft/Ansys for antenna and microwave circuit applications. One question that was asked in this investigation was whether such a tool could be used to predict the electromagnetic propagation characteristics of an ELF signal in a highly conductive environment. In Phase One and Two, the answer to this question was inconclusive due to source modeling issues. (In the Phase Three report, however, the answer will be more conclusive and positive.) Professor Jeffrey Young of the University of Idaho is the lead engineer of the HFSS effort.

Maxwell

Maxwell is also a commercial code developed by Ansoft/Ansys. However, unlike HFSS, it is a static solver for either electric or magnetic fields. Since ELF waves are static-like in the vicinity of the source, questions that have been raised by the team are these: 1) At what distance are the fields more static-like rather than wave-like and 2) can ELF waves be modeled by a static solver in some region about the source. Professor Jeffrey Young of the University of Idaho is the lead engineer of this effort.

Quasi-Static Method

A custom quasi-static method was also considered given that ELF signals are quasi-static in the vicinity of the source. By definition, the quasi-static method does not consider any wavelike mechanisms in Maxwell's equations; it assumes that the field lines are the same

as the static field, but oscillating. This is accomplished by neglecting magnetic displacement currents for electric sources. By doing so, simple solutions can be constructed that correlate well with other more advanced solutions, like HFSS and FDTD. Professor Jeffrey Young of the University of Idaho is the lead engineer of the quasi-static modeling effort.

Lake Parameters and Discretization

Unlike the December 2008 experiments in which the experiments were conducted in an open area of the lake, the domain for the March 2010 experiment encompasses significant geometrical features above and below water. This was purposefully chosen to be so in order to exercise the limits of the various numerical and analytical models. That is, we would expect the ELF signals in the open area to be far easier to model than those in a more cluttered environment, due to the changes in the material parameters and geometrical features of the environment. Hence, we wanted the most severe environment possible to see if the models would fail to produce the correct data.

The FDTD and HFSS numerical methods require a precise understanding of the electrical and geometrical features of the lake. The domain of interest considered in Phase Two is the area known as Idlewilde Bay and is shown below. The domain is about 6 km by 7 km on a side and represents the general area where actual experiments were performed in March 2010 using both electric and magnetic sources. (See the report entitled "ELF Phase Three Test 1" complied by Frank Jurenka, Chris Burgy and Vicki Pfeifer, July 15, 2010. Note: ARD expensed Phase Three funds while UI was still expensing Phase Two funds.)
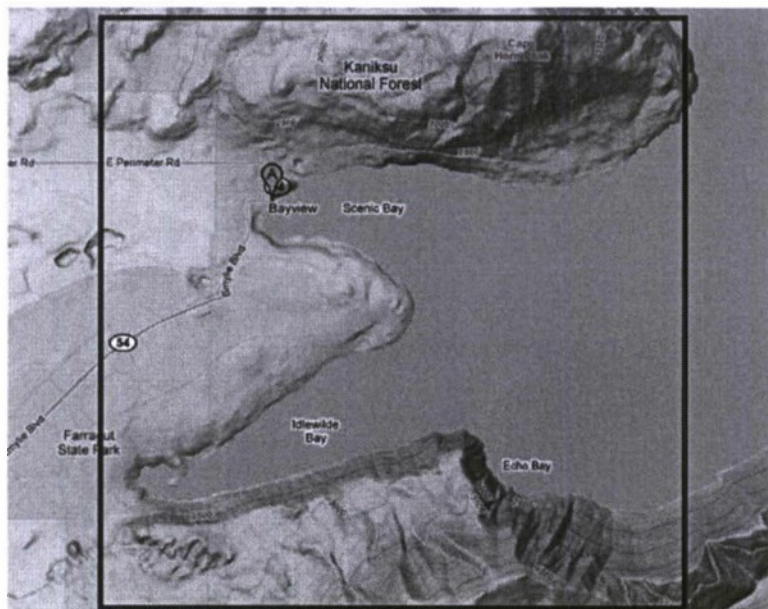
The terrain elevation data (relative to sea level) along with their corresponding coordinates (in varying forms) were extracted from three sources: a data set from insideidaho.org, an AUTOCAD file of Lake Pend Oreille Contours from the Idaho Geological Survey, and data points taken manually from a provisional map of Lake Pend Oreille. The coordinates of each data point were converted into meters northing and easting in Idaho West State Plane; any elevation data in feet were converted to meter – thus, all three data sets conform to the same system. All three data sets were compiled together (minor adjustments were made to eliminate conflict between the data sets). Interpolation of elevation data at all points along two vectors (in x and y direction that define the area to interpolate) was accomplished using the 'griddata' function in Matlab. This created a matrix height field that defines the elevation and depth of the terrain or lake at each point in 1m intervals. The matrix height field was then used as an input file for the various numerical solvers, i.e. FDTD, HFSS or Maxwell.

The height field, if used with HFSS or Maxwell, needs to be converted into a solid model. The first step is to extract data from the height field into x,y,z coordinates. Then, in AutoCAD, the command '3dmesh' is used to create a mesh that is up to 255x255 cells in dimension from those coordinates. Since the height field is 6240x7520 cells in size, the data is down-sampled so that it will be within the bounds of '3dmesh'. After meshing, an AutoCAD script, 'M2S-2007.lsp' is used to convert the mesh into a solid figure. This solid figure is then exported as an ACIS .sat file (which is supported by HFSS). However, the mesh on the surface of the solid is too refined and uniform for HFSS to use efficiently in data computation. Therefore, an additional remeshing step is necessary via the mesh tool Cubit. By combining all the surfaces of the original mesh into one composite surface, the composite surface is then meshed using one of Cubit's meshing schemes. Unfortunately, Cubit cannot imprint the new mesh onto the original AutoCAD solid; the new mesh must be converted into a solid itself. The mesh is exported into an .inp file and then re-imported into Cubit, which removes the AutoCAD solid and leaves only the Cubit mesh. The mesh is then converted into a solid within Cubit and is exported back into an ACIS .sat format. Clearly, this is an involved process, but a necessary one when using HFSS or Maxwell.

In addition to precise geometrical data, the various solvers also require precise knowledge of the conductivity of the lake and the mud at the bottom of the lake. The UI team used a value of 0.018 S/m for the water and 0.012 S/m for the mud floor. These numbers were previously measured by ARD during Phase One. As for the value of the dielectric permittivity of the lake, this was not deemed essential, since displacement currents in the lake are virtually insignificant relative to the conduction currents.

It should be noted that a major shortcoming of the modeling effort has nothing to do with the modeling methodology, but with the lack of information about the environment to be

modeled. For example, we treat the problem statement as if the environment is only comprised of three homogeneous substances: water, air and mud. Clearly, this is not so. The lake bottom, which we call mud, is actually an inhomogeneous substance of rock and silt that is saturated by water. The land, which is called mud, is an inhomogeneous substance of rock, dirt, trees and structures. Only the water and air are homogeneous for which numbers like permittivity and conductivity are known. Hence, errors between experimental data and simulation data can be attributed to the lack of knowledge of the environment and certain guesses about the quantification of the environment.

Electric and Magnetic Sources

Two kinds of electric sources were used in the March 2010 experiment: 1) a 4 meter, 2 Ampere (max) electric source placed on a boat hull that skimmed the surface of the water and 2) a 15 meter, 3 Ampere (max) portable electric source that was lowered from 15 meters in the water to the lake floor (i.e. about 152 meters). Additionally, a 3.6 meter by 3.6 meter, 12 turn, 20 Ampere magnetic source was also used to stimulate ELF signals; this source was rigidly placed on the shore at Farragut State Park. For both electric and magnetic sources, the ELF signals were measured using a portable electromagnetic array (EMA) that was lower into the water at depths ranging from 15 m to 152 m. Source and sensor locations associated with the March 2010 experiment are shown below.
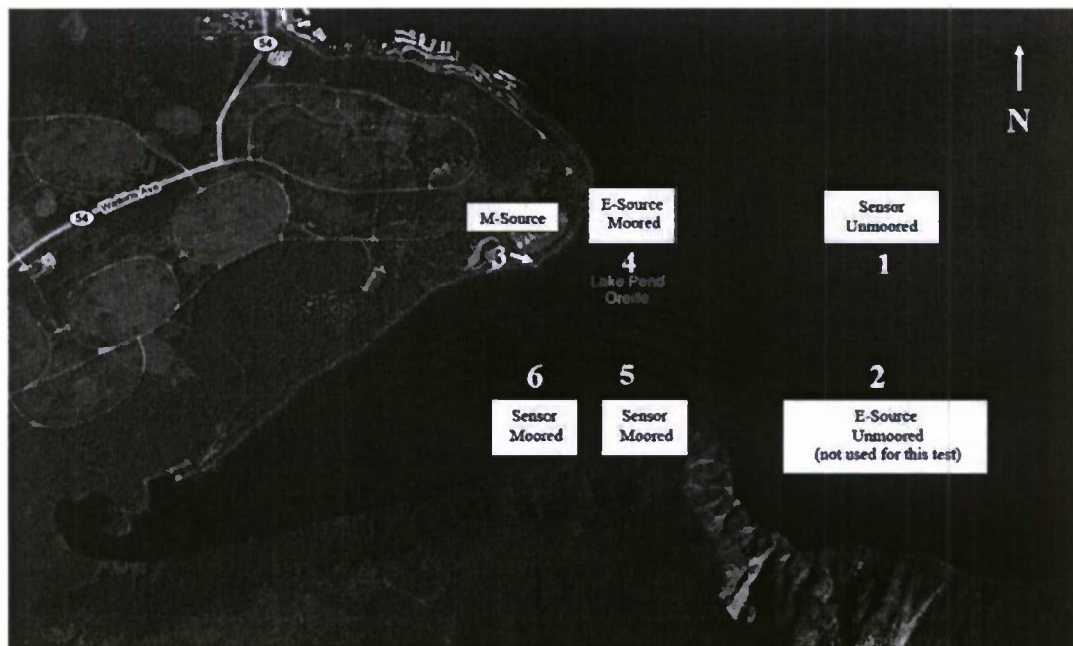
<u>Experimental Data Post-Processing</u>

Once the experimental data was collected, it was transferred to the University of Idaho in binary format for processing – particularly, to extract the desired frequency domain signals from the time-domain data. The first step was to pre-process the measured data into a useable format and to scale the data using appropriate scaling factors, as provided by ARD. Next the data was analyzed and plotted to identify experimental runs that correspond to fairly stationary source locations, since the ELF models assume both stationary sources and sensors. Typically, ten seconds of contiguous data sets can be obtained, which are transformed into the frequency domain using fast Fourier Transform (FFT) methods. The FFT data reveal the time-harmonic signal strength of each electromagnetic field component relative to the coordinate system of the experiment. To compare these data with simulation data, coordinate transformations are performed on the experimental data using GPS sensor data. The processing of the data is not completely automatic given random noise spikes and discontinuities in the data streams. To avoid post-processing conversion anomalies, only clean, contiguous data were processed.

Results

<u>Data Comparisons: Simulation Methods vs Sommerfeld Half Space Method</u>

As noted previously, the Sommerfeld Half-Space (SHS) Method, being an exact solution of Maxwell's equations, can be used to benchmark the accuracy of the various methods employed in this project. Two sets of plots are shown below for vertical magnetic dipole excitation and horizontal electric dipole excitation. For the former, it is clearly seen that the Sommerfeld data (identified as WSU, who were the developers) and the FDTD data are closely correlated, thus validating the FDTD methodology and code. There is fairly good correlation between the data sets of WSU and Maxwell and no correlation between the data sets of WSU and HFSS. This poor correlation is attributed to the way HFSS models Hertzian dipoles in lossy media. Although there are some "tricks" for getting better data, these tricks involve the use of scaling factors that cannot be rigorously justified by theory. Moreover, *a priori* reliability is never assured. (Research conducted during Phase Three has found much more reliable ways to assure good data; this will be reported in the Phase Three report.) Similar conclusions can be reached for the vertical electric dipole case, but with additional validation of the quasi-static method. Since Maxwell only predicts electric fields by assuming no excitation of the magnetic field and since the source only excites a y-component of the electric field, only a plot of E_y is shown. Yet for distances as far out as 675 meters, and low vertical depths, the quasi-static data agree with the Sommerfeld data reasonably well.
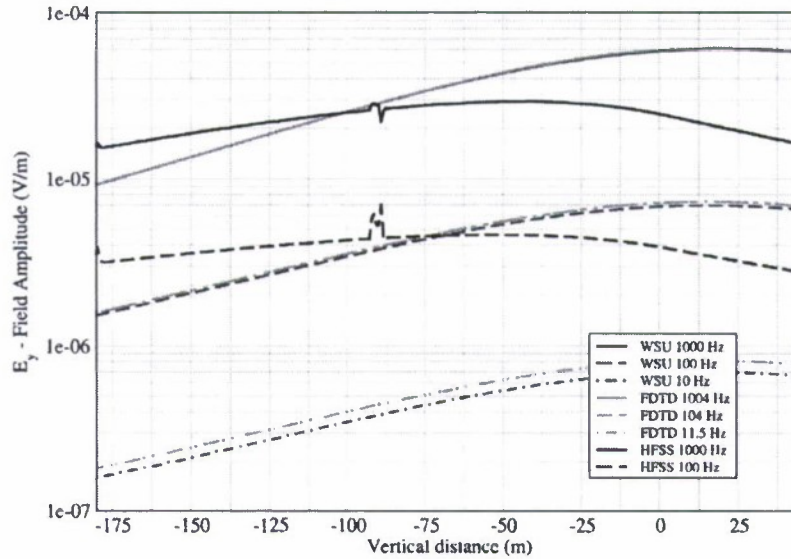
Figure 1: Electric field (*y*-component) of a 2500 A-m^2 vertical magnetic dipole (VMD) for a three layer, flat earth. The source is in air at a height of 15 m and the observation point is at a radial distance of 150 m. The field is a function of vertical distance from -180 m in water to 45 m in air.
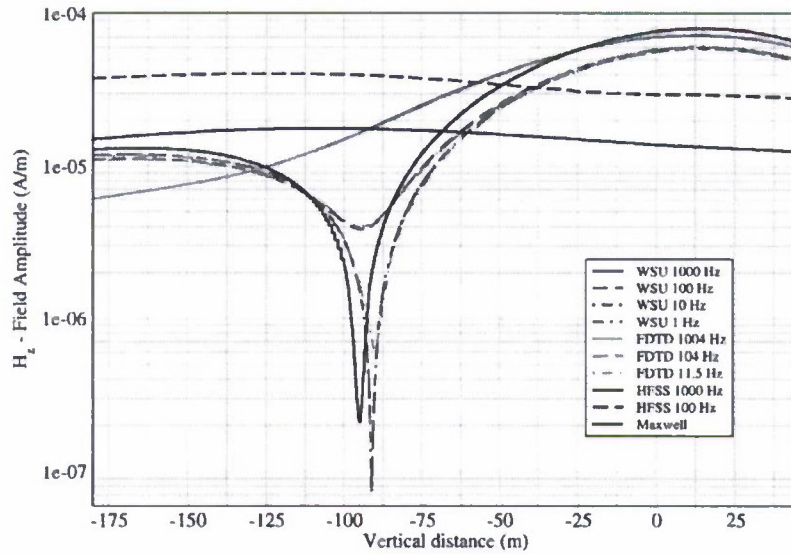

Figure 2: Magnetic field (*z*-component) of a 2500 A-m^2 vertical magnetic dipole (VMD) for a three layer, flat earth. The source is in air at a height of 15 m and the observation point is at a radial distance of 150 m. The field is a function of vertical distance from -180 m in water to 45 m in air.
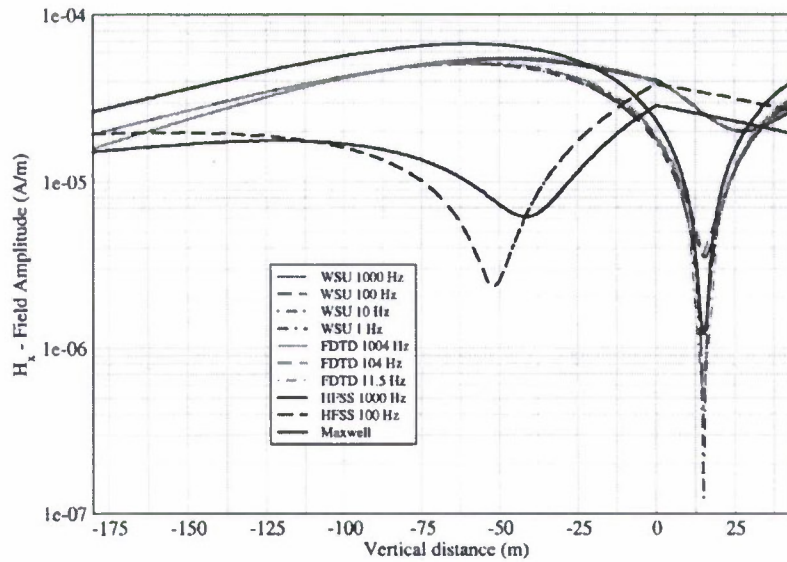
10

Figure 3: Magnetic field (*x*-component) of a 2500 A-m² vertical magnetic dipole (VMD) for a three layer, flat earth. The source is in air at a height of 15 m and the observation point is at a radial distance of 150 m. The field is a function of vertical distance from -180 m in water to 45 m in air.
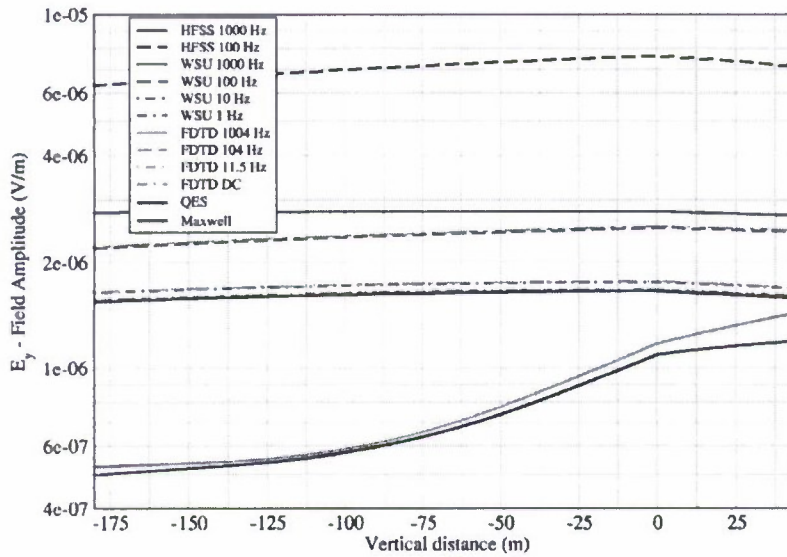

Figure 4: Electric field (*y*-component) of a 45 A-m horizontal electric dipole (HED) for a three layer, flat earth. The source is in water at a depth 90 m and the observation point is at a radial distance of 675 m. The field is a function of vertical distance from -180 m in water to 45 m in air.

11

Figure 5: Magnetic field (*z*-component) of a 45 A-m horizontal electric dipole (HED) for a three layer, flat earth. The source is in water at a depth 90 m and the observation point is at a radial distance of 675 m. The field is a function of vertical distance from -180 m in water to 45 m in air.
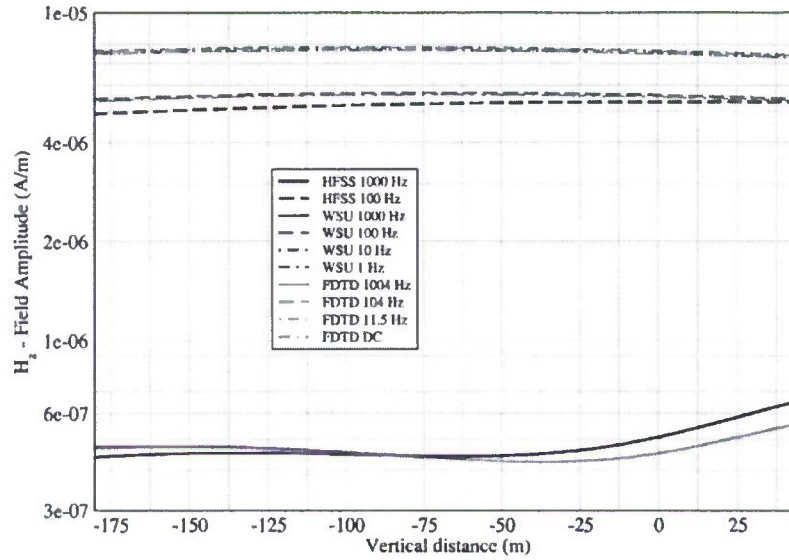

Figure 6: Magnetic field (*x*-component) of a 45 A-m horizontal electric dipole (HED) for a three layer, flat earth. The source is in water at a depth 90 m and the observation point is at a radial distance of 675 m. The field is a function of vertical distance from -180 m in water to 45 m in air.
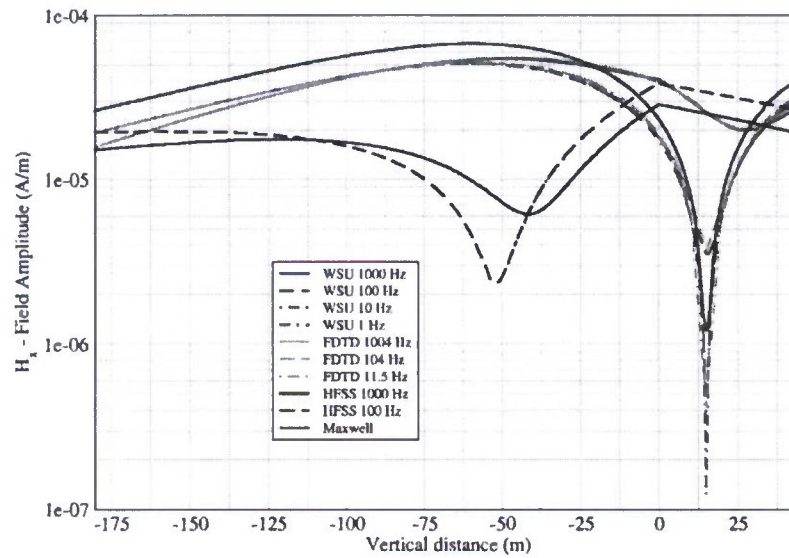
12

Data Comparisons: Simulation vs. Experimentation

The plots on the following pages show comparisons between data as obtained from experimentation and simulation. Actual experimental run numbers are shown in the figure captions. Experimental runs were selected based on those runs that had sufficient contiguous data streams unaffected by noise and random noise spikes. Runs were grouped to form a single reference set for comparison. Due to the way the experiments were conducted and the way the data was collected, it was not uncommon to have only three data points per set. Finally, not all of the March 2010 experimental data was processed during Phase II. Additional processing of that data is also occurring in Phase Three; which will be presented in the Phase Three Final Report. The following table correlates the figure numbers with the run numbers.

Figures 7, 8 and 9	Runs 3003, 3111 and 3203
Figures 10, 11 and 12	Runs 2003, 2007 and 2011
Figures 13, 14 and 15	Runs 2404, 2408 and 2412
Figures 16, 17 and 18	Runs 4304x, 4304y and 4304z

Figures 7-9 show the electric field components excited by a 100 Hz portable electric source at a depth of 15.2 meters at map location 4. The observation distance is 505 meters at map location 5. The data are presented as a function of sensor depth. The correlation between data sets is quite good for the E_y and E_z components; the correlation is less than adequate for the E_x component. However, the modeling data for E_x are grouped together with the experimental data being the outlier. This suggests that the models are consistent in the way that the experiment is interpreted but that interpretation may be wrong. Further study is needed to assess and rectify this problem.

Figures 10-12 show electric field excited by a 100 Hz portable electric source at a depth of 15.2, 72.2 and 131.7 meters at map location 4. The observation distance is 964 meters; see map location 6. The data are presented as a function of source depth. In this case, the correlation between data sets is much better, albeit not perfect. The y-component of the electric field has two experimental data points that lie near the modeling data; however, the third data point at 131 meters is an outlier. The correlations for E_x and E_z are much better. With respect to E_z, the quasi-static data is seen to be off by a factor of ten. Yet, since the observation distance is 964 meters, such distances fall outside the domain of validity for the quasi-static method.

Figures 13-15 show electric field excited by a 1,000 Hz portable electric source at a depth of 15.2, 76.2 and 121.9 meters at map location 4. The observation distance is 1,000 meters; see map location 6. The data are presented as a function of source depth. The

correlation between data sets is by far the worst. However, the quasi-static method appears to give the best results, even though the observation distance is far from the source.

Finally, Figure 16-18 show electric field excited by the magnetic source on the shore at map location 3. The observation distance is 675 meters at map location 6. The data are presented as a function of sensor depth. The HFSS data are clearly questionable. This poor data is attributed to the way the source is modeled in HFSS; a new source model has since been developed and is currently being tested. The FDTD method seems to give better results, but the data for E_x are particularly bad. This poor correlation can be explained by noting that the source is on the shore and the FDTD method models the shore as if it were a homogeneous substance of mud, which it is not. If the constitutive composition of the shore is not known somewhat precisely in the vicinity of the shore, then there is no expectation that the model will predict the experimental outcome.

To highlight this last comment, consider Figures 19 and 20. Both figures show the field data, as obtained from FDTD simulation, for two different value of shore conductivity (i.e. rock vs. mud); all other parts of the simulation are the same for the two cases (i.e. source, geometry, etc.). There is no question from this data that the fields are highly dependent on conductivity, thus supporting the previous claim that when the source (or observation point) is near a material boundary or interface, the constitutive composition of that material must be known to a high degree of accuracy if good data are to be obtained.

It should be noted that magnetic field data are not shown, even for magnetic source excitation. This is due to the very weak magnetic field signal that was received relative to the noise floor. Even when the source and observation points were close to each other (i.e. 100 meters), the signal was too weak to detect. The noise floor could be reduced by integrating the time domain data over longer periods of time, but that would require the sensor array to be stationary for long periods of time, which it was not. A Phase Three experiment will be conducted to rectify this latter problem along with new post-processing methods that will account for sensor motion.
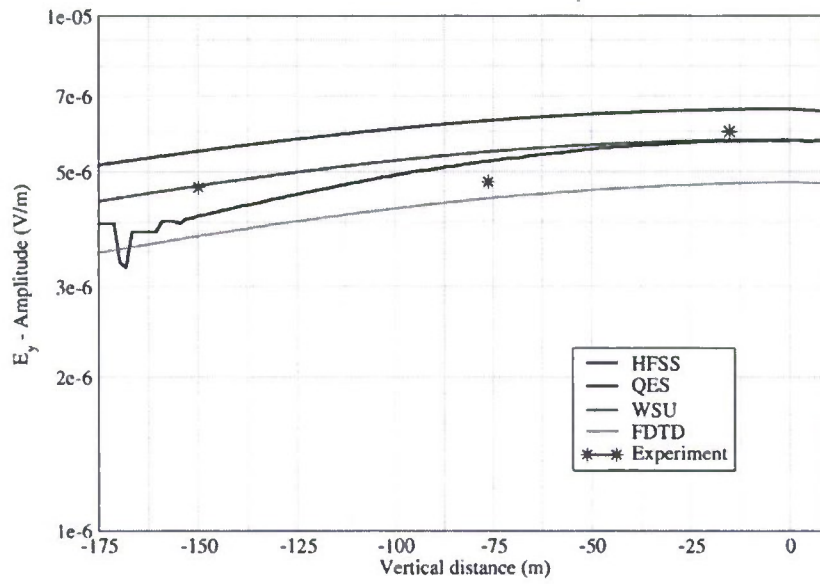
Figure 7: Electric field (*y*-component) excited by a 100 Hz portable electric source at a depth of 15.2 meters at map location 4. The observation distance is 505 meters at map location 5. The data are presented as a function of sensor depth and corresponds to runs 3003, 3111 and 3203.

Figure 8: Electric field (*x*-component) excited by a 100 Hz portable electric source at a depth of 15.2 meters at map location 4. The observation distance is 505 meters at map location 5. The data are presented as a function of sensor depth and corresponds to runs 3003, 3111 and 3203.
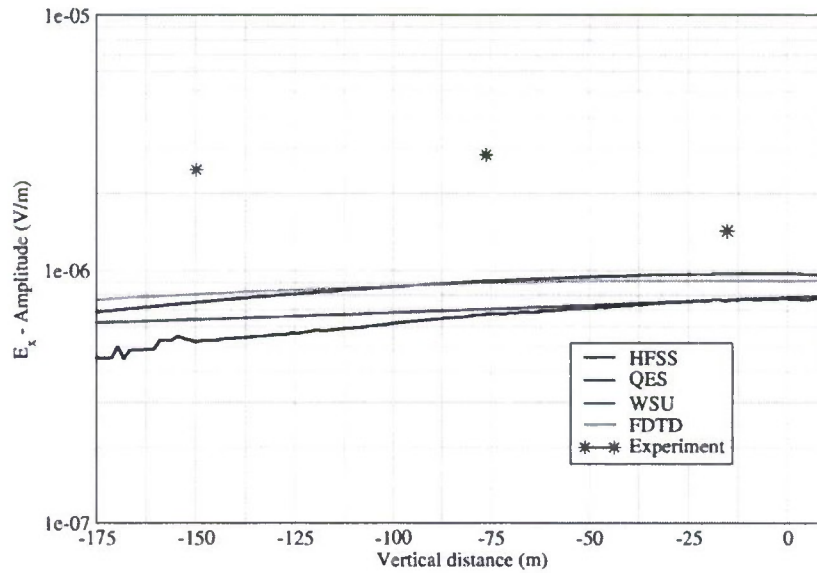
Figure 9: Electric field (*z*-component) excited by a 100 Hz portable electric source at a depth of 15.2 meters at map location 4. The observation distance is 505 meters at map location 5. The data are presented as a function of sensor depth and corresponds to runs 3003, 3111 and 3203. The dotted line is the experimental noise floor.
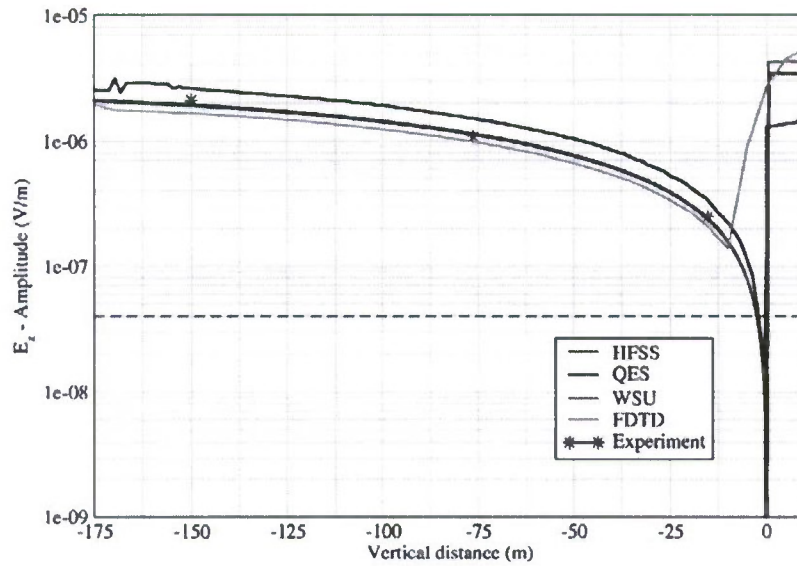

Figure 10: Electric field (*y*-component) excited by a 100 Hz portable electric source at a depth of 15.2, 72.2 and 131.7 meters at map location 4. The observation distance is 964 meters; see map location 6. The data are presented as a function of source depth and corresponds to runs 2003, 2007 and 2011. The dotted line is the experimental noise floor.
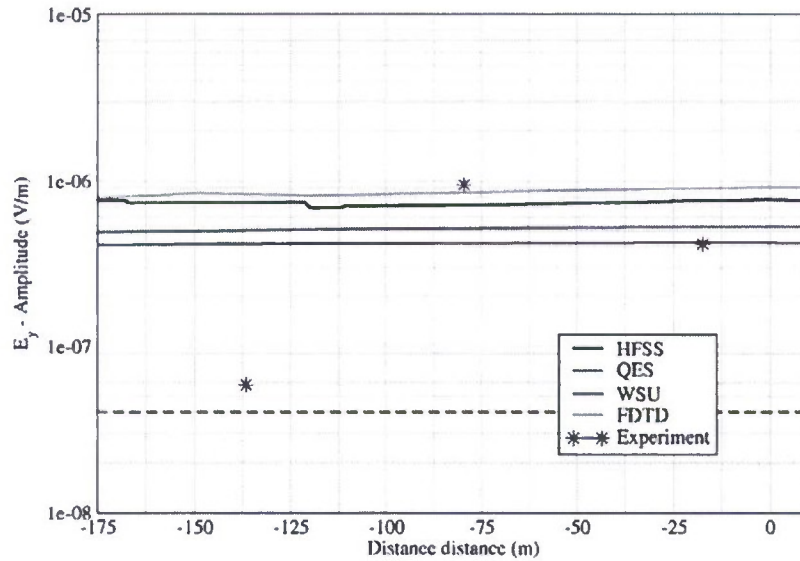
Figure 11: Electric field (*x*-component) excited by a 100 Hz portable electric source at a depth of 15.2, 72.2 and 131.7 meters at map location 4. The observation distance is 964 meters; see map location 6. The data are presented as a function of source depth and corresponds to runs 2003, 2007 and 2011. The dotted line is the experimental noise floor.

Figure 12: Electric field (*z*-component) excited by a 100 Hz portable electric source at a depth of 15.2, 72.2 and 131.7 meters at map location 4. The observation distance is 964 meters; see map location 6. The data are presented as a function of source depth and corresponds to runs 2003, 2007 and 2011. The dotted line is the experimental noise floor.
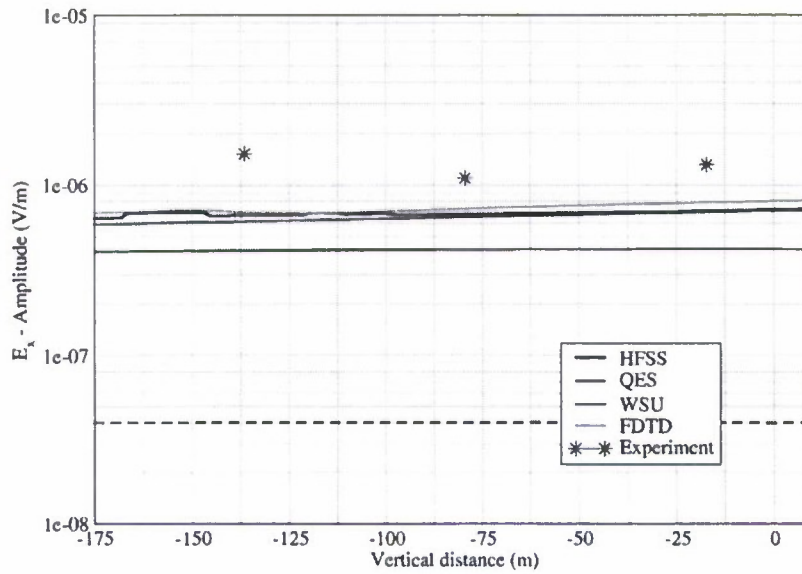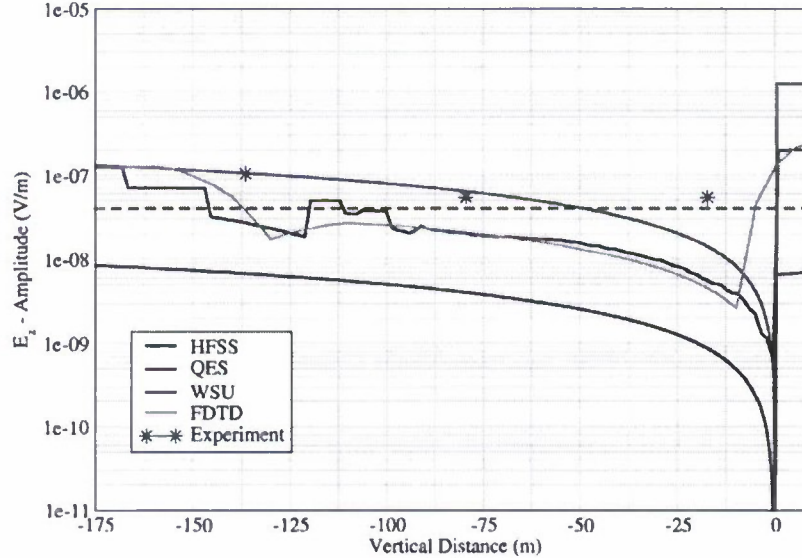
17

Figure 13: Electric field (*y*-component) excited by a 1,000 Hz portable electric source at a depth of 15.2, 76.2 and 121.9 meters at map location 4. The observation distance is 1,000 meters; see map location 6. The data are presented as a function of source depth and corresponds to runs 2404, 2408 and 2412. The dotted line is the experimental noise floor.

Figure 14: Electric field (*x*-component) excited by a 1,000 Hz portable electric source at a depth of 15.2, 76.2 and 121.9 meters at map location 4. The observation distance is 1,000 meters; see map location 6. The data are presented as a function of source depth and corresponds to runs 2404, 2408 and 2412. The dotted line is the experimental noise floor.
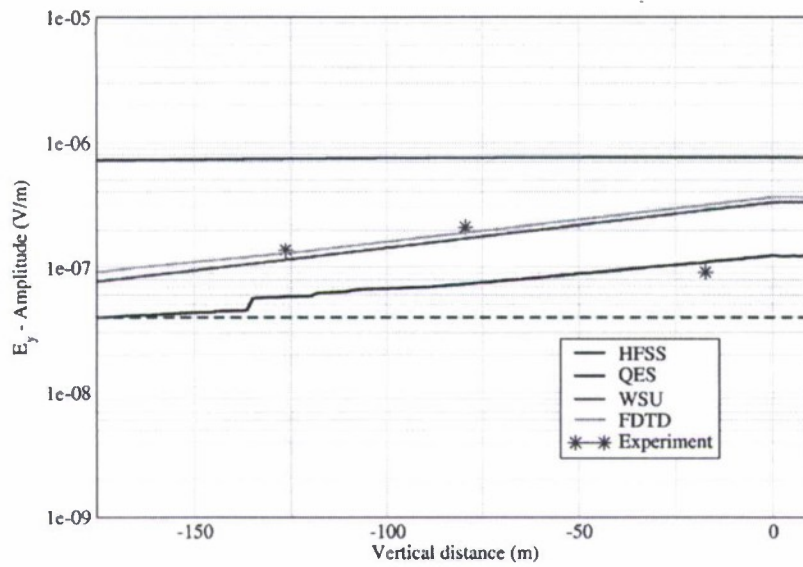
18

Figure 15: Electric field (z-component) excited by a 1,000 Hz portable electric source at a depth of 15.2, 76.2 and 121.9 meters at map location 4. The observation distance is 1,000 meters; see map location 6. The data are presented as a function of source depth and corresponds to runs 2404, 2408 and 2412. The dotted line is the experimental noise floor.
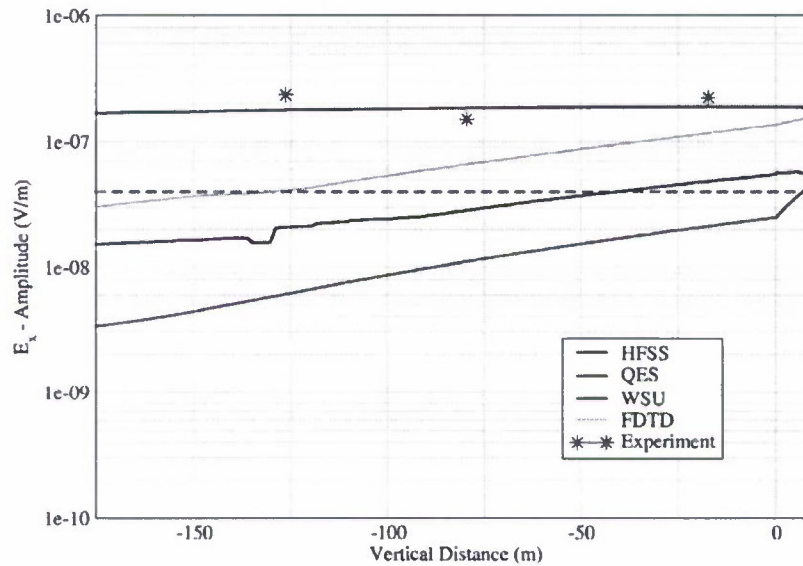

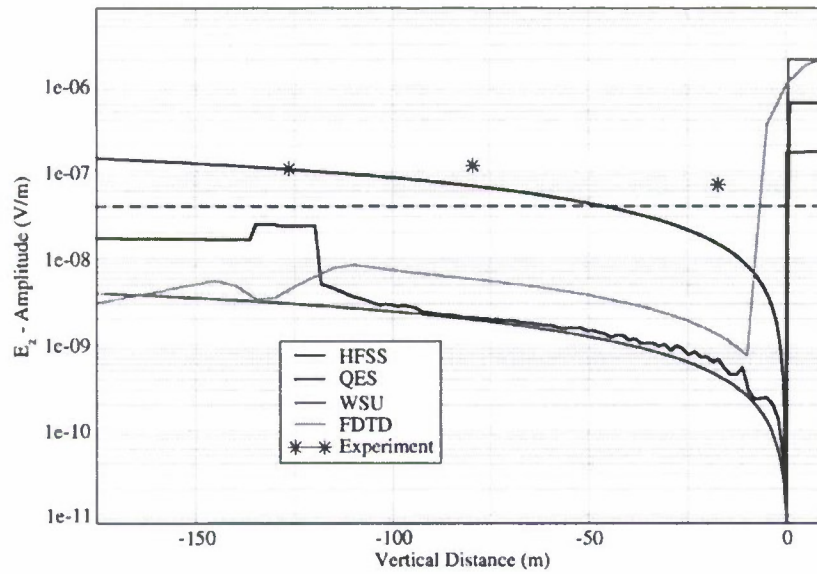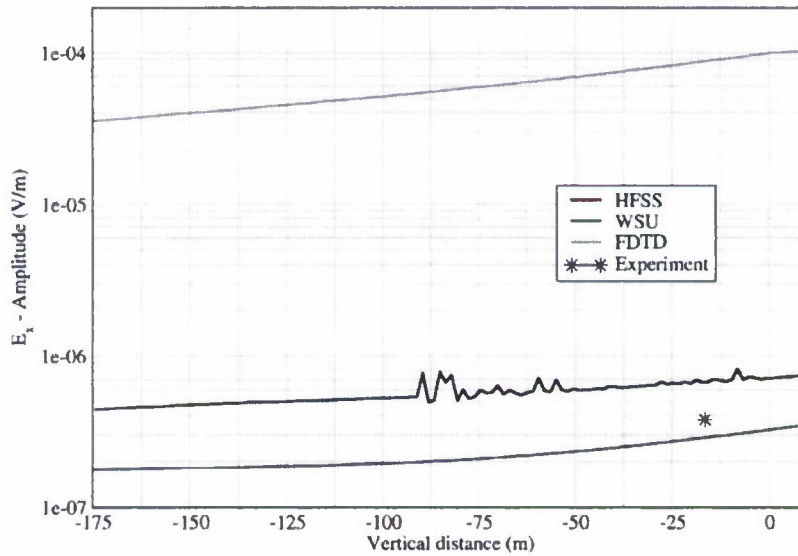**Figure 16**: Electric field (x-component) excited by the magnetic source on the shore at map location 3. The observation distance is 675 m at map location 6. The data are presented as a function of sensor depth and corresponds to runs 4304x, 4304y and 4304z.

Figure 17: Electric field (*z*-component) excited by the magnetic source on the shore at map location 3. The observation distance is 675 m at map location 6. The data are presented as a function of sensor depth and corresponds to runs 4304x, 4304y and 4304z.

Figure 18: Electric field (*y*-component) excited by the magnetic source on the shore at map location 3. The observation distance is 675 m at map location 6. The data are presented as a function of sensor depth and corresponds to runs 4304x, 4304y and 4304z.
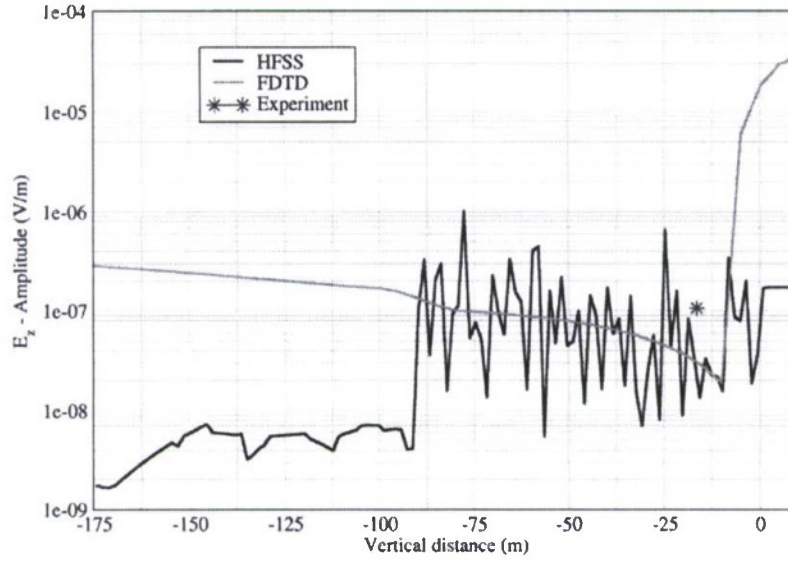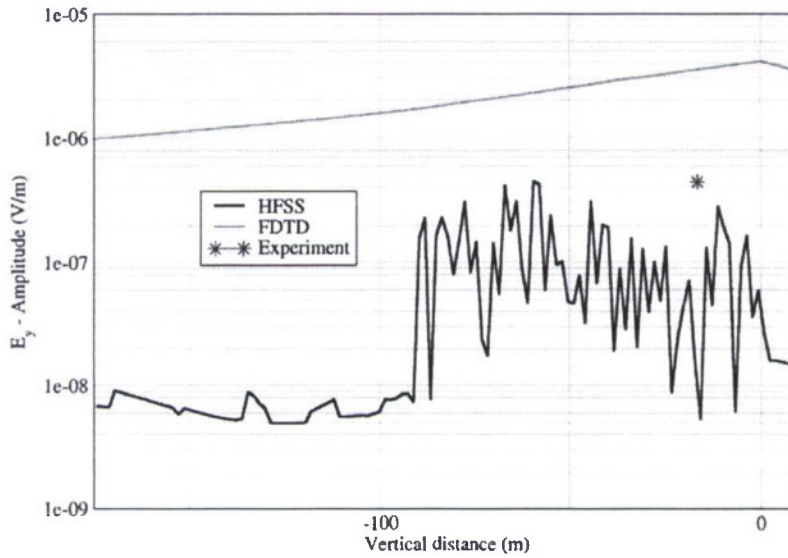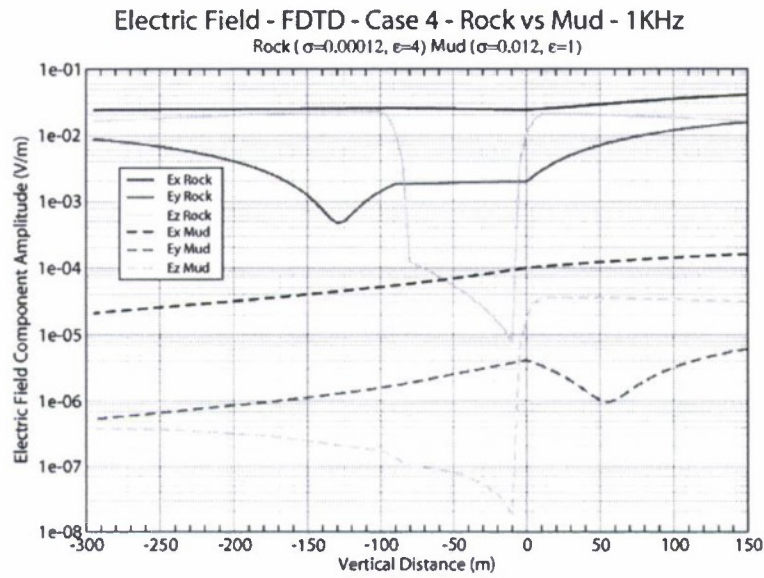
20

Figure 19: FDTD electric field data for different conductivities for the shore and lake bottom (i.e. rock vs. mud).
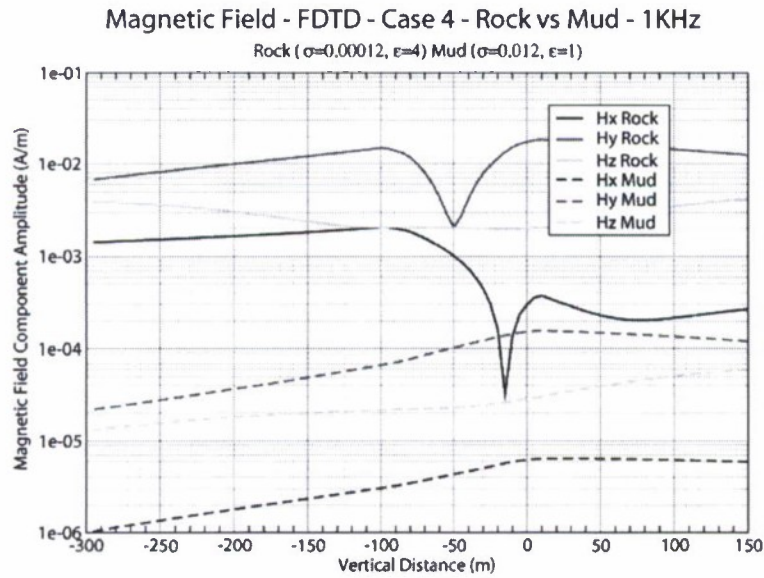

Figure 20: FDTD magnetic field data for different conductivities for the shore and lake bottom (i.e. rock vs. mud).

Future Work

Based on the previous discussions and the objectives of the project, the following future work is envisioned:

- Fully validate the new source model in HFSS.
- Implement a new data post-processing method that accounts for sensor and source rotation.
- Conduct one more set of experiments on the lake. Particular emphasis will be on source and sensor locations near the shore and on magnetic field sensing from the magnetic source when source and sensor are close to each other.
- Refine the FDTD and quasi-static codes to obtain better data as compared to the experimental data.
- Improve FDTD processing times using parallelization techniques.
- Deliver Phase Three user manuals and documentation for each of the developed models and codes.

Journals Articles to Date:

- Y. Xia and D.M. Sullivan, "Underwater FDTD simulations at extremely low frequencies," *IEEE Antennas and Wireless Propagation Letters*, vol. 7, pp. 661-664, 2008.
- Y. Xia and D. M. Sullivan, Z. Li, and R. Olsen "Dual problem space FDTD simulation for underwater ELF applications," *IEEE Antennas and Wireless Propagation Letters*, vol. 8, pp. 498-501, 2009.
- C. L. Wagner and J. L. Young, "FDTD numerical tests of the convolutional-PML at extremely low frequencies," *IEEE Antennas and Wireless Propagation Letters,* vol. 8, pp. 1398-1401, 2009.
- D. M. Sullivan, Y. Xia and D. Butherus, "A perfectly matched layer for lossy media at extremely low frequencies," *IEEE Antennas and Wireless Propagation Letters*, vol. 8, pp. 1080-1083, 2009.

These journal papers are appended to this report.

Papers in Preparation:

- R. G. Olsen and Z. Li, "A simple up-over-down model for low frequency horizontal electric dipole propagation near an interface," *IEEE Transactions on Antennas and Propagation.* (Appended to this document.)

22

Conference Publications to Date:

- D. M. Sullivan and Y. Xia, "Underwater ELF simulation using the FDTD method," IEEE International Antennas and Propagation Symposium and USNC/URSI Radio Science Meeting, San Diego, CA, June 5-11, 2008.
- Y. Xia and D. M. Sullivan, "Near to far field transformation for underwater ELF simulation," IEEE International Antennas and Propagation Symposium and USNC/URSI Radio Science Meeting, San Diego, CA, June 5-11, 2008.
- Y. Xia, A. Monsoori, D. M. Sullivan and J. Nadobny, "High resolution interpolation for underwater FDTD simulation at ELF frequencies," IEEE International Antennas and Propagation Symposium and USNC/URSI Radio Science Meeting, Charleston, SC, June 1-5, 2009.
- D. M. Sullivan, Y. Xia, "A perfectly matched layer for lossy media at extremely low frequencies," IEEE International Antennas and Propagation Symposium and USNC/URSI Radio Science Meeting, Charleston, SC, June 1-5, 2009.
- C. L. Wagner and J. L. Young, "Characterizing the convolutional perfectly matched layer at extremely low frequencies," 2010 IEEE International Symposium on Antennas and Propagation and CNC/USNC/URSI Radio Science Meeting, Toronto, Ontario, July 2010.
- D. Butherus, Y. Xia, D. M. Sullivan, "Time-domain near-to-far field transformation for underwater FDTD simulations at ELF frequencies," 2010 IEEE International Symposium on Antennas and Propagation and CNC/USNC/URSI Radio Science Meeting, Toronto, Ontario, July 2010.
- Y. Xia and D. M. Sullivan, "Underwater ELF Simulation using dedicated hardware," 2010 IEEE International Symposium on Antennas and Propagation and CNC/USNC/URSI Radio Science Meeting, Toronto, Ontario, July 2010.
- D. M. Sullivan, Y. Xia, A. Mansoori, "Large scale underwater FDTD ELF simulations using Acceleware and MPI parallel processing," URSI International Symposium on Electromagnetic Theory, Berlin, Germany, August 16-19, 2010.

Master of Science Theses:

- Y. Xia, "Three-Dimensional FDTD Simulation for Underwater ELF Signals," Master of Science in Electrical Engineering, University of Idaho, August, 2008.
- A. Mansoori, "Parallel Three-Dimensional FDTD Algorithm Using the MPI Library," Master of Science in Electrical Engineering, University of Idaho, August, 2010.

Appendix A

Electromagnetic Fields from an Electric or Magnetic Dipole in a

Three-layered Medium

Robert G. Olsen and Zhi Li

School of Electrical Engineering & Computer Science, Washington State University

Introduction

The electric (E) and magnetic (H) fields from a dipole (electric or magnetic), which is placed in the top half or buried in the middle layer of a three-layer medium, can be determined by the Sommerfeld integral method. The objective of this report is to find and validate the solutions to the E and H fields anywhere in the model in terms of the Sommerfeld integrals.

In the three-layered model, two half spaces occupy the top and bottom of the medium, which are denoted as #0 and #2 medium. The #0 medium is assumed to be free space and the #1 is lossy, representing lake bottom. And in between there is a layer conducting medium with a uniform thickness of d. The middle layer is denoted as #1 medium and it represents lake water. In this project, the dipole source is allowed to be placed in either #0 or #1 medium. Therefore, according to the type (electric or magnetic), orientation (vertical or horizontal) and position (in #0 or #1 medium), there are eight different cases of dipole source to be studied in this project. The eight cases and their assigned identifiers are shown in Table 1.

Table 1   Eight cases of dipole source

Case number	Descriptions	Identifier
1	Horizontal electric dipole (HED) in #0 medium;	HED^0
2	Horizontal electric dipole (HED) in #1 medium;	HED^1
3	Horizontal magnetic dipole (HMD) in #0 medium;	HMD^0
4	Horizontal magnetic dipole (HMD) in #1 medium;	HMD^1
5	Vertical electric dipole (VED) in #0 medium;	VED^0
6	Vertical electric dipole (VED) in #1 medium;	VED^1
7	Vertical magnetic dipole (VMD) in #0 medium;	VMD^0
8	Vertical magnetic dipole (VMD) in #1 medium.	VMD^1

Without losing generality, the case of HMD in #1 medium, HMD^1 is chosen as example in the report to show the detailed process how to find the solutions, by the Sommerfeld integral method, to E and H fields at the field point anywhere in the model. The results of the other seven cases will be listed at the end of the report.

Geometry of Case HMD^1

For the case HMD^1, a horizontal magnetic dipole (HMD) is placed in the middle layer (#1) of the three-layered medium. The 'y' oriented HMD, with a dipole moment of IdA (A-m^2), is on the 'z' axis and buried in medium #1 and 'h' meters below the interface between medium #0 and #1 ($-d < z < 0$). The cylindrical coordinate system (ρ, φ, z) is used in this paper, where $x = \rho\cos\varphi$ and $y = \rho\sin\varphi$. Thus, the observation (or field) point is assumed to be at (ρ, φ, z). Fig. 1 illustrates the model.
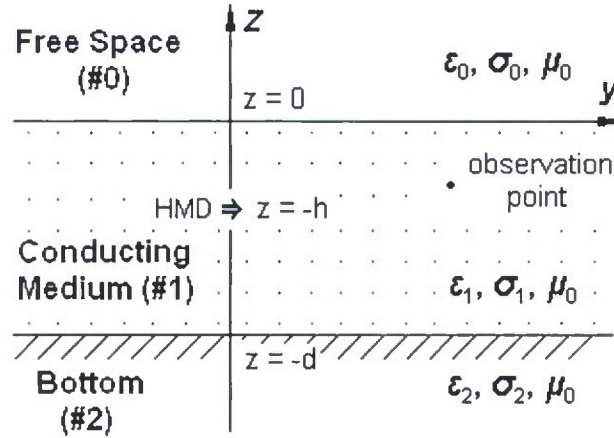
Fig. 1   Illustration of the model

As noted in the figure, ε_i and σ_i are the permittivity and conductivity of the ith half space ($i = 0$ and 1 for free space and conductor, respectively). $\varepsilon_i = \varepsilon_{ri}\varepsilon_0$, where ε_{ri} is the relative permittivity and ε_0 is the permittivity of free space. It is assumed that all materials have the permeability of free space μ_0. Before the derivations, some of the constants and variables need to be defined.

$$\gamma_i^2 = -\omega^2\mu\varepsilon_i' = -\omega^2\mu(\varepsilon_i - j\frac{\sigma_i}{\omega})$$

$$u_i = \sqrt{(\lambda^2 + \gamma_i^2)}$$

where $\varepsilon_i' = \varepsilon_i - j\sigma_i/\omega$ is the complex permittivity of the medium #i's ($i = 0$, 1 or 2), k_i is the wave number where $\text{Re}(\gamma_i) \leq 0$ and $\text{Re}(u_i) \geq 0$ defines the proper Reimann sheet of the complex plane.

25

Sommerfeld Integral Equations to E and H Fields

According to the theory of electromagnetics, the fields due to the dipole radiation should satisfy the boundary condition at both the interfaces. For the horizontal dipole case, to fulfill the boundary conditions two non-zero components of vector potentials are required. The pair can be a variety of combinations of the vector potentials. In this project, for the convenience of derivation, we choose F_y and F_z to be the only non-zero vector potentials. The vector potentials can be written in terms of Sommerfeld integrals as:

$$F_y^0 = k_1 \int_0^\infty f_1(\lambda) e^{-u_0 z} \lambda J_0(\lambda\rho) d\lambda \quad (z \geq 0) \tag{1}$$

$$F_y^1 = k_1 \frac{e^{\gamma_1 R}}{R} + k_1 \int_0^\infty \left[f_2(\lambda) e^{-u_1 z} + f_3(\lambda) e^{u_1 z} \right] \lambda J_0(\lambda\rho) d\lambda \quad (-d \leq z \leq 0) \tag{2}$$

$$F_y^2 = k_1 \int_0^\infty f_4(\lambda) e^{u_2 z} \lambda J_0(\lambda\rho) d\lambda \quad (z \leq -d) \tag{3}$$

where $\dfrac{e^{\gamma_1 R}}{R} = \begin{cases} \int_0^\infty u_1^{-1} e^{-u_1(z+h)} \lambda J_0(\lambda\rho) d\lambda & (z+h) \geq 0 \\ \int_0^\infty u_1^{-1} e^{u_1(z+h)} \lambda J_0(\lambda\rho) d\lambda & (z+h) \leq 0 \end{cases}$ is the source term and represents the

field directly from the dipole source, $R = (\rho^2 + z^2)^{1/2}$ is the distance from the dipole to the

observation point, and $k_1 = \dfrac{j\omega\mu\varepsilon_1' IdA}{4\pi}$. The superscripts, 0, 1 or 2, of vector potential

indicates which layer of medium the vector potential is related to.

$$F_z^0 = k_1 \frac{\partial}{\partial y} \int_0^\infty g_1(\lambda) e^{-u_0 z} \lambda J_0(\lambda\rho) d\lambda \quad (z \geq 0) \tag{4}$$

$$F_z^1 = k_1 \frac{\partial}{\partial y} \int_0^\infty \left[g_2(\lambda) e^{-u_1 z} + g_3(\lambda) e^{u_1 z} \right] \lambda J_0(\lambda\rho) d\lambda \quad (-d \leq z \leq 0) \tag{5}$$

$$F_z^2 = k_1 \frac{\partial}{\partial y} \int_0^\infty g_4(\lambda) e^{u_2 z} \lambda J_0(\lambda\rho) d\lambda \quad (z \leq -d) \tag{6}$$

Since the dipole is oriented in 'y' direction, only the F_y^1 component contains source

term, as shown in (2). In these equations, $f_1 \sim f_4$ and $g_1 \sim g_4$ are just some arbitrary coefficient functions of the integral variable λ to be determined by the boundary conditions. To find the solutions to the fields, the first step is to determine these

26

coefficient functions.

Coefficient Functions

Known the vector potentials, the electric and magnetic fields can be calculated by Maxwell's equations (7) and (8).

$$\overline{E}_F = -\frac{1}{\varepsilon}\nabla \times \overline{F} \tag{7}$$

$$\overline{H}_F = -j\omega\overline{F} - \frac{j}{\omega\mu\varepsilon}\nabla(\nabla \cdot \overline{F}) \tag{8}$$

Equation (9) to (14) give the expressions of each field components in terms of F_y and F_z.

$$E_x = -\frac{1}{\varepsilon}(\frac{\partial F_z}{\partial y} - \frac{\partial F_y}{\partial z}) \tag{9}$$

$$E_y = \frac{1}{\varepsilon}\frac{\partial F_z}{\partial x} \tag{10}$$

$$E_z = -\frac{1}{\varepsilon}\frac{\partial F_y}{\partial x} \tag{11}$$

$$H_x = -\frac{j}{\omega\mu\varepsilon} \cdot \frac{\partial}{\partial x}(\frac{\partial F_y}{\partial y} + \frac{\partial F_z}{\partial z}) \tag{12}$$

$$H_y = -\frac{j}{\omega\mu\varepsilon} \cdot \left[\frac{\partial}{\partial y}(\frac{\partial F_y}{\partial y} + \frac{\partial F_z}{\partial z}) - \gamma^2 F_y\right] \tag{13}$$

$$H_z = -\frac{j}{\omega\mu\varepsilon} \cdot \left[\frac{\partial}{\partial z}(\frac{\partial F_y}{\partial y} + \frac{\partial F_z}{\partial z}) - \gamma^2 F_z\right] \tag{14}$$

The boundary conditions to be satisfied are that all the tangential fields are continuous at both the upper and lower interfaces. At the upper interface ($z = 0$), they can be written as:

$$\frac{1}{\varepsilon_0'}F_z^0 = \frac{1}{\varepsilon_1'}F_z^1 \tag{15}$$

27

$$\frac{1}{\varepsilon_0'}\frac{\partial F_y^0}{\partial z} = \frac{1}{\varepsilon_1'}\frac{\partial F_y^1}{\partial z} \tag{16}$$

$$\frac{1}{\varepsilon_0'}\left(\frac{\partial F_y^0}{\partial y} + \frac{\partial F_z^0}{\partial z}\right) = \frac{1}{\varepsilon_1'}\left(\frac{\partial F_y^1}{\partial y} + \frac{\partial F_z^1}{\partial z}\right) \tag{17}$$

$$\frac{\gamma_0^2}{\varepsilon_0'}F_y^0 = \frac{\gamma_1^2}{\varepsilon_1'}F_y^1 \tag{18}$$

And at the lower interface ($z = -d$), they are:

$$\frac{1}{\varepsilon_2'}F_z^2 = \frac{1}{\varepsilon_1'}F_z^1 \tag{19}$$

$$\frac{1}{\varepsilon_2'}\frac{\partial F_y^2}{\partial z} = \frac{1}{\varepsilon_1'}\frac{\partial F_y^1}{\partial z} \tag{20}$$

$$\frac{1}{\varepsilon_2'}\left(\frac{\partial F_y^2}{\partial y} + \frac{\partial F_z^2}{\partial z}\right) = \frac{1}{\varepsilon_1'}\left(\frac{\partial F_y^1}{\partial y} + \frac{\partial F_z^1}{\partial z}\right) \tag{21}$$

$$\frac{\gamma_2^2}{\varepsilon_2'}F_y^2 = \frac{\gamma_1^2}{\varepsilon_1'}F_y^1 \tag{22}$$

Plugging all the vector potentials into (15) to (22) and simplifying the equations, it is obtained that

$$\frac{1}{\varepsilon_0'}g_1(\lambda) = \frac{1}{\varepsilon_1'}\left[g_2(\lambda) + g_3(\lambda)\right] \tag{23}$$

$$\frac{u_0}{\varepsilon_0'}f_1(\lambda) = \frac{1}{\varepsilon_1'}\left[e^{-u_1 h} + u_1 f_2(\lambda) - u_1 f_3(\lambda)\right] \tag{24}$$

$$\frac{1}{\varepsilon_0'}\left[f_1(\lambda) - u_0 g_1(\lambda)\right] = \frac{1}{\varepsilon_1'}\left[\frac{1}{u_1}e^{-u_1 h} + f_2(\lambda) + f_3(\lambda) - u_1 g_2(\lambda) + u_1 g_3(\lambda)\right] \tag{25}$$

$$f_1(\lambda) = \frac{1}{u_1}e^{-u_1 h} + f_2(\lambda) + f_3(\lambda) \tag{26}$$

$$\frac{1}{\varepsilon_2'}e^{-u_2 d}g_4(\lambda) = \frac{1}{\varepsilon_1'}\left[e^{u_1 d}g_2(\lambda) + e^{-u_1 d}g_3(\lambda)\right] \tag{27}$$

$$\frac{u_2}{\varepsilon_2'}e^{-u_2 d}f_4(\lambda) = \frac{1}{\varepsilon_1'}\left[e^{u_1(h-d)} - u_1 e^{u_1 d}f_2(\lambda) + u_1 e^{-u_1 d}f_3(\lambda)\right] \tag{28}$$

$$\frac{e^{-u_2 d}}{\varepsilon_2'}\left[f_4(\lambda) + u_2 g_4(\lambda)\right] = \frac{1}{\varepsilon_1'}\left[\frac{1}{u_1}e^{u_1(h-d)} + e^{u_1 d}f_2(\lambda) + e^{-u_1 d}f_3(\lambda) - u_1 e^{u_1 d}g_2(\lambda) + u_1 e^{-u_1 d}g_3(\lambda)\right] \tag{29}$$

$$e^{-u_2 d}f_4(\lambda) = \frac{1}{u_1}e^{u_1(h-d)} + e^{u_1 d}f_2(\lambda) + e^{-u_1 d}f_3(\lambda) \tag{30}$$

Let $(24) - (26) \times \dfrac{u_0}{\varepsilon_0'}$ to cancel the term of f_1, we have

$$\left(\frac{u_1}{\varepsilon_1'} - \frac{u_0}{\varepsilon_0'}\right)f_2 + \left(-\frac{u_1}{\varepsilon_1'} - \frac{u_0}{\varepsilon_0'}\right)f_3 = \frac{1}{u_1}\left(\frac{u_0}{\varepsilon_0'} - \frac{u_1}{\varepsilon_1'}\right)e^{-u_1 h} \tag{31}$$

Similarly, let $(28) - (30) \times \dfrac{u_2}{\varepsilon_2'}$ to get rid of f_4 such that

$$\left(-\frac{u_1}{\varepsilon_1'} - \frac{u_2}{\varepsilon_2'}\right)e^{u_1 d}f_2 + \left(\frac{u_1}{\varepsilon_1'} - \frac{u_2}{\varepsilon_2'}\right)e^{-u_1 d}f_3 = \frac{1}{u_1}\left(\frac{u_2}{\varepsilon_2'} - \frac{u_1}{\varepsilon_1'}\right)e^{u_1(h-d)} \tag{32}$$

Solve equation (31) and (32) together for f_2 and f_3

$$f_2 = \frac{1}{u_1 D}\left[\left(\varepsilon_1'u_0 - \varepsilon_0'u_1\right)\left(\varepsilon_2'u_1 - \varepsilon_1'u_2\right)e^{-u_1(h+d)} + \left(\varepsilon_1'u_0 + \varepsilon_0'u_1\right)\left(\varepsilon_1'u_2 - \varepsilon_2'u_1\right)e^{u_1(h-d)}\right] \tag{33}$$

$$f_3 = \frac{1}{u_1 D}\left[\left(\varepsilon_0'u_1 - \varepsilon_1'u_0\right)\left(\varepsilon_1'u_2 - \varepsilon_2'u_1\right)e^{u_1(h-d)} + \left(\varepsilon_1'u_0 - \varepsilon_0'u_1\right)\left(\varepsilon_1'u_2 + \varepsilon_2'u_1\right)e^{-u_1(h-d)}\right] \tag{34}$$

where $D = \left(\varepsilon_0'u_1 - \varepsilon_1'u_0\right)\left(\varepsilon_2'u_1 - \varepsilon_1'u_2\right)e^{-u_1 d} - \left(\varepsilon_0'u_1 + \varepsilon_1'u_0\right)\left(\varepsilon_1'u_2 + \varepsilon_2'u_1\right)e^{u_1 d}$. Then use (26) and (30) to find f_1 and f_4

$$f_1 = \frac{2\varepsilon_0'}{D}\left[\left(\varepsilon_1'u_2 - \varepsilon_2'u_1\right)e^{u_1(h-d)} - \left(\varepsilon_1'u_2 + \varepsilon_2'u_1\right)e^{-u_1(h-d)}\right] \tag{35}$$

29

$$f_4 = \frac{2\varepsilon_2' e^{u_2 d}}{D} \left[\left(\varepsilon_1' u_0 - \varepsilon_0' u_1 \right) e^{-u_1 h} - \left(\varepsilon_0' u_1 + \varepsilon_1' u_0 \right) e^{u_1 h} \right] \tag{36}$$

Next step is to solve equations (27) to (30) for $g_1 \sim g_4$. Before that, it's convenient to simplify (28) with (24)

$$-\frac{u_0}{\varepsilon_2'} g_1 = \left(\frac{1}{\varepsilon_1'} - \frac{1}{\varepsilon_0'} \right) f_1 - \frac{u_1}{\varepsilon_1'} g_2 + \frac{u_1}{\varepsilon_1'} g_3 \tag{37}$$

and to simplify (30) with (26)

$$\frac{u_2}{\varepsilon_2'} e^{-u_2 d} g_4 = \left(\frac{1}{\varepsilon_1'} - \frac{1}{\varepsilon_2'} \right) e^{-u_2 d} \cdot f_4 - \frac{u_1}{\varepsilon_1'} e^{u_1 d} g_2 + \frac{u_1}{\varepsilon_1'} e^{-u_1 d} g_3 \tag{38}$$

It is the similar routine to get g_2 and g_3, then g_1 and g_4. Let $(5) \times u_0 + (15)$:

$$(u_0 - u_1) g_2 + (u_0 + u_1) g_3 = \left(\frac{\varepsilon_1'}{\varepsilon_0'} - 1 \right) f_1 \tag{39}$$

and $(7) \times u_2 + (16)$:

$$(u_2 + u_1) e^{u_1 d} \cdot g_2 + (u_2 - u_1) e^{-u_1 d} \cdot g_3 = \left(1 - \frac{\varepsilon_1'}{\varepsilon_2'} \right) e^{-u_2 d} \cdot f_4 \tag{40}$$

Solve (39) and (40), we have

$$g_2 = \frac{\varepsilon_2'(\varepsilon_1' - \varepsilon_0')(u_2 - u_1) e^{-u_1 d} f_1 + \varepsilon_0'(\varepsilon_1' - \varepsilon_2')(u_0 + u_1) e^{-u_2 d} f_4}{\varepsilon_0' \varepsilon_2' \cdot D_1} \tag{41}$$

$$g_3 = \frac{\varepsilon_2'(\varepsilon_0' - \varepsilon_1')(u_1 + u_2) e^{u_1 d} f_1 + \varepsilon_0'(\varepsilon_2' - \varepsilon_1')(u_0 - u_1) e^{-u_2 d} f_4}{\varepsilon_0' \varepsilon_2' \cdot D_1} \tag{42}$$

where $D_1 = (u_0 - u_1)(u_2 - u_1) e^{-u_1 d} - (u_0 + u_1)(u_1 + u_2) e^{u_1 d}$. Then solve (23) and (27) to obtain g_1 and g_4.

$$g_1 = \frac{\varepsilon_2'(\varepsilon_1' - \varepsilon_0') \left[(u_2 - u_1) e^{-u_1 d} - (u_1 + u_2) e^{u_1 d} \right] f_1 + 2\varepsilon_0' u_1 (\varepsilon_1' - \varepsilon_2') e^{-u_2 d} f_4}{\varepsilon_1' \varepsilon_2' \cdot D_1} \tag{43}$$

30

$$g_4 = \frac{2\varepsilon_2' u_1 (\varepsilon_0' - \varepsilon_1') e^{u_2 d} f_1 + \varepsilon_0'(\varepsilon_1' - \varepsilon_2') \left[(u_0 + u_1) e^{u_1 d} - (u_0 - u_1) e^{-u_1 d} \right] f_4}{\varepsilon_0' \varepsilon_1' \cdot D_1} \qquad (44)$$

Integral Equations of E and H Fields

Since all the coefficient functions have been determined in part 2.1, the E and H fields anywhere in the model can be determined. After plugging the vector potentials in (1) to (6) into the Maxwell's equations (9) to (14) and some algebra manipulations, the components of E and H fields at the observation point can be obtained. The results are shown below. In medium #0 and #2, there is no dipole source. Therefore, the field component contains only the transmitted field from the interface. The transmitted field is denoted by a '*t*' in subscript of each field component.

The field component in medium #1 is formed by two parts: one is the incident field directly from the dipole source and the other one is the reflected field due to the two interfaces. They are denoted by '*i*' and '*r*' in the subscript of the corresponding field component.

In medium #0 the results are:

$$E_x^0 = E_{xt}^0 = -\frac{1}{\varepsilon_0'}\left(\frac{\partial F_z^0}{\partial y} - \frac{\partial F_y^0}{\partial z}\right) = \frac{k_1}{\varepsilon_0'}\left\{\int_0^\infty e^{-u_0 z} g_1 \cdot \left[\lambda J_0(\lambda\rho)\sin^2(\phi) + \frac{1}{\rho}J_1(\lambda\rho)\cos(2\phi)\right]\lambda^2 d\lambda - \int_0^\infty u_0 e^{-u_0 z} f_1 \lambda J_0(\lambda\rho)d\lambda\right\} \tag{45}$$

$$E_y^0 = E_{yt}^0 = \frac{1}{\varepsilon_0'}\frac{\partial F_z^0}{\partial x} = -\frac{k_1}{\varepsilon_0'}\int_0^\infty \left(e^{-u_0 z}g_1\right)\left[\lambda J_0(\lambda\rho) - \frac{2}{\rho}J_1(\lambda\rho)\right]\lambda^2\sin(\phi)\cos(\phi)d\lambda \tag{46}$$

$$E_z^0 = E_{zt}^0 = -\frac{1}{\varepsilon_0'}\frac{\partial F_y^0}{\partial x} = \frac{k_1}{\varepsilon_0'}\int_0^\infty e^{-u_0 z}f_1\lambda^2 J_1(\lambda\rho)\cos(\phi)d\lambda \tag{47}$$

$$H_x^0 = H_{xt}^0 = -\frac{j}{\omega\mu_0\varepsilon_0'}\frac{\partial}{\partial x}\left(\frac{\partial F_y^0}{\partial y} + \frac{\partial F_z^0}{\partial z}\right) = \frac{IdA\varepsilon_1'}{4\pi\varepsilon_0'}\int_0^\infty (u_0 g_1 - f_1)\left[\lambda J_0(\lambda\rho) - \frac{2}{\rho}J_1(\lambda\rho)\right]e^{-u_0 z}\lambda^2\sin(\phi)\cos(\phi)d\lambda \tag{48}$$

$$H_y^0 = H_{yt}^0 = -\frac{j}{\omega\mu_0\varepsilon_0'}\left[\frac{\partial}{\partial y}\left(\frac{\partial F_y^0}{\partial y} + \frac{\partial F_z^0}{\partial z}\right) - \gamma_0^2 F_y^0\right]$$
$$= \frac{IdA\varepsilon_1'}{4\pi\varepsilon_0'}\int_0^\infty (u_0 g_1 - f_1)\left[\lambda J_0(\lambda\rho)\sin^2(\phi) + \frac{1}{\rho}J_1(\lambda\rho)\cos(2\phi)\right]e^{-u_0 z}\lambda^2 d\lambda - \frac{IdA\varepsilon_1'}{4\pi\varepsilon_0'}\int_0^\infty \gamma_0^2 e^{-u_0 z}f_1\lambda J_0(\lambda\rho)d\lambda \tag{49}$$

$$H_z^0 = H_{zt}^0 = -\frac{j}{\omega\mu_0\varepsilon_0'}\left[\frac{\partial}{\partial z}\left(\frac{\partial F_y^0}{\partial y} + \frac{\partial F_z^0}{\partial z}\right) - \gamma_0^2 F_z^0\right] = \frac{IdA\varepsilon_1'}{4\pi\varepsilon_0'}\int_0^\infty \left(u_0 f_1 - \lambda^2 g_1\right)e^{-u_0 z}\lambda^2 J_1(\lambda\rho)\cos(\phi)d\lambda \tag{50}$$

In medium #1 the integral equations for the E and H fields are:

$$E_x^1 = -\frac{1}{\varepsilon_1'}\left(\frac{\partial F_z^1}{\partial y} - \frac{\partial F_y^1}{\partial z}\right) = E_{xi}^1 + E_{xr}^1 \tag{51a}$$

$$E_{xi}^1 = \frac{k_1}{\varepsilon_1'}\int_0^\infty \left(\begin{cases} -e^{-u_1(z+h)} & (z+h \geq 0) \\ e^{u_1(z+h)} & (z+h \leq 0) \end{cases}\right)\lambda J_0(\lambda\rho)d\lambda \tag{51b}$$

$$E_{xr}^1 = \frac{k_1}{\varepsilon_1'}\int_0^\infty \left[-u_1 e^{-u_1 z}f_2 + u_1 e^{u_1 z}f_3\right]\lambda J_0(\lambda\rho)d\lambda + \frac{k_1}{\varepsilon_1'}\int_0^\infty \left(e^{-u_1 z}g_2 + e^{u_1 z}g_3\right)\left[\lambda J_0(\lambda\rho)\sin^2(\phi) + \frac{1}{\rho}J_1(\lambda\rho)\cos(2\phi)\right]\lambda^2 d\lambda \tag{51c}$$

$$E_y^1 = \frac{1}{\varepsilon_1'}\frac{\partial F_z^1}{\partial x} = E_{yi}^1 + E_{yr}^1 \tag{52a}$$

$$E_{yi}^1 = 0 \tag{52b}$$

$$E_{yr}^1 = -\frac{k_1}{\varepsilon_1'}\int_0^\infty \left(e^{-u_1 z}g_2 + e^{u_1 z}g_3\right)\left[\lambda J_0(\lambda\rho) - \frac{2}{\rho}J_1(\lambda\rho)\right]\lambda^2 \sin(\phi)\cos(\phi)d\lambda \tag{52c}$$

$$E_z^1 = -\frac{1}{\varepsilon_1'}\frac{\partial F_y^1}{\partial x} = E_{zi}^1 + E_{zr}^1 \tag{53a}$$

33

$$E_{zi}^1 = \frac{k_1}{\varepsilon_1'} \int_0^\infty \left(\begin{cases} u_1^{-1} e^{-u_1(z+h)} & (z+h \geq 0) \\ u_1^{-1} e^{u_1(z+h)} & (z+h \leq 0) \end{cases} \right) \lambda^2 J_1(\lambda\rho)\cos(\phi)\, d\lambda \tag{53b}$$

$$E_{zr}^1 = \frac{k_1}{\varepsilon_1'} \int_0^\infty \left(e^{-u_1 z} f_2 + e^{u_1 z} f_3 \right) \lambda^2 J_1(\lambda\rho)\cos(\phi)\, d\lambda \tag{53c}$$

$$H_x^1 = -\frac{j}{\omega\mu\varepsilon_1'} \frac{\partial}{\partial x}\left(\frac{\partial F_y^1}{\partial y} + \frac{\partial F_z^1}{\partial z} \right) = H_{xi}^1 + H_{xr}^1 \tag{54a}$$

$$H_{xr}^1 = -\frac{IdA}{4\pi} \int_0^\infty \left(e^{-u_1 z} f_2 + e^{u_1 z} f_3 - u_1 e^{-u_1 z} g_2 + u_1 e^{u_1 z} g_3 \right)\left[\lambda J_0(\lambda\rho) - \frac{2}{\rho} J_1(\lambda\rho) \right] \lambda^2 \sin(\phi)\cos(\phi)\, d\lambda \tag{54b}$$

$$H_{xi}^1 = -\frac{IdA}{4\pi} \int_0^\infty \left(\begin{cases} u_1^{-1} e^{-u_1(z+h)} & (z+h \geq 0) \\ u_1^{-1} e^{u_1(z+h)} & (z+h \leq 0) \end{cases} \right)\left[\lambda J_0(\lambda\rho) - \frac{2}{\rho} J_1(\lambda\rho) \right] \lambda^2 \sin(\phi)\cos(\phi)\, d\lambda \tag{54c}$$

$$H_y^1 = -\frac{j}{\omega\mu\varepsilon_1'} \left[\frac{\partial}{\partial y}\left(\frac{\partial F_y^1}{\partial y} + \frac{\partial F_z^1}{\partial z} \right) - \gamma_1^2 F_y^1 \right] = H_{yi}^1 + H_{yr}^1 \tag{55a}$$

$$H_{yi}^1 = -\frac{IdA}{4\pi} \int_0^\infty \left(\begin{cases} u_1^{-1} e^{-u_1(z+h)} & (z+h \geq 0) \\ u_1^{-1} e^{u_1(z+h)} & (z+h \leq 0) \end{cases} \right)\left[\lambda J_0(\lambda\rho)\sin^2(\phi) + \frac{1}{\rho} J_1(\lambda\rho)\cos(2\phi) \right] \lambda^2 d\lambda - \frac{IdA}{4\pi} \int_0^\infty \left(\begin{cases} u_1^{-1} e^{-u_1(z+h)} & (z+h \geq 0) \\ u_1^{-1} e^{u_1(z+h)} & (z+h \leq 0) \end{cases} \right) \gamma_1^2 \lambda J_0(\lambda\rho)\, d\lambda \tag{55b}$$

34

$$H_{yr}^1 = -\frac{IdA}{4\pi}\left\{\int_0^\infty \left(e^{-u_1 z}f_2 + e^{u_1 z}f_3 - u_1 e^{-u_1 z}g_2 + u_1 e^{u_1 z}g_3\right)\left[\lambda J_0(\lambda\rho)\sin^2(\phi) + \frac{1}{\rho}J_1(\lambda\rho)\cos(2\phi)\right]\lambda^2 d\lambda + \int_0^\infty \left(e^{-u_1 z}f_2 + e^{u_1 z}f_3\right)\cdot\gamma_1^2\lambda J_0(\lambda\rho)d\lambda\right\}$$

(55c)

$$H_z^1 = -\frac{j}{\omega\mu\varepsilon_1'}\left[\frac{\partial}{\partial z}\left(\frac{\partial F_y^1}{\partial y} + \frac{\partial F_z^1}{\partial z}\right) - \gamma_1^2 F_z^1\right] = H_{zi}^1 + H_{zr}^1$$

(56a)

$$H_{zi}^1 = -\frac{IdA}{4\pi}\int_0^\infty \left(\begin{cases}-e^{-u_1(z+h)} & (z+h\geq 0)\\ e^{u_1(z+h)} & (z+h\leq 0)\end{cases}\right)\lambda^2 J_1(\lambda\rho)\sin(\phi)d\lambda$$

(56b)

$$H_{zr}^1 = -\frac{IdA}{4\pi}\int_0^\infty \left(-u_1 e^{-u_1 z}f_2 + u_1 e^{u_1 z}f_3 + \lambda^2 e^{-u_1 z}g_2 + \lambda^2 e^{u_1 z}g_3\right)\lambda^2 J_1(\lambda\rho)\sin(\phi)d\lambda$$

(56c)

Fields in medium #2 are:

$$E_x^2 = E_{xi}^2 = -\frac{1}{\varepsilon_2'}\left(\frac{\partial F_z^2}{\partial y} - \frac{\partial F_y^2}{\partial z}\right) = \frac{k_1}{\varepsilon_2'}\int_0^\infty e^{u_2 z}g_4\cdot\left[\lambda J_0(\lambda\rho)\sin^2(\phi) + \frac{1}{\rho}J_1(\lambda\rho)\cos(2\phi)\right]\lambda^2 d\lambda + \int_0^\infty u_2 e^{u_2 z}f_4\lambda J_0(\lambda\rho)d\lambda$$

(57)

$$E_y^2 = E_{yi}^2 = -\frac{1}{\varepsilon_2'}\frac{\partial F_z^2}{\partial x} = -\frac{k_1}{\varepsilon_2'}\int_0^\infty e^{u_2 z}g_4\left[\lambda J_0(\lambda\rho) - \frac{2}{\rho}J_1(\lambda\rho)\right]\lambda^2\sin(\phi)\cos(\phi)d\lambda$$

(58)

35

$$E_z^2 = E_{z1}^2 = -\frac{1}{\varepsilon_2'}\frac{\partial F_y^2}{\partial x} = \frac{k_1}{\varepsilon_2'}\int_0^\infty e^{u_2 z} f_4 \lambda^2 J_1(\lambda\rho)\cos(\phi)d\lambda \qquad (59)$$

$$H_x^2 = H_{xt}^2 = -\frac{j}{\omega\mu\varepsilon_2'}\frac{\partial}{\partial x}\left(\frac{\partial F_y^2}{\partial y} + \frac{\partial F_z^2}{\partial z}\right) = -\frac{IdA\varepsilon_1'}{4\pi\varepsilon_2'}\int_0^\infty (f_4 + u_2 g_4)\left[\lambda J_0(\lambda\rho) - \frac{2}{\rho}J_1(\lambda\rho)\right]e^{u_2 z}\lambda^2 \sin(\phi)\cos(\phi)d\lambda \qquad (60)$$

$$H_y^2 = H_{yt}^2 = -\frac{j}{\omega\mu\varepsilon_2'}\left[\frac{\partial}{\partial y}\left(\frac{\partial F_y^2}{\partial y} + \frac{\partial F_z^2}{\partial z}\right) - \gamma_2^2 F_y^2\right]$$
$$= -\frac{IdA\varepsilon_1'}{4\pi\varepsilon_2'}\left\{\int_0^\infty (f_4 + u_2 g_4)\left[\lambda J_0(\lambda\rho)\sin^2(\phi) + \frac{1}{\rho}J_1(\lambda\rho)\cos(2\phi)\right]e^{u_2 z}\lambda^2 d\lambda + \int_0^\infty \gamma_2^2 e^{u_2 z} f_4 \lambda J_0(\lambda\rho)d\lambda\right\} \qquad (61)$$

$$H_z^2 = H_{zt}^2 = -\frac{j}{\omega\mu\varepsilon_2'}\left[\frac{\partial}{\partial z}\left(\frac{\partial F_y^2}{\partial y} + \frac{\partial F_z^2}{\partial z}\right) - \gamma_2^2 F_z^2\right] = -\frac{IdA\varepsilon_1'}{4\pi\varepsilon_2'}\int_0^\infty (u_2 f_4 + \lambda^2 g_4)e^{u_2 z}\lambda^2 J_1(\lambda\rho)\cos(\phi)d\lambda \qquad (62)$$

36

Numerical Validation of the Results

To validate the results in (45) to (62), the electric and magnetic are numerically calculated and checked with some known results, such as the quasi-static fields in infinite medium. The values of the parameters used in the following calculation are listed in Table 2.

Table 2   List of parameters

Medium	#0	#1	#2
Relative permittivity, ε_r	1	81	3
Conductivity, σ (S/m)	0	4	0.01
Permeability, μ (H/m)	$4\pi\times10^{-7}$	$4\pi\times10^{-7}$	$4\pi\times10^{-7}$
d (m)	300		
h (m)	can vary from 0 to 300		
Dipole moment IdA ($A\cdot m^2$)	1		
Frequency f (Hz)	10 to 3000		

Numerical Integration

In this project we choose the composite Simpson's rule to do the numerical integration. For a given integrand $f(x)$, the Simpson's rule is used to obtain the integration of $f(x)$ over interval $[a, b]$. It is given as

$$\int_a^b f(x)dx = \frac{h}{3}\left[f(a)+4f(x_1)+f(b)\right]-\frac{h^5}{90}f^{(4)}(\xi) \tag{63}$$

where x_1 is the middle point of $[a, b]$, $a \le \xi \le b$. The Simpson's rule is usually inaccurate if used over large integration intervals. To avoid the problem, a piecewise approach, the composite Simpson's rule, is often applied. (Fig.2)
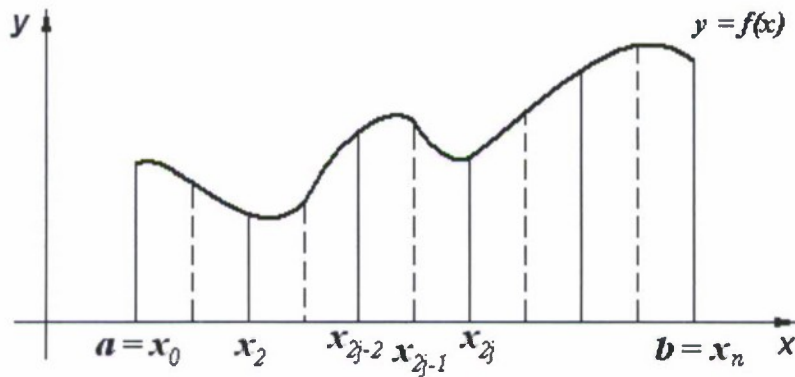

Fig. 2   Integration intervals for the composite Simpson's rule

First, the integration interval $[a, b]$ is divided into n equal-spaced subintervals, where n must be an even number. Then apply the Simpson's rule on each subinterval and combine all the integrations over every subinterval to get the final result. In formula, the composite Simpson's rule is described as

$$\int_a^b f(x)dx = \frac{h}{3}\left[f(x_0) + 2\sum_{j=1}^{(n/2)-1} f(x_{2j}) + 4\sum_{j=1}^{n/2} f(x_{2j-1}) + f(x_n) \right] - \frac{h^5}{90}\sum_{j=1}^{n/2} f^{(4)}(\xi_j) \qquad (64)$$

where $x_{2j-2} \leq \xi_j \leq x_{2j}$, for each $j = 1, 2, ..., n/2$. When the numerical integration is carried out, the error term is usually truncated.

$$\int_a^b f(x)dx \approx \frac{h}{3}\left[f(x_0) + 2\sum_{j=1}^{(n/2)-1} f(x_{2j}) + 4\sum_{j=1}^{n/2} f(x_{2j-1}) + f(x_n) \right] \qquad (65)$$

Theoretically, as shown in (45) to (62), the exact fields will be given by the integration from zero to infinity. But it is not possible to do this in a numerical manner. The computer program can only deal with integration over finite intervals. To make the fields calculation possible, some approximation should be made. An integral can be separated into two parts

$$\int_0^\infty f(x)dx = \int_0^b f(x)dx + \int_b^\infty f(x)dx \qquad (66)$$

If we can find a bound number 'b' such that the second integral on the right hand side is small enough compared to the first integral, the total integral can be approximated by the first term. Fortunately, we do can find such kind of 'b' for the field calculation because all the integrands in the field calculation equations have attenuation characteristics.

$$\int_0^\infty FI(\lambda)d\lambda = \int_0^{\lambda \max} FI(\lambda)d\lambda + \int_{\lambda \max}^\infty FI(\lambda)d\lambda$$
$$\approx \int_0^{\lambda \max} FI(\lambda)d\lambda \qquad (67)$$

where $FI(\lambda)$ represents integrand for field integration, λ_{max} is the upper limit of the integration interval to be used in numerical calculation.

In practice, we use 50 as the value of λ_{max} for all the terms derived from the source term,

$$\frac{e^{\gamma_1 R}}{R} = \begin{cases} \int_0^\infty u_1^{-1} e^{-u_1(z+h)} \lambda J_0(\lambda\rho)d\lambda & (z+h) \geq 0 \\ \int_0^\infty u_1^{-1} e^{u_1(z+h)} \lambda J_0(\lambda\rho)d\lambda & (z+h) \leq 0 \end{cases}$$

This value of λ_{max} will give us enough accuracy for calculation. However, for all the scattered-field terms, which contains the coefficient functions $f_1 \sim f_4$ and $g_1 \sim g_4$, the same λ_{max} doesn't work. If the λ_{max} value is too large, the calculation of the coefficient functions will exceed the operation limit of the computer (like 10^{324}). By testing, the λ_{max} is set at 1.2. Although it is much smaller than that for the source terms, the final results of calculation are still acceptable.

The integral step h is another important factor to the numerical integration. Too large steps not only bring big error but also cause bad behavior of the calculation. Small steps, however, slow down the speed of integration. In this project we choose the integral step h around 0.01 for both source term and scattered term integration. And it gives a good compromise between computing stability and speed.

If the HMD source is located in the middle of the water layer and we consider the area not too far away from the dipole, the scattered fields in this area will be so small that can be ignored. The total field then will behave exactly like that induced by a HMD radiating in an infinite uniform media of water. In order to verify the numerical results, those results are compared to the fields radiated by a HMD in the infinite water media.

Fig. 3 and Fig. 4 show an example of the comparison between the two set of results. The HMD is at $h = 150$m, which is in the middle of the water layer. The 'Φ' angle of the evaluating points is $\pi/4$ and $z = -149$m. For a HMD radiating in the infinite uniform conducting medium, E_y component is always zero. So there is no E_y presented in the comparison.

In those figures the solid line curve stands for the 3-layer results and the star-line curve for the uniform media results. It is clear that the two sets of the results match each other very well.
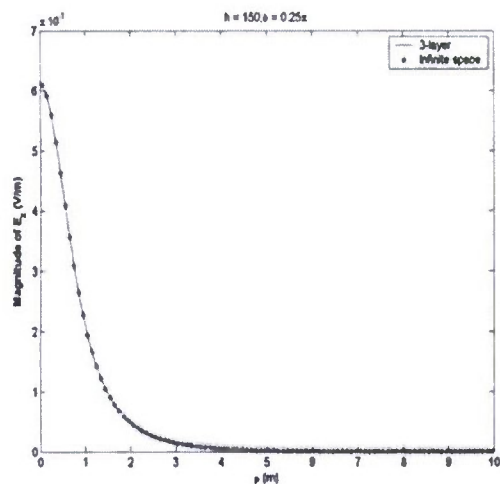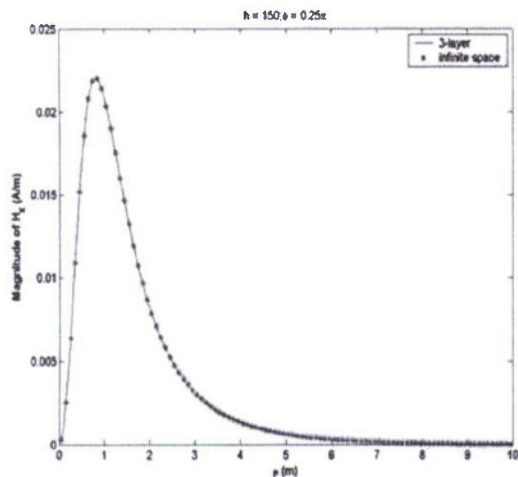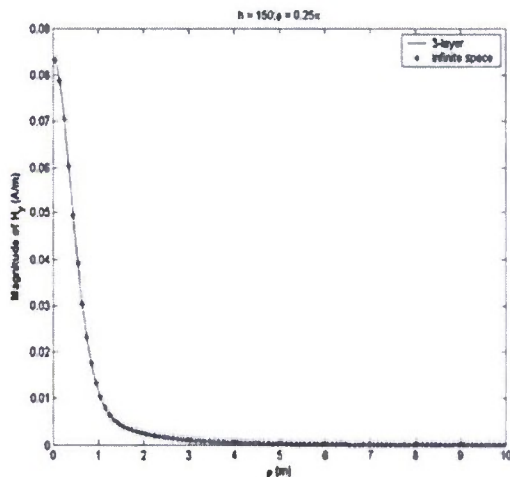
(a) E_x
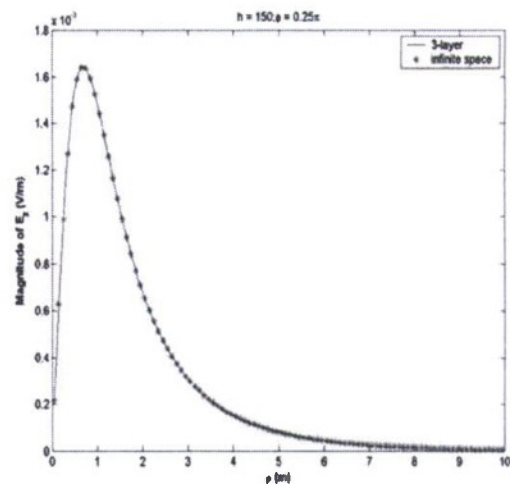
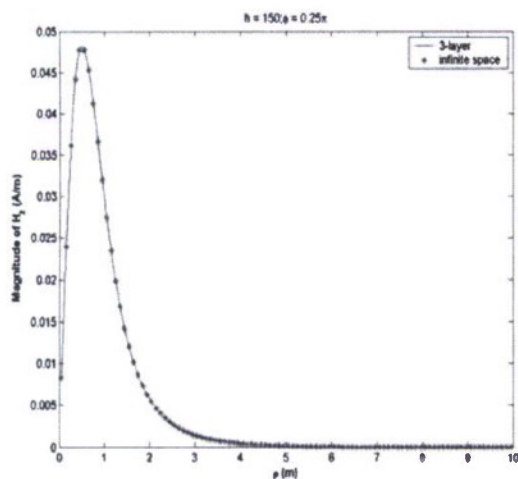(b) E_z

Fig. 3   Comparison of E fields between 3-layer results and uniform-media results

(a) H_x

(b) H_y

(c) H_z

Fig. 4   Comparison of H fields between 3-layer results and uniform-medium results

Checking Boundary Conditions

Checking boundary conditions at each interface provides another approach to validate the the solutions to the fields, equation (45) ~ (62). At the upper interface ($z = 0$), the tangential-field components are

$$E_x^0 = -\frac{k_1}{\varepsilon_0'} \int_0^\infty u_0 f_1 \lambda J_0(\lambda\rho) d\lambda + \frac{k_1}{\varepsilon_0'} \int_0^\infty g_1 \cdot \left[\lambda J_0(\lambda\rho) \sin^2(\phi) + \frac{1}{\rho} J_1(\lambda\rho) \cos(2\phi) \right] \lambda^2 d\lambda$$

$$E_x^1 = \frac{k_1}{\varepsilon_1'} \int_0^\infty \left[e^{-u_1 h} - u_1 f_2 + u_1 f_3 \right] \lambda J_0(\lambda\rho) d\lambda$$

$$+ \frac{k_1}{\varepsilon_1'} \int_0^\infty (g_2 + g_3) \left[\lambda J_0(\lambda\rho) \sin^2(\phi) + \frac{1}{\rho} J_1(\lambda\rho) \cos(2\phi) \right] \lambda^2 d\lambda$$

$$E_y^0 = -\frac{k_1}{\varepsilon_0'} \int_0^\infty g_1 \left[\lambda J_0(\lambda\rho) - \frac{2}{\rho} J_1(\lambda\rho) \right] \lambda^2 \sin(\phi) \cos(\phi) d\lambda$$

$$E_y^1 = -\frac{k_1}{\varepsilon_1'} \int_0^\infty (g_2 + g_3) \left[\lambda J_0(\lambda\rho) - \frac{2}{\rho} J_1(\lambda\rho) \right] \lambda^2 \sin(\phi) \cos(\phi) d\lambda$$

$$H_x^0 = \frac{IdA}{4\pi} \cdot \frac{\varepsilon_1'}{\varepsilon_0'} \int_0^\infty (u_0 g_1 - f_1) \left[\lambda J_0(\lambda\rho) - \frac{2}{\rho} J_1(\lambda\rho) \right] \lambda^2 \sin(\phi) \cos(\phi) d\lambda$$

$$H_x^1 = \frac{IdA}{4\pi} \int_0^\infty \left(u_1^{-1} e^{-u_1 h} + f_2 + f_3 - u_1 g_2 + u_1 g_3 \right) \cdot \left[\lambda J_0(\lambda\rho) - \frac{2}{\rho} J_1(\lambda\rho) \right] \lambda^2 \sin(\phi) \cos(\phi) d\lambda$$

$$H_y^0 = \frac{IdA}{4\pi} \cdot \frac{\varepsilon_1'}{\varepsilon_0'} \int_0^\infty (u_0 g_1 - f_1) \left[\lambda J_0(\lambda\rho) \sin^2(\phi) + \frac{1}{\rho} J_1(\lambda\rho) \cos(2\phi) \right] \lambda^2 d\lambda$$

$$- \frac{IdA}{4\pi} \cdot \frac{\varepsilon_1'}{\varepsilon_0'} \int_0^\infty \gamma_0^2 f_1 \lambda J_0(\lambda\rho) d\lambda$$

$$H_y^1 = -\frac{IdA}{4\pi} \int_0^\infty \left(u_1^{-1} e^{-u_1 h} + f_2 + f_3 - u_1 g_2 + u_1 g_3 \right) \left[\lambda J_0(\lambda\rho) \sin^2(\phi) + \frac{1}{\rho} J_1(\lambda\rho) \cos(2\phi) \right] \lambda^2 d\lambda$$

$$- \frac{IdA}{4\pi} \int_0^\infty \left(u_1^{-1} e^{-u_1 h} + f_2 + f_3 \right) \cdot \gamma_1^2 \lambda J_0(\lambda\rho) d\lambda$$

With the boundary conditions (23) ~ (26), it is not difficult to prove that

$$\begin{matrix} E_x^0 = E_x^1 \\ E_y^0 = E_y^1 \end{matrix} \quad \text{and} \quad \begin{matrix} H_x^0 = H_x^1 \\ H_y^0 = H_y^1 \end{matrix}.$$

So the boundary conditions are theoretically proved to be satisfied at the upper interface. Similarly, at the lower interface ($z = -d$) the tangential-field components are

$$E_x^2 = \frac{k_1}{\varepsilon_2'} \int_0^\infty u_2 e^{-u_2 d} f_4 \lambda J_0(\lambda\rho) d\lambda + \frac{k_1}{\varepsilon_2'} \int_0^\infty e^{-u_2 d} g_4 \cdot \left[\lambda J_0(\lambda\rho) \sin^2(\phi) + \frac{1}{\rho} J_1(\lambda\rho) \cos(2\phi) \right] \lambda^2 d\lambda$$

$$E_x^1 = \frac{k_1}{\varepsilon_1'} \int_0^\infty \left[e^{u_1(h-d)} - u_1 e^{u_1 d} f_2 + u_1 e^{-u_1 d} f_3 \right] \lambda J_0(\lambda\rho) d\lambda$$

$$+ \frac{k_1}{\varepsilon_1'} \int_0^\infty \left(e^{u_1 d} g_2 + e^{-u_1 d} g_3 \right) \left[\lambda J_0(\lambda\rho) \sin^2(\phi) + \frac{1}{\rho} J_1(\lambda\rho) \cos(2\phi) \right] \lambda^2 d\lambda$$

$$E_y^2 = -\frac{k_1}{\varepsilon_2'} \int_0^\infty e^{-u_2 d} g_4 \left[\lambda J_0(\lambda\rho) - \frac{2}{\rho} J_1(\lambda\rho) \right] \lambda^2 \sin(\phi) \cos(\phi) d\lambda$$

$$E_y^1 = -\frac{k_1}{\varepsilon_1'} \int_0^\infty \left(e^{u_1 d} g_2 + e^{-u_1 d} g_3 \right) \left[\lambda J_0(\lambda\rho) - \frac{2}{\rho} J_1(\lambda\rho) \right] \lambda^2 \sin(\phi) \cos(\phi) d\lambda$$

$$H_x^2 = -\frac{IdA}{4\pi} \cdot \frac{\varepsilon_1'}{\varepsilon_2'} \int_0^\infty (f_4 + u_2 g_4) e^{-u_2 d} \left[\lambda J_0(\lambda\rho) - \frac{2}{\rho} J_1(\lambda\rho) \right] \lambda^2 \sin(\phi) \cos(\phi) d\lambda$$

$$H_x^1 = \frac{IdA}{4\pi} \int_0^\infty \left(u_1^{-1} e^{u_1(h-d)} + e^{u_1 d} f_2 + e^{-u_1 d} f_3 - u_1 e^{u_1 d} g_2 + u_1 e^{-u_1 d} g_3 \right)$$

$$\cdot \left[\lambda J_0(\lambda\rho) - \frac{2}{\rho} J_1(\lambda\rho) \right] \lambda^2 \sin(\phi) \cos(\phi) d\lambda$$

$$H_y^2 = \frac{IdA}{4\pi} \cdot \frac{\varepsilon_1'}{\varepsilon_2'} \int_0^\infty -(f_4 + u_2 g_4) e^{-u_2 d} \left[\lambda J_0(\lambda\rho) \sin^2(\phi) + \frac{1}{\rho} J_1(\lambda\rho) \cos(2\phi) \right] \lambda^2 d\lambda$$

$$- \frac{IdA}{4\pi} \cdot \frac{\varepsilon_1'}{\varepsilon_2'} \int_0^\infty \gamma_0^2 e^{-u_2 d} f_4 \lambda J_0(\lambda\rho) d\lambda$$

$$H_y^1 = -\frac{IdA}{4\pi} \int_0^\infty \left(u_1^{-1} e^{u_1(h-d)} + e^{u_1 d} f_2 + e^{-u_1 d} f_3 - u_1 e^{u_1 d} g_2 + u_1 e^{-u_1 d} g_3 \right)$$

$$\cdot \left[\lambda J_0(\lambda\rho) \sin^2(\phi) + \frac{1}{\rho} J_1(\lambda\rho) \cos(2\phi) \right] \lambda^2 d\lambda$$

$$- \frac{IdA}{4\pi} \int_0^\infty \left(u_1^{-1} e^{u_1(h-d)} + e^{u_1 d} f_2 + e^{-u_1 d} f_3 \right) \cdot \gamma_1^2 \lambda J_0(\lambda\rho) d\lambda$$

By considering the equations (27) ~ (30), it also can be proved that

$$E_x^2 = E_x^1 \quad \text{and} \quad H_x^2 = H_x^1$$
$$E_y^2 = E_y^1 \qquad\qquad H_y^2 = H_y^1.$$

Then the boundary conditions are theoretically proved to be satisfied at the lower interface. Fig. 5 and Fig. 6 show the matching of boundary conditions at the lower interface. The HMD source is put at $h = 290$m. For the field points, $\Phi = \pi/4$. (Figures are on next page.)   As shown in the figures, the fields at the both sides match each other very well.
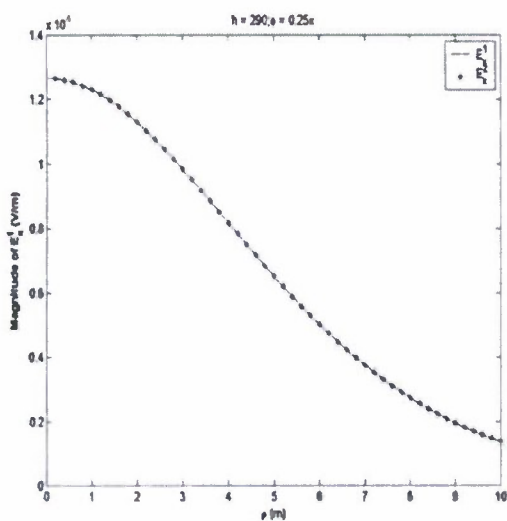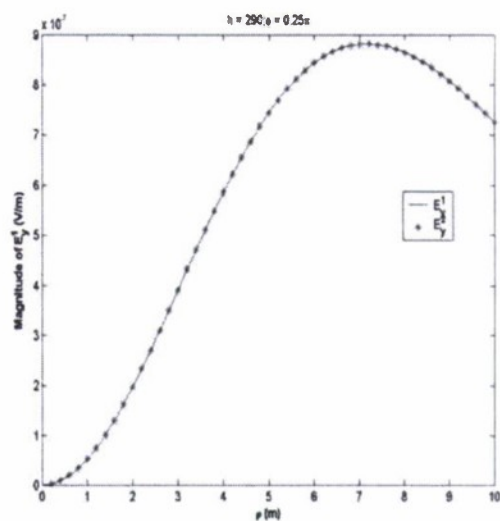
(a) E_x (b) E_y

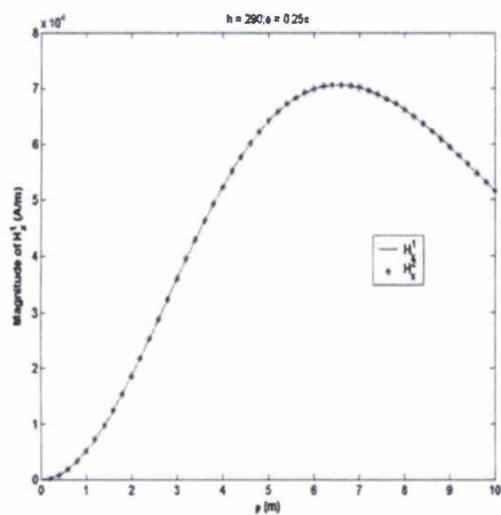Fig. 5   Checking tangential E fields along the water-bottom interface
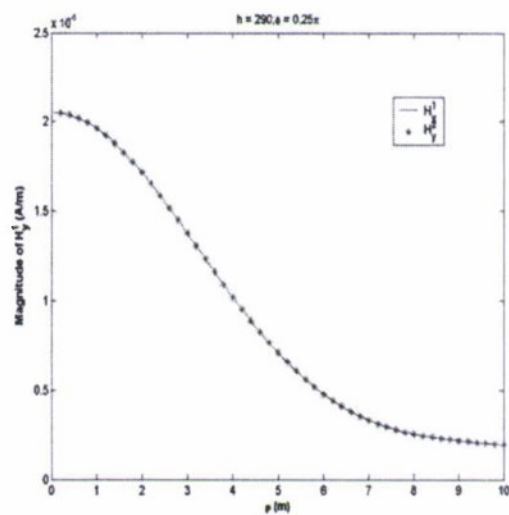
(a) H_x (b) H_y

Fig. 6   Checking tangential H fields along the water-bottom interface

Appendix:

Sommerfeld integral equations of E and H fields for other dipole cases

There are eight cases of different dipole source conditions interested in this project. In the previous sections of the report, the process of finding the Sommerfeld integral solutions to E and H fields for the case that HMD in #1 medium, HMD^1, has been introduced. By using the similar method, the solutions for the other seven cases can also be obtained. In this appendix, the results of the cases (in case identifier as shown in Table 1): HED^0, HED^1, HMD^0, VED^0, VED^1, VMD^0, and VMD^1 are provided.

Free Space (#0) HED ↑ z = h $\varepsilon_0, \sigma_0, \mu_0$ y

z = 0 · · · · · · · · · · observation point

Conducting Medium (#1) $\varepsilon_1, \sigma_1, \mu_0$

z = -d

Bottom (#2) $\varepsilon_2, \sigma_2, \mu_0$

HED (Dipole in #0 medium)

Vector potentials:

$$A_y^0 = k_0 \frac{e^{\gamma_0 R}}{R} + k_0 \int_0^\infty f_1 e^{-u_0 z} \lambda J_0(\lambda\rho)d\lambda \quad (z \geq 0); \quad \frac{e^{\gamma_0 R}}{R} = \begin{cases} \int_0^\infty u_0^{-1} e^{-u_0(z-h)} \lambda J_0(\lambda\rho)d\lambda & (z-h \geq 0) \\[2mm] \int_0^\infty u_0^{-1} e^{u_0(z-h)} \lambda J_0(\lambda\rho)d\lambda & (z-h \leq 0) \end{cases}$$

$$A_y^1 = k_0 \int_0^\infty \left[f_2 e^{-u_1 z} + f_3 e^{u_1 z} \right] \lambda J_0(\lambda\rho)d\lambda \quad (-d \leq z \leq 0); \quad A_y^2 = k_0 \int_0^\infty f_4 e^{u_2 z} \lambda J_0(\lambda\rho)d\lambda \quad (z \leq -d);$$

$$A_z^0 = k_0 \int_0^\infty g_1 e^{-u_0 z} \lambda J_0(\lambda\rho)d\lambda \quad (z \geq 0);$$

$$A_z^1 = k_0 \int_0^\infty \left[g_2 e^{-u_1 z} + g_3 e^{u_1 z} \right] \lambda J_0(\lambda\rho)d\lambda \quad (-d \leq z \leq 0);$$

$$A_z^2 = k_0 \int_0^\infty g_4 e^{u_2 z} \lambda J_0(\lambda\rho)d\lambda \quad (z \leq -d);$$

where $\gamma_i^2 = -\omega^2 \mu \varepsilon_i' = -\omega^2 \mu\left(\varepsilon_i - j\frac{\sigma_i}{\omega}\right)$; $u_i = \sqrt{(\lambda^2 + \gamma_i^2)}$; $k_0 = \frac{\mu I dl}{4\pi}$.

Boundary conditions

At $z = 0$ (upper) interface:

$$A_y^0 = A_y^1; \quad A_z^0 = A_z^1; \quad \frac{\partial A_y^0}{\partial z} = \frac{\partial A_y^1}{\partial z};$$

$$\frac{1}{\varepsilon_0'}\left(\frac{\partial A_y^0}{\partial y} + \frac{\partial A_z^0}{\partial z}\right) = \frac{1}{\varepsilon_1'}\left(\frac{\partial A_y^1}{\partial y} + \frac{\partial A_z^1}{\partial z}\right);$$

At $z = -d$ (lower) interface:

$$A_y^2 = A_y^1; \quad A_z^2 = A_z^1; \quad \frac{\partial A_y^2}{\partial z} = \frac{\partial A_y^1}{\partial z}.$$

$$\frac{1}{\varepsilon_2'}\left(\frac{\partial A_y^2}{\partial y} + \frac{\partial A_z^2}{\partial z}\right) = \frac{1}{\varepsilon_1'}\left(\frac{\partial A_y^1}{\partial y} + \frac{\partial A_z^1}{\partial z}\right);$$

Coefficient functions

$$f_1 = \frac{e^{-u_0 h}}{u_0 \cdot D}\left[(u_0 + u_1)(u_2 - u_1)e^{-u_1 d} + (u_1 - u_0)(u_1 + u_2)e^{u_1 d}\right]; \quad f_2 = \frac{2}{D}(u_2 - u_1)e^{-u_0 h}e^{-u_1 d};$$

$$f_3 = \frac{-2}{D}(u_2 + u_1)e^{-u_0 h}e^{u_1 d}; \quad f_4 = \frac{-4u_1 e^{-u_0 h}e^{u_2 d}}{D}; \quad \text{where } D = (u_1 - u_0)(u_1 - u_2)e^{-u_1 d} - (u_1 + u_0)(u_2 + u_1)e^{u_1 d}.$$
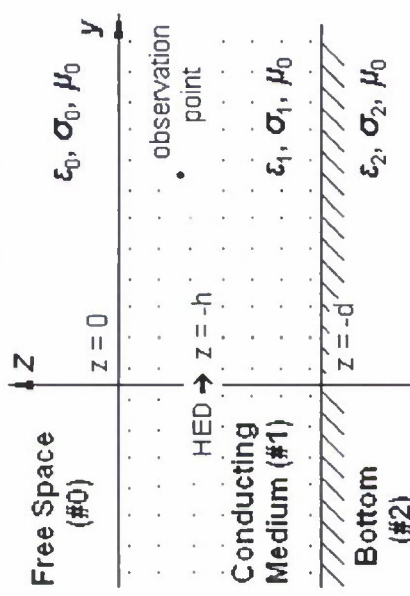
HED^0 – Dipole in #0 medium (free space)

Coefficient functions (contd.)	$g_1 = \dfrac{1}{D_1}\left\{(\varepsilon_1' - \varepsilon_0')\left[(\varepsilon_1'u_2 - \varepsilon_2'u_1)e^{-u_1 d} - (\varepsilon_1'u_2 + \varepsilon_2'u_1)e^{u_1 d}\right](f_2 + f_3) - 2\varepsilon_0'u_1(\varepsilon_2' - \varepsilon_1')e^{-u_2 d}f_4\right\}$; $g_2 = \dfrac{1}{D_1}\cdot\left[(\varepsilon_1' - \varepsilon_0')(\varepsilon_1'u_2 - \varepsilon_2'u_1)e^{-u_1 d}\left(f_2 + f_3\right) - (\varepsilon_2' - \varepsilon_1')(\varepsilon_1'u_0 + \varepsilon_0'u_1)e^{-u_2 d}f_4\right]$ $g_3 = \dfrac{1}{D_1}\left[(\varepsilon_0' - \varepsilon_1')(\varepsilon_2'u_1 + \varepsilon_1'u_2)e^{u_1 d}\left(f_2 + f_3\right) + (\varepsilon_2' - \varepsilon_1')(\varepsilon_1'u_0 - \varepsilon_0'u_1)e^{-u_2 d}f_4\right]$; $g_4 = \dfrac{1}{D_1}\left\{2\varepsilon_2'u_1(\varepsilon_0' - \varepsilon_1')e^{u_2 d}\left(f_2 + f_3\right) + (\varepsilon_2' - \varepsilon_1')\left[(\varepsilon_1'u_0 - \varepsilon_0'u_1)e^{-u_1 d} - (\varepsilon_0'u_1 + \varepsilon_1'u_0)e^{u_1 d}\right]f_4\right\}$; where $D_1 = (\varepsilon_1'u_0 - \varepsilon_0'u_1)(\varepsilon_1'u_2 - \varepsilon_2'u_1)e^{-u_1 d} - (\varepsilon_0'u_1 + \varepsilon_1'u_0)(\varepsilon_1'u_2 + \varepsilon_2'u_1)e^{u_1 d}$.

Field in #0 medium (free space)

E_x^0	$E_x^0 = -\dfrac{j}{\omega\mu\varepsilon_0'}\dfrac{\partial}{\partial x}\left(\dfrac{\partial A_y^0}{\partial y} + \dfrac{\partial A_z^0}{\partial z}\right) = E_{xi}^0 + E_{xr}^0$ $E_{xi}^0 = \dfrac{jIdl}{4\pi\omega\varepsilon_0'}\int_0^\infty \left(\begin{cases} u_0^{-1}e^{-u_0(z-h)} & (z-h\geq 0) \\ u_0^{-1}e^{u_0(z-h)} & (z-h\leq 0)\end{cases}\right)\cdot\left[\lambda J_0(\lambda\rho) - \dfrac{2}{\rho}J_1(\lambda\rho)\right]\lambda^2\sin(\phi)\cos(\phi)d\lambda$ $E_{xr}^0 = \dfrac{jIdl}{4\pi\omega\varepsilon_0'}\int_0^\infty \left(e^{-u_0 z}f_1 - u_0 e^{-u_0 z}g_1\right)\left[\lambda J_0(\lambda\rho) - \dfrac{2}{\rho}J_1(\lambda\rho)\right]\lambda^2\sin(\phi)\cos(\phi)d\lambda$
E_y^0	$E_y^0 = -\dfrac{j}{\omega\mu\varepsilon_0'}\left[\dfrac{\partial}{\partial y}\left(\dfrac{\partial A_y^0}{\partial y} + \dfrac{\partial A_z^0}{\partial z}\right) - \gamma_0^2 A_y^0\right] = E_{yi}^0 + E_{yr}^0$

HED⁰ – Dipole in #0 medium (free space)

	$$E_{yi}^0 = \frac{jIdl}{4\pi\omega\varepsilon_0'}\int_0^\infty\left(\begin{matrix}u_0^{-1}e^{-u_0(z-h)} & (z-h\geq 0)\\ u_0^{-1}e^{u_0(z-h)} & (z-h\leq 0)\end{matrix}\right)\cdot\left[\lambda J_0(\lambda\rho)\sin^2(\phi)+\frac{1}{\rho}J_1(\lambda\rho)\cos(2\phi)\right]\lambda^2 d\lambda$$ $$+\frac{jIdl}{4\pi\omega\varepsilon_0'}\int_0^\infty\left(\begin{matrix}u_0^{-1}e^{-u_0(z-h)} & (z-h\geq 0)\\ u_0^{-1}e^{u_0(z-h)} & (z-h\leq 0)\end{matrix}\right)\cdot\gamma_0^2\lambda J_0(\lambda\rho)d\lambda$$ $$E_{yr}^0 = \frac{jIdl}{4\pi\omega\varepsilon_0'}\int_0^\infty\left(e^{-u_0z}f_1-u_0e^{-u_0z}g_1\right)\left[\lambda J_0(\lambda\rho)\sin^2(\phi)+\frac{1}{\rho}J_1(\lambda\rho)\cos(2\phi)\right]\lambda^2 d\lambda+\frac{jIdl}{4\pi\omega\varepsilon_1'}\int_0^\infty e^{-u_0z}f_1\gamma_0^2\lambda J_0(\lambda\rho)d\lambda$$
E_z^0	$$E_z^0 = -\frac{j}{\omega\mu\varepsilon_0'}\left[\frac{\partial}{\partial z}\left(\frac{\partial A_y^0}{\partial y}+\frac{\partial A_z^0}{\partial z}\right)-\gamma_0^2 A_z^0\right]=E_{zi}^0+E_{zr}^0$$ $$E_{zi}^0 = \frac{jIdl}{4\pi\omega\varepsilon_0'}\int_0^\infty\left(\begin{matrix}-e^{-u_0(z-h)} & (z-h\geq 0)\\ e^{u_0(z-h)} & (z-h\leq 0)\end{matrix}\right)\cdot\lambda^2 J_1(\lambda\rho)\sin(\phi)d\lambda$$ $$E_{zr}^0 = \frac{jIdl}{4\pi\omega\varepsilon_0'}\int_0^\infty\left(-u_0e^{-u_0z}f_1+\lambda^2 e^{-u_0z}g_1\right)\lambda^2 J_1(\lambda\rho)\sin(\phi)d\lambda$$
H_x^0	$$H_x^0 = \frac{1}{\mu}\left(\frac{\partial A_z^0}{\partial y}-\frac{\partial A_y^0}{\partial z}\right)=H_{xi}^0+H_{xr}^0$$ $$H_{xi}^0 = -\frac{Idl}{4\pi}\int_0^\infty\left(\begin{matrix}-e^{-u_0(z-h)} & (z-h\geq 0)\\ e^{u_0(z-h)} & (z-h\leq 0)\end{matrix}\right)\cdot\lambda J_0(\lambda\rho)d\lambda$$ $$H_{xr}^0 = \frac{Idl}{4\pi}\int_0^\infty u_0e^{-u_0z}f_1\lambda J_0(\lambda\rho)d\lambda-\frac{Idl}{4\pi}\int_0^\infty e^{-u_0z}g_1\left[\lambda J_0(\lambda\rho)\sin^2(\phi)+\frac{1}{\rho}J_1(\lambda\rho)\cos(2\phi)\right]\lambda^2 d\lambda$$
H_y^0	$$H_y^0 = -\frac{1}{\mu}\frac{\partial A_z^0}{\partial x}=H_{yi}^0+H_{yr}^0$$ $$H_{yi}^0 = 0$$

48

HED⁰ -- Dipole in #0 medium (free space)

$$H_{yr}^0 = \frac{Idl}{4\pi}\int_0^\infty e^{-u_0 z} g_1 \left[\lambda J_0(\lambda\rho) - \frac{2}{\rho}J_1(\lambda\rho)\right]\lambda^2 \sin(\phi)\cos(\phi)d\lambda$$

H_z^0

$$H_z^0 = -\frac{1}{\mu}\frac{\partial A_y^0}{\partial x} = H_{zi}^0 + H_{zr}^0$$

$$H_{zi}^0 = -\frac{Idl}{4\pi}\int_0^\infty \left(\begin{matrix} u_0^{-1}e^{-u_0(z-h)} & (z-h\geq 0) \\ u_0^{-1}e^{u_0(z-h)} & (z-h\leq 0)\end{matrix}\right)\lambda^2 J_1(\lambda\rho)\cos(\phi)d\lambda$$

$$H_{zr}^0 = -\frac{Idl}{4\pi}\int_0^\infty e^{-u_0 z}f_1 \lambda^2 J_1(\lambda\rho)\cos(\phi)d\lambda$$

Field in #1 medium (middle layer, conducting medium)

E_x^1

$$E_x^1 = -\frac{j}{\omega\mu\varepsilon_1'}\frac{\partial}{\partial x}\left(\frac{\partial A_y^1}{\partial y} + \frac{\partial A_z^1}{\partial z}\right) = E_{xt}^1$$

$$= \frac{jIdl}{4\pi\omega\varepsilon_1'}\int_0^\infty \left(e^{-u_1 z}f_2 + e^{u_1 z}f_3 - u_1 e^{-u_1 z}g_2 + u_1 e^{u_1 z}g_3\right)\left[\lambda J_0(\lambda\rho) - \frac{2}{\rho}J_1(\lambda\rho)\right]\lambda^2 \sin(\phi)\cos(\phi)d\lambda$$

E_y^1

$$E_y^1 = -\frac{j}{\omega\mu\varepsilon_1'}\left[\frac{\partial}{\partial y}\left(\frac{\partial A_y^1}{\partial y} + \frac{\partial A_z^1}{\partial z}\right) - \gamma_1^2 A_y^1\right] = E_{yt}^1$$

$$= \frac{jIdl}{4\pi\omega\varepsilon_1'}\left\{\int_0^\infty \left(e^{-u_1 z}f_2 + e^{u_1 z}f_3 - u_1 e^{-u_1 z}g_2 + u_1 e^{u_1 z}g_3\right)\left[\lambda J_0(\lambda\rho)\sin^2(\phi) + \frac{1}{\rho}J_1(\lambda\rho)\cos(2\phi)\right]\lambda^2 d\lambda + \int_0^\infty \gamma_1^2\left(e^{-u_1 z}f_2 + e^{u_1 z}f_3\right)\lambda J_0(\lambda\rho)d\lambda\right\}$$

E_z^1

$$E_z^1 = -\frac{j}{\omega\mu\varepsilon_1'}\left[\frac{\partial}{\partial z}\left(\frac{\partial A_y^1}{\partial y} + \frac{\partial A_z^1}{\partial z}\right) - \gamma_1^2 A_z^1\right] = E_{zt}^1$$

$$= \frac{jIdl}{4\pi\omega\varepsilon_1'}\int_0^\infty \left(-u_1 e^{-u_1 z}f_2 + u_1 e^{u_1 z}f_3 + \lambda^2 e^{-u_1 z}g_2 + \lambda^2 e^{u_1 z}g_3\right)\lambda^2 J_1(\lambda\rho)\sin(\phi)d\lambda$$

HED^0 – Dipole in #0 medium (free space)

H_x^1	$H_x^1 = \dfrac{1}{\mu}\left(\dfrac{\partial A_z^1}{\partial y} - \dfrac{\partial A_y^1}{\partial z}\right) = H_{x1}^1$ $= -\dfrac{Idl}{4\pi}\displaystyle\int_0^\infty \left(e^{-u_1 z}g_2 + e^{u_1 z}g_3\right)\left[\lambda J_0(\lambda\rho)\sin^2(\phi) + \dfrac{1}{\rho}J_1(\lambda\rho)\cos(2\phi)\right]\lambda^2 d\lambda + \dfrac{Idl}{4\pi}\displaystyle\int_0^\infty u_1\left(e^{-u_1 z}f_2 - e^{u_1 z}f_3\right)\lambda J_0(\lambda\rho)d\lambda$
H_y^1	$H_y^0 = -\dfrac{1}{\mu}\dfrac{\partial A_z^1}{\partial x} = H_{y1}^1$ $= \dfrac{Idl}{4\pi}\displaystyle\int_0^\infty \left(e^{-u_1 z}g_2 + e^{u_1 z}g_3\right)\left[\lambda J_0(\lambda\rho) - \dfrac{2}{\rho}J_1(\lambda\rho)\right]\lambda^2 \sin(\phi)\cos(\phi)d\lambda$
H_z^1	$H_z^1 = \dfrac{1}{\mu}\dfrac{\partial A_y^1}{\partial x} = H_{z1}^1$ $= -\dfrac{Idl}{4\pi}\displaystyle\int_0^\infty \left(e^{-u_1 z}f_2 + e^{u_1 z}f_3\right)\lambda^2 J_1(\lambda\rho)\cos(\phi)d\lambda$

Field in #2 medium (bottom, conducting medium)

E_x^2	$E_x^2 = -\dfrac{j}{\omega\mu\varepsilon_2'}\dfrac{\partial}{\partial x}\left(\dfrac{\partial A_y^2}{\partial y} + \dfrac{\partial A_z^2}{\partial z}\right) = E_{x1}^2$ $= \dfrac{jIdl}{4\pi\omega\varepsilon_2'}\displaystyle\int_0^\infty \left(f_4 + u_2 g_4\right)e^{u_2 z}\left[\lambda J_0(\lambda\rho) - \dfrac{2}{\rho}J_1(\lambda\rho)\right]\lambda^2 \sin(\phi)\cos(\phi)d\lambda$
E_y^2	$E_y^2 = -\dfrac{j}{\omega\mu\varepsilon_2'}\left[\dfrac{\partial}{\partial y}\left(\dfrac{\partial A_y^2}{\partial y} + \dfrac{\partial A_z^2}{\partial z}\right) - \gamma_2^2 A_y^2\right] = E_{y1}^2$ $= \dfrac{jIdl}{4\pi\omega\varepsilon_2'}\displaystyle\int_0^\infty \left(f_4 + u_2 g_4\right)e^{u_2 z}\left[\lambda J_0(\lambda\rho)\sin^2(\phi) + \dfrac{1}{\rho}J_1(\lambda\rho)\cos(2\phi)\right]\lambda^2 d\lambda + \dfrac{jIdl}{4\pi\omega\varepsilon_2'}\displaystyle\int_0^\infty \gamma_2^2 e^{u_2 z}f_4\lambda J_0(\lambda\rho)d\lambda$

HED^0 – Dipole in #0 medium (free space)

E_z^2	$E_z^2 = -\dfrac{j}{\omega\mu\varepsilon_2'}\left[\dfrac{\partial}{\partial z}\left(\dfrac{\partial A_y^2}{\partial y}+\dfrac{\partial A_z^2}{\partial z}\right)-\gamma_2^2 A_z^2\right]=E_{z1}^2$ $= \dfrac{jIdl}{4\pi\omega\varepsilon_2'}\int_0^\infty\left(u_2 f_4 + \lambda^2 g_4\right)e^{u_2 z}\lambda^2 J_1(\lambda\rho)\cos(\phi)d\lambda$
H_x^2	$H_x^2 = \dfrac{1}{\mu_2}\left(\dfrac{\partial A_z^2}{\partial y}-\dfrac{\partial A_y^2}{\partial z}\right)=H_{x1}^2$ $= -\dfrac{Idl}{4\pi}\int_0^\infty e^{u_2 z} g_4\left[\lambda J_0(\lambda\rho)\sin^2(\phi)+\dfrac{1}{\rho}J_1(\lambda\rho)\cos(2\phi)\right]\lambda^2 d\lambda - \dfrac{Idl}{4\pi}\int_0^\infty u_2 e^{u_2 z} f_4 \lambda J_0(\lambda\rho)d\lambda$
H_y^2	$H_y^2 = \dfrac{1}{\mu}\dfrac{\partial A_z^2}{\partial x}=H_{y1}^2$ $= \dfrac{Idl}{4\pi}\int_0^\infty e^{u_2 z} g_4\left[\lambda J_0(\lambda\rho)-\dfrac{2}{\rho}J_1(\lambda\rho)\right]\lambda^2\sin(\phi)\cos(\phi)d\lambda$
H_z^2	$H_z^2 = \dfrac{1}{\mu}\dfrac{\partial A_y^2}{\partial x}=H_{z1}^2$ $= -\dfrac{Idl}{4\pi}\int_0^\infty e^{u_2 z} f_4 \lambda^2 J_1(\lambda\rho)\cos(\phi)d\lambda$

HED (Dipole in #1 medium)

Free Space (#0) $\varepsilon_0, \sigma_0, \mu_0$

$z = 0$

observation point

HED → $z = -h$

Conducting Medium (#1) $\varepsilon_1, \sigma_1, \mu_0$

$z = -d$

Bottom (#2) $\varepsilon_2, \sigma_2, \mu_0$

Vector potentials:

$$A_y^0 = k_1 \int_0^\infty f_1(\lambda) e^{-u_0 z} \lambda J_0(\lambda \rho) d\lambda \; ; \quad A_y^1 = k_1 \frac{e^{\gamma_1 R}}{R} + k_1 \int_0^\infty \left[f_2(\lambda) e^{-u_1 z} + f_3(\lambda) e^{u_1 z} \right] \lambda J_0(\lambda \rho) d\lambda \; ;$$

$$A_y^2 = k_1 \int_0^\infty f_4(\lambda) e^{u_2 z} \lambda J_0(\lambda \rho) d\lambda \; ; \text{ where } \frac{e^{\gamma_1 R}}{R} = \begin{cases} \int_0^\infty u_1^{-1} e^{-u_1(z+h)} \lambda J_0(\lambda \rho) d\lambda \;\; (z+h \geq 0) \\ \int_0^\infty u_1^{-1} e^{u_1(z+h)} \lambda J_0(\lambda \rho) d\lambda \;\; (z+h \leq 0) \end{cases}$$

$$A_z^0 = k_1 \frac{\partial}{\partial y} \int_0^\infty g_1(\lambda) e^{-u_0 z} \lambda J_0(\lambda \rho) d\lambda \; ; \quad A_z^1 = k_1 \frac{\partial}{\partial y} \int_0^\infty \left[g_2(\lambda) e^{-u_1 z} + g_3(\lambda) e^{u_1 z} \right] \lambda J_0(\lambda \rho) d\lambda \; ;$$

$$A_z^2 = k_1 \frac{\partial}{\partial y} \int_0^\infty g_4(\lambda) e^{u_2 z} \lambda J_0(\lambda \rho) d\lambda \; ;$$

where $\gamma_i^2 = -\omega^2 \mu \varepsilon_i' = -\omega^2 \mu (\varepsilon_i - j \frac{\sigma_i}{\omega}); \; u_i = \sqrt{(\lambda^2 + \gamma_i^2)}; \; k_1 = \frac{\mu Idl}{4\pi}.$

Boundary conditions	At $z = 0$ (upper) interface: $\frac{1}{\varepsilon_0'} \left(\frac{\partial A_y^0}{\partial y} + \frac{\partial A_z^0}{\partial z} \right) = \frac{1}{\varepsilon_1'} \left(\frac{\partial A_y^1}{\partial y} + \frac{\partial A_z^1}{\partial z} \right)$; $A_y^0 = A_y^1$; $A_z^0 = A_z^1$; $\frac{\partial A_y^0}{\partial z} = \frac{\partial A_y^1}{\partial z}$. At $z = -d$ (lower) interface: $\frac{1}{\varepsilon_2'} \left(\frac{\partial A_y^2}{\partial y} + \frac{\partial A_z^2}{\partial z} \right) = \frac{1}{\varepsilon_1'} \left(\frac{\partial A_y^1}{\partial y} + \frac{\partial A_z^1}{\partial z} \right)$; $A_y^2 = A_y^1$; $A_z^2 = A_z^1$; $\frac{\partial A_y^2}{\partial z} = \frac{\partial A_y^1}{\partial z}$.
Coefficient functions	$f_1 = \frac{2}{D} \left[(u_2 - u_1) e^{u_1(h-d)} - (u_2 + u_1) e^{-u_1(h-d)} \right]$; $f_2 = \frac{(u_2 - u_1)}{u_1 \cdot D} \left[(u_1 - u_0) e^{-u_1(h+d)} + (u_0 + u_1) e^{u_1(h-d)} \right]$; $f_3 = \frac{(u_0 - u_1)}{u_1 \cdot D} \left[(u_1 - u_2) e^{u_1(h-d)} + (u_2 + u_1) e^{-u_1(h-d)} \right]$; $f_4 = \frac{2e^{u_2 d}}{D} \left[(u_0 - u_1) e^{-u_1 h} - (u_0 + u_1) e^{u_1 h} \right]$; where $D = (u_1 - u_0)(u_1 - u_2) e^{-u_1 d} - (u_1 + u_2)(u_2 + u_1) e^{u_1 d}$.

52

Coefficient functions (contd.)	$g_1 = \dfrac{1}{D_1}\left\{(\varepsilon_1' - \varepsilon_0')f_1\left[(\varepsilon_2'u_1 - \varepsilon_1'u_2)e^{-u_1d} + (\varepsilon_2'u_1 + \varepsilon_1'u_2)e^{u_1d}\right] + 2\varepsilon_0'u_1(\varepsilon_2' - \varepsilon_1')e^{-u_2d}f_4\right\}$; $\quad$; $g_2 = \dfrac{1}{D_1}\cdot\left[(\varepsilon_0' - \varepsilon_1')(\varepsilon_1'u_2 - \varepsilon_2'u_1)e^{-u_1d}f_1 + (\varepsilon_2' - \varepsilon_1')(\varepsilon_1'u_0 + \varepsilon_0'u_1)e^{-u_2d}f_4\right]$ $g_3 = \dfrac{1}{D_1}\cdot\left[(\varepsilon_1' - \varepsilon_0')(\varepsilon_2'u_1 + \varepsilon_1'u_2)e^{u_1d}f_1 + (\varepsilon_2' - \varepsilon_1')(\varepsilon_0'u_1 - \varepsilon_1'u_0)e^{-u_2d}f_4\right]$; $g_4 = \dfrac{1}{D_1}\left\{2\varepsilon_2'u_1(\varepsilon_1' - \varepsilon_0')e^{-u_2d}f_1 + (\varepsilon_2' - \varepsilon_1')f_4\left[(\varepsilon_0'u_1 + \varepsilon_1'u_0)e^{u_1d} + (\varepsilon_0'u_1 - \varepsilon_1'u_0)e^{-u_1d}\right]\right\}$; where $D_1 = (\varepsilon_0'u_1 - \varepsilon_1'u_0)(\varepsilon_1'u_2 - \varepsilon_2'u_1)e^{-u_1d} + (\varepsilon_0'u_1 + \varepsilon_1'u_0)(\varepsilon_1'u_2 + \varepsilon_2'u_1)e^{u_1d}$.
Field in #0 medium (free space)	
E_x^0	$E_x^0 = -\dfrac{j}{\omega\mu\varepsilon_0'}\dfrac{\partial}{\partial x}\left(\dfrac{\partial A_y^0}{\partial y} + \dfrac{\partial A_z^0}{\partial z}\right) = E_{x1}^0$ $= \dfrac{jIdl}{4\pi\omega\varepsilon_0'}\int_0^\infty (f_1 - u_0 g_1)\left[\lambda J_0(\lambda\rho) - \dfrac{2}{\rho}J_1(\lambda\rho)\right]e^{-u_0z}\lambda^2\sin(\phi)\cos(\phi)d\lambda$
E_y^0	$E_y^0 = -\dfrac{j}{\omega\mu\varepsilon_0'}\left[\dfrac{\partial}{\partial y}\left(\dfrac{\partial A_y^0}{\partial y} + \dfrac{\partial A_z^0}{\partial z}\right) - \gamma_0^2 A_y^0\right] = E_{y1}^0$ $= \dfrac{jIdl}{4\pi\omega\varepsilon_0'}\int_0^\infty (f_1 - u_0 g_1)\left[\lambda J_0(\lambda\rho)\sin^2(\phi) + \dfrac{1}{\rho}J_1(\lambda\rho)\cos(2\phi)\right]e^{-u_0z}\lambda^2 d\lambda + \dfrac{jIdl}{4\pi\omega\varepsilon_0'}\int_0^\infty \gamma_0^2 e^{-u_0z}f_1\lambda J_0(\lambda\rho)d\lambda$

HED¹ -- Dipole in #1 medium (middle layer)

E_z^0	$$E_z^0 = -\frac{j}{\omega\mu\varepsilon_0'}\left[\frac{\partial}{\partial z}\left(\frac{\partial A_y^0}{\partial y} + \frac{\partial A_z^0}{\partial z}\right) - \gamma_0^2 A_z^0\right] = E_{zi}^0$$ $$= -\frac{jIdl}{4\pi\omega\varepsilon_0'}\int_0^\infty (u_0 f_1 - \lambda^2 g_1)\, e^{-u_0 z}\lambda^2 J_1(\lambda\rho)\sin(\phi)\,d\lambda$$
H_x^0	$$H_x^0 = \frac{1}{\mu}\left(\frac{\partial A_z^0}{\partial y} - \frac{\partial A_y^0}{\partial z}\right) = H_{xi}^0$$ $$= -\frac{Idl}{4\pi}\int_0^\infty e^{-u_0 z} g_1 \cdot \left[\lambda J_0(\lambda\rho)\sin^2(\phi) + \frac{1}{\rho}J_1(\lambda\rho)\cos(2\phi)\right]\lambda^2\, d\lambda + \frac{Idl}{4\pi}\int_0^\infty u_0 e^{-u_0 z} f_1 \lambda J_0(\lambda\rho)\,d\lambda$$
H_y^0	$$H_y^0 = -\frac{1}{\mu}\frac{\partial A_z^0}{\partial x} = H_{yi}^0$$ $$= -\frac{Idl}{4\pi}\int_0^\infty (e^{-u_0 z} g_1)\left[\lambda J_0(\lambda\rho) - \frac{2}{\rho}J_1(\lambda\rho)\right]\lambda^2\sin(\phi)\cos(\phi)\,d\lambda$$
H_z^0	$$H_z^0 = \frac{1}{\mu}\frac{\partial A_y^0}{\partial x} = H_{zi}^0$$ $$= -\frac{Idl}{4\pi}\int_0^\infty e^{-u_0 z} f_1 \lambda^2 J_1(\lambda\rho)\cos(\phi)\,d\lambda$$

Field in #1 medium (middle layer, conducting medium)

E_x^1	$$E_x^1 = -\frac{j}{\omega\mu\varepsilon_1'}\frac{\partial}{\partial x}\left(\frac{\partial A_y^1}{\partial y} + \frac{\partial A_z^1}{\partial z}\right) = E_{xi}^1 + E_{xr}^1$$ $$E_{xi}^1 = \frac{jIdl}{4\pi\omega\varepsilon_1'}\int_0^\infty \left\{\begin{array}{ll}u_1^{-1}e^{-u_1(z+h)} & (z+h\geq 0)\\ u_1^{-1}e^{u_1(z+h)} & (z+h\leq 0)\end{array}\right\}\cdot\left[\lambda J_0(\lambda\rho) - \frac{2}{\rho}J_1(\lambda\rho)\right]\lambda^2\sin(\phi)\cos(\phi)\,d\lambda$$

54

$$E_{xr}^1 = \frac{jIdl}{4\pi\omega\varepsilon_1'} \int_0^\infty \left(e^{-u_1 z} f_2 + e^{u_1 z} f_3 - u_1 e^{-u_1 z} g_2 + u_1 e^{u_1 z} g_3 \right) \cdot \left[\lambda J_0(\lambda\rho) - \frac{2}{\rho} J_1(\lambda\rho) \right] \lambda^2 \sin(\phi)\cos(\phi) d\lambda$$

E_y^1:

$$E_y^1 = -\frac{j}{\omega\mu\varepsilon_1'} \left[\frac{\partial}{\partial y} \left(\frac{\partial A_y^1}{\partial y} + \frac{\partial A_z^1}{\partial z} \right) - \gamma_1^2 A_y^1 \right] = E_{yi}^1 + E_{yr}^1$$

$$E_{yi}^1 = \frac{jIdl}{4\pi\omega\varepsilon_1'} \int_0^\infty \left(\begin{matrix} u_1^{-1} e^{-u_1(z+h)} & (z+h\geq 0) \\ u_1^{-1} e^{u_1(z+h)} & (z+h\leq 0) \end{matrix} \right) \cdot \left[\lambda J_0(\lambda\rho)\sin^2(\phi) + \frac{1}{\rho} J_1(\lambda\rho)\cos(2\phi) \right] \lambda^2 d\lambda$$

$$+ \frac{jIdl}{4\pi\omega\varepsilon_1'} \int_0^\infty \left(\begin{matrix} u_1^{-1} e^{-u_1(z+h)} & (z+h\geq 0) \\ u_1^{-1} e^{u_1(z+h)} & (z+h\leq 0) \end{matrix} \right) \cdot \gamma_1^2 \lambda J_0(\lambda\rho) d\lambda$$

$$E_{yr}^1 = \frac{jIdl}{4\pi\omega\varepsilon_1'} \int_0^\infty \left(e^{-u_1 z} f_2 + e^{u_1 z} f_3 - u_1 e^{-u_1 z} g_2 + u_1 e^{u_1 z} g_3 \right) \cdot \left[\lambda J_0(\lambda\rho)\sin^2(\phi) + \frac{1}{\rho} J_1(\lambda\rho)\cos(2\phi) \right] \lambda^2 d\lambda$$

$$+ \frac{jIdl}{4\pi\omega\varepsilon_1'} \int_0^\infty \left(e^{-u_1 z} f_2 + e^{u_1 z} f_3 \right) \cdot \gamma_1^2 \lambda J_0(\lambda\rho) d\lambda$$

E_z^1:

$$E_z^1 = -\frac{j}{\omega\mu\varepsilon_1'} \left[\frac{\partial}{\partial z} \left(\frac{\partial A_y^1}{\partial y} + \frac{\partial A_z^1}{\partial z} \right) - \gamma_1^2 A_z^1 \right] = E_{zi}^1 + E_{zr}^1$$

$$E_{zi}^1 = \frac{jIdl}{4\pi\omega\varepsilon_1'} \int_0^\infty \left(\begin{matrix} -e^{-u_1(z+h)} & (z+h\geq 0) \\ e^{u_1(z+h)} & (z+h\leq 0) \end{matrix} \right) \cdot \lambda^2 J_1(\lambda\rho)\sin(\phi) d\lambda$$

$$E_{zr}^1 = \frac{jIdl}{4\pi\omega\varepsilon_1'} \int_0^\infty \left(-u_1 e^{-u_1 z} f_2 + u_1 e^{u_1 z} f_3 + \lambda^2 e^{-u_1 z} g_2 + \lambda^2 e^{u_1 z} g_3 \right) \cdot \lambda^2 J_1(\lambda\rho)\sin(\phi) d\lambda$$

H_x^1:

$$H_x^1 = \frac{1}{\mu_1} \left(\frac{\partial A_z^1}{\partial y} - \frac{\partial A_y^1}{\partial z} \right) = H_{xi}^1 + H_{xr}^1$$

HED^1 -- Dipole in #1 medium (middle layer)

	$H_{xi}^1 = -\dfrac{Idl}{4\pi}\displaystyle\int_0^\infty \left[\begin{cases} -e^{-u_1(z+h)} & (z+h\geq 0) \\ e^{u_1(z+h)} & (z+h\leq 0) \end{cases}\right]\cdot \lambda J_0(\lambda\rho)d\lambda$ $H_{xr}^1 = \dfrac{Idl}{4\pi}\displaystyle\int_0^\infty \left(u_1 e^{-u_1 z}f_2 - u_1 e^{u_1 z}f_3\right)\lambda J_0(\lambda\rho)d\lambda - \dfrac{Idl}{4\pi}\displaystyle\int_0^\infty \left(e^{-u_1 z}g_2 + e^{u_1 z}g_3\right)\left[\lambda J_0(\lambda\rho)\sin^2(\phi)+\dfrac{1}{\rho}J_1(\lambda\rho)\cos(2\phi)\right]\lambda^2 d\lambda$
H_y^1	$H_y^1 = -\dfrac{1}{\mu}\dfrac{\partial A_z^1}{\partial x} = H_{yi}^1 + H_{yr}^1$ $H_{yi}^1 = 0$ $H_{yr}^1 = \dfrac{Idl}{4\pi}\displaystyle\int_0^\infty \left(e^{-u_1 z}g_2 + e^{u_1 z}g_3\right)\left[\lambda J_0(\lambda\rho)-\dfrac{2}{\rho}J_1(\lambda\rho)\right]\lambda^2 \sin(\phi)\cos(\phi)d\lambda$
H_z^1	$H_z^1 = \dfrac{1}{\mu_1}\dfrac{\partial A_y^1}{\partial x} = H_{zi}^1 + H_{zr}^1$ $H_{zi}^1 = -\dfrac{Idl}{4\pi}\displaystyle\int_0^\infty \left(\begin{cases} u_1^{-1}e^{-u_1(z+h)} & (z+h\geq 0) \\ u_1^{-1}e^{u_1(z+h)} & (z+h\leq 0) \end{cases}\right)\lambda^2 J_1(\lambda\rho)\cos(\phi)d\lambda$ $H_{zr}^1 = -\dfrac{Idl}{4\pi}\displaystyle\int_0^\infty \left(e^{-u_1 z}f_2 + e^{u_1 z}f_3\right)\lambda^2 J_1(\lambda\rho)\cos(\phi)d\lambda$

Field in #2 medium (bottom, conducting medium)

E_x^2	$E_x^2 = -\dfrac{j}{\omega\mu\varepsilon_2'}\dfrac{\partial}{\partial x}\left(\dfrac{\partial A_y^2}{\partial y}+\dfrac{\partial A_z^2}{\partial z}\right) = E_{xi}^2$ $= \dfrac{jIdl}{4\pi\omega\varepsilon_2'}\displaystyle\int_0^\infty \left(f_4 + u_2 g_4\right)\left[\lambda J_0(\lambda\rho)-\dfrac{2}{\rho}J_1(\lambda\rho)\right]e^{u_2 z}\lambda^2 \sin(\phi)\cos(\phi)d\lambda$

HED¹ -- Dipole in #1 medium (middle layer)

E_y^2	$E_y^2 = -\dfrac{j}{\omega\mu\varepsilon_2'}\left[\dfrac{\partial}{\partial y}\left(\dfrac{\partial A_y^2}{\partial y}+\dfrac{\partial A_z^2}{\partial z}\right)-\gamma_2^2 A_y^2\right]=E_{yt}^2$ $=\dfrac{jIdl}{4\pi\omega\varepsilon_2'}\int_0^\infty (f_4+u_2 g_4)\left[\lambda J_0(\lambda\rho)\sin^2(\phi)+\dfrac{1}{\rho}J_1(\lambda\rho)\cos(2\phi)\right]e^{u_2 z}\lambda^2 d\lambda + \dfrac{jIdl}{4\pi\omega\varepsilon_2'}\int_0^\infty \gamma_2^2 e^{u_2 z} f_4 \lambda J_0(\lambda\rho)d\lambda$
E_z^2	$E_z^2 = -\dfrac{j}{\omega\mu\varepsilon_2'}\left[\dfrac{\partial}{\partial z}\left(\dfrac{\partial A_y^2}{\partial y}+\dfrac{\partial A_z^2}{\partial z}\right)-\gamma_2^2 A_z^2\right]=E_{zt}^2$ $=\dfrac{jIdl}{4\pi\omega\varepsilon_2'}\int_0^\infty (u_2 f_4+\lambda^2 g_4)e^{u_2 z}\lambda^2 J_1(\lambda\rho)\cos(\phi)d\lambda$
H_x^2	$H_x^2 = \dfrac{1}{\mu_2}\left(\dfrac{\partial A_z^2}{\partial y}-\dfrac{\partial A_y^2}{\partial z}\right)=H_{xt}^2$ $=-\dfrac{Idl}{4\pi}\int_0^\infty e^{u_2 z}g_4\cdot\left[\lambda J_0(\lambda\rho)\sin^2(\phi)+\dfrac{1}{\rho}J_1(\lambda\rho)\cos(2\phi)\right]\lambda^2 d\lambda-\dfrac{Idl}{4\pi}\int_0^\infty u_2 e^{u_2 z}f_4 \lambda J_0(\lambda\rho)d\lambda$
H_y^2	$H_y^2 = \dfrac{1}{\mu}\dfrac{\partial A_z^2}{\partial x}=H_{yt}^2$ $=\dfrac{Idl}{4\pi}\int_0^\infty (e^{u_2 z}g_4)\left[\lambda J_0(\lambda\rho)-\dfrac{2}{\rho}J_1(\lambda\rho)\right]\lambda^2\sin(\phi)\cos(\phi)d\lambda$
H_z^2	$H_z^2 = -\dfrac{1}{\mu}\dfrac{\partial A_y^2}{\partial x}=H_{zt}^2$ $=-\dfrac{Idl}{4\pi}\int_0^\infty e^{u_2 z}f_4\lambda^2 J_1(\lambda\rho)\cos(\phi)d\lambda$

HMD^0 – Dipole in #0 medium (free space)

HMD (Dipole in #0 medium)

Free Space (#0) $\varepsilon_0, \sigma_0, \mu_0$

z y

HMD $\Rightarrow$ z = h

z = 0   • observation point

Conducting Medium (#1) $\varepsilon_1, \sigma_1, \mu_0$

z = –d

Bottom (#2) $\varepsilon_2, \sigma_2, \mu_0$

Vector potentials:

$$F_y^0 = k_0 \frac{e^{\gamma_0 R}}{R} + k_0 \int_0^\infty f_1 e^{-u_0 z}\lambda J_0(\lambda\rho)d\lambda \quad (z \geq 0);$$

$$\frac{e^{\gamma_0 R}}{R} = \begin{cases} \int_0^\infty u_0^{-1} e^{-u_0(z-h)}\lambda J_0(\lambda\rho)d\lambda \quad (z-h \geq 0) \\ \int_0^\infty u_0^{-1} e^{u_0(z-h)}\lambda J_0(\lambda\rho)d\lambda \quad (z-h \leq 0) \end{cases};$$

$$F_y^1 = k_0 \int_0^\infty \left[f_2 e^{-u_1 z} + f_3 e^{u_1 z}\right]\lambda J_0(\lambda\rho)d\lambda \quad (-d \leq z \leq 0); \quad F_y^2 = k_0 \int_0^\infty f_4 e^{u_2 z}\lambda J_0(\lambda\rho)d\lambda \quad (z \leq -d);$$

$$F_z^0 = k_0 \frac{\partial}{\partial y}\int_0^\infty g_1 e^{-u_0 z}\lambda J_0(\lambda\rho)d\lambda \quad (z \geq 0);$$

$$F_z^1 = k_0 \frac{\partial}{\partial y}\int_0^\infty \left[g_2 e^{-u_1 z} + g_3 e^{u_1 z}\right]\lambda J_0(\lambda\rho)d\lambda \quad (-d \leq z \leq 0);$$

$$F_z^2 = k_0 \frac{\partial}{\partial y}\int_0^\infty g_4 e^{u_2 z}\lambda J_0(\lambda\rho)d\lambda \quad (z \leq -d);$$

where $\gamma_i^2 = -\omega^2\mu\varepsilon_i' = -\omega^2\mu\left(\varepsilon_i - j\frac{\sigma_i}{\omega}\right)$; $u_i = \sqrt{(\lambda^2 + \gamma_i^2)}$; $k_0 = \frac{j\omega\mu\varepsilon_0' IdA}{4\pi}$.

Boundary conditions

At z = 0 (upper) interface: $\frac{1}{\varepsilon_0'}\left(\frac{\partial F_y^0}{\partial y} + \frac{\partial F_z^0}{\partial z}\right) = \frac{1}{\varepsilon_1'}\left(\frac{\partial F_y^1}{\partial y} + \frac{\partial F_z^1}{\partial z}\right)$; $F_y^0 = F_y^1$; $\frac{F_z^0}{\varepsilon_0'} = \frac{F_z^1}{\varepsilon_1'}$; $\frac{1}{\varepsilon_0'}\frac{\partial F_y^0}{\partial z} = \frac{1}{\varepsilon_1'}\frac{\partial F_y^1}{\partial z}$;

At z = –d (lower) interface: $\frac{1}{\varepsilon_2'}\left(\frac{\partial F_y^2}{\partial y} + \frac{\partial F_z^2}{\partial z}\right) = \frac{1}{\varepsilon_1'}\left(\frac{\partial F_y^1}{\partial y} + \frac{\partial F_z^1}{\partial z}\right)$; $F_y^2 = F_y^1$; $\frac{F_z^2}{\varepsilon_2'} = \frac{F_z^1}{\varepsilon_1'}$; $\frac{1}{\varepsilon_2'}\frac{\partial F_y^2}{\partial z} = \frac{1}{\varepsilon_1'}\frac{\partial F_y^1}{\partial z}$.

Coefficient functions

$$f_1 = \frac{e^{-u_0 h}\left[(\varepsilon_1'u_0 + \varepsilon_0'u_1)(\varepsilon_1'u_2 - \varepsilon_2'u_1)e^{-u_1 d} + (\varepsilon_0'u_1 - \varepsilon_1'u_0)(\varepsilon_1'u_2 + \varepsilon_2'u_1)e^{u_1 d}\right]}{u_0 \cdot D}; \quad f_2 = \frac{2\varepsilon_1'(\varepsilon_1'u_2 - \varepsilon_2'u_1)e^{-u_0 h}e^{-u_1 d}}{D};$$

$$f_3 = \frac{-2\varepsilon_1'(\varepsilon_1'u_2 + \varepsilon_2'u_1)e^{-u_0 h}e^{u_1 d}}{D}; \quad f_4 = \frac{-4\varepsilon_1'\varepsilon_2'u_1 e^{-u_0 h}e^{(u_1+u_2)d}}{D}; \quad \text{where } D = (\varepsilon_1'u_0 - \varepsilon_0'u_1)(\varepsilon_1'u_2 - \varepsilon_2'u_1)e^{-u_1 d} - (\varepsilon_0'u_1 + \varepsilon_1'u_0)(\varepsilon_1'u_2 + \varepsilon_2'u_1)e^{u_1 d}.$$

Coefficient functions (contd.)	$g_1 = \dfrac{\varepsilon_0'}{D_1}\left\{\varepsilon_2'(\varepsilon_0' - \varepsilon_1')\left[(u_1 - u_2)e^{-u_1 d} + (u_1 + u_2)e^{u_1 d}\right](f_2 + f_3) - 2\varepsilon_0'u_1(\varepsilon_2' - \varepsilon_1')e^{-u_1 d}f_4\right\}$; $g_2 = \dfrac{1}{D_1}\left[\varepsilon_2'(\varepsilon_1' - \varepsilon_0')(u_2 - u_1)e^{-u_1 d}(f_2 + f_3) - \varepsilon_0'(\varepsilon_2' - \varepsilon_1')(u_0 + u_1)e^{-u_1 d}f_4\right]$ $g_3 = \dfrac{-1}{D_1}\left[\varepsilon_2'(\varepsilon_1' - \varepsilon_0')(u_2 + u_1)e^{-u_1 d}(f_2 + f_3) - \varepsilon_0'(\varepsilon_2' - \varepsilon_1')(u_0 - u_1)e^{-u_1 d}f_4\right]$; $g_4 = \dfrac{1}{D_1}\left\{2\varepsilon_2'u_1(\varepsilon_0' - \varepsilon_1')e^{u_1 d}(f_2 + f_3) + \varepsilon_0'(\varepsilon_2' - \varepsilon_1')\left[(u_0 - u_1)e^{-u_1 d} - (u_0 + u_1)e^{u_1 d}\right]f_4\right\}$; where $D_1 = \varepsilon_0'\varepsilon_2'(u_0 - u_1)(u_2 - u_1)e^{-u_1 d} - \varepsilon_0'\varepsilon_2'(u_0 + u_1)(u_2 + u_1)e^{u_1 d}$.

Field in #0 medium (free space)

E_x^0	$E_x^0 = -\dfrac{1}{\varepsilon_0'}\left(\dfrac{\partial F_z^0}{\partial y} - \dfrac{\partial F_y^0}{\partial z}\right) = E_{xi}^0 + E_{xr}^0$ $E_{xi}^0 = \dfrac{k_0}{\varepsilon_0'}\int_0^\infty\left(\begin{matrix}-e^{-u_0(z-h)} & (z-h\geq 0)\\ e^{u_0(z-h)} & (z-h\leq 0)\end{matrix}\right)\lambda J_0(\lambda\rho)d\lambda$ $E_{xr}^0 = -\dfrac{k_0}{\varepsilon_0'}\int_0^\infty u_0 e^{-u_0 z}f_1\lambda J_0(\lambda\rho)d\lambda + \dfrac{k_0}{\varepsilon_0'}\int_0^\infty e^{-u_0 z}g_1\left[\lambda J_0(\lambda\rho)\sin^2(\phi) + \dfrac{1}{\rho}J_1(\lambda\rho)\cos(2\phi)\right]\lambda^2 d\lambda$
E_y^0	$E_y^0 = -\dfrac{1}{\varepsilon_0'}\dfrac{\partial F_z^0}{\partial x} = E_{yi}^0 + E_{yr}^0$ $E_{yi}^0 = 0$ $E_{yr}^0 = -\dfrac{k_0}{\varepsilon_0'}\int_0^\infty e^{-u_0 z}g_1\left[\lambda J_0(\lambda\rho) - \dfrac{2}{\rho}J_1(\lambda\rho)\right]\lambda^2\sin(\phi)\cos(\phi)d\lambda$

HMD^0 – Dipole in #0 medium (free space)

E_z^0	$E_z^0 = -\dfrac{1}{\varepsilon_0'}\dfrac{\partial F_y^0}{\partial x} = E_{zi}^0 + E_{zr}^0$ $E_{zi}^0 = \dfrac{k_0}{\varepsilon_0'}\displaystyle\int_0^\infty \left[\begin{array}{ll} u_0^{-1}e^{-u_0(z-h)} & (z-h\geq 0) \\ u_0^{-1}e^{u_0(z-h)} & (z-h\leq 0)\end{array}\right]\lambda^2 J_1(\lambda\rho)\cos(\phi)\,d\lambda$ $E_{zr}^0 = \dfrac{k_0}{\varepsilon_0'}\displaystyle\int_0^\infty e^{-u_0 z}f_1\lambda^2 J_1(\lambda\rho)\cos(\phi)\,d\lambda$
H_x^0	$H_x^0 = -\dfrac{j}{\omega\mu\varepsilon_0'}\dfrac{\partial}{\partial x}\left(\dfrac{\partial F_y^0}{\partial y}+\dfrac{\partial F_z^0}{\partial z}\right) = H_{xi}^0 + H_{xr}^0$ $H_{xi}^0 = -\dfrac{IdA}{4\pi}\displaystyle\int_0^\infty \left(\begin{array}{ll} u_0^{-1}e^{-u_0(z-h)} & (z-h\geq 0) \\ u_0^{-1}e^{u_0(z-h)} & (z-h\leq 0)\end{array}\right)\cdot\left[\lambda J_0(\lambda\rho)-\dfrac{2}{\rho}J_1(\lambda\rho)\right]\lambda^2\sin(\phi)\cos(\phi)\,d\lambda$ $H_{xr}^0 = \dfrac{IdA}{4\pi_0}\displaystyle\int_0^\infty (e^{-u_0 z}f_1 - u_0 e^{-u_0 z}g_1)\left[\lambda J_0(\lambda\rho)-\dfrac{2}{\rho}J_1(\lambda\rho)\right]\lambda^2\sin(\phi)\cos(\phi)\,d\lambda$
H_y^0	$H_y^0 = -\dfrac{j}{\omega\mu\varepsilon_0'}\left[\dfrac{\partial}{\partial y}\left(\dfrac{\partial F_y^0}{\partial y}+\dfrac{\partial F_z^0}{\partial z}\right)-\gamma_0^2 F_y^0\right] = H_{yi}^0 + H_{yr}^0$ $H_{yi}^0 = -\dfrac{IdA}{4\pi}\displaystyle\int_0^\infty \left(\begin{array}{ll} u_0^{-1}e^{-u_0(z-h)} & (z-h\geq 0) \\ u_0^{-1}e^{u_0(z-h)} & (z-h\leq 0)\end{array}\right)\left[\lambda J_0(\lambda\rho)\sin^2(\phi)+\dfrac{1}{\rho}J_1(\lambda\rho)\cos(2\phi)\right]\lambda^2\,d\lambda - \dfrac{IdA}{4\pi_0}\displaystyle\int_0^\infty \left(\begin{array}{ll} u_0^{-1}e^{-u_0(z-h)} & (z-h\geq 0) \\ u_0^{-1}e^{u_0(z-h)} & (z-h\leq 0)\end{array}\right)\gamma_0^2\lambda J_0(\lambda\rho)\,d\lambda$ $H_{yr}^0 = -\dfrac{IdA}{4\pi_0}\displaystyle\int_0^\infty (e^{-u_0 z}f_1 - u_0 e^{-u_0 z}g_1)\left[\lambda J_0(\lambda\rho)\sin^2(\phi)+\dfrac{1}{\rho}J_1(\lambda\rho)\cos(2\phi)\right]\lambda^2\,d\lambda - \dfrac{IdA}{4\pi_0}\displaystyle\int_0^\infty e^{-u_0 z}f_1\gamma_0^2\lambda J_0(\lambda\rho)\,d\lambda$
H_z^0	$H_z^0 = -\dfrac{j}{\omega\mu\varepsilon_0'}\left[\dfrac{\partial}{\partial z}\left(\dfrac{\partial F_y^0}{\partial y}+\dfrac{\partial F_z^0}{\partial z}\right)-\gamma_0^2 F_z^0\right] = H_{zi}^0 + H_{zr}^0$

	$H_{z\iota}^0 = -\dfrac{IdA}{4\pi}\displaystyle\int_b^\infty \left(\left\{\begin{array}{ll}-e^{-u_0(z-h)} & (z-h\geq 0)\\ e^{u_0(z-h)} & (z-h\leq 0)\end{array}\right\}\right)\cdot \lambda^2 J_1(\lambda\rho)\sin(\phi)d\lambda$
	$H_{zr}^0 = \dfrac{IdA}{4\pi}\displaystyle\int_b^\infty \left(u_0 e^{-u_0 z}f_1 - \lambda^2 e^{-u_0 z}g_1\right)\lambda^2 J_1(\lambda\rho)\sin(\phi)d\lambda$

Field in #1 medium (middle layer, conducting medium)

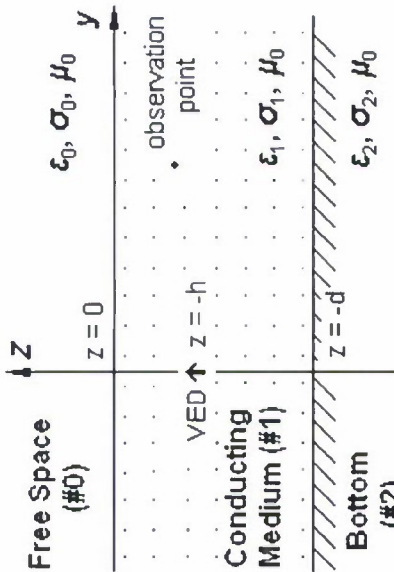|	
E_x^1	$E_x^1 = -\dfrac{1}{\varepsilon_1'}\left(\dfrac{\partial F_z^1}{\partial y} - \dfrac{\partial F_y^1}{\partial z}\right) = E_{x\iota}^1$ $= \dfrac{k_0}{\varepsilon_1'}\displaystyle\int_b^\infty \left(e^{-u_1 z}g_2 + e^{u_1 z}g_3\right)\left[\lambda J_0(\lambda\rho)\sin^2(\phi) + \dfrac{1}{\rho}J_1(\lambda\rho)\cos(2\phi)\right]\lambda^2 d\lambda - \dfrac{k_0}{\varepsilon_1'}\displaystyle\int_b^\infty u_1\left(e^{-u_1 z}f_2 - e^{u_1 z}f_3\right)\lambda J_0(\lambda\rho)d\lambda$
E_y^1	$E_y^0 = \dfrac{1}{\varepsilon_1'}\dfrac{\partial F_z^1}{\partial x} = E_{y\iota}^1$ $= -\dfrac{k_0}{\varepsilon_1'}\displaystyle\int_b^\infty \left(e^{-u_1 z}g_2 + e^{u_1 z}g_3\right)\left[\lambda J_0(\lambda\rho) - \dfrac{2}{\rho}J_1(\lambda\rho)\right]\lambda^2 \sin(\phi)\cos(\phi)d\lambda$
E_z^1	$E_z^1 = -\dfrac{1}{\varepsilon_1'}\dfrac{\partial F_y^1}{\partial x} = E_{z\iota}^1$ $= -\dfrac{k_0}{\varepsilon_1'}\displaystyle\int_b^\infty \left(e^{-u_1 z}f_2 + e^{u_1 z}f_3\right)\lambda^2 J_1(\lambda\rho)\cos(\phi)d\lambda$
H_x^1	$H_x^1 = -\dfrac{1}{\varepsilon_1'}\left(\dfrac{\partial F_z^1}{\partial y} - \dfrac{\partial F_y^1}{\partial z}\right) = H_{x\iota}^1$ $= -\dfrac{IdA\varepsilon_0'}{4\pi\varepsilon_1'}\displaystyle\int_b^\infty \left(e^{-u_1 z}f_2 + e^{u_1 z}f_3 - u_1 e^{-u_1 z}g_2 + u_1 e^{u_1 z}g_3\right)\left[\lambda J_0(\lambda\rho) - \dfrac{2}{\rho}J_1(\lambda\rho)\right]\lambda^2\sin(\phi)\cos(\phi)d\lambda$

61

HMD^0 – Dipole in #0 medium (free space)

H_y^1	$H_y^1 = -\dfrac{j}{\omega\mu\varepsilon_1'}\left[\dfrac{\partial}{\partial y}\left(\dfrac{\partial F_y^1}{\partial y}+\dfrac{\partial F_z^1}{\partial z}\right)-\gamma_1^2 F_y^1\right] = H_{yt}^1$ $= \dfrac{IdA\varepsilon_0'}{4\pi\varepsilon_1'}\left\{\displaystyle\int_0^\infty \left(e^{-u_1 z}f_2+e^{u_1 z}f_3-u_1 e^{-u_1 z}g_2+u_1 e^{u_1 z}g_3\right)\left[\lambda J_0(\lambda\rho)\sin^2(\phi)+\dfrac{1}{\rho}J_1(\lambda\rho)\cos(2\phi)\right]\lambda^2 d\lambda + \int_0^\infty \gamma_1^2\left(e^{-u_1 z}f_2+e^{u_1 z}f_3\right)\lambda J_0(\lambda\rho)d\lambda\right\}$
H_z^1	$H_z^1 = -\dfrac{j}{\omega\mu\varepsilon_1'}\left[\dfrac{\partial}{\partial z}\left(\dfrac{\partial F_y^1}{\partial y}+\dfrac{\partial F_z^1}{\partial z}\right)-\gamma_1^2 F_z^1\right] = H_{zt}^1$ $= \dfrac{IdA\varepsilon_0'}{4\pi\varepsilon_1'}\displaystyle\int_0^\infty \left(-u_1 e^{-u_1 z}f_2+u_1 e^{u_1 z}f_3+\lambda^2 e^{-u_1 z}g_2+\lambda^2 e^{u_1 z}g_3\right)\lambda^2 J_1(\lambda\rho)\sin(\phi)d\lambda$

Field in #2 medium (bottom, conducting medium)

E_x^2	$E_x^2 = -\dfrac{1}{\varepsilon_2'}\left(\dfrac{\partial F_z^2}{\partial y}-\dfrac{\partial F_y^2}{\partial z}\right) = E_{xt}^2$ $= \dfrac{k_0}{\varepsilon_2'}\displaystyle\int_0^\infty e^{u_2 z}g_4\left[\lambda J_0(\lambda\rho)\sin^2(\phi)+\dfrac{1}{\rho}J_1(\lambda\rho)\cos(2\phi)\right]\lambda^2 d\lambda + \dfrac{k_0}{\varepsilon_2'}\int_0^\infty u_2 e^{u_2 z}f_4\lambda J_0(\lambda\rho)d\lambda$
E_y^2	$E_y^2 = \dfrac{1}{\varepsilon_2'}\dfrac{\partial F_z^2}{\partial x} = E_{yt}^2$ $= -\dfrac{k_0}{\varepsilon_2'}\displaystyle\int_0^\infty e^{u_2 z}g_4\left[\lambda J_0(\lambda\rho)-\dfrac{2}{\rho}J_1(\lambda\rho)\right]\lambda^2 \sin(\phi)\cos(\phi)d\lambda$
E_z^2	$E_z^2 = -\dfrac{1}{\varepsilon_2'}\dfrac{\partial F_y^2}{\partial x} = E_{zt}^2$ $= \dfrac{k_0}{\varepsilon_2'}\displaystyle\int_0^\infty e^{u_2 z}f_4\lambda^2 J_1(\lambda\rho)\cos(\phi)d\lambda$

HMD^0 – Dipole in #0 medium (free space)

H_x^2	$H_x^2 = -\dfrac{j}{\omega\mu\varepsilon_2'}\dfrac{\partial}{\partial x}\left(\dfrac{\partial F_y^2}{\partial y}+\dfrac{\partial F_z^2}{\partial z}\right) = H_{xt}^2$ $= -\dfrac{IdA\varepsilon_0'}{4\pi\varepsilon_1'}\int_0^\infty (f_4+u_2 g_4)e^{u_2 z}\left[\lambda J_0(\lambda\rho)-\dfrac{2}{\rho}J_1(\lambda\rho)\right]\lambda^2\sin(\phi)\cos(\phi)d\lambda$
H_y^2	$H_y^2 = -\dfrac{j}{\omega\mu\varepsilon_2'}\left[\dfrac{\partial}{\partial y}\left(\dfrac{\partial F_y^2}{\partial y}+\dfrac{\partial F_z^2}{\partial z}\right)-\gamma_2^2 F_y^2\right]=H_{yt}^2$ $= -\dfrac{IdA\varepsilon_0'}{4\pi\varepsilon_1'}\int_0^\infty (f_4+u_2 g_4)e^{u_2 z}\left[\lambda J_0(\lambda\rho)\sin^2(\phi)+\dfrac{1}{\rho}J_1(\lambda\rho)\cos(2\phi)\right]\lambda^2 d\lambda -\dfrac{IdA\varepsilon_0'}{4\pi\varepsilon_1'}\int_0^\infty \gamma_2^2 e^{u_2 z}f_4\lambda J_0(\lambda\rho)d\lambda$
H_z^2	$H_z^2 = -\dfrac{j}{\omega\mu\varepsilon_2'}\left[\dfrac{\partial}{\partial z}\left(\dfrac{\partial F_y^2}{\partial y}+\dfrac{\partial F_z^2}{\partial z}\right)-\gamma_2^2 F_z^2\right]=H_{zt}^2$ $= -\dfrac{IdA\varepsilon_0'}{4\pi\varepsilon_1'}\int_0^\infty (u_2 f_4+\lambda^2 g_4)e^{u_2 z}\lambda^2 J_1(\lambda\rho)\sin(\phi)d\lambda$

63

VED^0 – Dipole in #0 medium (free space)

VED (Dipole in #0 medium)

Free Space (#0): VED
$\varepsilon_0, \sigma_0, \mu_0$ — y, $z = h$, $z = 0$, observation point

Conducting Medium (#1): $\varepsilon_1, \sigma_1, \mu_0$, $z = -d$

Bottom (#2): $\varepsilon_2, \sigma_2, \mu_0$

Vector potentials:

$$A_z^0 = k_0 \frac{e^{\gamma_0 R}}{R} + k_0 \int_0^\infty f_1 e^{-u_0 z}\,\lambda J_0(\lambda\rho)\,d\lambda \quad (z \geq 0);$$

$$A_z^1 = k_0 \int_0^\infty \left[f_2 e^{-u_1 z} + f_3 e^{u_1 z} \right] \lambda J_0(\lambda\rho)\,d\lambda \quad (-d \leq z \leq 0);$$

$$A_z^2 = k_0 \int_0^\infty f_4 e^{u_2 z}\,\lambda J_0(\lambda\rho)\,d\lambda \quad (z \leq -d);$$

$$\text{where } \frac{e^{\gamma_0 R}}{R} = \int_0^\infty \begin{cases} u_0^{-1} e^{-u_0(z-h)}\,\lambda J_0(\lambda\rho)\,d\lambda & (z - h \geq 0) \\ u_0^{-1} e^{u_0(z-h)}\,\lambda J_0(\lambda\rho)\,d\lambda & (z - h \leq 0) \end{cases}$$

$$\text{and } \gamma_i^2 = -\omega^2 \mu \varepsilon_i' = -\omega^2 \mu\left(\varepsilon_i - j\frac{\sigma_i}{\omega}\right); \quad u_i = \sqrt{(\lambda^2 + \gamma_i^2)}; \quad k_0 = \frac{\mu Idl}{4\pi}.$$

Boundary conditions

At $z = 0$ (upper) interface: $\quad A_z^0 = A_z^1$; $\quad \dfrac{1}{\varepsilon_0'}\dfrac{\partial A_z^0}{\partial z} = \dfrac{1}{\varepsilon_1'}\dfrac{\partial A_z^1}{\partial z}$;

At $z = -d$ (lower) interface: $\quad A_z^2 = A_z^1$; $\quad \dfrac{1}{\varepsilon_2'}\dfrac{\partial A_z^2}{\partial z} = \dfrac{1}{\varepsilon_1'}\dfrac{\partial A_z^1}{\partial z}$.

Coefficient functions

$$f_1 = \frac{e^{-u_0 h}}{u_0 D}\left[(\varepsilon_1' u_0 + \varepsilon_0' u_1)(\varepsilon_1' u_2 - \varepsilon_2' u_1)e^{-u_1 d} + (\varepsilon_1' u_0 + \varepsilon_0' u_1)(\varepsilon_1' u_2 + \varepsilon_2' u_1)e^{u_1 d} \right]; \quad f_2 = \frac{2\varepsilon_1'}{D}(\varepsilon_1' u_2 - \varepsilon_2' u_1)e^{-u_0 h}e^{-u_1 d};$$

$$f_3 = -\frac{2\varepsilon_1'}{D}(\varepsilon_1' u_2 + \varepsilon_2' u_1)e^{-u_0 h}e^{u_1 d}; \quad f_4 = -\frac{4\varepsilon_1'\varepsilon_2' u_1 e^{-u_0 h}e^{(u_1+u_2)d}}{D};$$

$$\text{where } D = (\varepsilon_1' u_0 - \varepsilon_0' u_1)(\varepsilon_1' u_2 - \varepsilon_2' u_1)e^{-u_1 d} - (\varepsilon_1' u_0 + \varepsilon_0' u_1)(\varepsilon_1' u_2 + \varepsilon_2' u_1)e^{u_1 d}.$$
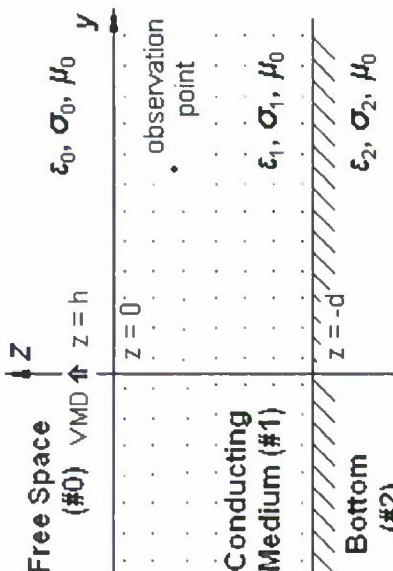
VED^0 – Dipole in #0 medium (free space)

Field in #0 medium (free space)

E_ρ^0

$$E_\rho^0 = -\frac{j}{\omega\mu\varepsilon_0'}\frac{\partial^2 A_z^0}{\partial\rho\partial z} = E_{\rho i}^0 + E_{\rho r}^0$$

$$E_{\rho i}^0 = \frac{jIdl}{4\pi\omega\varepsilon_0'}\int_0^\infty \left(\begin{cases} -e^{-u_0(z-h)} & (z-h\geq 0) \\ e^{u_0(z-h)} & (z-h\leq 0) \end{cases}\right)\lambda^2 J_1(\lambda\rho)d\lambda\,; \quad E_{\rho r}^0 = -\frac{jIdl}{4\pi\omega\varepsilon_0'}\int_0^\infty u_0 e^{-u_0 z} f_1 \lambda^2 J_1(\lambda\rho)d\lambda$$

E_z^0

$$E_z^0 = -\frac{j}{\omega\mu\varepsilon_0'}\left(\frac{\partial^2}{\partial z^2}-\gamma_0^2\right)A_z^0 = E_{zi}^0 + E_{zr}^0$$

$$E_{zi}^0 = -\frac{jIdl}{4\pi\omega\varepsilon_0'}\int_0^\infty \left(\begin{cases} u_0^{-1}e^{-u_0(z-h)} & (z-h\geq 0) \\ u_0^{-1}e^{u_0(z-h)} & (z-h\leq 0) \end{cases}\right)\lambda^3 J_0(\lambda\rho)d\lambda\,; \quad E_{zr}^0 = -\frac{jIdl}{4\pi\omega\varepsilon_0'}\int_0^\infty e^{-u_0 z} f_1 \lambda^3 J_0(\lambda\rho)d\lambda$$

H_ϕ^0

$$H_\phi^0 = -\frac{1}{\mu}\frac{\partial A_z^0}{\partial\rho} = H_{\phi i}^0 + H_{\phi r}^0$$

$$H_{\phi i}^0 = \frac{Idl}{4\pi}\int_0^\infty \left(\begin{cases} u_0^{-1}e^{-u_0(z-h)} & (z-h\geq 0) \\ u_0^{-1}e^{u_0(z-h)} & (z-h\leq 0) \end{cases}\right)\lambda^2 J_1(\lambda\rho)d\lambda\,; \quad H_{\phi r}^0 = \frac{Idl}{4\pi}\int_0^\infty e^{-u_0 z} f_1 \lambda^2 J_1(\lambda\rho)d\lambda$$

Field in #1 medium (middle layer, conducting medium)

E_ρ^1

$$E_\rho^1 = E_{\rho r}^1 = -\frac{j}{\omega\mu\varepsilon_1'}\frac{\partial^2 A_z^1}{\partial\rho\partial z} = \frac{jIdl}{4\pi\omega\varepsilon_1'}\int_0^\infty u_1\left[-e^{-u_1 z}f_2 + e^{u_1 z}f_3\right]\lambda^2 J_1(\lambda\rho)d\lambda$$

VED^0 – Dipole in #0 medium (free space)

E_z^1	$E_z^1 = E_{z1} = -\dfrac{j}{\omega\mu\varepsilon_1'}\left(\dfrac{\partial^2}{\partial z^2}-\gamma_1^2\right)A_z^1 = -\dfrac{jIdl}{4\pi\omega\varepsilon_1'}\int_0^\infty\left[e^{-u_1 z}f_2 + e^{u_1 z}f_3\right]\lambda^3 J_0(\lambda\rho)d\lambda$
H_ϕ^1	$H_\phi^1 = H_{\phi 1} = \dfrac{1}{\mu}\dfrac{\partial A_z^1}{\partial\rho} = \dfrac{Idl}{4\pi}\int_0^\infty\left[e^{-u_1 z}f_2 + e^{u_1 z}f_3\right]\lambda^2 J_1(\lambda\rho)d\lambda$

Field in #2 medium (bottom, conducting medium)

E_ρ^2	$E_\rho^2 = E_{\rho 1} = -\dfrac{j}{\omega\mu\varepsilon_2'}\dfrac{\partial^2 A_z^2}{\partial\rho\partial z} = \dfrac{jIdl}{4\pi\omega\varepsilon_2'}\int_0^\infty u_2 e^{u_2 z}f_4\lambda^2 J_1(\lambda\rho)d\lambda$
E_z^2	$E_z^2 = E_{z1} = -\dfrac{j}{\omega\mu\varepsilon_2'}\left(\dfrac{\partial^2}{\partial z^2}-\gamma_2^2\right)A_z^2 = -\dfrac{jIdl}{4\pi\omega\varepsilon_2'}\int_0^\infty e^{u_2 z}f_4\lambda^3 J_0(\lambda\rho)d\lambda$
H_ϕ^2	$H_\phi^2 = H_{\phi 1} = \dfrac{1}{\varepsilon_2'}\dfrac{\partial A_z^2}{\partial\rho} = \dfrac{Idl}{4\pi}\int_0^\infty e^{u_2 z}f_4\lambda^2 J_1(\lambda\rho)d\lambda$

VED[1] – Dipole in #1 medium (middle layer)

VED (Dipole in #1 medium)

	Vector potentials:
Free Space (#0) $\varepsilon_0,\ \sigma_0,\ \mu_0$ $z=0$ observation point VED $z=-h$ Conducting Medium (#1) $\varepsilon_1,\ \sigma_1,\ \mu_0$ $z=-d$ Bottom (#2) $\varepsilon_2,\ \sigma_2,\ \mu_0$	$A_z^0 = k_1 \int_0^\infty e^{-u_0 z} f_1 \lambda J_0(\lambda\rho)d\lambda \qquad (z \geq 0)\ ;$ $A_z^1 = k_1 \dfrac{e^{\gamma_1 R}}{R} + k_1 \int_0^\infty [e^{-u_1 z} f_2 + e^{u_1 z} f_3]\lambda J_0(\lambda\rho)d\lambda \qquad (-d \leq z \leq 0)\ ;$ $A_z^2 = k_1 \int_0^\infty e^{u_2 z} f_4 \lambda J_0(\lambda\rho)d\lambda \qquad (z \leq -d)\ ;$ where $\dfrac{e^{\gamma_1 R}}{R} = \begin{cases} \int_0^\infty u_1^{-1} e^{-u_1(z+h)}\lambda J_0(\lambda\rho)d\lambda\ (z+h \geq 0) \\ \int_0^\infty u_1^{-1} e^{u_1(z+h)}\lambda J_0(\lambda\rho)d\lambda\ (z+h \leq 0) \end{cases}$ and $\gamma_i^2 = -\omega^2 \mu \varepsilon_i' = -\omega^2\mu(\varepsilon_i - j\dfrac{\sigma_i}{\omega});\ u_i = \sqrt{(\lambda^2 + \gamma_i^2)}\ ;\ k_1 = \dfrac{Idl}{4\pi}.$

Boundary conditions	At $z = 0$ (upper) interface: $\quad A_z^0 = A_z^1;\quad \dfrac{1}{\varepsilon_0'}\dfrac{\partial A_z^0}{\partial z} = \dfrac{1}{\varepsilon_1'}\dfrac{\partial A_z^1}{\partial z}\ ;$ At $z = -d$ (lower) interface: $\quad A_z^2 = A_z^1;\quad \dfrac{1}{\varepsilon_2'}\dfrac{\partial A_z^2}{\partial z} = \dfrac{1}{\varepsilon_1'}\dfrac{\partial A_z^1}{\partial z}.$

Coefficient functions	$f_1 = \dfrac{2\varepsilon_0'}{D}\left[(\varepsilon_1'u_2 - \varepsilon_2'u_1)e^{u_1(h-d)} - (\varepsilon_1'u_2 + \varepsilon_2'u_1)e^{-u_1(h-d)}\right];\quad f_2 = \dfrac{(\varepsilon_1'u_2 - \varepsilon_2'u_1)}{u_1 D}\left[(\varepsilon_0'u_1 + \varepsilon_1'u_0)e^{u_1(h-d)} + (\varepsilon_0'u_1 - \varepsilon_1'u_0)e^{-u_1(h+d)}\right];$ $f_3 = \dfrac{(\varepsilon_0'u_1 - \varepsilon_1'u_0)}{u_1 D}\left[(\varepsilon_1'u_2 - \varepsilon_2'u_1)e^{u_1(h-d)} - (\varepsilon_1'u_2 + \varepsilon_2'u_1)e^{-u_1(h-d)}\right];\quad f_4 = \dfrac{2\varepsilon_2' e^{u_2 d}}{D}\left[(\varepsilon_1'u_0 - \varepsilon_0'u_1)e^{-u_1 h} - (\varepsilon_1'u_0 + \varepsilon_0'u_1)e^{u_1 h}\right];$ where $D = (\varepsilon_1'u_0 - \varepsilon_0'u_1)(\varepsilon_1'u_2 - \varepsilon_2'u_1)e^{-u_1 d} - (\varepsilon_1'u_0 + \varepsilon_0'u_1)(\varepsilon_1'u_2 + \varepsilon_2'u_1)e^{u_1 d}.$

VED[1] -- Dipole in #1 medium (middle layer)

Field in #0 medium (free space)

E_ρ^0	$E_\rho^0 = E_{\rho\lambda}^0 = -\dfrac{j}{\omega\mu\varepsilon_0'}\dfrac{\partial^2 A_z^0}{\partial\rho\partial z} = \dfrac{jIdl}{4\pi\omega\varepsilon_0'}\displaystyle\int_0^\infty u_0 e^{-u_0 z} f_1\lambda^2 J_1(\lambda\rho)\,d\lambda$
E_z^0	$E_z^0 = E_{z\lambda}^0 = -\dfrac{j}{\omega\mu\varepsilon_0'}\left(\dfrac{\partial^2}{\partial z^2}+\gamma_0^2\right)A_z^0 = -\dfrac{jIdl}{4\pi\omega\varepsilon_0'}\displaystyle\int_0^\infty e^{-u_0 z} f_1\lambda^3 J_0(\lambda\rho)\,d\lambda$
H_ϕ^0	$H_\phi^0 = H_{\phi\lambda}^0 = \dfrac{1}{\varepsilon_0'}\dfrac{\partial A_\rho^0}{\partial\rho} = \dfrac{Idl}{4\pi}\displaystyle\int_0^\infty e^{-u_0 z} f_1\lambda^2 J_1(\lambda\rho)\,d\lambda$

Field in #1 medium (middle layer, conducting medium)

E_ρ^1	$E_\rho^1 = -\dfrac{j}{\omega\mu\varepsilon_1'}\dfrac{\partial^2 A_z^1}{\partial\rho\partial z} = E_{\rho\lambda}^1 + E_{\rho r}^1$ $E_{\rho\lambda}^1 = \dfrac{jIdl}{4\pi\omega\varepsilon_1'}\displaystyle\int_0^\infty \left(\begin{cases}-e^{-u_1(z+h)} & (z+h\geq0)\\ e^{u_1(z+h)} & (z+h\leq0)\end{cases}\right)\lambda^2 J_1(\lambda\rho)\,d\lambda$; $\quad E_{\rho r}^1 = -\dfrac{jIdl}{4\pi\omega\varepsilon_1'}\displaystyle\int_0^\infty u_1\left[e^{-u_1 z} f_2 - e^{u_1 z} f_3\right]\lambda^2 J_1(\lambda\rho)\,d\lambda$
E_z^1	$E_z^1 = -\dfrac{j}{\omega\mu\varepsilon_1'}\left(\dfrac{\partial^2}{\partial z^2}-\gamma_1^2\right)A_z^1 = E_{z\lambda}^1 + E_{zr}^1$ $E_{z\lambda}^1 = -\dfrac{jIdl}{4\pi\omega\varepsilon_1'}\displaystyle\int_0^\infty \left(\begin{cases}u_1^{-1}e^{-u_1(z+h)} & (z+h\geq0)\\ u_1^{-1}e^{u_1(z+h)} & (z+h\leq0)\end{cases}\right)\lambda^3 J_0(\lambda\rho)\,d\lambda$; $\quad E_{zr}^1 = -\dfrac{jIdl}{4\pi\omega\varepsilon_1'}\displaystyle\int_0^\infty \left[e^{-u_1 z} f_2 + e^{u_1 z} f_3\right]\lambda^3 J_0(\lambda\rho)\,d\lambda$

VED[1] -- Dipole in #1 medium (middle layer)

H^1_ϕ	$H^1_\phi = -\dfrac{1}{\mu}\dfrac{\partial A^1_z}{\partial \rho} = H^1_{\phi i} + H^1_{\phi r}$ $H^1_{zi} = \dfrac{Idl}{4\pi}\int_0^\infty \left(\begin{cases} u_1^{-1}e^{-u_1(z+h)} & (z+h\geq 0) \\ u_1^{-1}e^{u_1(z+h)} & (z+h\leq 0) \end{cases} \right)\lambda^2 J_0(\lambda\rho)d\lambda; \quad H^1_{zr} = \dfrac{Idl}{4\pi_1}\int_0^\infty \left[e^{-u_2 z} f_2 + e^{u_1 z} f_3 \right]\lambda^2 J_0(\lambda\rho)d\lambda$

Field in #2 medium (bottom, conducting medium)

E^2_ρ	$E^2_\rho = E^2_{r\lambda} = -\dfrac{j}{\omega\mu\varepsilon'_2}\dfrac{\partial^2 A^2_z}{\partial\rho\partial z} = \dfrac{jIdl}{4\pi\omega\varepsilon'_2}\int_0^\infty u_2 e^{u_2 z} f_4 \lambda^2 J_1(\lambda\rho)d\lambda$
E^2_z	$E^2_z = E^2_{zi} = -\dfrac{j}{\omega\mu\varepsilon'_2}\left(\dfrac{\partial^2}{\partial z^2}-\gamma_2^2\right)A^2_z = -\dfrac{jIdl}{4\pi\omega\varepsilon'_2}\int_0^\infty e^{u_2 z} f_4 \lambda^3 J_0(\lambda\rho)d\lambda$
H^2_ϕ	$H^2_\phi = H^2_{\phi i} = -\dfrac{1}{\mu_2}\dfrac{\partial A^2_z}{\partial\rho} = \dfrac{Idl}{4\pi}\int_0^\infty e^{u_2 z} f_4 \lambda^2 J_1(\lambda\rho)d\lambda$

VMD⁰ – Dipole in #0 medium (free space)

VMD (Dipole in #0 medium)

Free Space (#0) VMD ⬆ z=h $\varepsilon_0, \sigma_0, \mu_0$ y

z=0 · · · · observation point

Conducting Medium (#1) $\varepsilon_1, \sigma_1, \mu_0$

z=-d

Bottom (#2) $\varepsilon_2, \sigma_2, \mu_0$

Vector potentials:

$$F_z^0 = k_0 \frac{e^{\gamma_0 R}}{R} + k_0 \int_0^\infty f_1 e^{-u_0 z} \lambda J_0(\lambda\rho) d\lambda \quad (z \geq 0);$$

$$F_z^1 = k_0 \int_0^\infty \left[f_2 e^{-u_1 z} + f_3 e^{u_1 z} \right] \lambda J_0(\lambda\rho) d\lambda \quad (-d \leq z \leq 0);$$

$$F_z^2 = k_0 \int_0^\infty f_4 e^{u_2 z} \lambda J_0(\lambda\rho) d\lambda \quad (z \leq -d);$$

where $\dfrac{e^{\gamma_0 R}}{R} = \begin{cases} \displaystyle\int_0^\infty u_0^{-1} e^{-u_0(z-h)} \lambda J_0(\lambda\rho) d\lambda & (z-h \geq 0) \\ \displaystyle\int_0^\infty u_0^{-1} e^{u_0(z-h)} \lambda J_0(\lambda\rho) d\lambda & (z-h \leq 0) \end{cases}$

and $\gamma_i^2 = -\omega^2 \mu \varepsilon_i' = -\omega^2 \mu \left(\varepsilon_i - j \frac{\sigma_i}{\omega}\right)$; $u_i = \sqrt{(\lambda^2 + \gamma_i^2)}$; $k_0 = \dfrac{j\omega\mu\varepsilon_0' I dA}{4\pi}$.

Boundary conditions

At $z = 0$ (upper) interface: $\dfrac{1}{\varepsilon_0'} F_z^0 = \dfrac{1}{\varepsilon_1'} F_z^1$; $\dfrac{1}{\varepsilon_0'}\dfrac{\partial F_z^0}{\partial z} = \dfrac{1}{\varepsilon_1'}\dfrac{\partial F_z^1}{\partial z}$;

At $z = -d$ (lower) interface: $\dfrac{1}{\varepsilon_1'} F_z^1 = \dfrac{1}{\varepsilon_2'} F_z^2$; $\dfrac{1}{\varepsilon_1'}\dfrac{\partial F_z^1}{\partial z} = \dfrac{1}{\varepsilon_2'}\dfrac{\partial F_z^2}{\partial z}$.

Coefficient functions

$$f_1 = \frac{e^{-u_0 h}}{u_0 D}\left[(u_0+u_1)(u_2-u_1)e^{-u_1 d} + (u_1-u_0)(u_1+u_2)e^{u_1 d}\right];\quad f_2 = \frac{2\varepsilon_1'}{\varepsilon_0' D}(u_2-u_1)\cdot e^{-u_0 h}e^{-u_1 d};$$

$$f_3 = -\frac{2\varepsilon_1'}{\varepsilon_0' D}(u_1+u_2)e^{-u_0 h}e^{u_1 d};\quad f_4 = -\frac{4\varepsilon_2' u_1 e^{-u_0 h}e^{u_2 d}}{\varepsilon_0' D};\quad \text{where } D=(u_0-u_1)(u_2-u_1)e^{-u_1 d} - (u_0+u_1)(u_1+u_2)e^{u_1 d}.$$

VMD^0 – Dipole in #0 medium (free space)

Field in #0 medium (free space)

E_ϕ^0

$$E_\phi^0 = \frac{1}{\varepsilon_0'}\frac{\partial F_z^0}{\partial \rho} = E_{\phi i}^0 + E_{\phi r}^0$$

$$E_{\phi i}^0 = -\frac{k_0}{\varepsilon_0'}\int_0^\infty \left(\begin{array}{l} u_0^{-1} e^{-u_0(z-h)} \ (z-h \geq 0) \\ u_0^{-1} e^{u_0(z-h)} \ (z-h \leq 0) \end{array}\right) \lambda^2 J_1(\lambda\rho)d\lambda \ ; \quad E_{\phi r}^0 = -\frac{k_0}{\varepsilon_0'}\int_0^\infty e^{-u_0 z} f_1 \lambda^2 J_1(\lambda\rho)d\lambda$$

H_ρ^0

$$H_\rho^0 = -\frac{j}{\omega\mu\varepsilon_0'}\frac{\partial^2 F_z^0}{\partial\rho\partial z} = H_{\rho i}^0 + H_{\rho r}^0$$

$$H_{\rho i}^0 = \frac{IdA}{4\pi}\int_0^\infty \left(\begin{array}{l} e^{-u_0(z-h)} \ (z-h\geq 0) \\ -e^{u_0(z-h)}\,(z-h\leq 0)\end{array}\right)\lambda^2 J_1(\lambda\rho)d\lambda \ ; \quad H_{\rho r}^0 = \frac{IdA}{4\pi}\int_0^\infty u_0 e^{-u_0 z} f_1 \lambda^2 J_1(\lambda\rho)d\lambda$$

H_z^0

$$H_z^0 = -\frac{j}{\omega\mu\varepsilon_0'}\left(\frac{\partial^2}{\partial z^2}-\gamma_0^2\right)F_z^0 = H_{zi}^0 + H_{zr}^0$$

$$H_{zi}^0 = \frac{IdA}{4\pi}\int_0^\infty \left(\begin{array}{l} u_0^{-1}e^{-u_0(z-h)} \ (z-h\geq 0) \\ u_0^{-1}e^{u_0(z-h)} \ (z-h\leq 0)\end{array}\right)\lambda^3 J_0(\lambda\rho)d\lambda \ ; \quad H_{zr}^0 = \frac{IdA}{4\pi}\int_0^\infty e^{-u_0 z} f_1 \lambda^3 J_0(\lambda\rho)d\lambda$$

Field in #1 medium (middle layer, conducting medium)

E_ϕ^1

$$E_\phi^1 = E_{\phi i}^1 = \frac{1}{\varepsilon_1'}\frac{\partial F_z^1}{\partial \rho} = -\frac{k_0}{\varepsilon_1'}\int_0^\infty \left[e^{-u_1 z} f_2 + e^{u_1 z} f_3\right]\lambda^2 J_1(\lambda\rho)d\lambda$$

71

H_ρ^1	$H_\rho^1 = H_{\rho A}^1 = -\dfrac{j}{\omega\mu\varepsilon_1'}\dfrac{\partial^2 F_z^1}{\partial\rho\partial z} = \dfrac{IdA\varepsilon_0'}{4\pi\varepsilon_1'}\int_0^\infty u_1\left[e^{-u_1 z}f_2 - e^{u_1 z}f_3\right]\lambda^2 J_1(\lambda\rho)d\lambda$
H_z^1	$H_z^1 = H_{z1}^1 = -\dfrac{j}{\omega\mu\varepsilon_1'}\left(\dfrac{\partial^2}{\partial z^2} - \gamma_1^2\right)F_z^1 = \dfrac{IdA\varepsilon_0'}{4\pi\varepsilon_1'}\int_0^\infty \left[e^{-u_1 z}f_2 + e^{u_1 z}f_3\right]\lambda^3 J_0(\lambda\rho)d\lambda$

Field in #2 medium (bottom, conducting medium)

E_ϕ^2	$E_\phi^2 = E_\phi^2 = \dfrac{1}{\varepsilon_2'}\dfrac{\partial F_z^2}{\partial\rho} = -\dfrac{k_0}{\varepsilon_2'}\int_0^\infty e^{u_2 z}f_4\lambda^2 J_1(\lambda\rho)d\lambda$
H_ρ^2	$H_\rho^2 = H_{\rho A}^2 = -\dfrac{j}{\omega\mu\varepsilon_2'}\dfrac{\partial^2 F_z^2}{\partial\rho\partial z} = -\dfrac{IdA\varepsilon_0'}{4\pi\varepsilon_2'}\int_0^\infty u_2 e^{u_2 z}f_4\lambda^2 J_1(\lambda\rho)d\lambda$
H_z^2	$H_z^2 = H_{z1}^2 = -\dfrac{j}{\omega\mu\varepsilon_2'}\left(\dfrac{\partial^2}{\partial z^2} - \gamma_2^2\right)F_z^2 = \dfrac{IdA\varepsilon_0'}{4\pi\varepsilon_2'}\int_0^\infty e^{u_2 z}f_4\lambda^3 J_0(\lambda\rho)d\lambda$

72

VMD (Dipole in #1 medium)

Free Space (#0) $\varepsilon_0, \sigma_0, \mu_0$ y

$z = 0$

observation point

VMD $z = -h$

Conducting Medium (#1) $\varepsilon_1, \sigma_1, \mu_0$

$z = -d$

Bottom (#2) $\varepsilon_2, \sigma_2, \mu_0$

Vector potentials:

$F_z^0 = k_1 \int_0^\infty e^{-u_0 z} f_1 \lambda J_0(\lambda\rho) d\lambda \qquad (z \geq 0)$;

$F_z^1 = k_1 \frac{e^{\gamma_1 R}}{R} + k_1 \int_0^\infty [e^{-u_1 z} f_2 + e^{u_1 z} f_3] \lambda J_0(\lambda\rho) d\lambda \qquad (-d \leq z \leq 0)$;

$F_z^2 = k_1 \int_0^\infty e^{u_2 z} f_4 \lambda J_0(\lambda\rho) d\lambda \qquad (z \leq -d)$;

where $\dfrac{e^{\gamma_1 R}}{R} = \begin{cases} \displaystyle\int_0^\infty u_1^{-1} e^{-u_1(z+h)} \lambda J_0(\lambda\rho) d\lambda & (z+h \geq 0) \\[2mm] \displaystyle\int_0^\infty u_1^{-1} e^{u_1(z+h)} \lambda J_0(\lambda\rho) d\lambda & (z+h \leq 0) \end{cases}$

and $\gamma_i^2 = -\omega^2 \mu \varepsilon_i' = -\omega^2 \mu \left(\varepsilon_i - j\frac{\sigma_i}{\omega}\right)$; $u_i = \sqrt{(\lambda^2 + \gamma_i^2)}$; $k_1 = \dfrac{j\omega\mu\varepsilon_1' I dA}{4\pi}$.

Boundary conditions

At $z = 0$ (upper) interface: $\dfrac{1}{\varepsilon_0'} F_z^0 = \dfrac{1}{\varepsilon_1'} F_z^1$; $\dfrac{1}{\varepsilon_0'}\dfrac{\partial F_z^0}{\partial z} = \dfrac{1}{\varepsilon_1'}\dfrac{\partial F_z^1}{\partial z}$;

At $z = -d$ (lower) interface: $\dfrac{1}{\varepsilon_1'} F_z^1 = \dfrac{1}{\varepsilon_2'} F_z^2$; $\dfrac{1}{\varepsilon_1'}\dfrac{\partial F_z^1}{\partial z} = \dfrac{1}{\varepsilon_2'}\dfrac{\partial F_z^2}{\partial z}$.

Coefficient functions

$f_1 = -\dfrac{2\varepsilon_0'}{\varepsilon_1' D}\left[(u_1+u_2)e^{-u_1(h-d)} + (u_1-u_2)e^{u_1(h-d)}\right]$; $f_2 = \dfrac{(u_1-u_2)e^{-u_1 d}}{u_1 D}\left[u_0(e^{-u_1 h} - e^{u_1 h}) - u_1(e^{-u_1 h} + e^{u_1 h})\right]$;

VMD⁰ -- Dipole in #0 medium (free space)

	$f_3 = \dfrac{(u_0 - u_1)}{u_1 D}\left[(u_1 - u_2)e^{u_1(h-d)} + (u_1 + u_2)e^{-u_1(h-d)}\right]$; $\quad f_4 = \dfrac{2\varepsilon_2' e^{u_2 d}}{\varepsilon_1' D}\left[(u_0 - u_1)e^{-u_1 h} - (u_0 + u_1)e^{u_1 h}\right]$; where $\;D = (u_0 - u_1)(u_2 - u_1)e^{-u_1 d} - (u_0 + u_1)(u_2 + u_1)e^{u_1 d}\,$.
Field in #0 medium (free space)	
E_ϕ^0	$E_\phi^0 = E_{\phi t}^0 = \dfrac{1}{\varepsilon_0'}\dfrac{\partial F_z^0}{\partial \rho} = -\dfrac{k_1}{\varepsilon_0'}\displaystyle\int_0^\infty e^{-u_0 z} f_1 \lambda^2 J_1(\lambda\rho)d\lambda$
H_ρ^0	$H_\rho^0 = H_{\rho t}^0 = -\dfrac{j}{\omega\mu\varepsilon_0'}\dfrac{\partial^2 F_z^0}{\partial\rho\partial z} = \dfrac{IdA\varepsilon_1'}{4\pi\varepsilon_0'}\displaystyle\int_0^\infty u_0 e^{-u_0 z} f_1 \lambda^2 J_1(\lambda\rho)d\lambda$
H_z^0	$H_z^0 = H_{zt}^0 = -\dfrac{j}{\omega\mu\varepsilon_0'}\left(\dfrac{\partial^2}{\partial z^2} + \gamma_0^2\right)F_z^0 = \dfrac{IdA\varepsilon_1'}{4\pi\varepsilon_0'}\displaystyle\int_0^\infty e^{-u_0 z} f_1 \lambda^3 J_0(\lambda\rho)d\lambda$
Field in #1 medium (middle layer, conducting medium)	
E_ϕ^1	$E_\phi^1 = \dfrac{1}{\varepsilon_1'}\dfrac{\partial F_z^1}{\partial\rho} = E_{\phi t}^1 + E_{\phi r}^1$

VMD^0 -- Dipole in #0 medium (free space)

	$E_{z}^{1} = -\dfrac{k_1}{\varepsilon_1'}\displaystyle\int_0^\infty\left(\begin{cases} u_1^{-1}e^{-u_1(z+h)} & (z+h\geq 0) \\ u_1^{-1}e^{u_1(z+h)} & (z+h\leq 0)\end{cases}\right)\lambda^2 J_1(\lambda\rho)d\lambda; \quad E_{\phi r}^{1} = -\dfrac{k_1}{\varepsilon_1'}\displaystyle\int_0^\infty\left[e^{-u_1 z}f_2(\lambda)+e^{u_1 z}f_3(\lambda)\right]\lambda^2 J_1(\lambda\rho)d\lambda$
H_ρ^1	$H_\rho^1 = -\dfrac{j}{\omega\mu\varepsilon_1'}\dfrac{\partial^2 F_z^1}{\partial\rho\partial z} = H_{\rho i}^1 + H_{\rho r}^1$ $H_{\rho i}^1 = -\dfrac{IdA}{4\pi}\displaystyle\int_0^\infty\left(\begin{cases}-e^{-u_1(z+h)} & (z+h\geq 0)\\ e^{u_1(z+h)} & (z+h\leq 0)\end{cases}\right)\lambda^2 J_1(\lambda\rho)d\lambda; \quad H_{\rho r}^1 = \dfrac{IdA}{4\pi}\displaystyle\int_0^\infty u_1\left[e^{-u_1 z}f_2 - e^{u_1 z}f_3\right]\lambda^2 J_1(\lambda\rho)d\lambda$
H_z^1	$H_z^1 = -\dfrac{j}{\omega\mu\varepsilon_1'}\left(\dfrac{\partial^2}{\partial z^2}-\gamma_1^2\right)F_z^1 = H_{zi}^1 + H_{zr}^1$ $H_{zi}^1 = \dfrac{IdA}{4\pi}\displaystyle\int_0^\infty\left(\begin{cases}u_1^{-1}e^{-u_1(z+h)} & (z+h\geq 0)\\ u_1^{-1}e^{u_1(z+h)} & (z+h\leq 0)\end{cases}\right)\lambda^3 J_0(\lambda\rho)d\lambda; \quad H_{zr}^1 = \dfrac{IdA}{4\pi}\displaystyle\int_0^\infty\left[e^{-u_1 z}f_2 + e^{u_1 z}f_3\right]\lambda^3 J_0(\lambda\rho)d\lambda$
	Field in #2 medium (bottom, conducting medium)
E_ϕ^2	$E_\phi^2 = E_{\phi r}^2 = \dfrac{1}{\varepsilon_2'}\dfrac{\partial F_z^2}{\partial\rho} = -\dfrac{k_1}{\varepsilon_2'}\displaystyle\int_0^\infty e^{u_2 z}f_4\lambda^2 J_1(\lambda\rho)d\lambda$

75

H_ρ^2	$H_\rho^2 = H_{\rho\lambda}^2 = -\dfrac{j}{\omega\mu\varepsilon_2'}\dfrac{\partial^2 F_z^2}{\partial\rho\partial z} = -\dfrac{IdA\varepsilon_1'}{4\pi\varepsilon_2'}\displaystyle\int_0^\infty u_2 e^{u_2 z} f_4 \lambda^2 J_1(\lambda\rho)\,d\lambda$
H_z^2	$H_z^2 = H_{zz}^2 = -\dfrac{j}{\omega\mu\varepsilon_2'}\left(\dfrac{\partial^2}{\partial z^2}+\gamma_2^2\right)F_z^2 = \dfrac{IdA\varepsilon_1'}{4\pi\varepsilon_2'}\displaystyle\int_0^\infty e^{u_2 z} f_4 \lambda^3 J_0(\lambda\rho)\,d\lambda$

Appendix B

Maximum Detectable Range for Electromagnetic Fields from

Dipole Sources Near an Air-Water Interface

Robert G. Olsen and Zhi Li

School of Electrical Engineering & Computer Science, Washington State University

Introduction

In Phase II of this Project, a Matlab program based on the Sommerfeld integral formulation to calculate the electromagnetic fields from electric or magnetic dipole sources in a three-layered medium was developed. The program allows four types/orientations of dipole sources which are: vertical electric dipole (VED), horizontal electric dipole (HED), vertical (VMD), and horizontal (HMD) magnetic dipole. The three layers are numbered, from the top to the bottom, as layer 0, 1, and 2, respectively. The top (0) and the bottom (2) layers extent to +/- ∞ respectively. Layer 0 is assumed to be free space, while layers 1 and 2 are conducting media and the dipole source can be placed in either layer 0 or 1. Fig. 1 illustrates the case for an HED in layer 1.
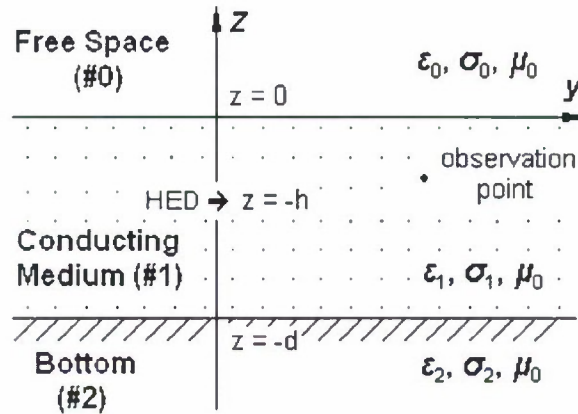
Fig. 1.   Model of a HED placed in #1 medium.

Detectable Range

Using this program, the electric (E) and the magnetic (H) fields anywhere in space can be calculated. This provides the basis for determining the detectable range from the source if the maximum dipole moment and the minimum detectable signal for the measuring equipment are given. In these simulations, it was assumed that the maximum dipole moments for electric and magnetic dipoles are 50 A-m and 2500 A-m^2 respectively and that the minimum detectable electric and magnetic fields are

$1\mu V/m$ and $40\mu A/m$ respectively. It was observed from the simulations that the horizontal electric field component perpendicular to the HED direction can nearly always be detected at a distance much larger than that for any other field component from any other dipole source[1].

Figs. 2 - 10 show the variation of the maximum detectable range of E_x with dipole frequency. Figs. 2 - 4 are the results for the cases that the dipole is 2 meters below the upper interface and the field point is 5, 20 and 50 meters below the upper interface, respectively. The dipole moment for these three simulations is $Idl = 50$ A-m.
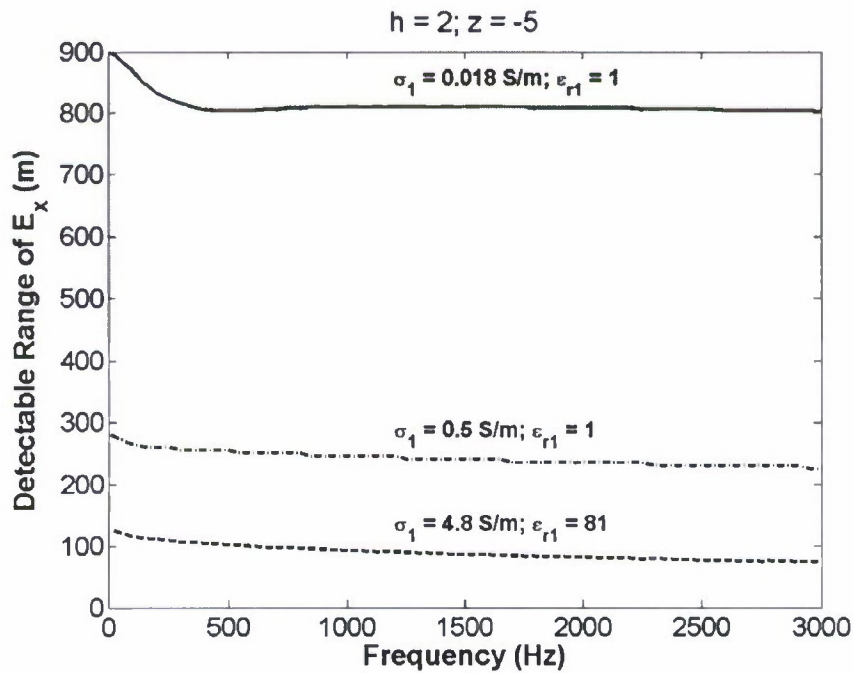
Fig. 2. Detectable range of E_x as a function of dipole frequency (HED is 2 meters below the upper interface, $h = 2$, field point is 5 meters below the interface, $z = -5$).

---

[1] For a conductivity of 4.8 S/m, the HED magnetic field has a higher detectable range for frequencies less than 500 Hz. At smaller conductivities, the frequency at which this occurs is smaller than this.
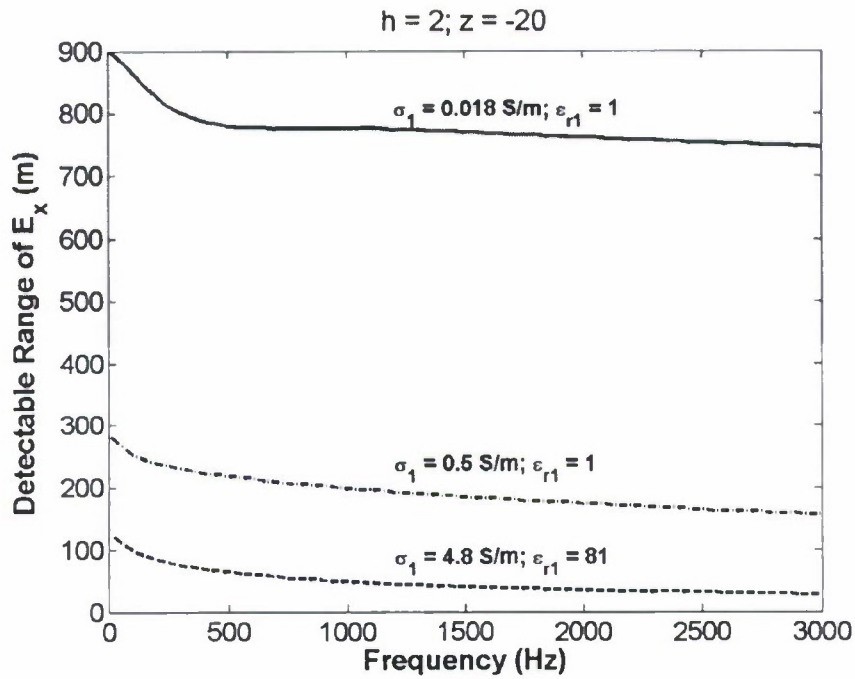
Fig. 3. Detectable range of E_x as a function of dipole frequency (HED is 2 meters below the upper interface, $h = 2$, field point is 20 meters below the interface, $z = -20$).
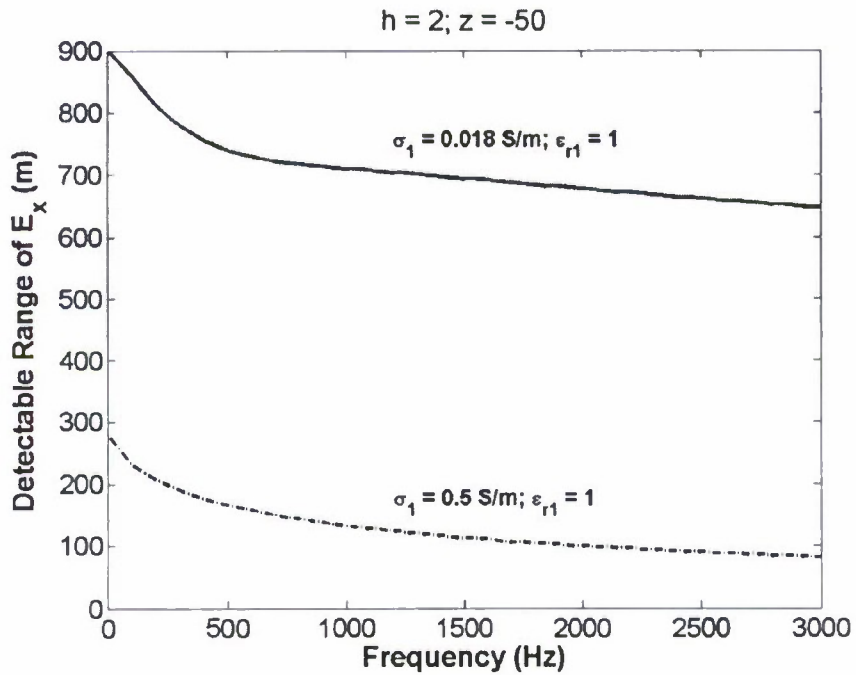
Fig. 4. Detectable range of E_x as a function of dipole frequency (HED is 2 meters below the upper interface, $h = 2$, field point is 50 meters below the interface, $z = -50$).

In Figs. 2 and 3, the curves at the top and bottom represent the simulation results for lake water and sea water. The conductivity for the curve in the middle is an arbitrarily chosen value between that for lake water and sea water. The detectable range for sea water when the field point is at $z = -50$m is so short that it is not shown in Fig. 4.

The simulations for Figs. 5 to 7 are respectively similar to that for Figs. 2 - 4. The only difference is that the dipole moment and the minimum detectable field are assumed to be increased and reduced by three times, respectively.

$$Idl^{new} = 3 \times Idl$$

$$E^{new}_{\min-detectable} = E_{\min-detectable} / 3$$

The detectable ranges in these cases are much larger than their counterparts in Figs. 2 - 4 due to the increase of both the strength of source signal (i.e., the dipole moment) and the ability of detection (i.e., minimum detectable field). In Figs. 8 - 10, the dipole moment and ability of detection are increased by five times:

$$Idl^{new} = 5 \times Idl$$

$$E^{new}_{\min-detectable} = E_{\min-detectable} / 5$$

The increases of the detectable range of E_x become more obvious.
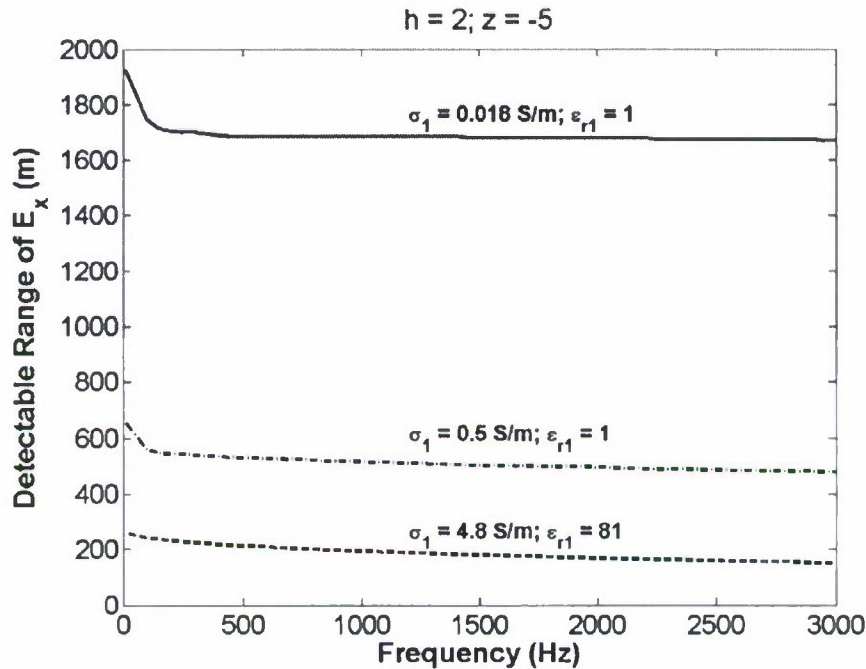
Fig. 5. Detectable range of E_x as a function of dipole frequency when the dipole moment and the detectability are both increased by three times ($Idl_{new} = 3*Idl$, $E_{min,new} = E_{min}/3$; $h = 2$, and $z = -5$).

80
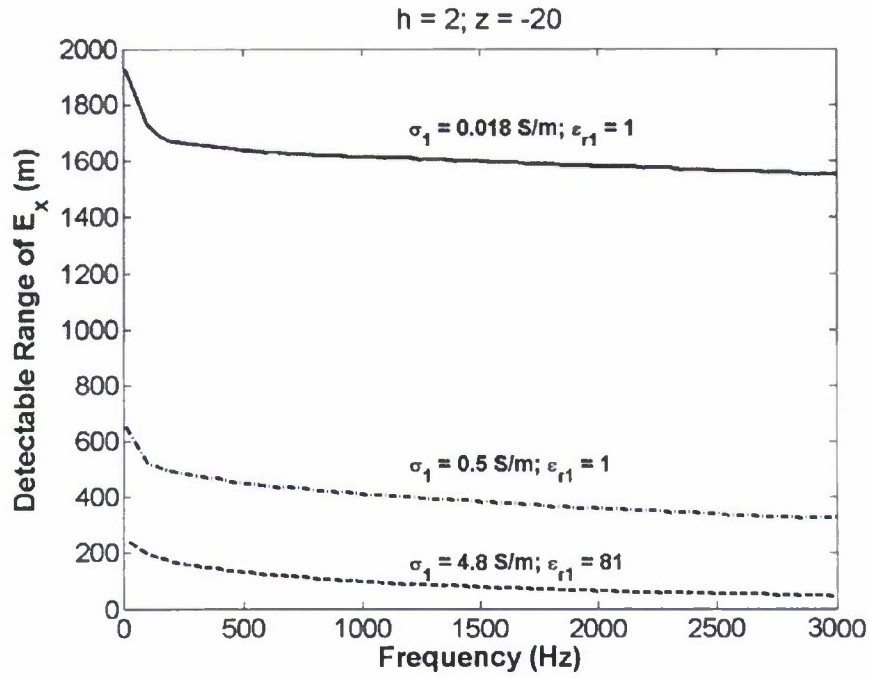
Fig. 6. Detectable range of E_x as a function of dipole frequency when the dipole moment and the detectability are both increased by three times ($Idl_{new} = 3*Idl$, $E_{min,new} = E_{min}/3$; $h = 2$, and $z = -20$).
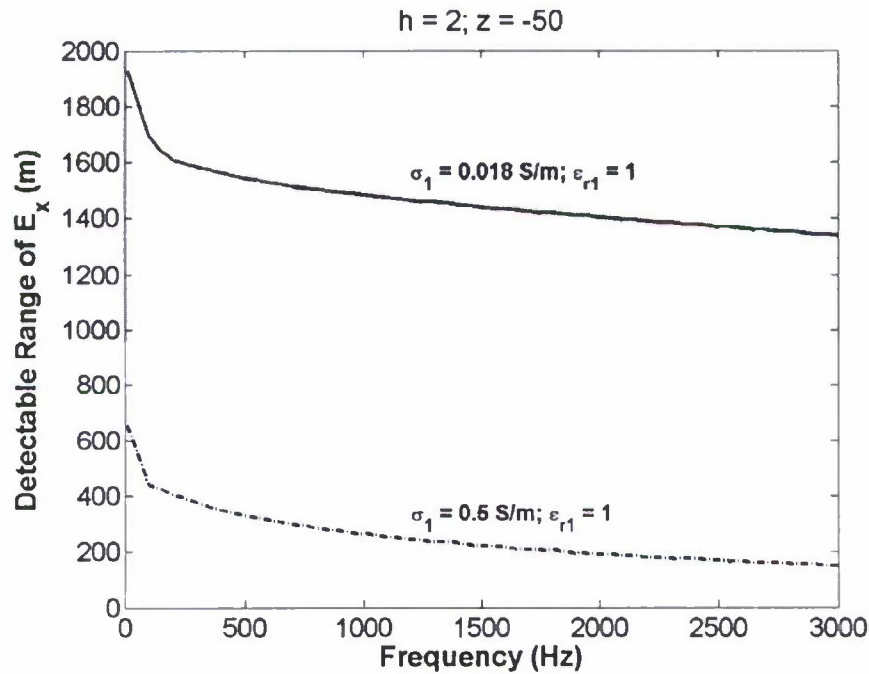
Fig. 7. Detectable range of E_x as a function of dipole frequency when the dipole moment and the detectability are both increased by three times ($Idl_{new} = 3*Idl$, $E_{min,new} = E_{min}/3$; $h = 2$, and $z = -50$).
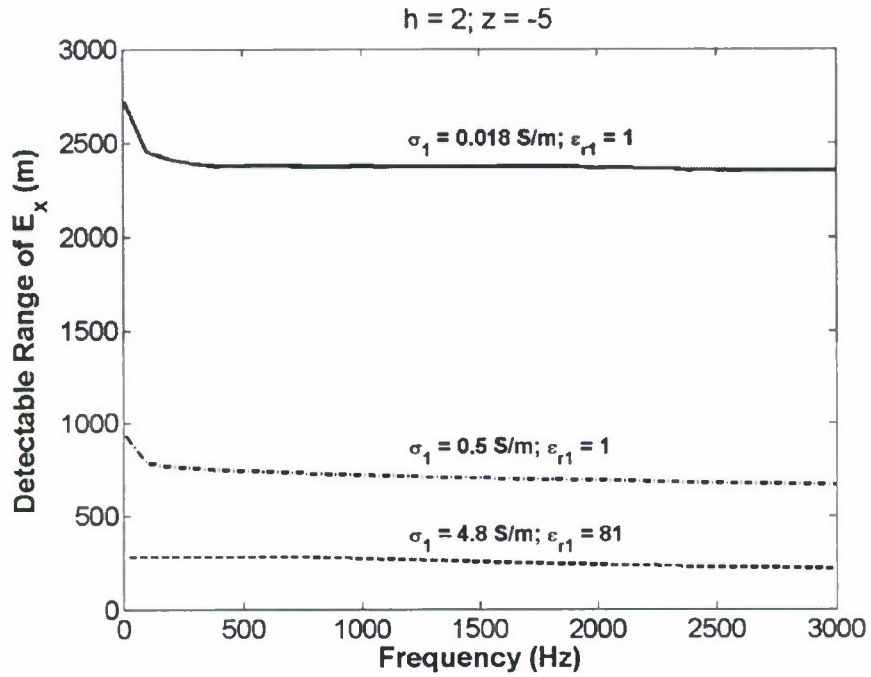
Fig. 8. Detectable range of E_x as a function of dipole frequency when the dipole moment and the detectability are both increased by five times ($Idl_{new} = 5*Idl$, $E_{min,new} = E_{min}/5$; $h = 2$, and $z = -5$).
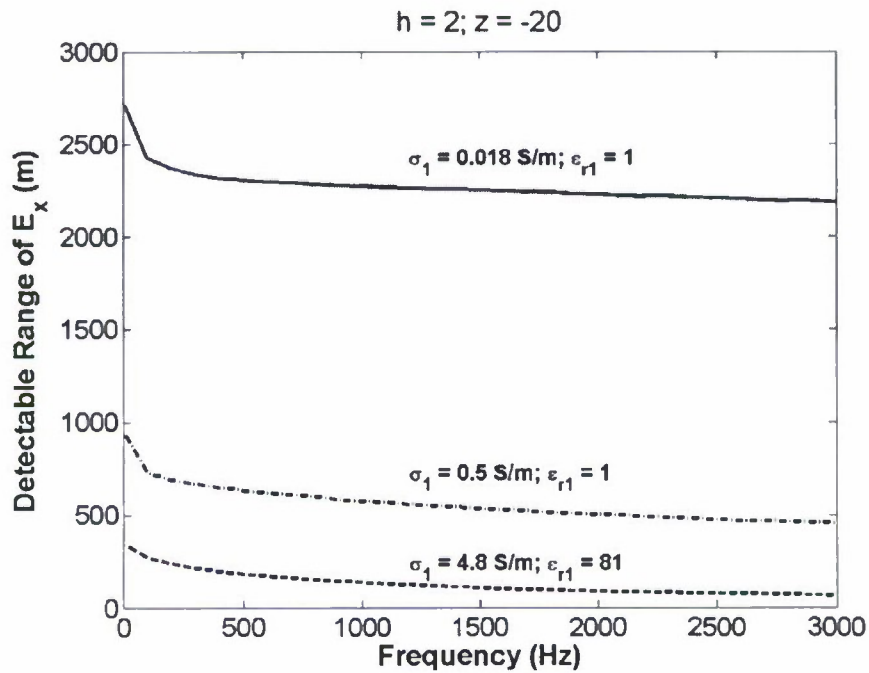
Fig. 9. Detectable range of E_x as a function of dipole frequency when the dipole moment and the detectability are both increased by five times ($Idl_{new} = 5*Idl$, $E_{min,new} = E_{min}/5$; $h = 2$, and $z = -20$).
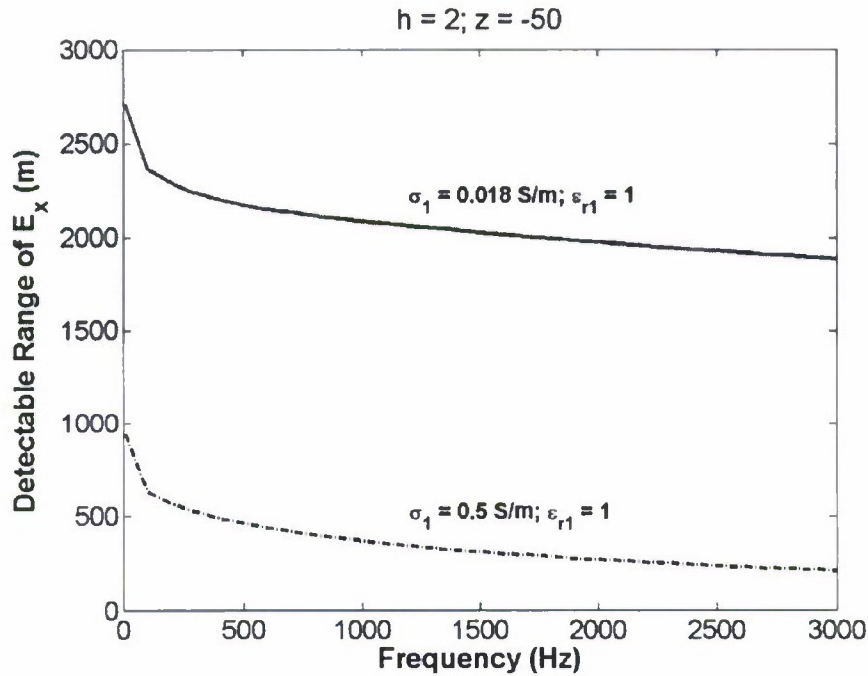
Fig. 10. Detectable range of E_x as a function of dipole frequency when the dipole moment and the detectability are both increased by five times ($Idl_{new} = 5*Idl$, $E_{min,new} = E_{min}/5$; $h = 2$, and $z = -50$).

Up-over-and-down Model

Another part of work accomplished in Phase II is the study of an up-over-and-down model for HED propagation near an interface [1]. In this study, the HED is assumed to be buried in the lower (lossy) half medium of a two-half-space model. Note that the bottom layer of Fig. 1 can often be neglected if source and field point are much closer to the top interface than the lower one. The top half is free space. The model is shown in Fig. 11.
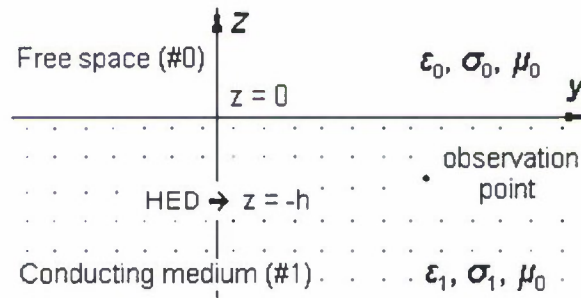
Fig. 11. Geometry of the model

When the HED and the field point, (ρ, φ, z), are both close to the interface, the Sommerfeld integrals for the electric and magnetic fields in the lower half space can be simplified and a set of simple approximations for the fields obtained. For example,

83

if the depths of the HED and field point are much smaller than the horizontal distance between them, the x-component of electric field in the conducting medium can be approximated by

$$E_x^1 \approx 2jA_1k_0^3 \cdot e^{jk_1(z-h)} \frac{e^{-jk_0\rho}}{(jk_0\rho)^3}\left[3+\frac{5}{(jk_1\rho)^3}\right]\cdot\sin\phi\cos\phi \qquad (1)$$

where $A_1 = \dfrac{jIdl}{4\pi\omega\varepsilon_1'}$. Equation (1) was used to do the similar simulations for determining the detectable range. Fig. 12 and Fig. 13 show the comparisons between the results obtained by (1) and that found by Sommerfeld integral method, shown in Fig.2 and Fig. 5, respectively. It is obvious that the approximation of the field in (1) gives very good result over the most portion of the frequency range interested. Since the approximation (1) has no integral in it, the calculation time can be significantly reduced by using it. Therefore, the approximation based on the up-over-and-down model provides us a fast but relatively accurate approach to determine the electromagnetic field in the conducting medium when the third layer can be neglected.
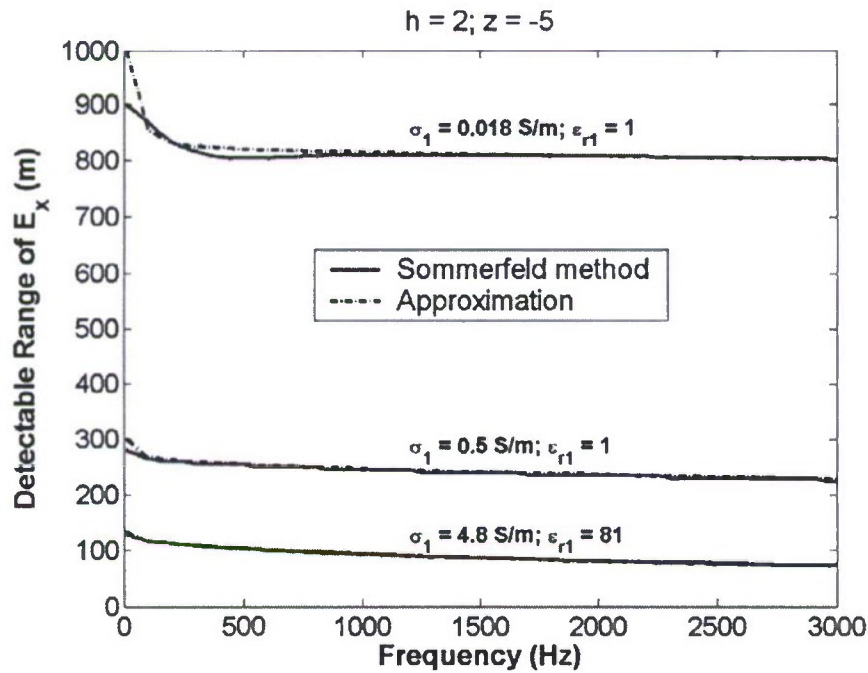
Fig. 12. Comparison between Sommerfeld method and up-over-and-down approximation for detectable range of E_x. (HED is 2 meters below the upper interface, $h = 2$, field point is 5 meters below the interface, $z = -5$).
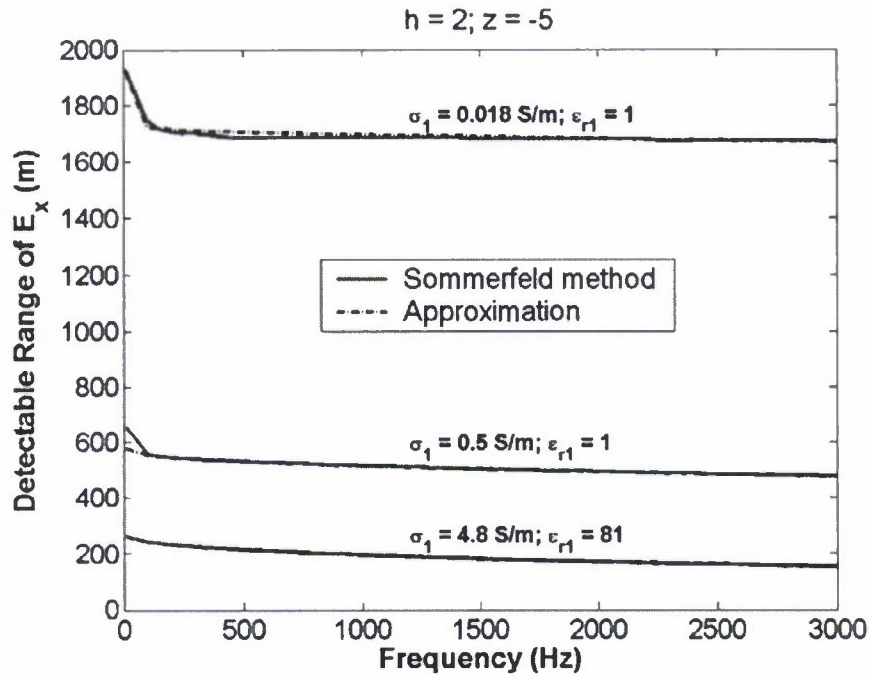
Fig. 13. Comparison between Sommerfeld method and up-over-and-down approximation for detectable range of E_x. The dipole moment and the detectability are both increased by three times ($Idl_{new} = 3*Idl$, $E_{min,new} = E_{min}/3$; $h = 2$, and $z = -5$).

Reference

1. R.G. Olsen and Z., Li, A Simple Up-over-and-down Model for Low Frequency Horizontal Electric Dipole Propagation near and Interface,   in preparation for submission to the *IEEE Transactions on Antennas and Propagation*

Appendix C

FDTD Parallelization Methods

Dennis Sullivan

Department of Electrical and Computer Engineering, University of Idaho

Introduction

In the past year, the FDTD simulation group has accomplished the following:

1. The FDTD codes were reformulated using the Message Passing Interface (MPI) software. The purpose was to achieve more efficient parallelization of the code. It was also to make the code more flexible by allowing it to be distributed over several computers [1, 2].

2. The FDTD codes were implemented using dedicated hardware from the Acceleware corporation. This system uses graphics cards to do the bulk of the FDTD calculation. This is controlled through the software development kit (SDK) from Acceleware [2, 3].

3. The near-to-far field formulation was implemented in the time domain instead of the frequency domain. This method allows greater flexibility and provides more information. Wavelet theory was used for data compression to avoid the storage of large amounts of time-domain data [4].

Implementation of the FDTD simulation using MPI

Modern compilers on computers with multiple CPUs will parallelize computer programs using an option called Open MP. Open MP distributes the code among the available CPUs in a computer. It will not distribute the code among different computers.

Message Passing Interface (MPI) is a software package that allows the programmer to decide how the computation is distributed among the CPUs in one machine, or among the CPUs in several machines [5-8]. The implementation using MPI requires considerable additional programming effort. This was done in the hope of surpassing the speed achieved by Open MP, as well as acquiring the ability to distribute the program over several computers.

MPI utilizes the Domain Decomposition Method (DDM), a protocol that solves large numerical boundary value problems by splitting the main problem space into smaller sub-domains. Each sub-domain retains the original qualities of the main domain and follows the same coordinate structure as the original problem space. The non-overlapping DDM requires some communication among the sub-domains, creating the need for a message passing interface like the MPI library. Figure 1.1 shows an example of a problem space that is 100^3 cells that can be divided into eight sections of 50^3 sub-domains.
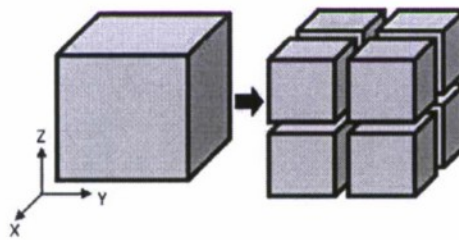
Figure 1.1. Domain decomposition into eight independent sub-domains.

The setup illustrated in Fig. 1.1 is as balanced as possible and creates a parallel environment so each sub-domain can communicate to the same number of neighboring sub-domains. This minimizes the lag that can occur when a core has to wait for data from another to continue processing. The number of sub-domains depends on the number of sections on each side of the main domain. A sub-domain that has all six neighbors is illustrated in Fig. 1.2.
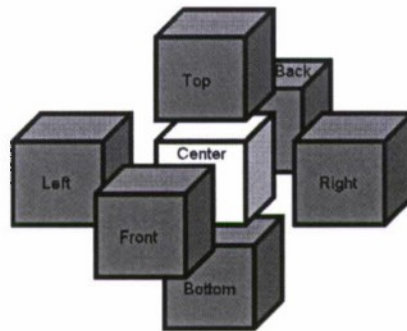
Figure. 1.2. An illustration of how one sub-domain sees its six surrounding sub-domains.

Decomposition of the PML and the lossy media is related to the position of each sub-domain. Figure 1.3 illustrates a two-dimensional domain that has been divided into four sub-domains, where each contains different media and PML. The process takes in the topographic data in the format of the main domain by each processing core and keeps only the data that applies to its related sub-domain. The algorithm uses the

87

position data to realize its correct place among other sub-domains and compares that to the main domain's three-dimensional mesh.
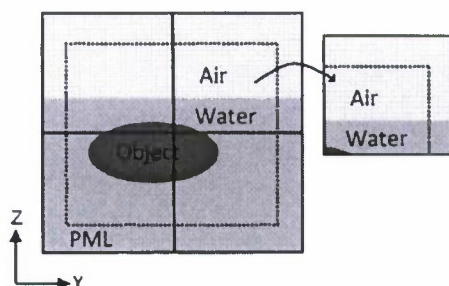
Figure 1.3. Two-dimensional illustration of the PML and Media defined for 4 sub-domains.

The Message Passing Interface Library makes communication at the sub-domain boundaries possible. Communication between the sub-domains is facilitated by MPI's blocking receive operation (*MPI_Recv*) and MPI's non-blocking send operation (*MPI_iSend*). The blocking receive operation keeps each sub-domain from continuing with the calculation of the E and H fields, until the needed parameters are received. However, the non-blocking send operation sends the data to the addressed sub-domain and continues with the rest of the FDTD calculation. Using a combination of non-blocking send operations and blocking receive operations reduces the chance of possible software hang-ups. In this case hang-ups occur either when a message is needed that has not been sent or a sub-domain is awaiting a successful sent confirmation that has not been received by the other sub-domain. Figure 1.4 shows the fields that must be passed to the neighboring sub-domains.
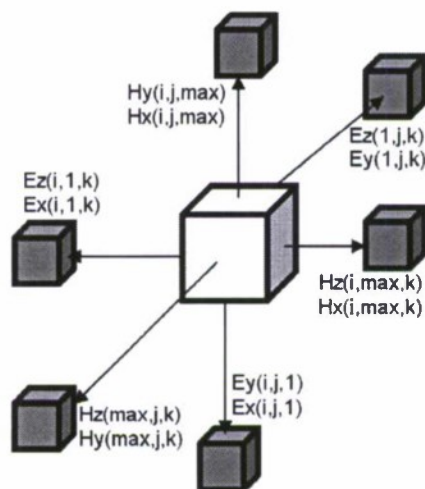
Figure 1.4. Field information transferred at the boundaries of sub-domains.

The following sequence insures that the parallel FDTD algorithm performs smoothly.

Step 1) Send the correct E-fields to the back, left, and bottom sub-domains.
Step 2) After receiving the required E-fields from the front, right, and top sub-domains, calculate the H-fields.
Step 3) Send the correct H-fields to the right, top, and front sub-domains.
Step 4) Update the D-fields. The sub-domains must receive the required H-fields from the back, left, and bottom sub-domains.
Step 5) Calculate the E-fields from the D-fields.

As a result of the parallel FDTD calculation, the electromagnetic field data are defined for each sub-domain and each sub-domain can be simulated separately. At the end of the parallel FDTD process in each sub-domain the resulting E and H fields are present. The last sub-domain accumulates all the fields in one large array. These E and H fields will look similar to results from the regular FDTD method after executing sequentially across only one core. This is illustrated in Fig. 1.5.
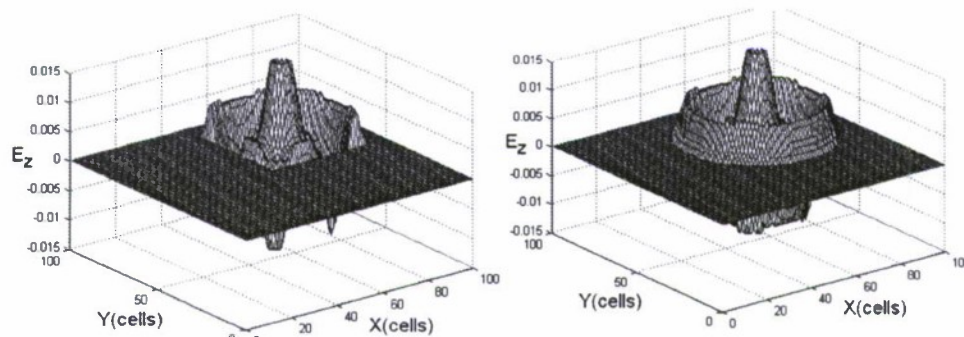
Figure 1.5. A three-dimensional view of the E-field in sub-domain 1 (left) and the entire domain (fight).

Once the FDTD code had been programmed using MPI, a comparison was made with a similar program that only used the Open MP. The program problem space was $(120)^3$ cells. It was distributed among 27 cores. A total of 30,000 time steps were needed. Open MP preformed the simulation in 15 minutes, 56 seconds. The MPI code performed the same simulation in 9 minutes, 54 seconds. Therefore, MPI reduced the computation time by 35 % [1, 2].

Implementation of the FDTD code using dedicated hardware.

Another approach to increasing the speed of very large FDTD programs was the implementation on dedicated hardware using a system from Acceleware Corporation.

Acceleware systems exploit the performance of video graphics cards to obtain substantial speed-up (Fig. 2.1) [9].
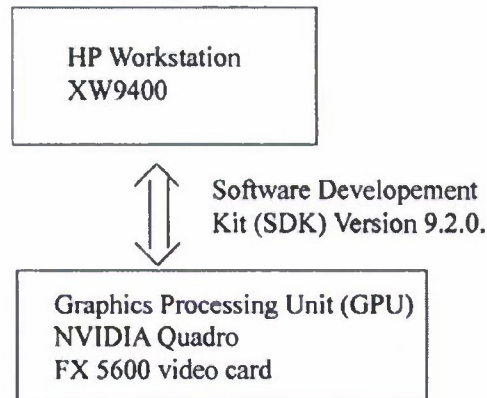
Figure 2.1.   Block diagram of the Acceleware system

The Software Development Kit (SDK) is provided by Acceleware.   It is a high-level programming language written in C++.   The FDTD codes must be rewritten in this language.   This language incorporates "handles" which represent different parts of the FDTD simulation.   Table 2.1 is a list of some of the important handles and their functions.   Figure 2.2 is a flow chart showing the steps for the implementation of an FDTD program using Acceleware.

Table 2.1.   The Handles used in SDK

Handle	Type
Ax_timeexc_t	Time excitation
Ax_rgnhandle_t	Region
Ax_mathandle	Material
Ax_simhandle	Simulation handle

Programming Flow
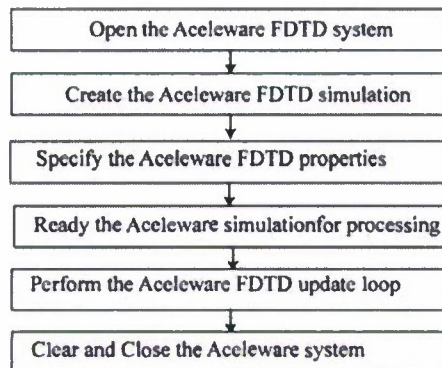
Figure 2.2.   The programming flow to implement an FDTD
program in Acceleware.

A test was made to insure that the Acceleware FDTD was in agreement with the
standard FDTD.   The simulation problem space and the results are shown in Fig. 2.3.
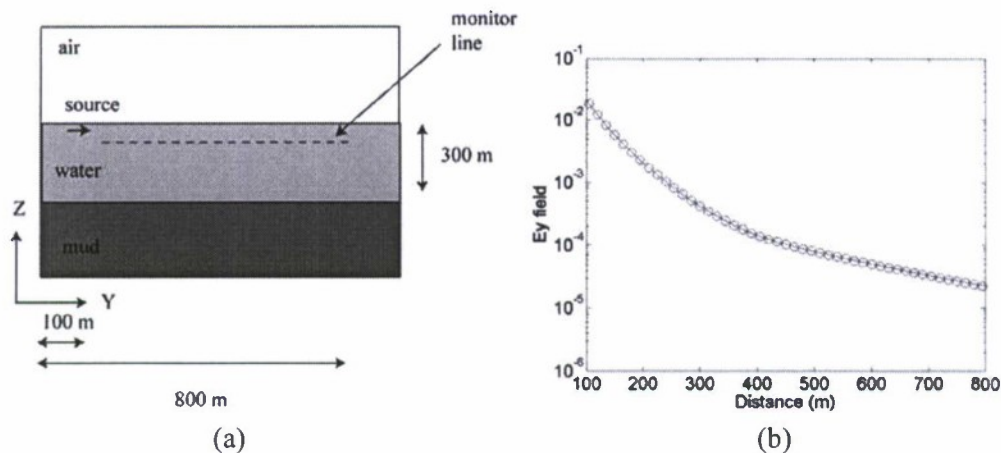
Figure 2.3. (a) Test configuration (b) Previous FDTD (solid line) vs. Acceleware calculation (circles).

Table 2.2 summarizes the wall clock times needed for an FDTD simulation of $(120)^3$
cells over 30,000 time steps.

Table 2.2.   The wall clock times required for an FDTD simulations
of $(120)^3$ cells for 30,000 time steps.   The first three entries were using
the 8 Quad-core AMD Opteron™ Processor 8380.   The Acceleware
simulation was done with Acceleware libray version 9.2.0 and a NVIDIA

91

Quadro FX 5600 video card.

1 core	63 m 18s
32 core (Open MP)	12m 56s
27 core (MPl)	9m 54s
Acceleware	4m 32s

Time-domain Near to Far Field Transformation

A near-to-far field transformation had previously been developed [10]. This transformation was developed to address the problem of having to model an electromagnetic source like a ship at one a relatively small resolution like 10 meters, and yet having to model a very large problem space where larger resolution like 50 meters would be more desirable (Fig. 3.1) The previous formulation of this near-to-far field transformation stored the amplitude and phase of selected frequencies of each of the E fields on the equivalence surface. This amplitude and phase was used in generating the sinusoidal source for the far field. The disadvantage of this approach is that a separate simulation is needed at every frequency of interest in the far field. If instead the time domain data at the fields on the equivalence surface could be stored, then information at all frequencies of interest could be obtained in the far field with just one simulation. The problem is that the time domain data in the near field could be several thousand points, and storing all this data at all the fields of interest is not practical.
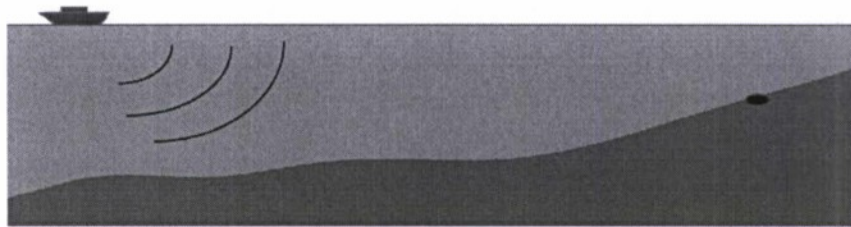
(a) It might be desirable to model the EM radiation of a ship over very large distances.
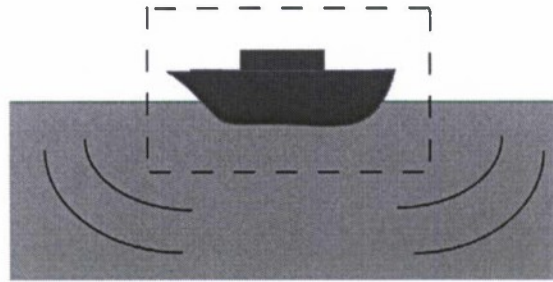
(b) Near field (10 m^3 cells)
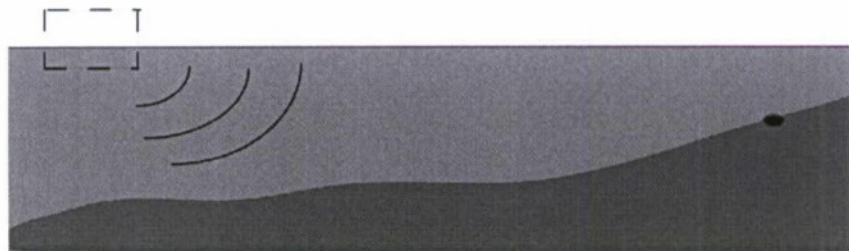
(c) Far field (50 m^3 cells)

Figure 3.1. (a) A projected simulation problem where it would be desirable for a source of EM radiation, such as a ship, to be modeled with relatively small cells of about ten meters squared. However, problem spaces ranging over distances of three or more kilometers would require too many cells. (b) A near field calculation determines the radiation from the source at an equivalence surface surrounding the source. (c) This equivalence surface is then used as the source in an FDTD problem with much larger cells.

In order to minimize the amount of data that has to be stored in the near to far field transformation, wavelets are being used to compress the data [11]. The technique of compressing data in an FDTD simulation has been used by this research group previously [12, 13]. The type of wavelet processing structure being used is illustrated in Figure 3.2. The circles with arrows pointing downwards indicate "down-sampling," i.e., every other data point is eliminated. The circles with arrows pointing up indicate "up-sampling," i.e., a zero is added after each data point. The squares indicate convolution with the filter written inside. One such group of filters is shown in Figure 3.3.
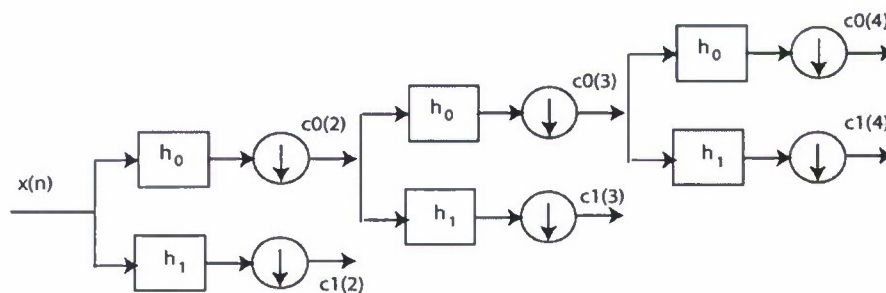
(a) Analysis tree
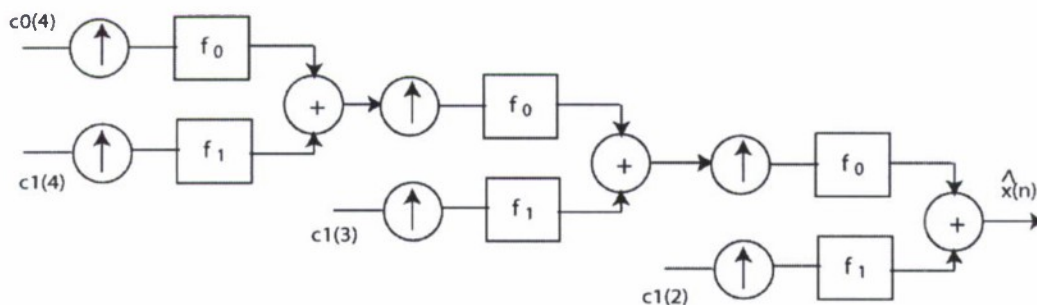
(b) Synthesis tree

Figure 3.2. The type of structures being used to achieve data compression and reconstruction using wavelets. The circles with arrows pointing downwards indicate "down-sampling," i.e., every other data point is eliminated. The circles with arrows pointing up indicate "up-sampling," i.e., a zero is added after each data point. The squares indicate convolution with the filter written inside. Each stage in the analysis tree separates the data into low pass parts (c0s) and high pass parts (c1s). Note that it is only the low pass part that is processed further. The values obtained from the analysis can be used to reconstruct the original waveform in the synthesis tree.
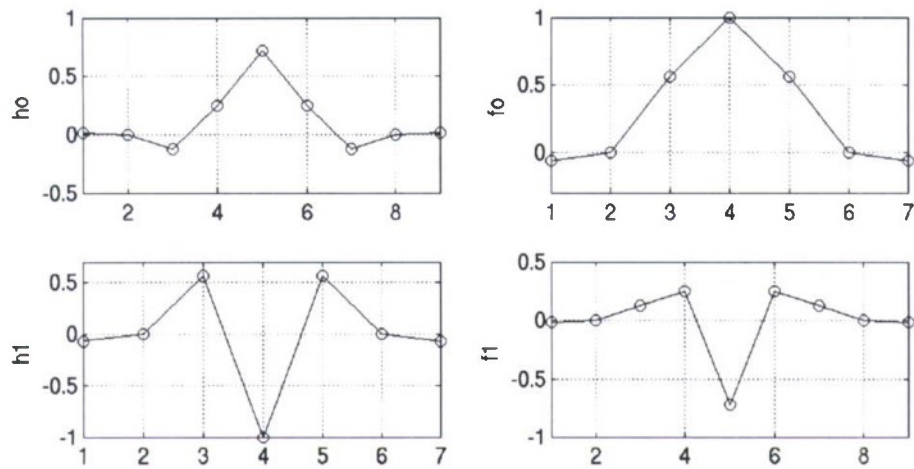
Figure 3.3. Four filters of the type used by the structure shown if Fig. 3.2. The filters h_0 and f_0 are low pass filters while h_1 and f_1 are high pass filters.

As an example, Fig. 3.4 shows a waveform of 6000 time steps. An analysis tree of eight levels is used to produce the data shown. The low pass components are the solid lines while the high pass components are the dashed lines. Notice that the dashed lines are virtually zero compared with the solid lines. Therefore, all high pass data can be discarded and the original waveform can be reconstructed from the forty-five points of level eight as shown in Fig. 3.5.

Since we have determined that only the low-pass parts of the analysis and synthesis trees are needed, the implementation of the analysis or synthesis only requires about ten lines of additional code in the FDTD simulations.
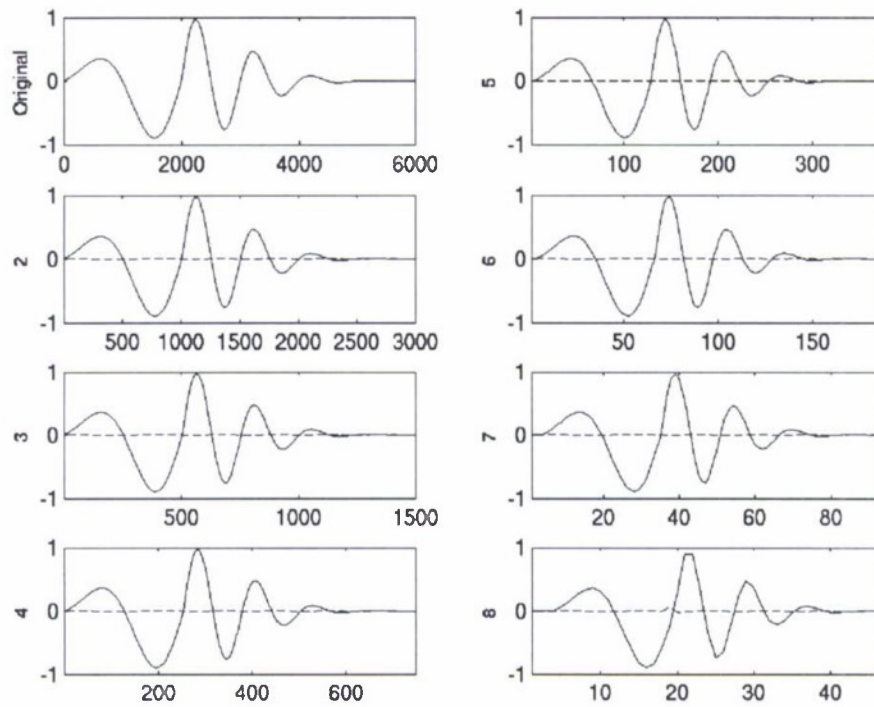
Figure 3.4. A waveform with 6000 points (top, left). The subsequent plots show the outputs of the various levels in the analysis tree. By level 8 (lower right), only forty-five points are needed to represent the original signal.
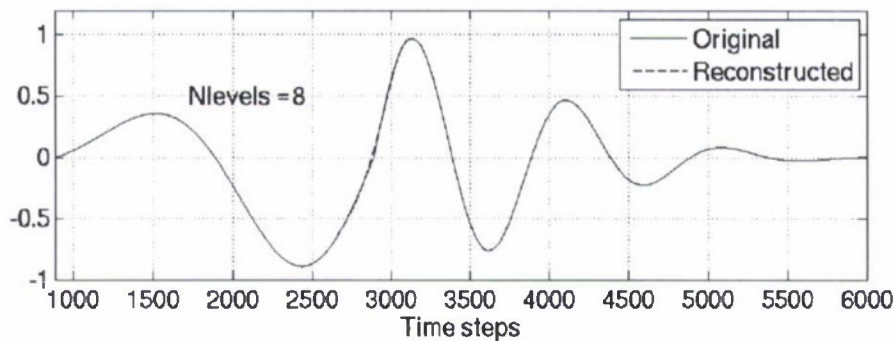
Figure. 3.5. The reconstructed waveform (dashed line) and the original (solid line).

Figure 3.6 is an illustration of a simulation to show that the near-to-far field transformation gives the same results as a corresponding FDTD program with no transformation. The source is a magnetic dipole just below the water surface. The near field program is $(120)^3$ cells. Each cell is ten meters cubed. The far field

96

simulation is only $(60)^3$ cells, but the cells are fifty meters cubed.   Comparisons are made at three points which are a lateral distance of 500 m from the dipole.   Point A is 100 m above the water surface, point B is 100 m below the surface, and point C is 300 m below the surface.   The results are shown in Fig. 3.7.
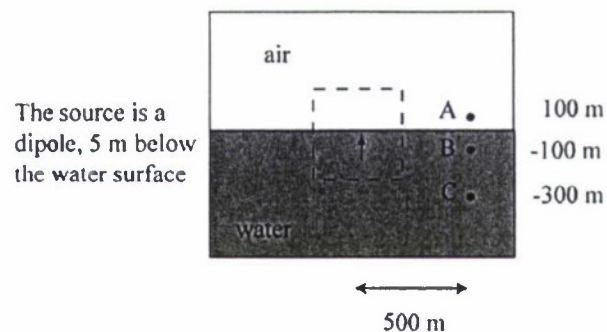
Figure 3.6.   Diagram of the near field problem space used to shown that the field produced in the far field are the same.
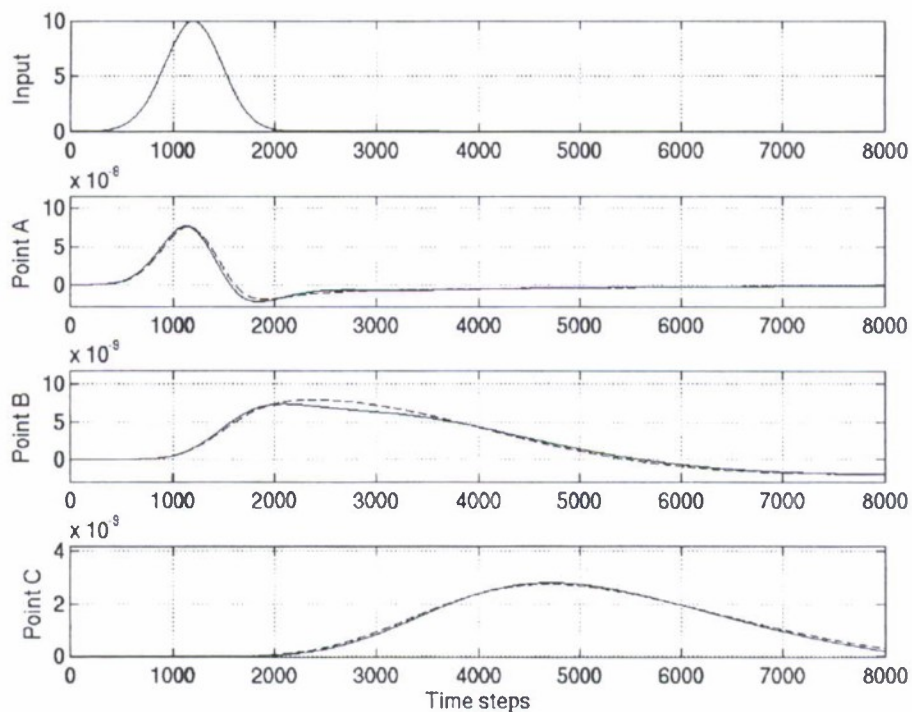
Figure 3.7.   Results of the test described in Fig. 3.6.   The waveform on top is source at the dipole. The next three plots compare the near and far field Hz fields at points A, B, and C.   The solid lines are from the near field calculation; the dashed lines are from the far field calculation.

References

1. Mansoori, Alireza, "Parallel Three-Dimensional FDTD Algorithm Using the MPI Library," Master of Science in Electrical Engineering, University of Idaho, May, 2010.

2. Sullivan, D. M., Xia, Y., Mansoori, A., "Large scale underwater FDTD ELF simulations using Acceleware and MPI parallel processing," URSI Intern'l Symposium on EM Theory, Aug. 16-19, 2010, Berlin, Germany.

3. Xia, Y., Sullivan, D. M., "Underwater ELF Simulation using dedicated Hardware," IEEE APS Intern'l Sym, July 11-17, 2010, Toronto, CA.

4. Butherus, D, Xia, Y, Sullivan, D. M., "Time-domain near-to-far field transformation for underwater FDTD simulations at ELF frequencies," IEEE APS Intern'l Sym, July 11-17, 2010, Toronto, CA.

5. Yu, W, Mittra, R, SU, T, Liu, Y, and Yang, X., *Paraleel finite-difference time-domain method,* Boston, MA: Artech House, 2006.

6. V. Varadarajan and R. Mittra, "Finite-difference time domain (FDTD), analysis using distributed computing," *IEEE Microwave and Guided Wave Letters*, Vol. 4, No. 5, 144-145, 1994.

7. K. C. Chew and V. F. Fusco, "A Parallel Implementation of the Finite Difference Time Domain Algorithm," *International Journal of Numerical Modeling Electronic Networks, Devices and Fields*, 8, 1995, pp. 293-299.

8. W. Gropp, E. Lusk, and A. Skjellum, *Using MPI. Portable Parallel Programming with the Message Passing Interface*, Cambridge, Massachusetts, MIT Press, 1994.

9. Ong C., Weldon M., Cyca D., Okoniewski M., "Acceleration of large-scale FDTD simulations on high performance GPU clusters," IEEE *APS Intern'l Sym*, June 15, 2009, Charleston, SC.

10. Xia Y, and Sullivan D. M., "Duel problem space FDTD simulation for underwater LEF applications," *IEEE Antennas and Wireless Prop*, Vol. 8, pp. 498-501, 2009.

11. Akansu, A. N, Haddad, R. A., *Multiresolution Signal Decomposition*, New York, NY: Academic Press, Inc, 1992.

12. Sullivan, D. M., Liu, J., and Kuzyk, M., "Three-dimensional optical pulse

simulation using the FDTD method," *IEEE Trans. Microw. Theory Tech.*, Vol 48, pp. 1127-1133, July, 2000.

13. Sullivan, D. M., Young, J. L, "Far-field time-domain calculation from aperture radiators using the FDTD method," *IEEE Trans. Antennas and Prop.*, Vol 49, pp. 464469, March, 2001.

Appendix D

Multiple-layered Quasi-Electrostatic (QES) Development

Robert Rebich, Jeffrey Young and Chris Wagner

Department of Electrical and Computer Engineering, University of Idaho

Analytical Development

Assume a domain where the media is composed of simple matter, in which case

$$\mathbf{D} = \epsilon\mathbf{E} \tag{1}$$

$$\mathbf{B} = \mu\mathbf{H} \tag{2}$$

$$\mathbf{J}^c = \sigma\mathbf{E}. \tag{3}$$

Here $\mathbf{D}$ is the electric displacement density, $\mathbf{B}$ is the magnetic flux density, $\mathbf{J}^c$ is the electrical conduction current density, $\mathbf{E}$ is the electric field intensity and $\mathbf{H}$ is the magnetic field intensity. The permittivity ϵ is a product of the relative and free space permittivity so that $\epsilon = \epsilon_r\epsilon_0$, where $\epsilon_0 = 8.854 \times 10^{-12}$ F/m. The domain is absent of all magnetic materials so that the permeability is equal to that of free space, $\mu = \mu_0$, where $\mu_0 = 4\pi \times 10^{-7}$ H/m. The electrical conductivity is represented by σ.

The fields within the domain are deemed quasi-electrostatic when the magnetic field has little to no time variation such that

$$\frac{\partial\mathbf{H}}{\partial t} \approx 0. \tag{4}$$

As a consequence of Eqn. (4), Faraday's law states that the curl of the electric field is then approximately zero, in which case

$$\nabla \times \mathbf{E} \approx 0. \tag{5}$$

From Ampere's law,

$$\nabla \times \mathbf{H} = \frac{\partial\mathbf{D}}{\partial t} + \mathbf{J}, \tag{6}$$

where $\mathbf{J}$ represents the combination of conduction and impressed current densities:

$$\mathbf{J} = \mathbf{J}^c + \mathbf{J}^i. \tag{7}$$

By taking the divergence of Eqn. (6) and knowing that the divergence of a curl is always zero, we find that

$$\nabla \cdot \left(\frac{\partial \mathbf{D}}{\partial t} + \mathbf{J} \right) = \nabla \cdot (\nabla \times \mathbf{H}) = 0. \tag{8}$$

Given Eqn. (5), the electric field at a given point in space is equal to the negative gradient of the electric scalar potential V at that point;

$$\mathbf{E} = -\nabla V. \tag{9}$$

For homogeneous media, it follows from Eqns. (8) and (9) and from the constitutive relationships of Eqns. (1) and (2) that

$$\epsilon \frac{\partial}{\partial t} \nabla^2 V + \sigma \nabla^2 V = \nabla \cdot \mathbf{J}^i, \tag{10}$$

where ∇^2 is the Laplacian operator. The equation of continuity states that,

$$\nabla \cdot \mathbf{J}^i = -\frac{\partial \rho}{\partial t}, \tag{11}$$

where ρ is the impressed charge density, so that

$$\epsilon \frac{\partial}{\partial t} \nabla^2 V + \sigma \nabla^2 V = -\frac{\partial \rho}{\partial t}. \tag{12}$$

In the frequency domain, equation Eqn. (12) is similar to

$$\nabla^2 V = -\frac{j\omega\rho}{\sigma + j\omega\epsilon}, \tag{13}$$

where an $e^{+j\omega t}$ time factor is assumed. A special note is made that V and ρ in Eqn. (12) are referenced in the time domain (i.e. $V = V(t), \rho = \rho(t)$) and V and ρ in Eqn. (13) are referenced in the frequency domain (i.e. $V = V(\omega), \rho = \rho(\omega)$). Subsequent analysis will be restricted to the frequency domain so that no ensuing confusion should remain.

Suppose we have an interface of two dissimilar media according to Figure 1. It then follows from Eqn. (5) that

$$(\mathbf{E}_A - \mathbf{E}_B) \times \mathbf{n} = 0. \tag{14}$$

The total induced current within a specific region is given by,

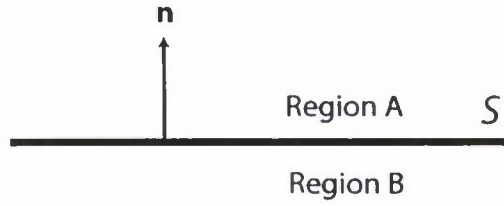$$\mathbf{J}^t = (\sigma + j\omega\epsilon)\,\mathbf{E}. \tag{15}$$

101

Figure 1: A depiction showing **n** for a two-layered geometry

Given Eqn. (15), continuity of normal current states that

$$\mathbf{n} \cdot \mathbf{J}_A^t = \mathbf{n} \cdot \mathbf{J}_B^t \tag{16}$$

or,

$$(\sigma_A + j\omega\epsilon_A)\,\mathbf{n} \cdot \mathbf{E}_A = (\sigma_B + j\omega\epsilon_B)\,\mathbf{n} \cdot \mathbf{E}_B. \tag{17}$$

Once V is determined from solving Eqn. (13) in the context of the boundary conditions of Eqns. (14) and (17) we then use Eqn. (9) to determine the electric field **E**.

Let us now consider a single point charge of strength q located at the origin in unbounded media. The electric potential is a solution to Eqn. (13) such that

$$V = \frac{j\omega q}{4\pi(\sigma + j\omega\epsilon)r} \tag{18}$$

where

$$r = \sqrt{x^2 + y^2 + z^2} = \sqrt{\rho^2 + z^2}. \tag{19}$$

Eqn. (18) is known as the Green's function solution of a point charge at the origin in a lossy homogeneous medium. This solution can be equally expressed in integral form by noting that $\frac{\partial}{\partial\phi} = 0$, in which case Eqn. (13) is equivalent to

$$\frac{1}{\rho}\frac{\partial}{\partial\rho}\left(\rho\frac{\partial V}{\partial\rho}\right) + \frac{\partial^2 V}{\partial z^2} = -\frac{j\omega\rho}{\sigma + j\omega\epsilon}. \tag{20}$$

The solution to Eqn. (20) is a combination of Bessel and exponential functions:

$$V = \frac{j\omega q}{4\pi(\sigma + j\omega\epsilon)} \int_0^\infty J_0(\lambda\rho)\, e^{-\lambda|z|} d\lambda. \tag{21}$$

Now if the charge is located at $z = h$, Eqn. (21) may be written as

$$V = \frac{j\omega q}{4\pi(\sigma + j\omega\epsilon)} \int_0^\infty J_0(\lambda\rho)\, e^{-\lambda|z-h|} d\lambda. \tag{22}$$

With the potential determined for a charge in a single homogeneous media, the analysis can be further extended to a three-layered media problem depicted in Figures 2. Charges and observations in region 3 will be ignored for the remaining development.
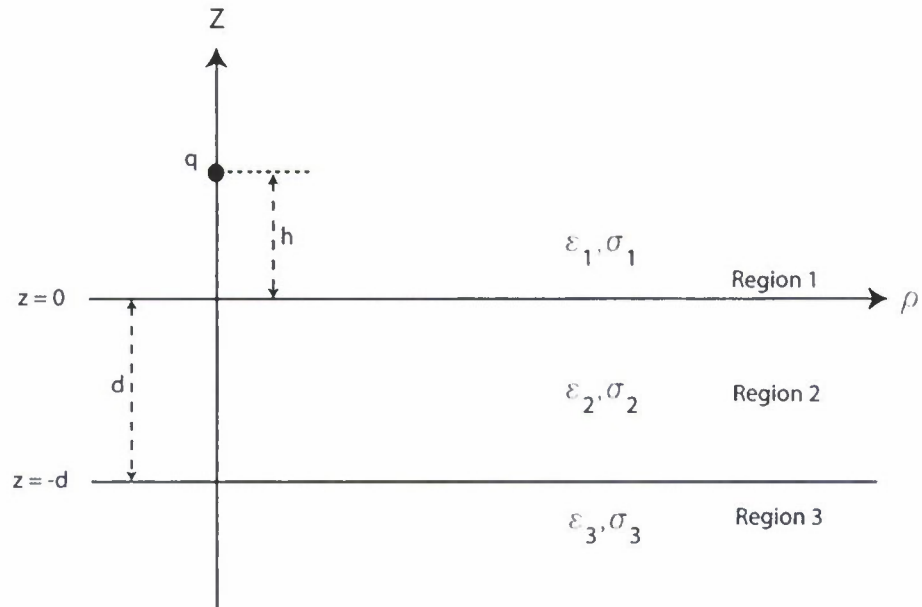
102

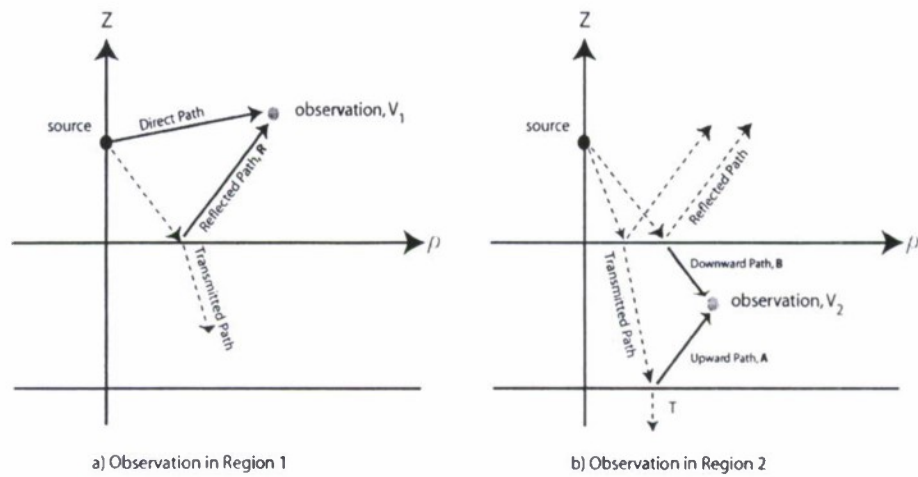Figure 2: Point charge in region 1 for a three-layer configuration.

a) Observation in Region 1

b) Observation in Region 2

Figure 3: Superposition of potentials for regions 1 and 2.

103

Source Charge in Region 1

According to Figure 2, the charge is placed in region 1 at a distance h above the $z = 0$ interface. We construct potential solutions for each region as follows. For observation locations in region 1, where $z > 0$, the total potential at any given point is the superposition of two individual potentials as shown in Figure 3a. The first potential represents the direct path from the charge to observer and is of unity strength. The second potential represents the reflected path from the $z = 0$ boundary and is of strength R. The total potential at any location in region 1 is given by,

$$V_1 = \frac{jwq}{4\pi Y_1} \int_0^\infty \left[e^{-\lambda|z-h|} + Re^{-\lambda(z+h)} \right] J_0(\lambda\rho)d\lambda, \qquad (23)$$

where,

$$Y_1 = \sigma_1 + j\omega\epsilon_1, \qquad (24)$$

which is the admittivity of region 1. For observation locations in region 2, where $z < 0$ and $z > -d$, the total potential at any given point is the superposition of two individual potentials as shown in Figure 3b. The first potential represents the downward traveling path caused by the transmission of the direct path through the $z = 0$ boundary and is of strength B. The second potential represents the upward traveling path caused by the downward path reflection at the $z = -d$ boundary and is of strength A. The total potential at any location in region 2 is given by,

$$V_2 = \frac{jwq}{4\pi Y_1} \int_0^\infty \left[Ae^{-\lambda(z+h)} + Be^{\lambda(z-h)} \right] J_0(\lambda\rho)d\lambda. \qquad (25)$$

For observation locations in region 3, where $z < -d$, the potential at any given point represents the transmitted path of the downward traveling path in region 2 as it encounters the $z = -d$ boundary and is of strength T. This situation is shown in Figure 3b. The total potential at any location in region 3 is given by,

$$V_3 = \frac{jwq}{4\pi Y_1} \int_0^\infty Te^{\lambda(z-h)} J_0(\lambda\rho)d\lambda. \qquad (26)$$

Now that the potential solutions are formulated, the unknowns coefficients R, A, B, T are found by applying the boundary conditions of Eqns. (14) and (17) in the context of Eqn. (9). The boundary conditions must be applied at both region interfaces, i.e. the $z = 0$ and $z = -d$ boundaries. Hence,

$$\begin{aligned} V_1\big|_{z=0} &= V_2\big|_{z=0} \\ V_2\big|_{z=-d} &= V_3\big|_{z=-d}, \end{aligned} \qquad (27)$$

and

$$\begin{aligned} Y_1\frac{dV_1}{dz}\bigg|_{z=0} &= Y_2\frac{dV_2}{dz}\bigg|_{z=0} \\ Y_2\frac{dV_2}{dz}\bigg|_{z=-d} &= Y_3\frac{dV_3}{dz}\bigg|_{z=-d}. \end{aligned} \qquad (28)$$

104

Applying the above boundary conditions to the potentials of Eqns. (23) - (26), we obtain a set of four equations with four unknowns given by,

$$1 + R = A + B \tag{29}$$

$$Ae^{\lambda d} + Be^{-\lambda d} = Te^{-\lambda d} \tag{30}$$

$$1 - R = \frac{Y_2}{Y_1}(B - A) \tag{31}$$

$$Be^{-\lambda d} - Ae^{\lambda d} = \frac{Y_3}{Y_2}Te^{-\lambda d}. \tag{32}$$

After many algebraic steps, we find that,

$$R = \frac{R_{23}e^{-2\lambda d} - R_{21}}{1 - R_{23}R_{21}e^{-2\lambda d}} \tag{33}$$

$$A = \frac{R_{23}(1 - R_{21})e^{-2\lambda d}}{1 - R_{23}R_{21}e^{-2\lambda d}} \tag{34}$$

$$B = \frac{(1 - R_{21})}{1 - R_{23}R_{21}e^{-2\lambda d}} \tag{35}$$

$$T = \frac{(1 - R_{21})(1 + R_{23})}{1 - R_{23}R_{21}e^{-2\lambda d}}, \tag{36}$$

where the interfacial reflection-like coefficients are given by,

$$R_{21} = \frac{Y_2 - Y_1}{Y_1 + Y_2} \tag{37}$$

$$R_{23} = \frac{Y_2 - Y_3}{Y_2 + Y_3}. \tag{38}$$

The potential integrals for charge in region 1 as stated by Eqns. (23) - (26) are now fully specified and can be computed numerically, or by image summations, as described next.

Source Charge in Region 1, Observation in Region 1

In this section we will take the rather complex potential integral of Eqn. (23) and simplify it into the form of an infinite summation. This is necessary because the integral will eventually be solved in a numerical fashion and the form of Eqn. (23) can be difficult to integrate numerically. The following procedure will make the numerical solution quick, efficient and very robust.

The potential expression of Eqn. (23) is first separated into two parts:

$$V_1 = K_1 \int_0^\infty e^{-\lambda|z-h|} J_0(\lambda\rho)d\lambda + K_1 \int_0^\infty Re^{-\lambda(z+h)} J_0(\lambda\rho)d\lambda, \tag{39}$$

where K_1 is the normalized point charge strength in region 1 defined by,

$$K_1 = \frac{j\omega q}{4\pi Y_1}. \tag{40}$$

The first term of Eqn. (39) can be equally represented in closed-form by comparing Eqns. (18) and (21), in which case,

$$K_1 \int_0^\infty e^{-\lambda|z-h|} J_0(\lambda\rho)d\lambda = \frac{K_1}{r}. \tag{41}$$

In the present context, r is defined by,

$$r = \sqrt{\rho^2 + (z-h)^2} \tag{42}$$

with,

$$\rho = \sqrt{x^2 + y^2}. \tag{43}$$

Eqn. (41) is commonly referred to as the Weber integral [2]. Equation (39) is equally stated as,

$$V_1 = \frac{K_1}{r} + K_1 \int_0^\infty Re^{-\lambda(z+h)} J_0(\lambda\rho)d\lambda. \tag{44}$$

We next insert R from Eqn. (33) into our expression to obtain,

$$V_1 = \frac{K_1}{r} + K_1 \int_0^\infty \left[\frac{R_{23}e^{-2\lambda d} - R_{21}}{1 - R_{23}R_{21}e^{-2\lambda d}} \right] e^{-\lambda(z+h)} J_0(\lambda\rho)d\lambda. \tag{45}$$

This integral can be expressed as an infinite summation by the following Taylor series expansion,

$$\frac{1}{1-x} = \sum_{n=0}^\infty x^n \qquad \text{for} \qquad |x| < 1. \tag{46}$$

This allows us to rewrite Eqn. (45) as,

$$V_1 = \frac{K_1}{r} + K_1 \sum_{n=0}^\infty R_{23}^n R_{21}^n \int_0^\infty \left(R_{23}e^{-2\lambda d} - R_{21} \right) e^{-\lambda(z+h+2nd)} J_0(\lambda\rho)d\lambda. \tag{47}$$

A close inspection of the previous integral shows that it has a closed-form solution [1];

$$\int_0^\infty e^{-a\lambda} J_0(\lambda\rho)d\lambda = \frac{1}{\sqrt{a^2 + \rho^2}}. \tag{48}$$

From this integral identity, it follows that Eqn. (47) is equivalent to

$$V_1 = \frac{K_1}{r} + K_1 \sum_{n=0}^\infty R_{23}^n R_{21}^n \left[\frac{R_{23}}{\sqrt{D_1^2 + \rho^2}} - \frac{R_{21}}{\sqrt{D_2^2 + \rho^2}} \right] \tag{49}$$
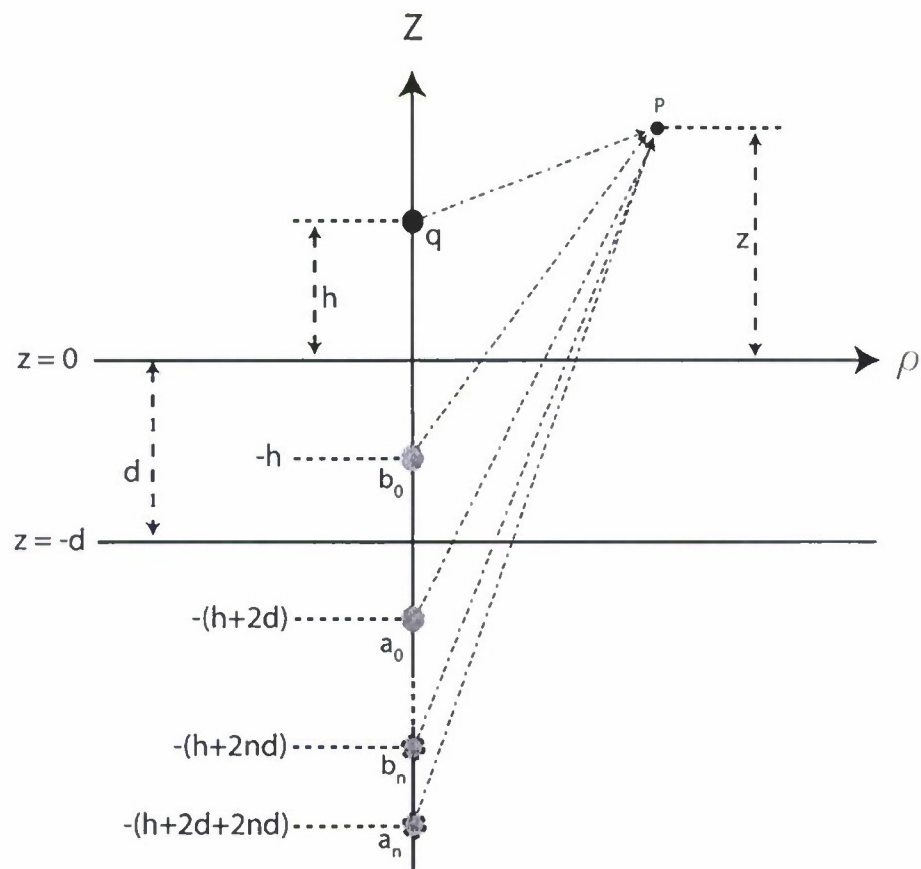
where,

$$D_1 = z + h + 2d(n+1) \tag{50}$$

106

Figure 4: A depiction of the image principle per Eqn. (49).

$$D_2 = z + h + 2dn. \tag{51}$$

The infinite summation in Eqn. (49) allows us to view the potential at some observation location as an infinite summation of equivalent charges at different locations with different strengths and phases. Figure 4 shows the corresponding image locations and strengths represented by Eqn. (49). The fully filled black circle with strength q represents the original charge and is located at height h. Images a_0 and b_0 represent the first and second terms from the summation of Eqn. (49) when $n = 0$ and are presented as gray shaded circles. The image depths are shown relative to the $z = 0$ interface. The remaining image terms, a_n and b_n represent the infinite number of concurring images and are presented as light gray circles with dashed outlines. According to Eqn. (49), we see that the strengths for the corresponding weighted images are as follows,

$$a_0 = K_1 R_{23} \tag{52}$$

$$b_0 = K_1 R_{21} \tag{53}$$

$$a_n = K_1 R_{23}^{n+1} R_{21}^n \tag{54}$$

$$b_n = K_1 R_{23}^n R_{21}^{n+1}. \tag{55}$$

It is insightful to note that the image charges are proportional to the original charge q. For example, we can take Eqn. (52) and substitute K_1 from Eqn. (40) to obtain

$$a_0 = \frac{j\omega q R_{23}}{4\pi Y_1} = W_{a_0} q, \tag{56}$$

where, W can be defined as a weighting term,

$$W_{a_0} = \frac{j\omega R_{23}}{4\pi Y_1}. \tag{57}$$

It is now obvious that each image term is of strength q multiplied by a complex weighting term W. This suggests that the image charges are out of phase with the original charge and scaled appropriately. It is also important to note that as n increases, the weighting terms become increasing small and the distances relative to the observation point become increasingly large. This means that the summation of the images converges very rapidly. No more than a few terms from the summation are needed for accurate results when dealing with any combination of charge and observation locations.

The electric field vector can be determined by taking the gradient of the potential Eqn. (49),

$$\mathbf{E} = -\nabla V = -\left(\frac{\partial V}{\partial x} \hat{\mathbf{a}}_x + \frac{\partial V}{\partial y} \hat{\mathbf{a}}_y + \frac{\partial V}{\partial z} \hat{\mathbf{a}}_z \right). \tag{58}$$

The electric field components are hence given by,

$$E_x = \frac{K_1}{r^3} x + K_1 x \sum_{n=0}^{\infty} R_{23}^n R_{21}^n \left[\frac{R_{23}}{\sqrt{D_1^2 + \rho^2}^3} - \frac{R_{21}}{\sqrt{D_2^2 + \rho^2}^3} \right] \tag{59}$$

108

$$E_y = \frac{K_1}{r^3} y + K_1 y \sum_{n=0}^{\infty} R_{23}^n R_{21}^n \left[\frac{R_{23}}{\sqrt{D_1^2 + \rho^2}^3} - \frac{R_{21}}{\sqrt{D_2^2 + \rho^2}^3} \right] \tag{60}$$

$$E_z = \frac{K_1}{r^3} z + K_1 \sum_{n=0}^{\infty} R_{23}^n R_{21}^n \left[\frac{R_{23}D_1}{\sqrt{D_1^2 + \rho^2}^3} - \frac{R_{21}D_2}{\sqrt{D_2^2 + \rho^2}^3} \right]. \tag{61}$$

Source Charge in Region 1, Observation in Region 2

The aforementioned procedure may also be applied to Eqn. (25) to change the complex integral into an infinite summation. The detailed steps will not be shown for this equation due to the similarity with the previous process. The final form of the summation equation is given by,

$$V_2 = K_1(1 - R_{21}) \sum_{n=0}^{\infty} R_{23}^n R_{21}^n \left[\frac{R_{23}}{\sqrt{D_1^2 + \rho^2}} + \frac{1}{\sqrt{D_3^2 + \rho^2}} \right] \tag{62}$$

where,
$$D_3 = h - z + 2dn. \tag{63}$$

Figure 5 shows the corresponding image locations and strengths represented by Eqn. (62). The strengths for the corresponding weighted images are as follows,

$$a_0 = K_1(1 - R_{21}) \tag{64}$$

$$b_0 = K_1(1 - R_{21})R_{23} \tag{65}$$

$$a_1 = K_1(1 - R_{21})R_{23}R_{21} \tag{66}$$

$$b_1 = K_1(1 - R_{21})R_{23}^2 R_{21} \tag{67}$$

$$a_n = K_1(1 - R_{21})R_{23}^n R_{21}^n \tag{68}$$

$$b_n = K_1(1 - R_{21})R_{23}^{n+1} R_{21}^n. \tag{69}$$

The electric field components are hence given by,

$$E_x = K_1 x(1 - R_{21}) \sum_{n=0}^{\infty} R_{23}^n R_{21}^n \left[\frac{R_{23}}{\sqrt{D_1^2 + \rho^2}^3} + \frac{1}{\sqrt{D_3^2 + \rho^2}^3} \right] \tag{70}$$

$$E_y = K_1 y(1 - R_{21}) \sum_{n=0}^{\infty} R_{23}^n R_{21}^n \left[\frac{R_{23}}{\sqrt{D_1^2 + \rho^2}^3} + \frac{1}{\sqrt{D_3^2 + \rho^2}^3} \right] \tag{71}$$

$$E_z = K_1(1 - R_{21}) \sum_{n=0}^{\infty} R_{23}^n R_{21}^n \left[\frac{R_{23}D_1}{\sqrt{D_1^2 + \rho^2}^3} - \frac{D_3}{\sqrt{D_3^2 + \rho^2}^3} \right]. \tag{72}$$
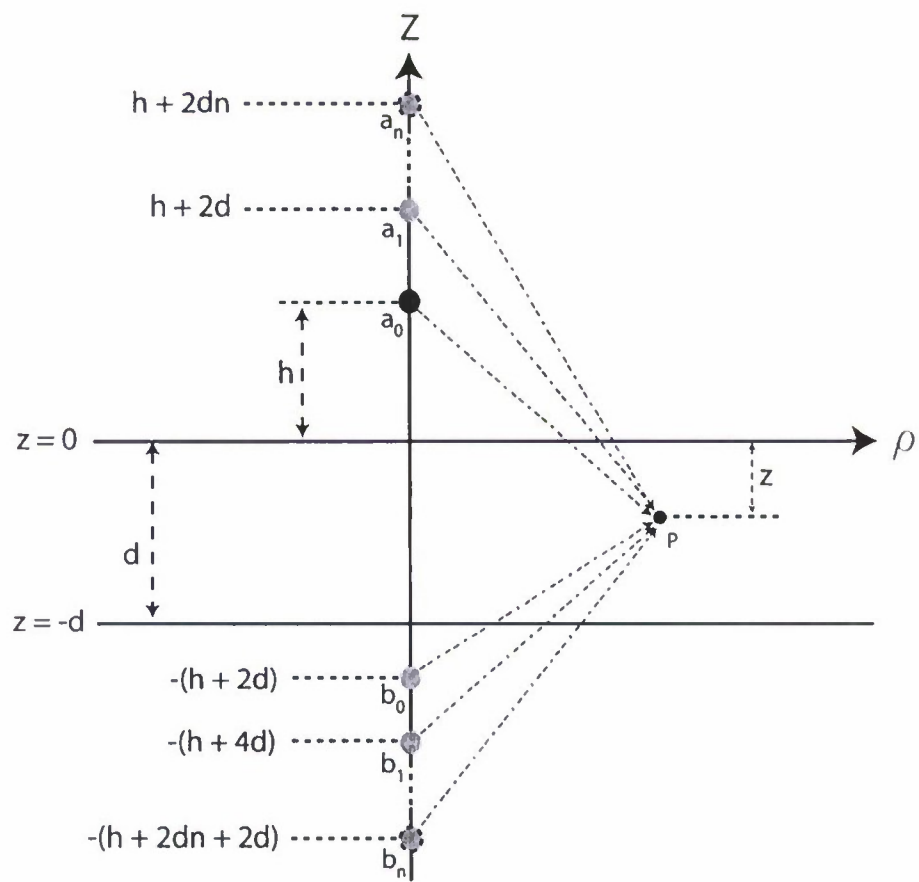
Figure 5: A depiction of the image principle per Eqn. (62).

Source Strength K_1

In this section the point charge strength K_1 will be specified in terms of a two electrode problem. We will begin with the definition of K_1 from Eqn. (40). We will assume the existence of two spherical electrodes of charge $+q$ and $-q$, of radius a and of separation L. We will define the configuration of two oppositely charged electrodes as a *source*. If we assume the charge distribution is uniform across the entire surface of both electrodes then Eqn. (49) is valid for the following procedure. Given the charge separation, a potential V_0 is assumed to exist between the electrodes. Let P_1 be any point on the negative charged sphere and P_2 be any point on the positive charged sphere. Then by Eqn. (49) for source location in region 1 and from superposition, we have,

$$V_0 = K_1 \left[\frac{1}{r} + \sum_{n=0}^{\infty} R_{23}^n R_{21}^n \left[\frac{R_{23}}{\sqrt{D_1^2 + \rho^2}} - \frac{R_{21}}{\sqrt{D_2^2 + \rho^2}} \right] \right]_{P_1}^{P_2}. \tag{73}$$

We will define the geometrical factor G_1 to be the following:

$$G_1 = \left[\frac{1}{r} + \sum_{n=0}^{\infty} R_{23}^n R_{21}^n \left[\frac{R_{23}}{\sqrt{D_1^2 + \rho^2}} - \frac{R_{21}}{\sqrt{D_2^2 + \rho^2}} \right] \right]_{P_1}^{P_2}. \tag{74}$$

The source strength is now determined by supplying the potential between the two electrodes and calculating the geometrical factor;

$$K_1 = \frac{V_0}{G_1}. \tag{75}$$

Source Charge in Region 2

In Figure 6 the charge is located in region 2 at a distance $-h$ below the $z = 0$ interface. We construct potential solutions according to Eqn. (22) for each region as follows. For observation locations in region 1, where $z > 0$, the total potential at any given observation point is equal to the upward transmitted path through the $z = 0$ boundary, which is of strength T_1 and is shown in Figure 7a. The total potential is given by,

$$V_1 = \frac{jwq}{4\pi Y_2} \int_0^{\infty} T_1 e^{-\lambda z} J_0(\lambda \rho) d\lambda. \tag{76}$$

For observation locations in region 2, where $z < 0$ and $z > -d$, the total potential at any given observation point is equal to the superposition of three different potentials and is shown in Figure 7b. The first is the direct path from charge to observer and is of unity strength. The second is the upward traveling path caused by the reflection from the direct charge from the $z = -d$ boundary and is of strength A. The last
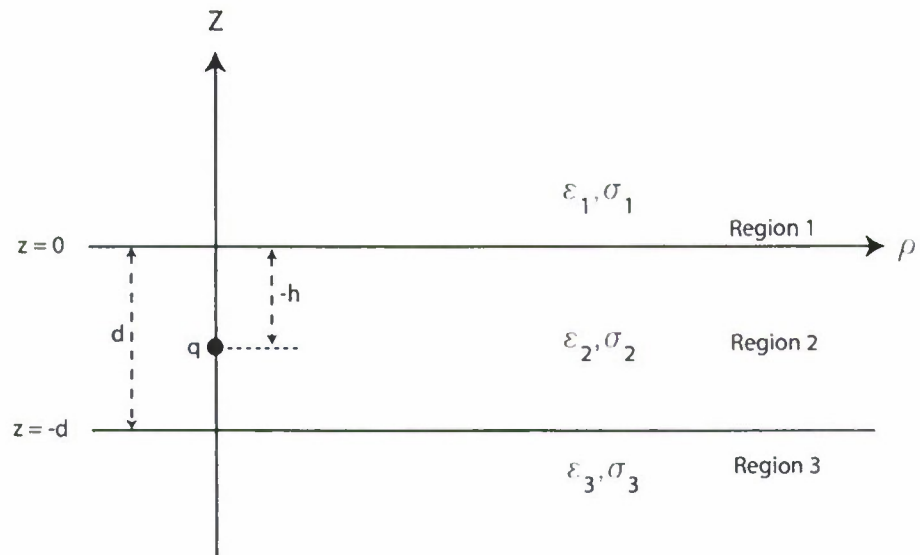
Figure 6: Point charge in region 2 for a three-layer configuration.

a) Observation in Region 1
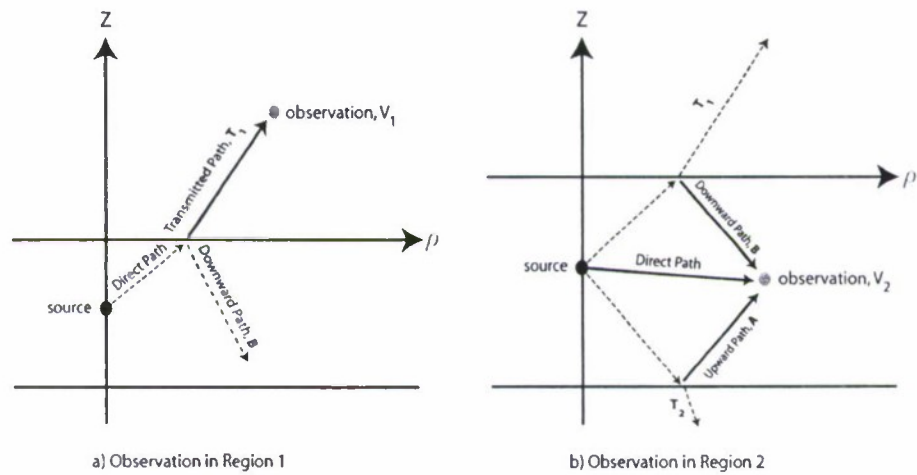
b) Observation in Region 2

Figure 7: Superposition of potentials for regions 1 and 2.

is the downward traveling path caused by the reflection of the direct charge off the $z = 0$ boundary and is of strength B. The total potential is given by,

$$V_2 = \frac{jwq}{4\pi Y_2} \int_0^\infty [e^{-\lambda|z-h|} + Ae^{-\lambda z} + Be^{\lambda z}]J_0(\lambda\rho)d\lambda. \tag{77}$$

For observation locations in region 2, where $z < -d$, the total potential is equal to the direct charge transmitted path through the $z = -d$ boundary and is of strength T_2, and is shown in Figure 7b. The total potential is given by,

$$V_3 = \frac{jwq}{4\pi Y_2} \int_0^\infty T_2 e^{\lambda z} J_0(\lambda\rho)d\lambda. \tag{78}$$

The same boundary conditions of Eqns. (27) and (28) still apply. Applying these boundary conditions, we obtain a set of four equations with four unknowns:

$$T_1 = e^{\lambda h} + A + B \tag{79}$$

$$T_2 e^{-\lambda d} = e^{-\lambda(h+d)} + Ae^{\lambda d} + Be^{-\lambda d} \tag{80}$$

$$Y_1 T_1 = Y_2(e^{\lambda h} + A - B) \tag{81}$$

$$Y_2(Ae^{\lambda d} - Be^{-\lambda d} - e^{-\lambda(h+d)}) = -Y_3 T_2 e^{-\lambda d}. \tag{82}$$

Solving for the unknown coefficients of interest, we obtain the following equations:

$$T_1 = \frac{(R_{21} + 1)(e^{\lambda h} + R_{23}e^{-\lambda(h+2d)})}{1 - R_{23}R_{21}e^{-2\lambda d}} \tag{83}$$

$$A = \frac{R_{23}(1 + R_{21}e^{2\lambda h})e^{-\lambda(h+2d)}}{1 - R_{23}R_{21}e^{-2\lambda d}} \tag{84}$$

$$B = \frac{R_{21}e^{\lambda h} + R_{23}R_{21}e^{-\lambda(h+2d)}}{1 - R_{23}R_{21}e^{-2\lambda d}}. \tag{85}$$

Source Charge in Region 2, Observation in Region 1

The image solution for the configuration of Figure 6 with observation in region 1 as stated by Eqn. (76) is given as,

$$V_1 = K_2(1 + R_{21}) \sum_{n=0}^\infty R_{23}^n R_{21}^n \left[\frac{R_{23}}{\sqrt{D_1^2 + \rho^2}} + \frac{1}{\sqrt{D_4^2 + \rho^2}} \right], \tag{86}$$

where,

$$D_4 = z - h + 2dn \tag{87}$$

and K_2 is the point source strength in region 2 defined by,

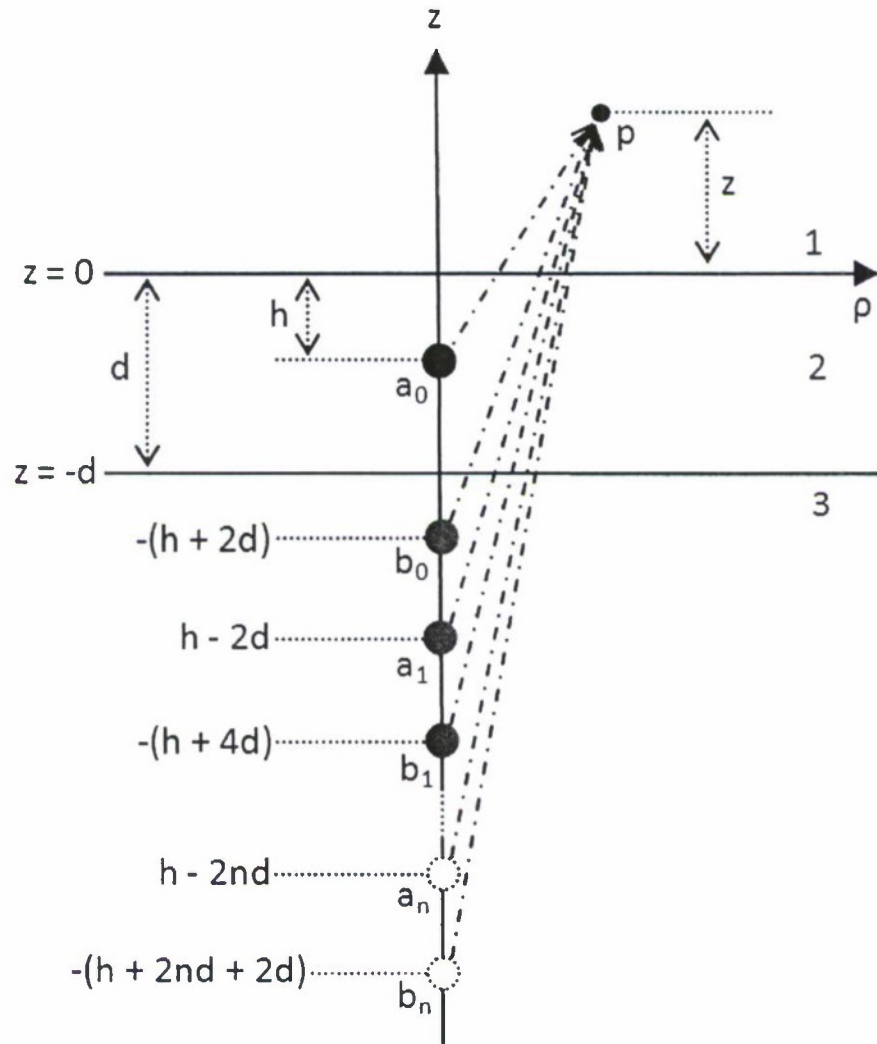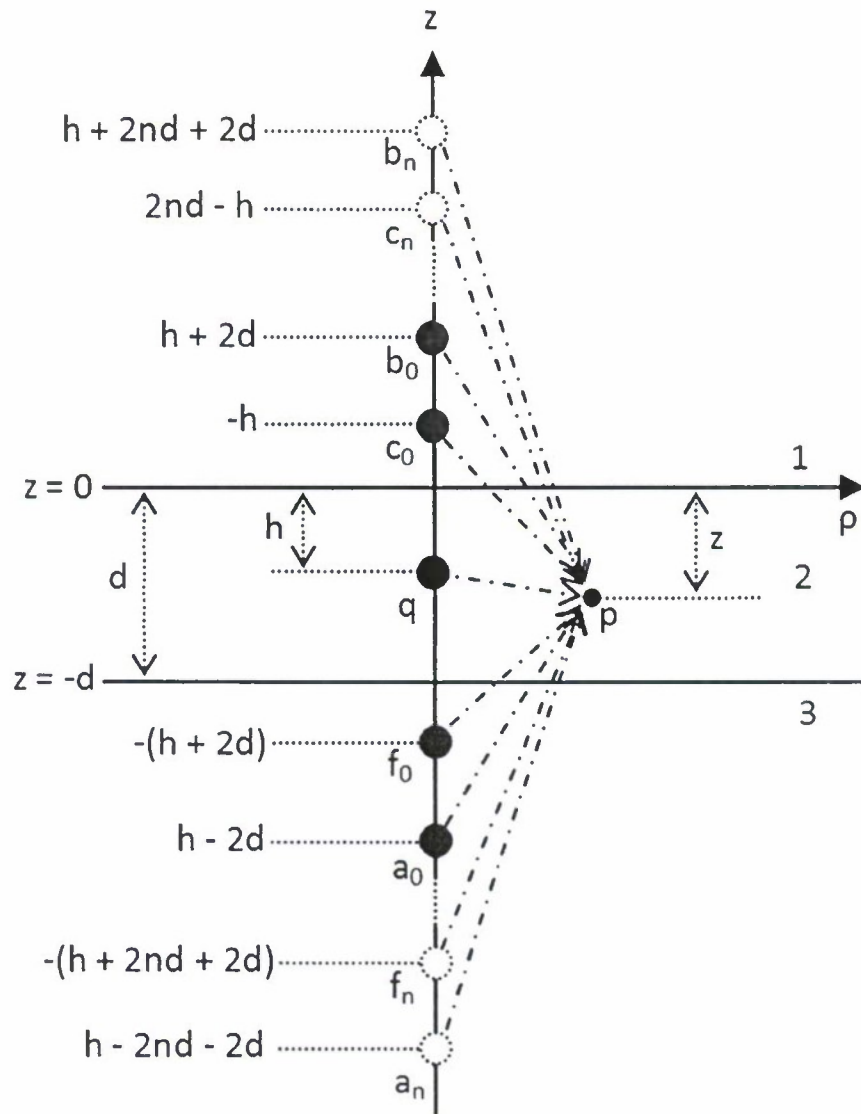$$K_2 = \frac{jwq}{4\pi Y_2}. \tag{88}$$

113

Figure 8: A depiction of the image principle per Eqn. (86).

Figure 8 shows the corresponding image locations and strengths represented by Eqn. (86). The strengths for the corresponding weighted images are as follows,

$$a_0 = K_2(1 + R_{21}) \tag{89}$$

$$b_0 = K_2 R_{23}(1 + R_{21}) \tag{90}$$

$$a_1 = K_2 R_{23}(1 + R_{21})R_{21} \tag{91}$$

$$b_1 = K_2 R_{23}^2(1 + R_{21})R_{21} \tag{92}$$

$$a_n = K_2 R_{23}^n(1 + R_{21})R_{21}^n \tag{93}$$

$$b_n = K_2 R_{23}^{n+1}(1 + R_{21})R_{21}^n. \tag{94}$$

The electric field components are hence given by,

$$E_x = K_1 x(1 + R_{21}) \sum_{n=0}^{\infty} R_{23}^n R_{21}^n \left[\frac{R_{23}}{\sqrt{D_1^2 + \rho^2}^3} + \frac{1}{\sqrt{D_4^2 + \rho^2}^3} \right] \tag{95}$$

$$E_y = K_1 y(1 + R_{21}) \sum_{n=0}^{\infty} R_{23}^n R_{21}^n \left[\frac{R_{23}}{\sqrt{D_1^2 + \rho^2}^3} + \frac{1}{\sqrt{D_4^2 + \rho^2}^3} \right] \tag{96}$$

$$E_z = K_1(1 + R_{21}) \sum_{n=0}^{\infty} R_{23}^n R_{21}^n \left[\frac{D_1 R_{23}}{\sqrt{D_1^2 + \rho^2}^3} + \frac{D_4}{\sqrt{D_4^2 + \rho^2}^3} \right]. \tag{97}$$

Source Charge in Region 2, Observation in Region 2

The image solution for the configuration of Figure 6 with observation in region 1 as stated by Eqn. (77) is given as,

$$V_2 = \frac{K_2}{r} + K_2 \sum_{n=0}^{\infty} R_{23}^n R_{21}^n \left[\frac{R_{23}}{\sqrt{D_1^2 + \rho^2}} + \frac{R_{23}R_{21}}{\sqrt{D_5^2 + \rho^2}} \right.$$
$$\left. + \frac{R_{23}R_{21}}{\sqrt{D_6^2 + \rho^2}} + \frac{R_{21}}{\sqrt{D_7^2 + \rho^2}} \right], \tag{98}$$

where,

$$D_5 = z - h + 2d(n + 1), \tag{99}$$

$$D_6 = h - z + 2d(n + 1), \tag{100}$$

$$D_7 = 2nd - z - h. \tag{101}$$

Figure 9: A depiction of the image principle per Eqn. (98).

116

Figure 9 shows the corresponding image locations and strengths represented by Eqn. (98). The strengths for the corresponding weighted images are as follows,

$$a_0 = K_2 R_{23} R_{21} \tag{102}$$

$$b_0 = K_2 R_{23} R_{21} \tag{103}$$

$$c_0 = K_2 R_{21} \tag{104}$$

$$f_0 = K_2 R_{23} \tag{105}$$

$$a_n = K_2 R_{23}^{n+1} R_{21}^{n+1} \tag{106}$$

$$b_n = K_2 R_{23}^{n+1} R_{21}^{n+1} \tag{107}$$

$$c_n = K_2 R_{23}^{n} R_{21}^{n+1} \tag{108}$$

$$f_n = K_2 R_{23}^{n+1} R_{21}^{n}. \tag{109}$$

The electric field components are hence given by,

$$E_x = \frac{K_2}{r^3} x + K_2 x \sum_{n=0}^{\infty} R_{23}^n R_{21}^n \left[\frac{R_{23}}{\sqrt{D_1^2 + \rho^2}^3} + \frac{R_{23} R_{21}}{\sqrt{D_5^2 + \rho^2}^3} \right.$$
$$\left. + \frac{R_{23} R_{21}}{\sqrt{D_6^2 + \rho^2}^3} + \frac{R_{21}}{\sqrt{D_7^2 + \rho^2}^3} \right] \tag{110}$$

$$E_y = \frac{K_2}{r^3} y + K_2 y \sum_{n=0}^{\infty} R_{23}^n R_{21}^n \left[\frac{R_{23}}{\sqrt{D_1^2 + \rho^2}^3} + \frac{R_{23} R_{21}}{\sqrt{D_5^2 + \rho^2}^3} \right.$$
$$\left. + \frac{R_{23} R_{21}}{\sqrt{D_6^2 + \rho^2}^3} + \frac{R_{21}}{\sqrt{D_7^2 + \rho^2}^3} \right] \tag{111}$$

$$E_z = \frac{K_2}{r^3} z + K_2 \sum_{n=0}^{\infty} R_{23}^n R_{21}^n \left[\frac{D_1 R_{23}}{\sqrt{D_1^2 + \rho^2}^3} + \frac{D_5 R_{23} R_{21}}{\sqrt{D_5^2 + \rho^2}^3} \right.$$
$$\left. - \frac{D_6 R_{23} R_{21}}{\sqrt{D_6^2 + \rho^2}^3} - \frac{D_7 R_{21}}{\sqrt{D_7^2 + \rho^2}^3} \right]. \tag{112}$$

Source Strength K_2

For source location in region 2 and by Eqn. (98) we have:

$$V_0 = K_2 \left[\frac{1}{r} + \sum_{n=0}^{\infty} R_{23}^n R_{21}^n \left[\frac{R_{23}}{D_1^2 + \rho^2} + \frac{R_{23} R_{21}}{D_5^2 + \rho^2} + \frac{R_{23} R_{21}}{D_6^2 + \rho^2} + \frac{R_{21}}{D_7^2 + \rho^2} \right] \right]_{P_1}^{P_2}. \tag{113}$$

117

We will define the geometrical factor G_2 for the two electrode scenario to be the following:

$$G_2 = \frac{1}{r} + \sum_{n=0}^{\infty} R_{23}^n R_{21}^n \left[\frac{R_{23}}{D_1^2 + \rho^2} + \frac{R_{23}R_{21}}{D_5^2 + \rho^2} + \frac{R_{23}R_{21}}{D_6^2 + \rho^2} + \frac{R_{21}}{D_7^2 + \rho^2} \right]_{P_1}^{P_2}. \quad (114)$$

We now can determine the source strength by supplying the potential between the two electrodes and calculating the geometrical factor;

$$K_2 = \frac{V_0}{G_2}. \quad (115)$$

Results

In this section we will use the closed form Sommerfeld solution (denoted as WSU, per Appendix B) to compare and validate the QES solution. The Sommerfeld solution has been fully validated and is regarded as the exact full-wave solution. For the first scenario we place the source in region 2 along the x-axis at a depth of 10m with a normalized strength of 1 A-m. Regions 1, 2 and 3 will be that of air, water and mud respectively, as specified in Table 1. The electric field magnitude is observed along the horizontal x-axis at a depth of 50m. The WSU solution relies on a point source, so for an equivalent scenario, the QES source will be made small. The QES source electrodes have a radius of 0.2m and are separated by 1m. The results for this scenario are shown in Figure 10. The QES solution has little change with frequency while the WSU solution is frequency dependent. For this scenario the QES solution falls within 50 percent of the WSU solution for frequncies up to 1000 Hz and is very accurate at lower frequencies.   For the next scenario, the same

Table 1: Material Properties

	Region 1	Region 2	Region 3
ϵ_r	1	81	1
σ	0	0.018	0.012

source location and strength will be used. Region properties will be consistent with Table 1. We observe the electric field magnitude along the vertical z-axis at a radial distance of 100m. The results are shown in Figure 11. The results are similar to that of the first scenario except more accurate. Consider the scenario when the source is moved further in the water to a depth of 50m and the observation is moved out a distance of 300m. The data for this scenario is shown in Figure 12. We can see that the QES solution is highly accurate when the frequency is low. For this scenario, when the frequency is increased upwards to 1000 Hz, the QES solution over predicts the magnitude of the electric field by up to 150 percent but is still precise at low freqeuncies. Clearly the region of validity for the QES solution is determined
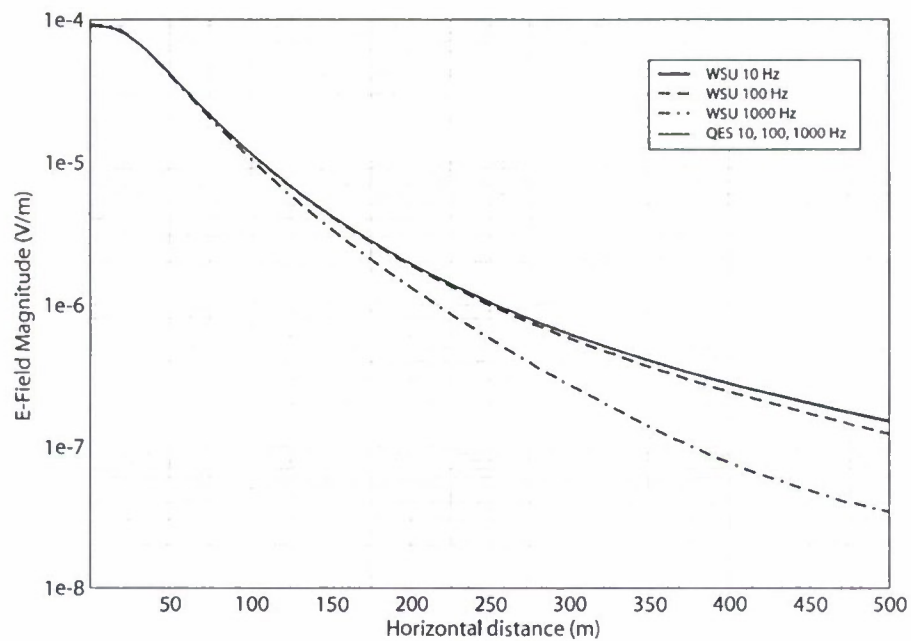
Figure 10: HED in water - Horizontal sweep

by the relative distance between source and observation, and frequency. In the near field, the QES solution predicts to a high level of accurately while in the far field, the QES solution becomes increasingly inaccurate. Also we notice that the QES solution error is larger in water than in air. Further work is needed to ascertain the QES region of validity.
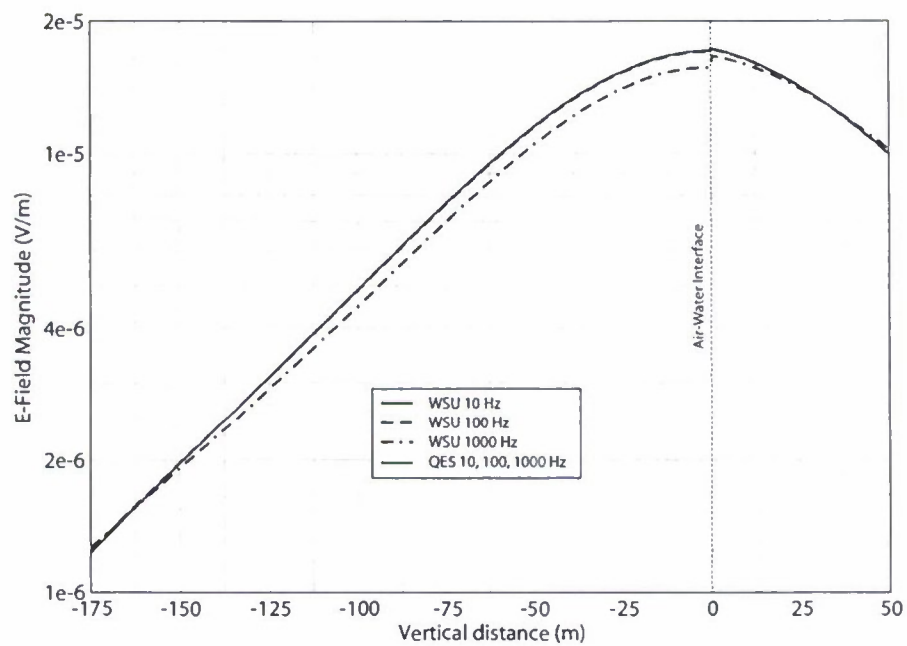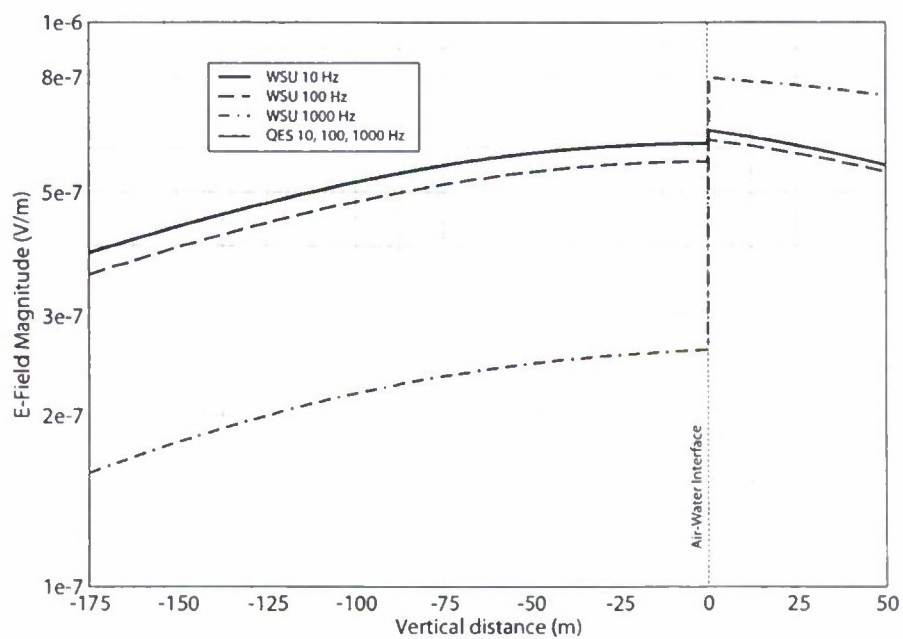
Figure 11: HED in water - Vertical sweep 100m away

Figure 12: HED in water - Vertical sweep 300m away

120

References

[1] I. S. Gradshteyn and I.M. Ryzhik. *Table of Integrals, Series and, Products*, page 707. Academic Press, Florida, corrected and enlarged edition, 1980.

[2] J. R. Wait. *Electromagnetic Wave Theory*, page 19. Harper and Row, New York, 1985.

A Perfectly Matched Layer for Lossy Media at Extremely Low Frequencies

Dennis M. Sullivan, *Senior Member, IEEE*, Yang Xia, and Das Butherus

Abstract—The perfectly matched layer (PML) has proven to be an effective means of absorbing outgoing waves for finite-difference time-domain (FDTD) simulations. This letter describes the development of a PML specifically for underwater simulations at low frequencies. This is a significant development for this project that involves simulations of electromagnetic signals for long distances under water.

Index Terms—finite-difference time-domain (FDTD) methods, perfectly matched layer (PML).

I. Introduction

THE single largest threat to surface warships is mines. These mines are often detonated by the electromagnetic signature of a surface ship [1]. For this reason, it is desirable to have simulation methods to study the propagation of extremely low frequency (ELF) electromagnetic waves under water. The finite-difference time-domain (FDTD) method [2], [3] is one of the most widely used methods in electromagnetic simulation and has recently been adapted for ELFs under water [4], [5]. In FDTD simulations, it is necessary to have an absorbing boundary condition (ABC) to truncate the problem space and absorb outgoing waves. One of the most widely used and versatile ABCs is the perfectly matched layer (PML) [6], [7]. There has been some activity in the development of PMLs that are effective in low frequency or dispersive media [8]–[11]. In this letter, we describe the development of a PML that is specifically suited for very lossy media at ELFs.

II. Implementation of the PML

A. Berenger's PML in Free Space

Berenger [6] assumed that any plane wave propagating in the direction d near the PML could be broken up into the part traveling perpendicular to the PML $d_\perp$ and the part traveling parallel $d_\parallel$ (Fig. 1). The two conditions for the PML are the following:
1) It must have the same impedance as free space and not present a loss to the wave traveling parallel to the interface.
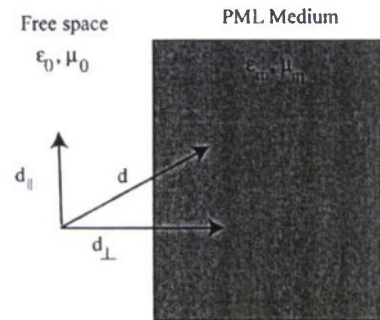
Fig. 1. The PML is implemented by assuming any propagating wave can be broken up into a part that is perpendicular to the PML interface and a part that is parallel to it.

2) It must increase the artificial electric and magnetic conductivities such that the impedance still matches that of the free space.

Both of these conditions are met by increasing the electric and magnetic conductivities in the PML such that

$$\eta = \sqrt{\frac{\mu_0}{\varepsilon_0}} = \sqrt{\frac{\mu_0\left(1 + \frac{\sigma_H}{j\omega\mu_0}\right)}{\varepsilon_0\left(1 + \frac{\sigma_E}{j\omega\varepsilon_0}\right)}}. \tag{1}$$

Note that this impedance is a real number.

Berenger implemented (1) into the FDTD formulation by a split-step formulation that broke each electric and magnetic field into two components. Most applications assume that the background medium in the main problem space is free space.

B. The PML in a Lossy Medium at ELFs

When the background medium is lake water and the frequencies are in the ELF region, the situation is different. Lake water has a dielectric constant of 80 and a conductivity of 0.018 S/m [12]. For lake water at 1 kHz, the complex dielectric constant is

$$\varepsilon_w^* = \varepsilon_w + \frac{\sigma_w}{j\omega\varepsilon_0} = 80 + \frac{0.018}{j\left(2\pi \times 10^3\right)\left(8.85 \times 10^{-12}\right)}$$
$$= 80 - j3.24 \times 10^5 \cong -j3.24 \times 10^5.$$

Therefore, the impedance is

$$\eta_w = \sqrt{\frac{\mu_0}{\varepsilon_w^*\varepsilon_0}} \cong \sqrt{\frac{\mu_0}{\varepsilon_0\left(\frac{\sigma_w}{j\omega\varepsilon_0}\right)}} = \sqrt{\frac{\mu_0}{\frac{\sigma_w}{j\omega}}}. \tag{2}$$

This impedance can be written in polar coordinates as

$$\eta_w = |\eta_w| \angle 45^\circ.$$

Notice that because the loss term dominates, the impedance is at 45°. The impedance of the PML material must remain at this value, but at the same time increase the loss further as it goes perpendicular into the PML. This can be accomplished by adding a factor s to the conductivity and the permeability

$$\eta_{pml} = \sqrt{\frac{s \cdot \mu_0}{\frac{s \cdot \sigma_w}{j\omega}}}. \tag{3}$$

This addition of the s term causes the PML medium to absorb outgoing waves faster than the water medium, but also avoids reflections from the PML medium. The factor s equals one in the background medium, but increases as it goes into the PML.

This implementation may bare a superficial representation to the "stretched coordinates" proposed by Chew and Weedon [13]. However, the s in (3) is a real number as opposed to the complex numbers used in the stretched coordinates. There have been other methods proposed for the PML in lossy media [10], [11] where the conductivity is large enough that it plays a substantial role in the complex dielectric constant. However, the impedance in (3) is for the situation when the imaginary part of the dielectric constant dominates completely.

C. Implementation Into FDTD

We begin with the following formulation of the Maxwell equations for a lossy media:

$$\varepsilon_r \varepsilon_0 \frac{\partial E}{\partial t} - \sigma E = \nabla \times H$$
$$\mu_0 \frac{\partial H}{\partial t} = -\nabla \times E.$$

We will restrict the discussion to the implementation of E_x and H_z propagating in the y-direction perpendicular to the PML

$$\varepsilon_w \varepsilon_0 \frac{\partial E_x}{\partial t} + \sigma_w E_x = \frac{\partial H_z}{\partial y} - \frac{\partial H_y}{\partial z} \tag{4a}$$
$$\mu_0 \frac{\partial H_z}{\partial t} = \frac{\partial E_x}{\partial y} - \frac{\partial E_y}{\partial x}. \tag{4b}$$

The FDTD formulation leads to the following coupled equations:

$$E_x^{n+1}(i,j,k)$$
$$= \frac{\varepsilon_w \varepsilon_0}{(\varepsilon_w \varepsilon_0 + \sigma_w \cdot \Delta t)} E_x^n(i,j,k) + \frac{\left(\frac{\Delta t}{\Delta x}\right)}{(\varepsilon_w \varepsilon_0 + \sigma_w \cdot \Delta t)}$$
$$\cdot \begin{bmatrix} H_z^{n+1/2}(i,j,k) - H_z^{n+1/2}(i,j-1,k) \\ -H_y^{n+1/2}(i,j,k) + H_y^{n+1/2}(i,j,k-1) \end{bmatrix} \tag{5a}$$
$$H_z^{n+1/2}(i,j,k)$$
$$= H_z^{n-1/2}(i,j,k) + \frac{\Delta t}{(\mu_0 \Delta x)}$$
$$\cdot \begin{bmatrix} E_x^{n+1}(i,j+1,k) - E_x^{n+1}(i,j,k) \\ E_y^{n+1}(i,j,k) - E_y^{n+1}(i+1,j,k) \end{bmatrix} \tag{5b}$$

where Δx and Δt are the cell size and time-step, respectively. The implementation of the PML in the H_z field in the y-direction is relatively straightforward. The term s is added only to the y differential

$$H_z^{n+1/2}(i,j,k)$$
$$= H_z^{n-1/2}(i,j,k)$$
$$+ \frac{\Delta t}{(\mu_0 \Delta x)} \left[E_y^{n+1}(i,j,k) - E_y^{n+1}(i+1,j,k) \right]$$
$$+ \frac{\Delta t}{(s \cdot \mu_0 \Delta x)} \left[E_x^{n+1}(i,j+1,k) - E_x^{n+1}(i,j,k) \right]. \tag{6}$$

Instead of changing the entire term containing s above, we have found it expedient to include a one-dimensional array

$$gy(j) = \frac{1}{s} \tag{7}$$

so (6) becomes

$$H_z^{n+1/2}(i,j,k)$$
$$= H_z^{n-1/2}(i,j,k)$$
$$+ \frac{\Delta t}{(\mu_0 \Delta x)} \left[E_y^{n+1}(i,j,k) - E_y^{n+1}(i+1,j,k) \right]$$
$$+ gy(j) \frac{\Delta t}{(\mu_0 \Delta x)}$$
$$\cdot \left[E_x^{n+1}(i,j+1,k) - E_x^{n+1}(i,j,k) \right]. \tag{8}$$

Adding the PML to the calculation of the E_x field requires that the calculation be split into two equations for propagation in the y and z directions. The s term is only added to the conductivity in the y-direction

$$E_{xy}^{n+1}(i,j,k)$$
$$= \frac{\varepsilon_w \varepsilon_0}{(\varepsilon_w \varepsilon_0 + s \cdot \sigma_w \cdot \Delta t)} E_{xy}^n(i,j,k) + \frac{\left(\frac{\Delta t}{\Delta x}\right)}{(\varepsilon_w \varepsilon_0 + s \cdot \sigma_w \Delta t)}$$
$$\cdot \left[H_z^{n+1/2}(i,j,k) - H_z^{n+1/2}(i,j-1,k) \right] \tag{9a}$$
$$E_{xz}^{n+1}(i,j,k)$$
$$= \frac{\varepsilon_w \varepsilon_0}{(\varepsilon_w \varepsilon_0 + \sigma_w \cdot \Delta)} E_z^n(i,j,k) + \frac{\left(\frac{\Delta t}{\Delta x}\right)}{(\varepsilon_w \varepsilon_0 + \sigma_w \cdot \Delta t)}$$
$$\cdot \left[H_y^{n+1/2}(i,j,k-1) - H_y^{n+1/2}(i,j,k) \right]. \tag{9b}$$

Once again, it is expedient to implement this by an additional one-dimensional array. Equation (9a) becomes

$$E_{xy}^{n+1}(i,j,k) = fy(j) \cdot ca \cdot E_{xy}^n(i,j,k)$$
$$+ fy(j) \cdot cb \cdot \left[H_z^{n+1/2}(i,j,k) - H_z^{n+1/2}(i,j-1,k) \right] \tag{10}$$
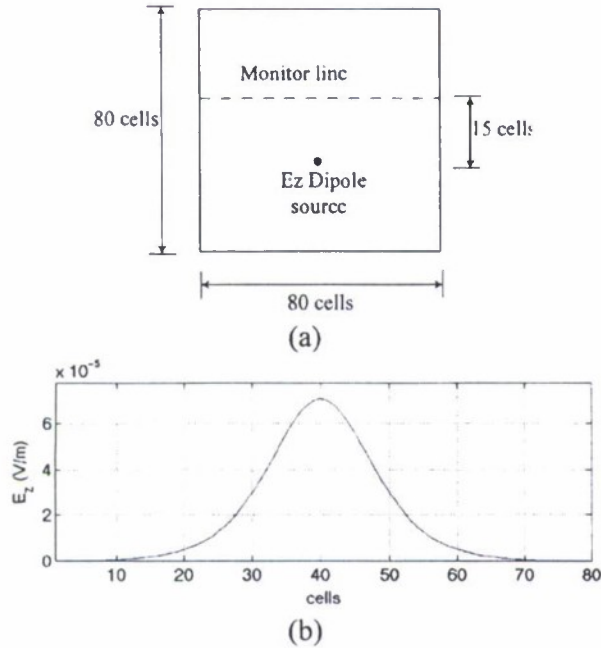
(a)

(b)

Fig. 2. (a) A dipole source is located in the 80^3 problem space. Once steady state has been reached, the amplitude is determined at a transverse line 15 cells from the source. The cells are 25 m^3. (b) The amplitude at the monitor line after 4000 time-steps.

where

$$ca = \frac{\varepsilon_w \varepsilon_0}{(\varepsilon_w \varepsilon_0 + \sigma_w \cdot \Delta)} \tag{11a}$$

$$cb = \frac{\left(\frac{\Delta t}{\Delta x}\right)}{(\varepsilon_w \varepsilon_0 + \sigma_w \cdot \Delta t)} \tag{11b}$$

$$fy(j) = \frac{\left(1 + \sigma_w \cdot \frac{\Delta t}{\varepsilon_w \varepsilon_0}\right)}{\left(1 + s \cdot \sigma_w \cdot \frac{\Delta t}{\varepsilon_w \varepsilon_0}\right)}. \tag{11c}$$

In summary, the PML is implemented in the y-direction by the one-dimensional arrays

$$gy(j) = \frac{1}{s} \tag{7*}$$

$$fy(j) = \frac{\left(1 + \sigma_w \cdot \frac{\Delta t}{\varepsilon_w \varepsilon_0}\right)}{\left(1 + s \cdot \sigma_w \cdot \frac{\Delta t}{\varepsilon_w \varepsilon_0}\right)}. \tag{11c*}$$

It has been found empirically that an effective formula for the s factor as it goes into the PML is

$$s = 0.2 \cdot (j - j_{\text{edge}})^3 \tag{12}$$

where j_{edge} is the beginning of the PML. This formulation also prevents the largest stretched cells from exceeding the skin depth.

III. RESULTS

In this section, we illustrate the effectiveness of the lossy medium ELF PML. We will start with the problem space illustrated in Fig. 2(a), which is 80 cells cubed. Each cell is 25 m
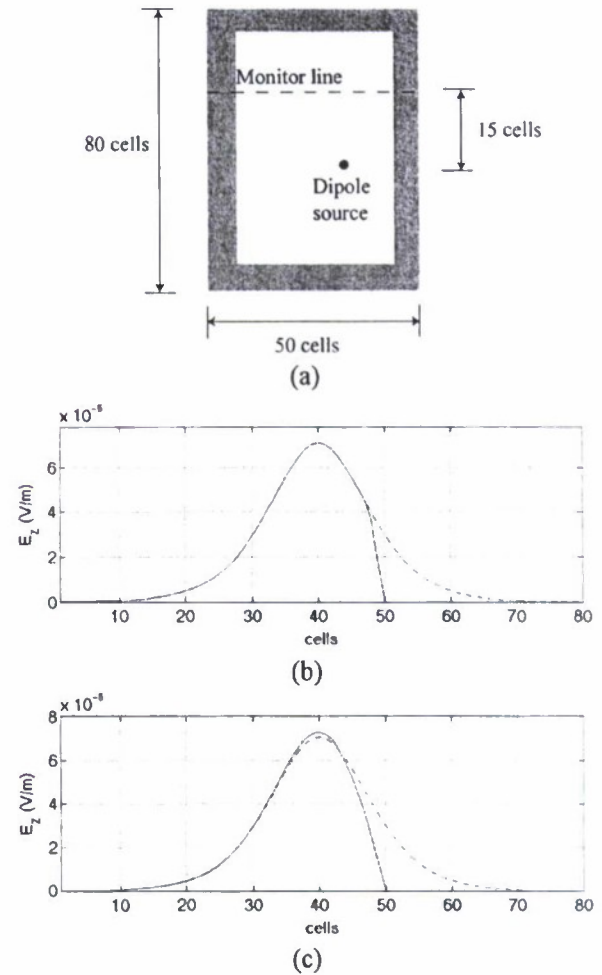

(a)

(b)

(c)

Fig. 3. (a) The problem space is truncated to 10 cells to the right of the source. A four-cell lossy PML has been added to each boundary. (b) The solid line is the amplitude for the simulation in (a), while the dashed line is from the 80 cell monitor line of Fig. 2. (c) The same simulation with no PML.

cubed. The size of 80^3 was needed so that boundary plays no role in the results of the simulation. The source is a single-cell electric dipole. After 4000 time-steps, the amplitude is calculated via the method of two equations, two unknowns (2E2U) [14] at a monitor line 15 cells from the dipole, as shown in Fig. 2(b).

The simulation is then repeated for the truncated problem space shown in Fig. 3(a), where a four-cell PML has been added. In this simulation, the right wall has been moved in to within 10 cells of the source. The results are plotted in Fig. 3(b) (solid line) along with the results of the previous simulation (dashed line). For comparison, Fig. 3(c) is the same simulation with no PML on the truncated wall. Clearly, substantial errors appear when the PML is not present.

In one final simulation, the problem space is reduced to $60 \times 20 \times 20$ cells, as illustrated in Fig. 4(a). The results are shown in Fig. 4(b), where the results of the original simulation of Fig. 2 are presented for comparison. The amplitudes on the monitor line within five cells of the center are identical. Once again, the results without the PML are shown in Fig. 4(c), demonstrating the expected error when no PML is present.
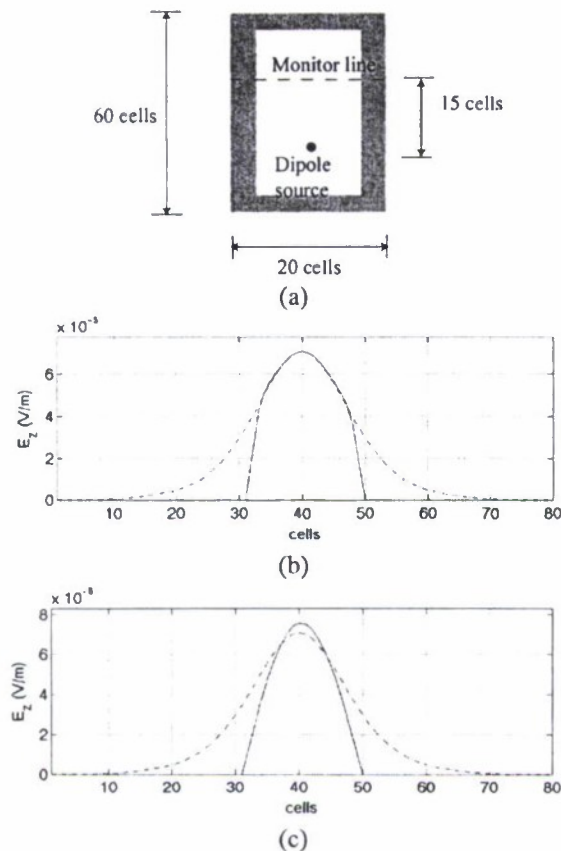
Fig. 4. (a) A simulation similar to Fig. 2 but with the problem space truncated to $60 \times 20 \times 20$ cells. (b) The solid line is the amplitude for the smaller problem space, while the dashed line is the larger problem space of Fig. 2. (c) The same comparison when a $60 \times 20 \times 20$ problem space with no PML is used.

IV. DISCUSSION

A PML has been developed for applications involving ELFs in lossy media. As opposed to the original Berenger PML in free space, this one requires a split E-field, but not a split H-field. Although the use of a PML is not as crucial as it might be in

free space or other lossless media, it substantially decreases the needed computer resources. For instance, in the examples in Section III, it was found that a problem space of 80^3 was necessary to insure that the boundaries were not influencing the results when there was no PML. After the PML was added, the problem space was reduced to $60 \times 20 \times 20$. This represents a reduction in the problems space from 512 000 cells to 24 000 cells.

REFERENCES

[1] J. J. Holmes, *Exploitation of a Ship's Magnetic Field Signatures*. San Rafael, CA: Morgan & Claypool, 2006.

[2] K. S. Yee, "Numerical solution of initial boundary value problems involving Maxwell's equations in isotropic media," *IEEE Trans. Antennas Propag.*, vol. AP-14, no. 3, pp. 302–307, May 1966.

[3] D. M. Sullivan, *Electromagnetic Simulation Using the FDTD Method*. New York: IEEE Press, 2000.

[4] Y. Xia and D. M. Sullivan, "Underwater FDTD simulation at extremely low frequencies," *IEEE Antennas Wireless Propag. Lett.*, vol. 7, pp. 661–664, 2008.

[5] Y. Xia and D. M. Sullivan, "Dual problem space FDTD simulation for underwater ELF applications," *IEEE Antennas Wireless Propag. Lett.*, vol. 8, pp. 498–501, 2009.

[6] J. P. Berenger, "A perfectly matched layer for the absorption of electromagnetic waves," *J. Comput. Phys.*, vol. 114, pp. 185–200, 1994.

[7] J. P. Berenger, *Perfectly Matched Layer (PML) for Computational Electromagnetics*. San Rafael, CA: Morgan & Claypool, 2007.

[8] J. De Moerloose and M. A. Stuchly, "Behavior of Berenger's ABC for evanescent waves," *IEEE Microw. Guided Wave Lett.*, vol. 5, no. 10, pp. 344–346, Oct. 1995.

[9] S. A. Cummer, "A simple, nearly perfectly matched layer for general electromagnetic media," *IEEE Microw. Wireless Comput. Lett.*, vol. 13, no. 3, pp. 128–130, Mar. 2003.

[10] J. Fang and Z. Wu, "Generalized perfectly matched layer—An extension of Berenger's perfectly matched layer boundary conditions," *IEEE Microw. Guided Waves Lett.*, vol. 5, no. 12, pp. 451–453, Dec. 1995.

[11] Q. H. Liu, "An FDTD algorithm with perfectly matched layers for conductive media," *Microw. Opt. Technol. Lett.*, vol. 14, pp. 134–137, 1997.

[12] D. K. Chen, *Field and Wave Electromagnetics*, 2nd ed. New York: Addison-Wesley, 1989.

[13] W. C. Chew and W. H. Weedon, "A 3D perfectly matched medium from modified Maxwell's equations with stretched coordinates," *Microw. Opt. Technol. Lett.*, vol. 11, pp. 599–604, Jul. 1994.

[14] C. M. Furse, "Faster than Fourier—Ultra-efficient time-to-frequency domain conversions for FDTD simulations," *IEEE Antennas Propag. Mag.*, vol. 42, no. 6, pp. 24–34, Dec. 2000.

Underwater FDTD Simulation at Extremely Low Frequencies

Yang Xia and Dennis M. Sullivan, *Senior Member, IEEE*

Abstract—This letter describes the application of the finite-difference time-domain (FDTD) method to the simulation of extremely low frequency (ELF) electromagnetic signals under water. This requires substantial modification to the traditional FDTD method, as well as the development of an analytic method needed to verify the accuracy of the FDTD method.

Index Terms—Electromagnetic propagation in absorbing media, extremely low frequencies, finite-difference time-domain (FDTD) methods.

I. INTRODUCTION

MODERN antiship mines can be detonated by the electromagnetic signature of a surface ship [1]. For this reason, it is desirable to have simulation methods to study the propagation of extremely low-frequency (ELF) electromagnetic waves under water. The finite-difference time-domain (FDTD) method [2], [3] is one of the most widely used methods in electromagnetic simulation. However, it has seen limited use for low frequencies in lossy media. In this letter, we describe the use of FDTD for ELF simulation under water. In Section II, we describe the formulation of the FDTD method that has been found to be most appropriate for this application. Section III describes the method of two equations, two unknowns (2E2U) that is used to determine the resulting amplitudes when the FDTD program has reached steady state. Section IV describes an analytic method that was developed to evaluate the accuracy of FDTD at ELF. Section V presents an example of ELF simulation in shallow water, the type of problem that will be of interest for this project. Section VI ends in a discussion, including remarks on future areas of research.

II. METHOD

We begin with the time-domain Maxwell's equations

$$\varepsilon_r \varepsilon_0 \frac{\partial E}{\partial t} = \nabla \times H - \sigma E \tag{1a}$$

$$\mu_0 \frac{\partial H}{\partial t} = -\nabla \times E. \tag{1b}$$

Equation (1) is for three dimensions, but for the purpose of illustration, we limit the discussion to the E_x and H_y fields propagating in the z direction. Equation (1a) can be taken into the sampled time domain using the usual finite-differencing procedures

$$\varepsilon_r \frac{E_x^{n+1}(k) - E_x^n(k)}{\Delta t} + \left(\frac{\sigma}{\varepsilon_0}\right) E_x^{n+1}$$
$$= \frac{1}{\varepsilon_0} \frac{H_y^{n+1/2}(k+1/2) - H_y^{n+1/2}(k-1/2)}{\Delta x}.$$

We assume the cell size is Δx and the time step is Δt. The E_x^{n+1} can now be calculated from

$$E_x^{n+1}(k) = ca(k)E_x^n(k)$$
$$+ cb(k)\left[H_y^{n+1/2}(k+1/2) - H_y^{n+1/2}(k-1/2)\right] \tag{2a}$$

where

$$ca = \left(1 + \frac{\Delta t \cdot \sigma}{\varepsilon_r \varepsilon_0}\right)^{-1}, \quad cb = ca\frac{\Delta t}{(\varepsilon_r \varepsilon_0 \Delta x)}. \tag{2b}$$

There is a crucial choice that was made here. Usually, the E_x term next to the conductivity is averaged across the two time steps

$$\varepsilon_r \frac{E_x^{n+1}(k) - E_x^n(k)}{\Delta t} + \left(\frac{\sigma}{\varepsilon_0}\right)\left(\frac{E_x^{n+1}(k) + E_x^n(k)}{2}\right)$$
$$= \frac{1}{\varepsilon_0} \frac{H_y^{n+1/2}(k+1/2) - H_y^{n+1/2}(k-1/2)}{\Delta x},$$

which would lead to the following expression for ca:

$$ca = \left(1 - \frac{\Delta t \cdot \sigma}{2\varepsilon_r \varepsilon_0}\right) \Big/ \left(1 + \frac{\Delta t \cdot \sigma}{2\varepsilon_r \varepsilon_0}\right). \tag{3}$$

At ELF frequencies in lossy media, the ca of (3) would be negative, leading to a potentially unstable condition. (The implementation of (1b) into FDTD is straight-forward and will not be presented here).

There is another choice that leads to substantially larger time steps, and therefore, substantially faster solutions [4]. Once the cell size Δx is chosen, the time step must be chosen to satisfy the Courant condition, which in three dimensions is

$$\Delta t \leq \frac{\Delta x}{\sqrt{3} \cdot c_{max}} \tag{4}$$

where c_{max} is usually the speed of light in a vacuum. The materials that will be of interest for this project are listed in Table I. (An early goal of this project is to study propagation in lakes.

TABLE I
THE PROPERTIES OF THE MATERIALS USED IN THE SIMULATIONS DESCRIBED
IN THIS PAPER [5]

Material	ε_r	$\sigma \, (S/m)$
Water	80	0.018
Air	1	0
Lake water	80	0.018
Mud	40	0.002
Metal	1	10^7

That is the reason that lake water is used instead of sea water.)
The complex dielectric constant is calculated by

$$\varepsilon_r^* = \varepsilon_r + \frac{\sigma}{j\omega\varepsilon_0}.$$

At ELF frequencies, the imaginary part of the dielectric constant
will dominate the magnitude for all the materials except air.
Therefore, increasing the dielectric constants of mud or metal
to 80 would make very little difference. If we assume every
material in Table I has a real dielectric constant of 80, then
$c_{\max} = c_0/\sqrt{80}$ and the time step is almost an order of magni-
tude greater. (c_0 is the speed of light in a vacuum). Even though
air is one of the materials listed in Table I, air is a boundary
medium in this project. It presents almost perfect reflection to
an electromagnetic signal in water, even if the higher dielectric
constant is used.

III. THE METHOD OF TWO EQUATIONS, TWO UNKOWNS

FDTD is a time-domain method. Once the steady state has
been reached for a simulation problem, it is desirable to know
the resulting amplitude and phase at certain locations in the
problem space. For frequencies of about 100 kHz and above,
the discrete Fourier transform is the preferred method [6]. We
have found that at ELF frequencies, the method of two equa-
tions, two unknowns (2E2U) is preferable [7]. In this method,
two sample points are taken

$$E_1 = A\sin(\omega_{\text{in}}t_1 + \theta) \tag{5a}$$
$$E_2 = A\sin(\omega_{\text{in}}t_2 + \theta). \tag{5b}$$

Since the input frequency ω_{in} as well as the two sample points
t_1 and t_2 are known, the only unknowns are the amplitude A and
the phase θ. The concept of solving for two unknowns from the
two equations is straight-forward, but the fact that the inverse
trigonometric identities must be taken can lead to inconsisten-
cies. It has been found expedient to add an offset time

$$t_{\text{off}} = \frac{1}{2}\left[\frac{\pi}{\omega} - t_1 - t_2\right] \tag{6}$$

to each of the times t_1 and t_2. This centers the two sample points
symmetrically on the ninety degree axis and avoids problems
when taking inverse trigonometric functions.

IV. VERIFICATION OF THE ACCURACY OF THE METHOD

An analytic solution is needed to verify the accuracy of the
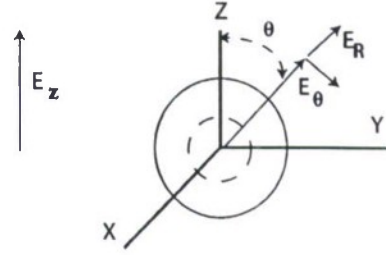FDTD method at ELF. One such method that is often used to

Fig. 1. A layered dielectric sphere in a constant E field.

verify FDTD formulations is a layered dielectric sphere illumi-
nated by a plane wave. A Bessel function expansion is used to
calculate the resulting fields [8]. This method is not valid below
about 100 kHz.

At low frequencies, the near field can be regarded as a static
field. A solution for a layered sphere in a static electric field was
developed, as illustrated in Fig. 1. A spherical boundary-value
problem has solutions of the form [5]

$$V(R,\theta) = \sum_{n=0}^{\infty}\left[A_n R^n + B_n R^{-(n+1)}\right] P_n(\cos\theta). \tag{7}$$

$P_n(\cos\theta)$ are the Legendre polynomials. In the limit far from
the sphere, $V_o(R,\theta)|_{R\to\infty} \cong -E_0 R\cos\theta$, and inside the
sphere $V_1(R,\theta) = A_1 R\cos\theta$. There are two boundary con-
ditions at a dielectric boundary: $E_{1t} = E_{2t}, \varepsilon_1 E_{1n} = \varepsilon_2 E_{2n}$.
The two equations resulting from the boundary conditions are

$$B_m + A_m r_m^3 - B_{m+1} - A_{m+1} r_m^3 = 0 \tag{8a}$$

and

$$-2\frac{\varepsilon_m}{\varepsilon_{m+1}}B_m + \frac{\varepsilon_m}{\varepsilon_{m+1}}A_m r_m^3 + 2B_{m+1}$$
$$- A_{m+1}r_m^3 = 0. \tag{8b}$$

The constants are determined by Gaussian elimination. Once
the potential V is known, the E fields are determined by

$$\mathbf{E} = -\nabla V = -\frac{\partial}{\partial R}V\mathbf{a}_R - \frac{1}{R}\frac{\partial}{\partial\theta}V\mathbf{a}_\theta \tag{9}$$

which can be converted to rectangular coordinates.

In order to compare the FDTD results with the analytic
method, we use the three-dimensional problem space illus-
trated in Fig. 2. A plane wave polarized in the z direction is
generated at one end and subtracted out the other end. The
cells used in the simulations are five meters cubed and the time
steps are 75 ns. A layered sphere with dielectric properties to
simulate various materials lies in the center of the total field.
The amplitude of the E_z field is determined along the major
axes for comparison with the analytic method to evaluate the
accuracy of the FDTD simulation. These axes go through the
sphere and extend five cells out in each direction. The problem
space is 50 cells cubed.

The results of the simulations are shown in Fig. 3. The solid
lines are the analytic results and the circles are the FDTD values.
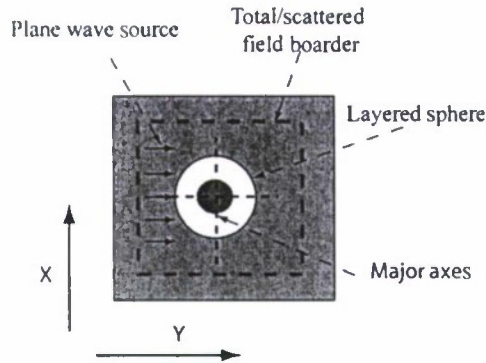Clearly, the comparisons are very good. In Fig. 3(c), there is

Fig. 2. The configuration of the three-dimensional simulation space used to evaluate the accuracy of the method.

some discrepancy in the air layer in the middle. This is not too worrisome because in our problems of interest, air is a boundary, not a central part of the problem space. Note that this condition was not caused by increasing the dielectric to 80 as discussed above; the same result is obtained using a dielectric of 1 or 80.

V. EXAMPLE

Fig. 4 illustrates the type of simulation of interest for this project. Two dipoles, one used as a transmitter and one as a receiver, are submerged in shallow water. The problem space is $40 \times 60 \times 40$ cells and each cell is 10 m squared. The transmitting current is simulated by the H fields surrounding the middle of the transmitting dipole

$$I_{\text{trans}} = \oint_S H \cdot dl \cong 4\Delta x$$
$$\cdot \left(\begin{array}{c} H_y(i,j,k) - H_y(i-1,j,k) \\ -H_x(i,j,k) + H_x(i,j-1,k) \end{array} \right). \quad (10)$$

The resulting current on the receiver is calculated with a similar equation. Each simulation required 2000 time steps. The results are shown in Fig. 5. The important quantity, H, the transfer function, is the ratio of received current to transmitted current, which is plotted as a function of frequency.

VI. DISCUSSION

A method has been described to simulate electromagnetic waves propagating under water at extremely low frequencies. This approach necessitated substantial modification to the usual FDTD formulations. Furthermore, an analytic method based on the Legendre polynomials was developed to verify the accuracy of the FDTD method.

Those familiar with FDTD methods will notice the lack of discussion on absorbing boundary conditions (ABCs). ABCs are usually required to prevent outgoing signals from being reflected back into the problem space. The very lossy background medium of lake water has prevented this from being a concern for the examples presented in this letter. However, it is likely that an appropriate ABC, probably one based on the perfectly
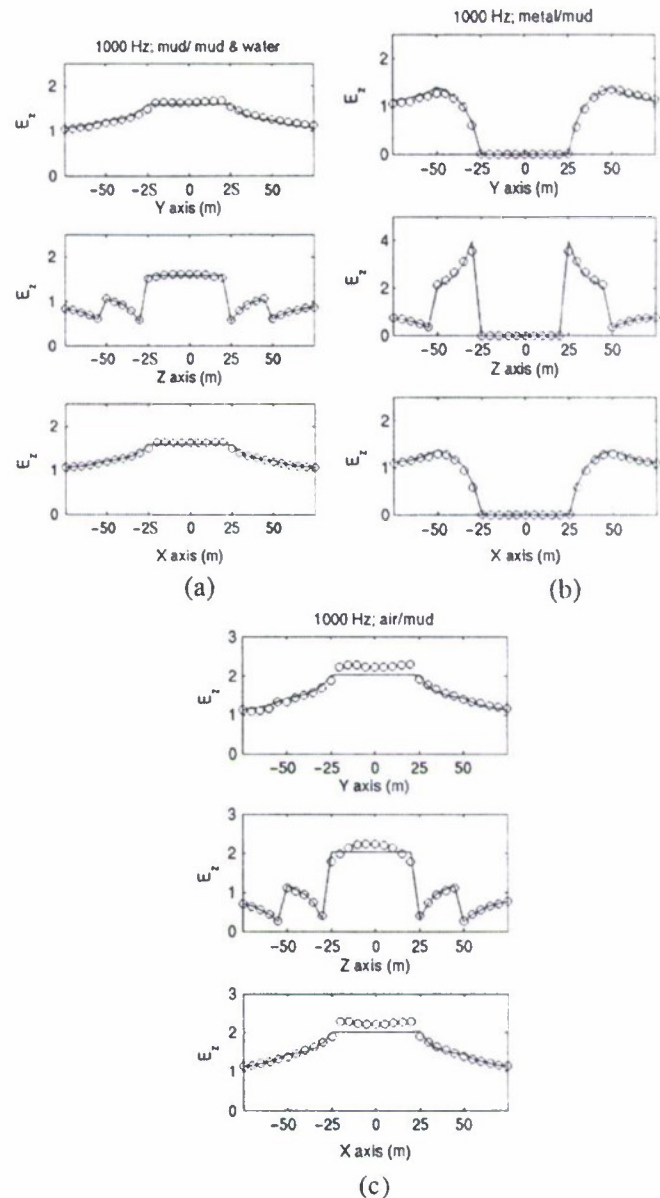

(a)   (b)

(c)

Fig. 3. Comparison of the FDTD values (circles) versus the analytic values (lines) for an incident plane wave at 1 kHz and a layered sphere composed of different media. (a) The inner layer is mud, the outer layer is mud and water. (b) The inner layer is metal, the outer layer is mud. (c) The inner layer is air, the outer layer is mud.
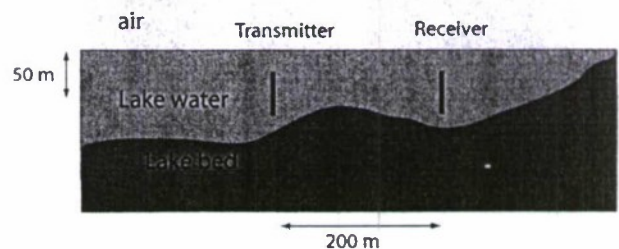

Fig. 4. Two dipoles are submerged in shallow water. One is used as a transmitter and the other as a receiver.
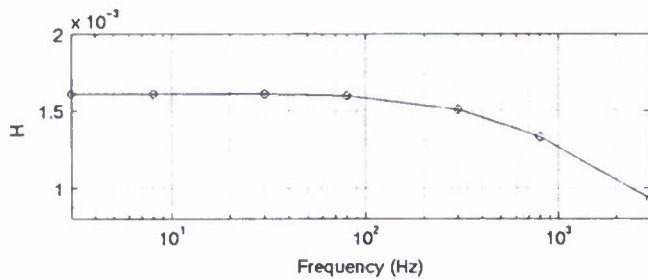
Fig. 5. The transfer function of the two-dipole simulation shown in Fig. 4. The frequency range is 3 Hz to 3 kHz.

matched layer (PML) [9], will be necessary for simulation over long distances.

In this project, it is anticipated that simulation over distances of several kilometers will be required. Some form of near-to-far field transformation will be developed to model the EM sources with relatively high resolution while using lower resolution to model greater distances in the far field.

REFERENCES

[1] J. J. Holmes, *Exploitotion of o Ship's Magnetic Field Signatures.* : Morgan and Claypool Publishers, 2006.
[2] K. S. Yee, "Numerical solution of initial boundary value problems involving Maxwell's equations in isotropic media," *IEEE Trans. Antennos Propag.*, vol. 17, pp. 585–589, 1966.
[3] D. M. Sullivan, *Electromognetic Simulotion Using the FDTD Method.* Piscataway, NJ: IEEE Press, 2000.
[4] D. M. Sullivan, "Exceeding the courant condition with the FDTD method," *IEEE Microw. Guided Wave Lett.*, vol. 6, pp. 289–291, 1996.
[5] D. K. Chen, *Field ond Wave Electromagnetics*, 2nd ed. Reading, PA: Addison-Wesley, 1989.
[6] C. M. Furse, S. P. Mathur, and O. P. Gandhi, "Improvements to the finite-difference time-domain method for calculating the radar cross section of a perfectly conducting target," *IEEE Trans. Microw. Theory Techn.*, vol. 38, no. 7, pp. 919–927, 1990.
[7] C. M. Furse, "Faster than Fourier—Ultra-efficient time-to-frequency domain conversions for FDTD simulations," *IEEE Antennas Propag. Mag.*, vol. 42, no. 6, pp. 24–34, 2000.
[8] R. Harrington, *Time-Hornonic Electromagnetic Fields.* New York: McGraw-Hill, 1961.
[9] J. P. Berenger, "A perfectly matched layer for the absorption of electromagnetic waves," *J. Comp. Phys.*, vol. 114, pp. 185–200, 1994.

FDTD Numerical Tests of the Convolutional—PML at Extremely Low Frequencies

Christopher L. Wagner and Jeffrey L. Young, *Fellow, IEEE*

Abstract—Numerical evaluation of the finite-differencec time-domain (FDTD) convolutional perfectly matched layer (CPML) at extremely low frequencies (ELF) is conducted herein to arrive at acceptable values for the PML parameters. This is accomplished by conducting numerous simulations of an electric dipole in a $60 \times 60 \times 120$ free-space domain and by benchmarking the simulation data against reference data for strategic observation points within the domain. Results show that PML attenuation on the order of 60 to 70 dB can be obtained for 10 to 1000 Hz signals in the quasi-static region of the dipole.

Index Terms—Absorbing boundary condition, finite-difference time-domain (FDTD) methods, perfectly matched layer (PML).

I. INTRODUCTION

I T IS well known in oceanic environments that only extremely low-frequency (ELF) electromagnetic waves will propagate over long distances due to the high conductivity of saltwater. For this reason, such waves are quite useful in communication links, or can be undesirable emissions, as caused by high-powered electric drives on a ship platform. In either case, the propagation characteristics of these waves can be understood from computer finite-difference time-domain (FDTD) simulation, particularly in the littoral region, where the topological and bathymetry features can be geometrically complex. To accomplish such a simulation, a suitable domain truncation technique is needed for both the water and air regions of the domain. Since the ELF signals are naturally attenuated in the water, the perfectly matched layer (PML) development for the air is the most challenging.

Classical PMLs used in FDTD truncation have poor performance at low frequencies and potentially suffer late-time growth [1]–[3]. The complex frequency stretching scheme introduced by Kuzuoglu and Mittra [4] alleviates these problems. The FDTD CPML implementation of [4] was introduced by Roden and Gedney [5] and is evaluated here for ELF performance. For this work, we consider 10 to 1000 Hz to be the ELF band.

II. FORMULATION

A. The FDTD Problem Statement

The FDTD simulations presented herein used 64-bit double precision calculations. All simulations are performed at the Courant stability limit to minimize dispersion error and to advance time as fast as possible. The FDTD code is a cubic cell implementation, with a cell size of 20 m. The medium is free space. The test domain size is $60 \times 60 \times 120$ cells, including the 10-cell-thick PML. The electromagnetic field is excited by a current source that is at node coordinate (30,20,40). A time-differentiated Gaussian waveform is used as the excitation pulse. This pulse has no dc component, so no persistent charge will be deposited into the grid, which would produce undesirably large dc electric fields [6], [7]. The field is quantified at six observation points located at (30,10,80), (30,20,80), (30,30,80), (30,40,80), (30,50,80), and (50,20,40), respectively. The first set of grid numbers is regarded as observation point 1, the second set as observation point 2, etc. Since the free-space wavelength of a 10-Hz signal is 3000 km, it is clear that the observation points are within the quasi-static region of the dipole. Such near-field observations pose significant challenges to FDTD PML development.

Several test cases are considered that are associated with various PML parameters. The efficacy of each PML is obtained by benchmarking the FDTD data against a reference solution, as described next.

B. Reference Free-Space Problem

To provide a reference solution, a large free-space $200 \times 200 \times 260$ domain with perfect electric conductor (PEC) walls is used. The geometry of the source and receiver points is the same as the PML test cases, but the free-space domain is larger than the test case domains by 140 cells in each direction. This reference domain is large enough that the direct signal is fully resolved from the reflections from the walls, so the reflections can be removed by time-gating. The reference problem only needs to run for a few hundred time-steps to obtain a clean direct signal. This type of reference solution includes all FDTD numerical errors, thus allowing us to isolate the effect of the PML induced errors from all others.

C. Signal Processing

To extract the frequency response data from the time-domain data, fast Fourier transforms (FFT) are used [9]. The simulations are conducted using 200 K time steps, which unfortunately does not give sufficient frequency resolution to observe the ELF response. To circumvent this problem, the time-domain data set is extended with zeros to a length sufficient to obtain the lowest frequency needed. For signals that decay to zero (as is the case

with good PMLs), zero extension is proper. For numerical purposes, we define "zero" as less then 10^{-12} relative to the peak value. The zero extended data sets are then transformed with the FFT. The transformed data sets are then used to compute the frequency-domain performance metric. The time-domain and frequency-domain metrics are described next.

D. The Performance Metrics

To measure the performance of the PMLs, an energy metric is used. The energy includes all the field components in the metric. This eliminates the possibility of choosing an especially strong or weak field component at random. We present both time- and frequency-domain metrics. The time-domain metric is broadband, which contains all spectral information contained in the excitation signal. The frequency-domain metrics are narrowband, calculated at selected frequencies of interest.

In the time domain, the residual energy error metric is

$$r = \frac{\sum_t \left(\delta w_e(t) + \delta w_h(t) \right)}{\sum_t \left(w'_e(t) + w'_h(t) \right)}, \tag{1}$$

where $w'_e(t)$ and $w'_h(t)$ are the electric and magnetic energy densities in the time-gated reference signal, and $\delta w_e(t)$, $\delta w_h(t)$ are the residual energy densities associated with the PML. The summations are over the full simulation time. The reference energy electric and magnetic densities are defined as

$$w'_e(t) = \frac{1}{2} \epsilon \mathbf{e}'(t) \cdot \mathbf{e}'(t) \tag{2}$$

and

$$w'_h(t) = \frac{1}{2} \mu \mathbf{h}'(t) \cdot \mathbf{h}'(t) \tag{3}$$

where $\mathbf{e}'(t)$ is the time-gated reference FDTD electric field vector and $\mathbf{h}'(t)$ is the reference FDTD magnetic field vector. The residual electric energy is given by

$$\delta w_e(t) = \frac{1}{2} \epsilon \left(\mathbf{e}(t) - \mathbf{e}'(t) \right) \cdot \left(\mathbf{e}(t) - \mathbf{e}'(t) \right) \tag{4}$$

where $\mathbf{e}$ is the PML FDTD electric field vector. Similarly, the residual magnetic energy is

$$\delta w_h(t) = \frac{1}{2} \mu \left(\mathbf{h}(t) - \mathbf{h}'(t) \right) \cdot \left(\mathbf{h}(t) - \mathbf{h}'(t) \right) \tag{5}$$

where again the primed vector is the reference solution and the unprimed vector is the PML FDTD solution.

In the frequency domain, the residual energy error metric at angular frequency ω is

$$R(\omega) = \frac{\delta W_E(\omega) + \delta W_H(\omega)}{W'_E(\omega) + W'_H(\omega)} \tag{6}$$

where the residual and reference energies are defined in a manner similar to the time-domain case.

E. The PMLs

In the frequency domain, the CPML tensor coefficient as given by Kuzuoglu [4] is

$$s_i = \kappa_i + \sigma_i / (\alpha_i + j\omega\epsilon_o), \quad i = x, y, z. \tag{7}$$
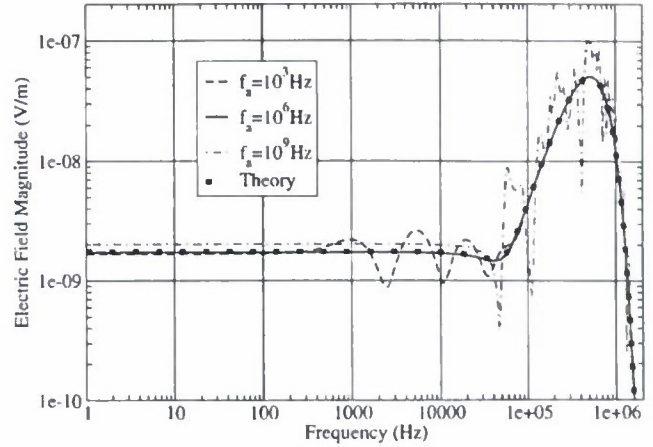

Fig. 1. Hertzian dipole field at observation point 1 for several different PMLs with $\kappa = 1$. The rapid fall-off of amplitude after 1 MHz is due to the limited bandwidth of the source current waveform.

The real coordinate stretch κ, conductivity σ, complex frequency stretch α, and their polynomial scaling characterize the PML.

The test PMLs are 10 cells thick, with the parameters having polynomial scaling. The conductivity σ and coordinate stretch κ use a fourth-order scaling polynomial, while the complex frequency stretch α uses third-order. As is usual with the CPML, the scaling polynomial for the conductivity and real coordinate stretch increases into the PML, while the complex frequency stretch polynomial decreases into to PML. The maximum conductivity is set according to the optimum [8] given by

$$\sigma_{\text{opt}} = \frac{m + 1}{150\pi\sqrt{\varepsilon_r}\Delta_x} \tag{8}$$

where m is the polynomial order, Δ_x is the space grid size, and ε_r is the relative dielectric constant. The maximum complex frequency stretch α is set by

$$\alpha_{\text{max}} = 2\pi\varepsilon_0 f_a \tag{9}$$

where f_a is the CPML break frequency.

The problem is to find ranges for the parameters f_a and κ that provide good performance at ELF. This can only be done empirically. Representative test cases are provided next to demonstrate this empirical process.

III. RESULTS

To validate the simulations, the exact Hertzian dipole, frequency-domain solution is compared to the transformed FDTD simulation data in Fig. 1. The field is observed at point 1. When f_a is small, the low-frequency performance of the PML is poor. Likewise, when f_a is excessively large, the PML performs poorly at high frequencies. A PML with a reasonable value of the break frequency provides a simulation that closely matches the theoretical prediction over the full excited frequency band. We have found empirically that $f_a \approx 1$ MHz seems optimum for ELF simulations. This conclusion is also valid when the field is observed at other strategic observation points, i.e. 2, 3, 4, 5, and 6.
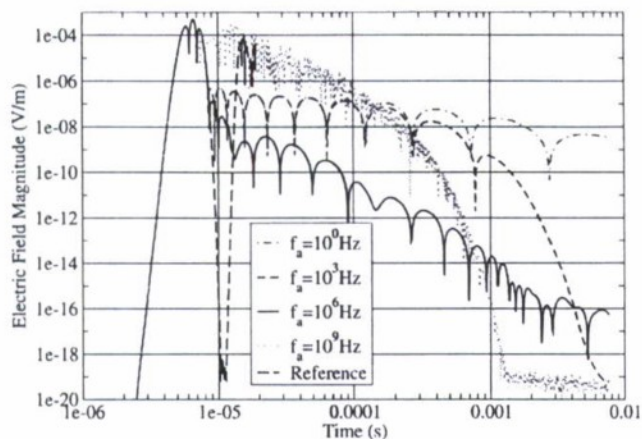
Fig. 2. Time-domain results at observation point 1 for $\kappa = 1$. For times less than about 8e-6 s, the direct signal is seen. After the direct pulse has passed by the sample point, various levels of residual fields are seen.
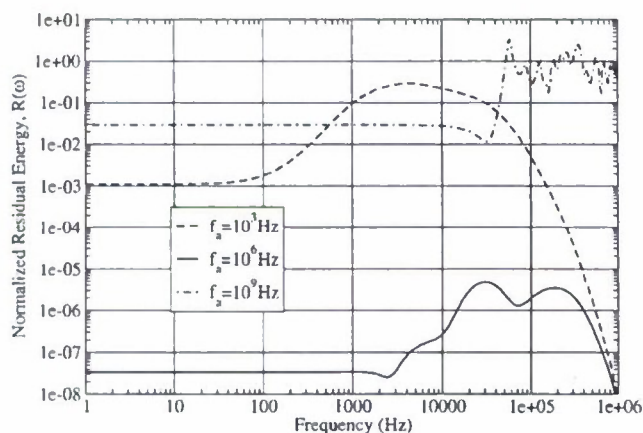

Fig. 3. Normalized PML frequency response at observation point 1 for $\kappa = 1$. Lower amplitudes are better performing PMLs.
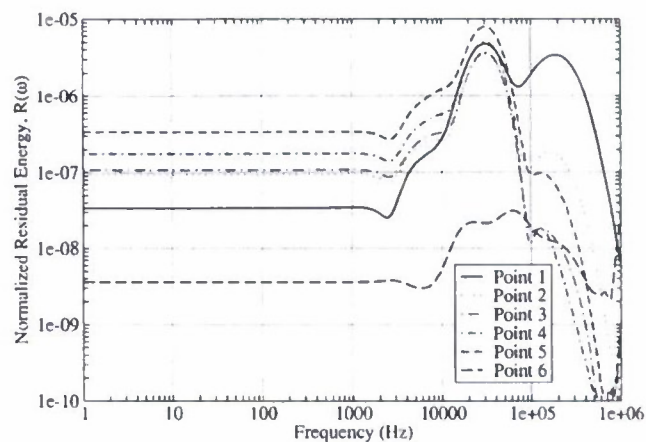

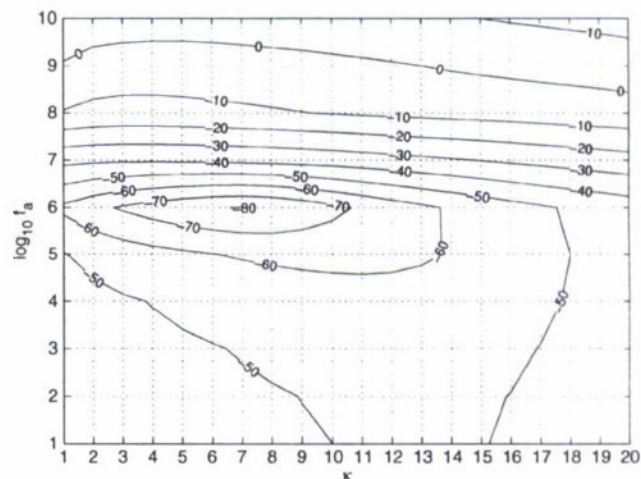Fig. 4. PML frequency response for $f_a = 10^6$ Hz and $\kappa = 1$ for the six observation points.

Fig. 5. Time-domain PML residual energy error metric at observation point 1 for various values of the real coordinate stretch κ and the break frequency f_a. FDTD simulations are performed at each grid-line intersection.

See Fig. 2 for the time-domain performance of four test and the reference simulations. The reference simulation shows the direct signal clearly separated from the reflected signals, the latter of which can be removed by time-gating, as noted previously. With $f_a = 1$ Hz, there is slow long-term decay. (In some simulations, when $f_a = 0$, slow growth has even been reported [3].) As f_a is increased to the optimum, the absorption increases relative to the $f_a = 1$ Hz case. As f_a is increased further, the absorption degrades, but still with good late-time fall-off.

In Fig. 3, the frequency-domain residual energy error metric as computed by (6) is shown for observation point 1. In this plot, a better PML will have a lower response. The PML is tested with various break frequencies f_a, each with $\kappa = 1$. With f_a too large or small, there is poor PML absorption. As can be seen in both the time-domain and frequency-domain plots, there is an optimum value for the break frequency for ELF simulations. For the tests performed here, $f_a \approx 1$ MHz provides the best PML absorption at ELF with a relative error on the order of 0.02%.

There is up to a factor of 100 variation in error in PML absorption across the six sample points, as shown in Fig. 4. Surprisingly, sample point 1 has better ELF performance than sample point 5. From a wave perspective, sample point 1 is the grazing incidence case; however, given that the fields are quasi-static,

grazing incidence has no real meaning. Clearly from Figs. 3 and 4, good choices of parameters provide better than 70 dB of PML absorption over the ELF band at favorable observation locations and more than 60 dB attenuation in unfavorable locations.

A. Time-Domain (Broadband) Performance

Figs. 5 and 6 show the time-domain contours of $10\log_{10} r$ as κ varies from 1 to 20 and as f_a varies from 1 to 10^{10} Hz for observation points 1 and 5, respectively. There is variation in the location and depth of the global minimum across the six observation points. However, with $f_a \approx 1$ MHz and $3 \lesssim \kappa \lesssim 8$, the PML provides -70 dB or better performance at all six observation locations.

B. Frequency-Domain (Narrowband) Performance

Figs. 7–9 show the frequency-domain PML performance at 100 Hz, 10 kHz, and 1 MHz, respectively. The 1 Hz to 1 kHz optima vary widely with κ, f_a, and observation position. For some specific test locations, frequencies, and PML parameters, there are very deep minima on the order of -120 dB in some cases. Because the location and parameters of these minima do
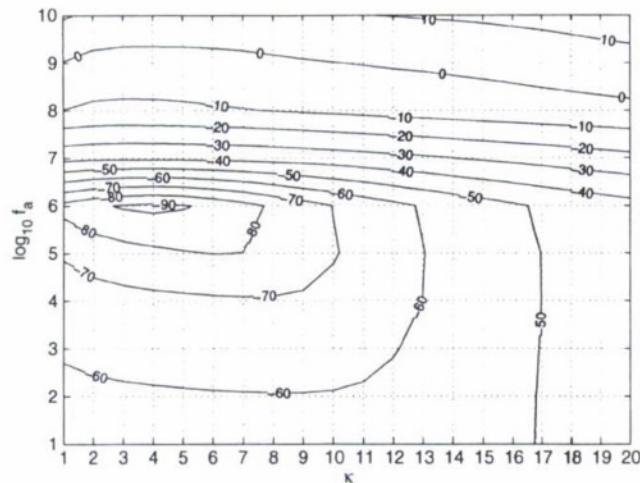
Fig. 6. Time-domain PML residual energy error metric at observation point 5.

Fig. 8. 10-kHz frequency-domain PML residual energy error metric at observation point 1.
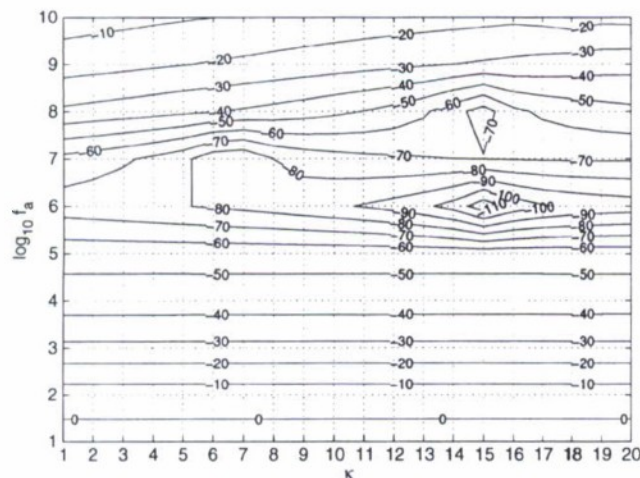

Fig. 7. 100-Hz frequency-domain PML residual energy error metric at observation point 1. At the same observation point, the 1 to 100 Hz results look essentially identical.
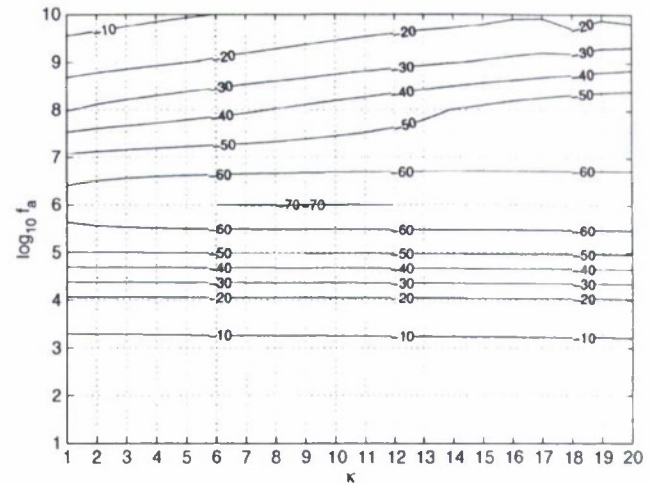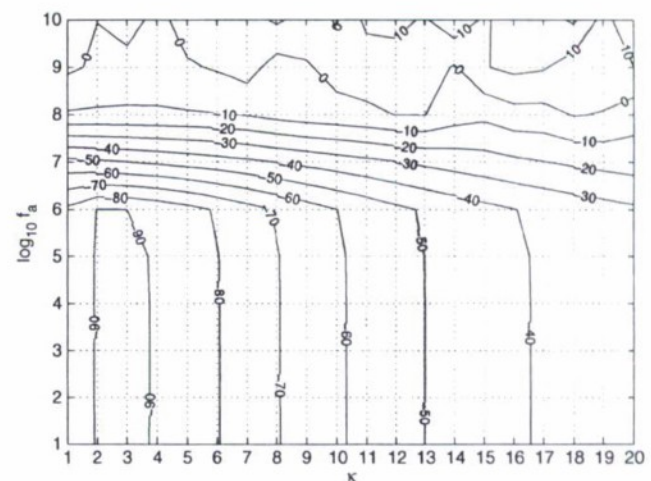

Fig. 9. 1-MHz frequency-domain PML residual energy error metric at observation point 1.

not vary in a regular way, it is important to select operating conditions for the PML based on the performance at several observation locations. For example, at 10 Hz, 100 Hz, and 1 kHz, $f_a \approx 10^6$ Hz with $1 \leq \kappa \leq 20$ provides -60 dB or better PML performance at all six observation points. If $18 \leq \kappa \leq 20$, then the PML provides -70 dB or better performance at all six observation points. Apparently, the narrowband metrics at ELF are improved with larger values of κ as compared to the wideband time-domain metric. Fig. 9 shows that at 1 MHz, smaller values for κ provide the best PML absorption. The optimum PML parameters depend on the metric used and on the frequencies of interest.

IV. CONCLUSION

For ELF PML development, our empirical research shows that when $f_a \approx 1$ MHz, $\kappa \approx 6$, $\sigma = \sigma_{\text{opt}}$, fourth-order polynomials for σ and κ are invoked, and a third-order polynomial for α is invoked, then at least 60 dB of PML attenuation is obtained in the quasi-static region (i.e. very near-field) of the dipole, for both the wideband and ELF narrowband metrics. This is more than adequate for high-quality FDTD simulations in the ELF band.

REFERENCES

[1] S. Abarbanel and D. Gottlieb, "A mathematical analysis of the PML method," *J. Comput. Phys.*, vol. 134, pp. 357–363, 1997.
[2] F. L. Teixeira and W. C. Chew, "Perfectly matched layer in cylindrical coordinates," *IEEE Trans. Geosci. Remote Sens.*, vol. 38, no. 4, pp. 1530–1543, Jul. 2000.
[3] E. Bécache, P. G. Petropoulos, and S. D. Gedney, "On the long-time behavior of unsplit perfectly matched layers," *IEEE Trans. Antennas Propag.*, vol. 52, no. 5, pp. 1335–1342, May 2004.
[4] M. Kuzuoglu and R. Mittra, "Frequency dependence of the constitutive parameters of causal perfectly matched anisotropic absorbers," *IEEE Microw. Guided Wave Lett.*, vol. 6, no. 12, pp. 447–449, Dec. 1996.
[5] J. A. Roden and S. D. Gedney, "Convolution PML (CPML): An efficient FDTD implementation of the CFS-PML for arbitrary media," *Microw. Opt. Technol. Lett.*, vol. 27, no. 5, pp. 334–339, Dec. 2000.
[6] C. L. Wagner and J. B. Schneider, "Divergent fields, charge, and capacitance in FDTD simulations," *IEEE Trans. Microw. Theory Tech.*, vol. 46, no. 12, pp. 2131–2136, Dec. 1998.
[7] C. M. Furse, D. H. Roper, D. N. Buechler, D. A. Christensen, and C. H. Durney, "The problem and treatment of DC offsets in FDTD simulations," *IEEE Trans. Antennas Propag.*, vol. 48, no. 8, pp. 1198–1201, Aug. 2000.
[8] A. Taflove and S. Hagness, *Computational Electrodynamics: The Finite-Difference Time-Domain Method*, 3rd ed. Norwood, MA: Artech House, 2005.
[9] M. Frigo and S. G. Johnson, "The design and implementation of FFTW3," *Proc. IEEE*, vol. 93, no. 2, pp. 216–231, 2005.

A Simple Up-over-and-down Model for Low Frequency Horizontal Electric Dipole Propagation Near An Interface

Robert G. Olsen, *Fellow, IEEE*, and Zhi Li, *Student Member, IEEE*

Abstract—The propagation of electromagnetic fields from an electric or magnetic dipole near an interface has been described mathematically for many years using Sommerfeld integrals. In the high frequency case for which the dipole and field point are buried in the lower (and much lossier) medium, simple approximations have been derived that can be interpreted as up-over-and-down propagation (i.e., plane wave from source to the surface – surface wave to a point above the field point – plane wave to the field point). In this paper, a simple expression valid for the low frequency case (i.e., relevant dimensions in the upper medium are electrically small) is derived. In this case the up-over-and-down propagation is described as near field propagation from source to the surface, quasi-static propagation along the interface to above the field point and plane wave propagation to the field point.

Index Terms—Electromagnetic fields, electromagnetic propagation, extremely low frequency.

I. INTRODUCTION

THE electric (E) and magnetic (H) fields due to a dipole (vertical or horizontal, electric or magnetic) buried in a conducting half-space have been well studied for decades and can be written in terms of Sommerfeld integrals [1] – [4]. When the dipole and the observation point are both in the conducting medium close to the interface relative to their horizontal spacing and the frequency is "low", it is possible to interpret the propagation mechanism as a simple up-over-and-down process. Here, up-over-and-down means that the field propagates vertically up crossing the interface to the free space medium, then propagates horizontally along the interface, and finally propagates vertically down to the observation point. While this behavior is somewhat similar to the high frequency phenomenon observed by previous authors, it is also different because the fields in the free space region are quasi-static [5].

The formulas for the fields given by Sommerfeld integrals are, while exact, very complicated. In this paper, the integrals are simplified by using some reasonable assumptions given the range of parameters of interest. Then a set of simple but very

good approximations to the electric and magnetic fields are obtained. Based on these approximations, the up-over-and-down behavior is observed and discussed. The dipole source here is chosen to be a horizontal electric dipole (HED). The HED was selected because, using achievable dipole moments and commonly available receiving equipment, it can be shown that the HED fields are detectable at larger distances than those of other dipole types (i.e., vertical electric dipole (VED) or vertical (VMD) or horizontal (HMD) magnetic dipoles). To be more specified, it was assumed from this study that the maximum dipole moments for electric and magnetic dipoles are 50 A-m and 2500 A-m^2 respectively and that the minimum detectable electric and magnetic fields are $1\mu V/m$ and $40\mu A/m$ respectively. Using these values, the horizontal electric field component that is perpendicular to the HED direction can be detected to a distance of 800 meters to the source. No other field component from any other dipole can be detected beyond about 200 meters.

II. GEOMETRY

The geometry of the model is shown in Fig. 1. A 'y' oriented HED, which has a dipole moment of Idl, is on the 'z' axis and buried 'h' meters below the surface in a conducting half-space ($z < 0$). The upper half space (i.e., $z > 0$) is assumed to be free space.
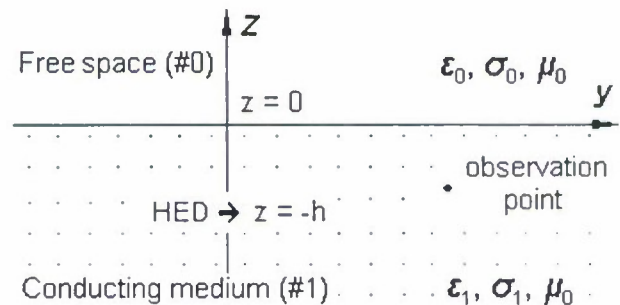

Fig. 1. Geometry of the model

As noted in the figure, ε_i and σ_i are the permittivity and conductivity of the ith half space ($i = 0$ and 1 for free space and conductor, respectively). $\varepsilon_i = \varepsilon_{ri}\varepsilon_0$, where ε_{ri} is the relative permittivity and ε_0 is the permittivity of free space. It is assumed that all materials have the permeability of free space μ_0. The cylindrical coordinate system (ρ, φ, z) is used in this

paper, where $x = \rho\cos\varphi$ and $y = \rho\sin\varphi$.

III. SOMMERFELD INTEGRAL METHOD

The Sommerfeld integral method will be very briefly introduced here. This method uses the integral representations of vector potentials to determine the E and H fields. To find the E and H fields due to the HED, two non-zero components of vector potential are required [6, 7]. Here, the y and z components of the magnetic vector potential, A_y and A_z, are chosen.

$$A_y^0 = K_1 \int_0^\infty f_1(\lambda)e^{-u_0 z} \lambda J_0(\lambda\rho)d\lambda \quad (z \geq 0) \qquad (1)$$

$$A_y^1 = K_1 \frac{e^{-jk_1 R}}{R} + K_1 \int_0^\infty f_2(\lambda)e^{u_1 z} \lambda J_0(\lambda\rho)d\lambda$$
$$\qquad\qquad\qquad\qquad\qquad\qquad\qquad (2)$$
$$= K_1 \frac{e^{-jk_1 R}}{R} + K_1 I_{y1} \quad (z \leq 0)$$

$$A_z^0 = K_1 \frac{\partial}{\partial y} \int_0^\infty g_1(\lambda)e^{-u_0 z} \lambda J_0(\lambda\rho)d\lambda \quad (z \geq 0) \quad (3)$$

$$A_z^1 = K_1 \frac{\partial}{\partial y} \int_0^\infty g_2(\lambda)e^{u_1 z} \lambda J_0(\lambda\rho)d\lambda$$
$$\qquad\qquad\qquad\qquad\qquad\qquad\qquad (4)$$
$$= K_1 \frac{\partial}{\partial y} I_{z1} \quad (z \leq 0)$$

where $J_0(\lambda\rho)$ is the Bessel function of the first kind of order zero and

$$k_i^2 = \omega^2 \mu_0 \varepsilon_i' = \omega^2 \mu_0 (\varepsilon_i - j\frac{\sigma_i}{\omega})$$

$$u_i = \sqrt{(\lambda^2 - k_i^2)}$$

$$K_1 = \frac{\mu_0 Idl}{4\pi}$$

$\varepsilon_i' = \varepsilon_i - j\sigma_i/\omega$ is the complex permittivity of the ith half space ($i = 0$ or 1), k_i is the wave number where $\text{Re}(k_i) \geq 0$ and $\text{Re}(u_i) \geq 0$ defines the proper Reimann sheet of the complex plane. The first term in (2) is the source term and $R = (\rho^2 + z^2)^{1/2}$ is the distance from the dipole to the observation point. I_{y1} and I_{z1} represent the integral terms in (2) and (4), respectively. The source term $K_1 \dfrac{e^{-jk_1 R}}{R}$ in A_y^1 is the vector potential of the dipole itself in an infinite homogeneous conducting medium. It can be written in integral form as

$$\frac{e^{-jk_1 R}}{R} = \begin{cases} \int_0^\infty u_1^{-1} e^{-u_1(z+h)} \lambda J_0(\lambda\rho)d\lambda & (z+h) \geq 0 \\ \int_0^\infty u_1^{-1} e^{u_1(z+h)} \lambda J_0(\lambda\rho)d\lambda & (z+h) \leq 0 \end{cases} \quad (5)$$

Functions f_1, f_2, g_1 and g_2 are arbitrary coefficient functions of the integration variable λ. They are determined by matching the boundary conditions at $z = 0$. Given the vector potentials A_y and A_z the E and H field can be obtained from:

$$E_x = -\frac{j}{\omega\mu\varepsilon} \cdot \frac{\partial}{\partial x}(\frac{\partial A_y}{\partial y} + \frac{\partial A_z}{\partial z}) \qquad (6)$$

$$E_y = -\frac{j}{\omega\mu\varepsilon} \cdot \left[\frac{\partial}{\partial y}(\frac{\partial A_y}{\partial y} + \frac{\partial A_z}{\partial z}) + k^2 A_y \right] \qquad (7)$$

$$E_z = -\frac{j}{\omega\mu\varepsilon} \cdot \left[\frac{\partial}{\partial z}(\frac{\partial A_y}{\partial y} + \frac{\partial A_z}{\partial z}) + k^2 A_z \right] \qquad (8)$$

$$H_x = \frac{1}{\mu}(\frac{\partial A_z}{\partial y} - \frac{\partial A_y}{\partial z}) \qquad (9)$$

$$H_y = -\frac{1}{\mu} \frac{\partial A_z}{\partial x} \qquad (10)$$

$$H_z = \frac{1}{\mu} \frac{\partial A_y}{\partial x} \qquad (11)$$

By matching boundary conditions, i.e., the tangential components of E and H fields are continuous cross the $z = 0$ plane, the coefficient functions can be determined as

$$f_1 = \frac{2e^{-u_1 h}}{u_0 + u_1} \qquad (12)$$

$$f_2 = \frac{(u_1 - u_0)e^{-u_1 h}}{u_1 \cdot (u_0 + u_1)} \qquad (13)$$

$$g_1 = g_2 = \frac{2(\varepsilon_1' - \varepsilon_0')e^{-u_1 h}}{(u_0 + u_1)(\varepsilon_1' u_0 + \varepsilon_0' u_1)} \qquad (14)$$

The E and H fields in the conducting medium can be formulated by inserting (2), (4), (13) and (14) into (6) ~ (11).

IV. SIMPLIFICATION OF THE INTEGRAL FOR A_z^1

The objective of this paper is to derive simple but acceptable approximations for the fields, which can be interpreted to provide good insight into the physical behavior of the wave propagating from source to receiver. One fundamental problem with evaluating the integrals shown in (1) to (4) is that, for large values of ρ compared to h and z, the rapid oscillations of the Bessel function cause difficulties with the numerical integration. To remedy this problem, the contours of integration will be deformed in the complex plane so that the integrand decays exponentially for large values of ρ. This transformation will also allow other simplifying approximations that will lead to a simple interpretation of the final result.

A. Deformation of The Integral Contour

If (14) is inserted into the integral portion of (4) and the exponential term is removed from $g_2(\lambda)$, this integral becomes

$$I_{z1} = \int_0^\infty g_2'(\lambda)e^{u_1(z-h)} \lambda J_0(\lambda\rho)d\lambda \qquad (15)$$

where

$$g_2'(\lambda) = \frac{2(\varepsilon_1' - \varepsilon_0')}{(u_0 + u_1)(\varepsilon_1' u_0 + \varepsilon_0' u_1)} \qquad (16)$$

Using the identities

$$J_0(x) = \frac{1}{2}\left[H_0^{(1)}(x) + H_0^{(2)}(x)\right]$$

$$H_0^{(1)}(-x) = -H_0^{(2)}(x)$$

where $H_0^{(1)}(x)$ and $H_0^{(2)}(x)$ are the Hankel functions of the first and second kind of order zero, respectively, the integral range in (15) can be expanded to (-∞, +∞). Since u_0, u_1, and $g_2'(\lambda)$ are all even functions of λ

$$I_{z1} = \frac{1}{2}\int_{-\infty}^{+\infty} g_2'(\lambda)e^{u_1(z-h)}\lambda H_0^{(2)}(\lambda\rho)d\lambda \qquad (17)$$

For the function $g_2'(\lambda)$, there is one pole, λ_p, and two branch points, k_0 and k_1, in the complex λ plane. The branch cuts are selected to be vertical lines from the branch points to negative infinity. Then the integral contour in (17) can be deformed into a contour C_B which is illustrated with the dashed line in Fig. 2.
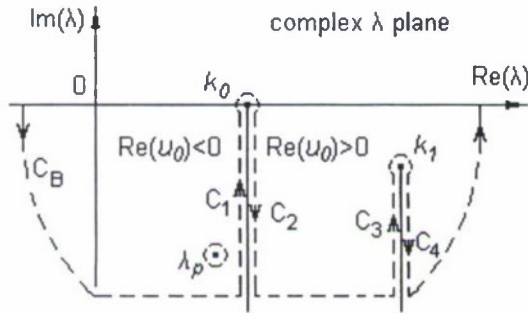

Fig. 2. Deformation of the integral contour.

With this deformation and the fact that the Hankel function goes to zero exponentially along the infinite semi-circle, the integral along the real axis is converted to the residue of the pole, R_{λ_p}, plus the integrations along $C_1 \rightarrow C_4$, which encompass the two branch cuts. Thus

$$I_{z1} = \frac{1}{2}\int_{C_1+C_2+C_3+C_4} g_2'(\lambda)e^{u_1(z-h)}\lambda H_0^{(2)}(\lambda\rho)d\lambda + R_{\lambda_p}$$

For $|k_1| \gg |k_0|$, the integral along the branch cut of k_1 is much smaller than that of k_0 and can be ignored. Note that, in the complex plane, the sign of u_0 will change when crossing the branch cut associated with k_0. Given the choice of branch cut, $Re(u_0)<0$ and $Re(u_0)>0$ on the left and right sides, respectively, as shown in Fig. 2. In addition while the pole is in the proximity of the branch cut integration and is evident in the integrand, its contribution to the integral is negligible for the low frequencies considered here. Thus the pole residue can be ignored. Therefore

$$I_{z1} \approx \frac{1}{2}\int_{C_1+C_2} g_2'(\lambda)e^{u_1(z-h)}\lambda H_0^{(2)}(\lambda\rho)d\lambda \qquad (18)$$

It has been shown that (18) is valid when $h, z \ll \rho$, $|k_1| \gg |k_0|$ and $|k_1\rho| \gg 1$.

The parameters and their values / value ranges used for the simulations are listed in Table 1. The conductivity and permittivity of the lower medium represent typical lake water. They will also be used for all the following simulations in this paper.

	Free space	Conducting medium *
Relative permittivity, ε_{rt} ($\varepsilon_t = \varepsilon_{rt}\varepsilon_0$)	1	1
Conductivity, σ (S/m)	0	0.018
Permeability, μ (H/m)	$4\pi\times10^{-7}$	$4\pi\times10^{-7}$
Dipole depth, h (m)	20	
z (m)	-10	
Horizontal distance, ρ (m)	100 - 10000	
Dipole moment, Idl (A-m)	1	
Frequency, f (Hz)	100 - 3000	

B. Simplification of The Integrand

Since for $\rho \gg |h|, |z|$, the decay of the integrand along C_1 and C_2 is controlled by the value of $|\lambda\rho|$, the integral can be truncated at $|\lambda\rho|=10$ and since we assume $|\lambda\rho| \gg 1$

$$u_1 = (\lambda^2 - k_1^2)^{1/2} \approx jk_1 \qquad (19)$$

With (19) the exponential term in (18) can be extracted from the integral, which leads to

$$I_{z1} \approx \frac{e^{jk_1(z-h)}}{2}\int_{C_1+C_2} g_2'(\lambda)\lambda H_0^{(2)}(\lambda\rho)d\lambda \qquad (20)$$

Further since $|k_0\rho| \ll 1$ (i.e., quasi-static for $z>0$), it is reasonable to assume that

$$u_0 = \pm(\lambda^2 - k_0^2)^{1/2} \approx \pm\lambda \qquad (21)$$

because $|k_0|$ is very small compared to $|\lambda|$ over the largest portion of the integral. The approximations have been made here can be summarized as

$$\rho \gg |h|, |z|$$
$$|k_0\rho| \ll 1$$
$$|k_1\rho| \ll 1$$

Now, if the approximations (19), (21) and $|\varepsilon'_1| \gg |\varepsilon'_0|$ are made in (16) then

$$g_2'(\lambda) \approx \frac{2(\varepsilon'_1)}{(\pm\lambda + jk_1)(\pm\varepsilon'_1\lambda)} = \frac{2}{\lambda^2 \pm jk_1\lambda}.$$

If $g_2'^{(+)}(\lambda) = \frac{2}{\lambda^2 + jk_1\lambda}$ and $g_2'^{(-)}(\lambda) = \frac{2}{\lambda^2 - jk_1\lambda}$, represent $g_2'(\lambda)$ on the right side and left side of the branch cut of k_0, respectively, then the integral in (20) can be approximated as

$$I_{z1}' \approx \int_{C_1} \frac{2}{\lambda - jk_1} H_0^{(2)}(\lambda\rho)d\lambda + \int_{C_2} \frac{2}{\lambda + jk_1} H_0^{(2)}(\lambda\rho)d\lambda \qquad (22)$$

Using the asymptotic approximation

$$H_0^{(2)}(\lambda\rho) \approx \sqrt{\frac{2j}{\pi\lambda\rho}} \cdot e^{-j\lambda\rho}$$ for large $|\lambda\rho|$ (i.e., most of the integral)

$$I'_{z1} \approx 2\sqrt{\frac{2j}{\pi\rho}}\left\{\int_{l_1}\frac{e^{-j\lambda\rho}}{\sqrt{\lambda}\left(\lambda-jk_1\right)}d\lambda \right.$$

$$\left. +\int_{l_2}\frac{e^{-j\lambda\rho}}{\sqrt{\lambda}\left(\lambda+jk_1\right)}d\lambda\right\} \tag{23}$$

Letting $\lambda = k_0 - js$, and changing the integral variable from λ to s, I'_{z1} finally becomes

$$I'_{z1} \approx 2\sqrt{\frac{2j}{\pi\rho}}\cdot e^{-jk_0\rho}\left\{\int_0^\infty \frac{je^{-\rho s}ds}{\sqrt{k_0-js}\left(k_0-js-jk_1\right)}\right.$$

$$\left. -\int_0^\infty \frac{je^{-\rho s}ds}{\sqrt{k_0-js}\left(k_0-js+jk_1\right)}\right\} \tag{24}$$

Ignoring k_0 in both the denominators of the two integrands, which is reasonable because $|k_0|$ is very small compared to $|s|$ over most of the integral, I'_{z1} reduces to

$$I'_{z1} \approx -2j\sqrt{\frac{2}{\pi\rho}}\cdot e^{-jk_0\rho}\left(I_1-I_2\right) \tag{25}$$

where $I_1 = \int_0^\infty \frac{e^{-\rho s}}{\sqrt{s}\left(s+k_1\right)}ds$ and $I_2 = \int_0^\infty \frac{e^{-\rho s}}{\sqrt{s}\left(s-k_1\right)}ds$.

Therefore, the calculation of the complicated integral in (18) is reduced to the problem of evaluating the two relatively simple integrals in (25). I_1 can be analytically evaluated as [8]

$$I_1 = \sqrt{\frac{2\pi}{k_1}}\cdot D_{-1}\left(\sqrt{2k_1\rho}\right)e^{\frac{k_1\rho}{2}}$$

where $D_{-1}\left(\sqrt{2k_1\rho}\right)$ is the parabolic cylinder function of argument $\sqrt{2k_1\rho}$ with

$$D_{-1}\left(\sqrt{2k_1\rho}\right) = \sqrt{\frac{\pi}{2}}\left[1-\Phi(\sqrt{k_1\rho})\right]e^{\frac{k_1\rho}{2}}$$

The second term in the bracket, $\Phi(\sqrt{k_1\rho})$, is the probability integral, which has the asymptotic approximation for $|k_1\rho|>>1$:

$$\Phi(\sqrt{k_1\rho}) \approx 1-\frac{1}{\sqrt{\pi}}\cdot\frac{e^{-k_1\rho}}{\sqrt{k_1\rho}}$$

Using this result in I_1, results in

$$I_1 \approx \sqrt{\pi}/\left(k_1\sqrt{\rho}\right)$$

Similarly for I_2

$$I_2 \approx -\sqrt{\pi}/\left(k_1\sqrt{\rho}\right).$$

Therefore, the integral in (25) is

$$I'_{z1} \approx -4\sqrt{2}j\frac{e^{-jk_0\rho}}{k_1\rho}$$

The integral I_{z1} then can be approximated as

$$I_{z1} \approx -2\sqrt{2}je^{jk_1(z-h)}\cdot\frac{e^{-jk_0\rho}}{k_1\rho} \tag{26}$$

It can be shown that (26) is approximately a factor of 1.4 larger than the exact result in (15) and that this difference is relatively stable over a wide range of parameters. Given this

and the fact that an attempt to find a missing $\sqrt{2}$ factor did not succeed, a further study of the approximation used to derive (26) was carried out. This study indicated that the dominant part of the error resulted from the replacement of the Hankel function by its asymptotic expansion. Given this, a correction term can be written as

$$I_C \; \square \; 2e^{-jk_0\rho}\int_0^B\left[\frac{1}{s-k_1}-\frac{1}{s+k_1}\right]$$

$$\times\left[H_0^{(2)}(-j\rho s)e^{jk_0\rho}-\sqrt{\frac{-2}{\pi\rho s}}e^{-\rho s}\right]ds \tag{27}$$

Clearly most of the contribution to this integral comes from small values of ρs. Thus the integral is (somewhat arbitrarily) truncated at $\rho s = B = 0.3$ and the Hankel function is replaced by its small argument expansion. Given this, the correction term is written as

$$I_C \approx 2e^{-jk_0\rho}\int_0^M\left[\frac{1}{s-k_1}-\frac{1}{s+k_1}\right]$$

$$\times\left[1-\frac{2j}{\pi}\ln\left(\frac{-j1.781\rho s}{2}\right)-\sqrt{\frac{-2}{\pi\rho s}}\right]ds \tag{28}$$

where inside the integral $e^{jk_0\rho}\;\square\;e^{-\rho s}\;\square\;1$ and $M = B/\rho$. The integral in (28) can be analytically evaluated and the result is

$$I_C \approx I_{C1}+I_{C2}+I_{C3} \tag{29}$$

where

$$I_{C1} = c\cdot\ln\left(\frac{k_1-B}{k_1+B}\right)e^{-jk_0\rho}$$

$$I_{C2} = -\frac{8jB}{\pi k_1}e^{-jk_0\rho}$$

$$I_{C3} = 2je^{-jk_0\rho}\sqrt{\frac{-2}{\pi k_1\rho}}\left[\ln\left(\frac{k_1-B+2j\sqrt{k_1B}}{k_1+B}\right)\right.$$

$$\left. +j\ln\left(\frac{k_1+B-2j\sqrt{-k_1B}}{k_1-B}\right)\right]$$

$$c = 2\left[1-\frac{2j}{\pi}\ln\left(\frac{-j1.781B\rho}{2}\right)\right].$$

I_{C1} and I_{C3} can be further simplified by expanding the natural logarithm function in Taylor series.

$$I_{C1} \approx -2c\frac{M}{k_1\rho}e^{-jk_0\rho} \text{ and } I_{C3} \approx 8\sqrt{\frac{2}{\pi M}}\frac{jM}{k_1\rho}e^{-jk_0\rho}$$

The correction term is then rewritten as

$$I_C \approx \frac{jN}{k_1\rho}e^{-jk_0\rho} \tag{30}$$

where $N = M\left[-2c-\frac{8}{\pi}+8\sqrt{\frac{2}{\pi M}}\right]$ is a constant. It is interesting to note that the functional dependence of (30) is identical to that of (26). Hence adding (30) to (26) results in

$$I_{z1} \approx \frac{e^{jk_1(z-h)}}{2} \cdot \frac{je^{-jk_0\rho}}{k_1\rho}\left[-4\sqrt{2} + N\right] \qquad (31)$$

which is identical to (26) except for the constant and that this constant is approximately $1/1.4$ times the constant in (26) when $M = 0.3$ (i.e., $N \approx 1.72$). Then (31) becomes

$$I_{z1} \approx -2je^{jk_1(z-h)} \cdot \frac{e^{-jk_0\rho}}{k_1\rho} \qquad (32)$$

When $h, z \ll \rho$, $|k_1| \gg |k_0|$ and $|k_1\rho| \gg 1$, (32) approximates the exact integral very well. These conditions are roughly mapped to the following range of parameters: $h, z < 100$m, 100Hz $< f <$ 3000Hz, 500m $< \rho < 10000$m and 0.001S/m $< \sigma < 100$S/m. The error of (32) compared to the exact integral of I_{z1} in (15) is less than 10% when 100Hz $< f < 3000$Hz and 500m $< \rho < 10000$m. Fig. 3 shows the comparisons of magnitude and phase angle between the approximation in (32) and the exact integral in (15), with dipole frequency of 1000Hz.
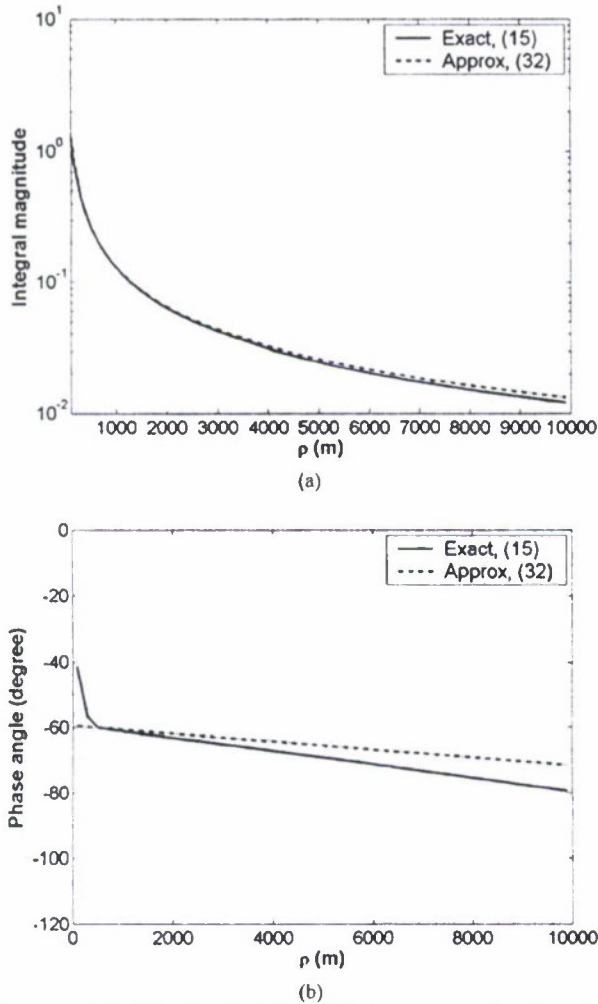

(a)

(b)

Fig. 3. Exact integral of I_{z1} vs. approximation, $f = 1000$Hz: (a) magnitude, (b) phase angle.

This analysis is helpful for understanding the error incurred during the derivation of the approximation for (15). Further, the correction term significantly reduces the error and can be easily calculated. It is shown in (32) and can be used to derive simple

results for the E and H fields. Therefore, (32) will be used as the approximation of I_{z1}.

V. SIMPLIFICATION OF THE INTEGRAL FOR A_y^1

If the exponential term is pulled out from $f_2(\lambda)$, I_{y1} of (2) can be rewritten as

$$I_{y1} = \int_0^\infty f_2'(\lambda)e^{u_1(z-h)}\lambda J_0(\lambda\rho)d\lambda \qquad (33)$$

where $f_2'(\lambda) = \frac{u_1 - u_0}{u_1 \cdot (u_0 + u_1)}$.

At this point, the strategy for simplifying I_{y1} is the same as that used for I_{z1}. First, the integral contour is expanded and deformed. The deformed contour is the same as that illustrated in Fig. 2 except that there is no pole in this case.

$$I_{y1} = \frac{1}{2}\int_{C_B} f_2'(\lambda)e^{u_1(z-h)}\lambda H_0^{(2)}(\lambda\rho)d\lambda$$

Again, using the argument that the integral along the branch cut of k_0 dominates the total integral, I_{y1} can be approximated as the sum of the integrals along C_1 and C_2

$$I_{y1} \approx \frac{1}{2}\int_{C_1+C_2} f_2'(\lambda)e^{u_1(z-h)}\lambda H_0^{(2)}(\lambda\rho)d\lambda \qquad (34)$$

The approximations given in (19) and (21) still work and given these the function reduces to $f_2'(\lambda) \approx \frac{jk_1 \mp \lambda}{jk_1 \cdot (jk_1 \pm \lambda)}$.

The change of signs in it is due to that u_0 takes different signs on the left and right sides of the branch cut of k_0. The integral in (34) becomes

$$I_{y1} \approx \frac{e^{jk_1(z-h)}}{2jk_1}\left[\int_{C_1} \frac{jk_1 + \lambda}{jk_1 - \lambda}\lambda H_0^{(2)}(\lambda\rho)d\lambda \right.$$
$$\left. + \int_{C_2} \frac{jk_1 - \lambda}{jk_1 + \lambda}\lambda H_0^{(2)}(\lambda\rho)d\lambda\right]$$

Combining the two integrals on the right hand side results in

$$I_{y1} \approx \frac{e^{jk_1(z-h)}}{2}\int_{C_2} \frac{4\lambda^2}{k_1^2 + \lambda^2} H_0^{(2)}(\lambda\rho)d\lambda.$$

Use the asymptotic approximation of the Hankel function $H_0^{(2)}(\lambda\rho) \approx \sqrt{\frac{2j}{\pi\lambda\rho}} \cdot e^{-j\lambda\rho}$, and the variable change $\lambda = k_0 - js$, I_{y1} becomes

$$I_{y1} \approx -2j\sqrt{\frac{2j}{\pi\rho}}e^{jk_1(z-h)}e^{-jk_0\rho} \cdot \int_0^\infty \frac{(k_0 - js)^{3/2}}{k_1^2 + (k_0 - js)^2}e^{-\rho s}ds$$

Since $|s| \gg |k_0|$, all k_0's in the integrand can be ignored and

$$I_{y1} \approx 2\sqrt{\frac{2}{\pi\rho}}e^{jk_1(z-h)}e^{-jk_0\rho} \cdot I_3 \qquad (35)$$

where $I_3 = \int_0^\infty \frac{s^{3/2}}{s^2 - k_1^2}e^{-\rho s}ds$. From the table of integrals [8], I_3 can be analytically evaluated and further simplified as

$$I_3 \approx -\frac{3\sqrt{\pi}}{4k_1^2} \cdot \frac{1}{\rho^{5/2}}$$

and the integral I_{y1} is

$$I_{y1} \approx -\frac{3\sqrt{2}}{2k_1^2} e^{jk_1(z-h)} \frac{e^{-jk_0\rho}}{\rho^3} \quad (36)$$

Numerical calculations indicate that the approximation, (36), is approximately 5% larger in magnitude than the exact integral, (33). This error is relatively stable over the parameter range $100\text{Hz} < f < 3000\text{Hz}$ and $\rho > 500\text{m}$. Since the error is small for this case, it is not necessary to add a correction term to (36). Rather the factor of $3\sqrt{2}/4 \approx 1.06$ is simply set equal to 1 resulting in:

$$I_{y1} \approx -\frac{2}{k_1^2} e^{jk_1(z-h)} \frac{e^{-jk_0\rho}}{\rho^3} \quad (37)$$

Again, when h, $z \ll \rho$, $|k_1| \gg |k_0|$ and $|k_1\rho| \gg 1$, (37) approximates the exact integral (33) very well. Fig. 4 (a) and (b) give the comparisons of the magnitude and the phase angle, respectively, between the exact integral of (33) and its approximation (37). For this case, the magnitude error of (37) is even less than 6% when $\rho > 500\text{m}$.
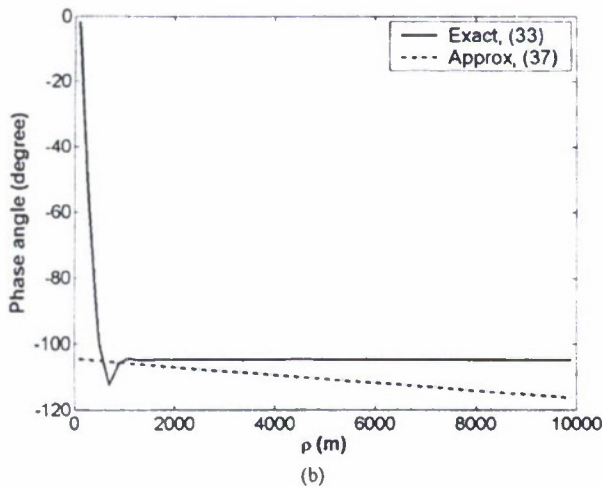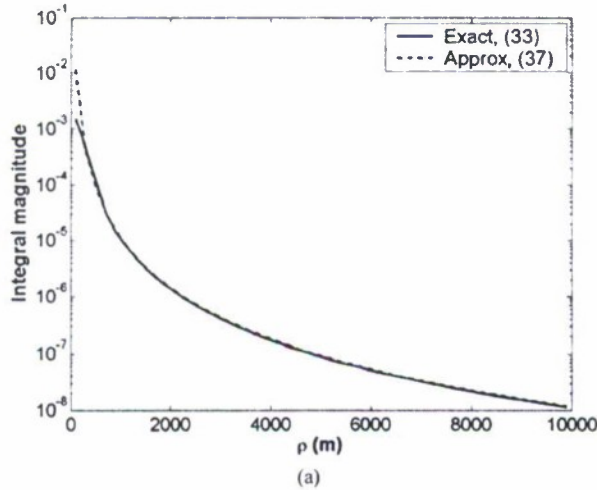

(a)

(b)

VI. THE APPROXIMATIONS FOR E & H FIELD

Given the approximations (32) and (37) for the integral portions of the vector potentials A_z^1 and A_y^1, respectively, the electromagnetic fields can be found. The approximate results for I_{z1} and I_{y1} in (32) and (37), respectively, can be used in (2) and (4) and (6) ~ (11) to find the complete set of E and H fields in region #1. The components of total E and H fields can be written as the combination of the source terms and the reflected terms.

$$E_x^1 = E_{xs}^1 + E_{xr}^1; \quad E_y^1 = E_{ys}^1 + E_{yr}^1; \quad E_z^1 = E_{zs}^1 + E_{zr}^1;$$

$$H_x^1 = H_{xs}^1 + H_{xr}^1; \quad H_y^1 = H_{ys}^1 + H_{yr}^1; \quad H_z^1 = H_{zs}^1 + H_{zr}^1.$$

where the components with 's' in the subscript refer to the source terms of the fields and those with 'r' in the subscript refer to the reflected fields. The source terms of the fields are

$$E_{xs}^1 = A_1 \cdot \frac{e^{-jk_1R}}{R^3} \left(k_1^2 R^2 - 3jk_1R - 3 \right) \cdot \sin\phi\cos\phi \quad (38a)$$

$$E_{ys}^1 = A_1 \cdot \frac{e^{-jk_1R}}{R^3} \left[\left(-k_1^2 R^2 + jk_1R + 1 \right) \right. \\ \left. + \left(k_1^2 R^2 - 3jk_1R - 3 \right) \cdot \left(\sin\phi \right)^2 \right] \quad (38b)$$

$$E_{zs}^1 = A_1 \cdot \frac{(z+h)e^{-jk_1R}}{R^5} \left(k_1^2 R^2 - 3jk_1R - 3 \right) \cdot \sin\phi \quad (38c)$$

$$H_{xs}^1 = \frac{Idl}{4\pi} \cdot \frac{(z+h)e^{-jk_1R}}{R^3} \left(jk_1R + 1 \right) \quad (38d)$$

$$H_{ys}^1 = 0 \quad (38e)$$

$$H_{zs}^1 = -\frac{Idl}{4\pi} \cdot \frac{e^{-jk_1R}}{R^3} \left(jk_1R + 1 \right) \cdot \cos\phi \quad (38f)$$

where $A_1 = \frac{jIdl}{4\pi\omega\varepsilon_1'}$. The simplified reflected fields are

$$E_{xr}^1 \approx 2jA_1 k_0^3 \cdot e^{jk_1(z-h)} \frac{e^{-jk_0\rho}}{(jk_0\rho)^3} \left[3 + \frac{5}{(jk_1\rho)^3} \right] \cdot \sin\phi\cos\phi \ (\\ \qquad\qquad\qquad\qquad\qquad\qquad\qquad\qquad (39a)$$

$$E_{yr}^1 \approx -2jA_1 k_0^3 \cdot e^{jk_1(z-h)} \frac{e^{-jk_0\rho}}{(jk_0\rho)^3} \left[2 + \frac{3 - 15(\sin\phi)^2}{(jk_1\rho)^2} \right] \\ \qquad\qquad\qquad\qquad\qquad\qquad\qquad\qquad (39b)$$

$$E_{zr}^1 \approx -\frac{2jA_1 k_0^4}{k_1} \cdot e^{jk_1(z-h)} \frac{e^{-jk_0\rho}}{(jk_0\rho)^4} \cdot \sin\phi \quad (39c)$$

$$H_{xr}^1 \approx \frac{Idl \cdot k_0^3}{2\pi k_1} \cdot e^{jk_1(z-h)} \frac{e^{-jk_0\rho}}{(jk_0\rho)^3} \left[2 - 3(\sin\phi)^2 \right] \quad (39d)$$

$$H_{yr}^1 \approx \frac{Idl \cdot k_0^3}{2\pi k_1} \cdot e^{jk_1(z-h)} \frac{3e^{-jk_0\rho}}{(jk_0\rho)^3} \cdot \sin\phi\cos\phi \quad (39e)$$

$$H_{zr}^1 \approx \frac{Idl \cdot k_0^4}{2\pi k_1^2} \cdot e^{jk_1(z-h)} \frac{3e^{-jk_0\rho}}{(jk_0\rho)^4} \cdot \cos\phi \quad (39f)$$

The results for E and H fields calculated by (39) are compared to the results from the exact Sommerfeld integral formulas. Fig. 5 shows the comparing result of the reflected field E_{yr}^1. For the reflected magnetic field, similar result can be obtained.
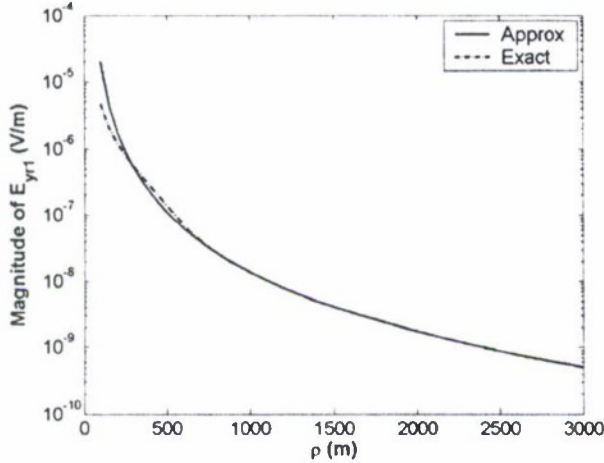

Fig. 5. Exact reflected field E_{yr1} vs. its approximation (39b), $\Phi = \pi$.

VII. DISCUSSION

At any observation point P, (ρ, φ, z), in the lower conducting medium $(z<0)$, the total field is the combination of the incident field directly from the dipole and the reflected field due to the interface, as shown in (38) and (39), respectively. In the far field of the conducting medium $(|k_1\rho|>>h, z)$, the incident field decays much faster than the reflected field, which suggests that the propagation mechanism may involve some fields propagating in the low loss free space region. For the set of parameters considered the source term can be ignored beyond approximately 500m.

In fact, the approximations (39a) ~ (39f) can be interpreted to have an up-over-and-down behavior, similar (but not identical) to the mechanism that has been studied in propagation of high frequency radio waves near a boundary [5]. The extremely low frequency (ELF) case is different because the fields in air are quasi-static. Here, some insight into this behavior will be given.

Consider the E_x component, which is perpendicular to the HED's orientation and easier to be detected, at the observation point P (ρ, φ, z). As already discussed, the total field component can be approximated by the corresponding reflected field component in the far field. Thus, the total x component of the electric field can be approximated by (39a). In the far field of the conducting medium the second term in the bracket is small compared to the constant '3' and can be ignored. Given this, the right hand side of this equation can be rewritten as

$$E_x^1 \approx -\frac{3j\eta_1 Idl \cdot e^{-jk_1h}}{2k_1} \cdot \frac{e^{-jk_0\rho}}{\rho^3} \sin\phi\cos\phi \cdot e^{jk_1z} \quad (40)$$

For the up-over-and-down process, , as illustrated in Fig. 6, the wave induced by the dipole (HED) first propagates upward (Part I) and crosses the interface into the free space region. It is attenuated by a transmission coefficient T_{up}. Second, the wave spreads out horizontally (Part II) along the interface. Note that since the upper medium is free space and for the whole range of

ρ (100 ~ 10000m) considered here, $|k_0\rho|<<1$, the fields are quasi-static. Finally, at the position on the interface right above P, the wave crosses the interface again after attenuation by a transmission coefficient T_{down} and propagates vertically down (Part III) to the observation point.
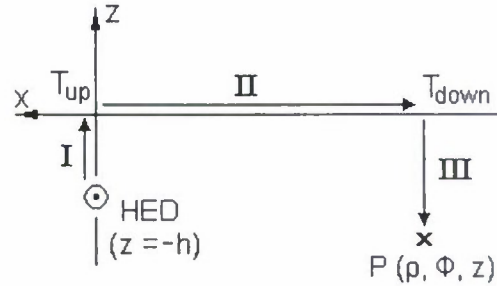

Fig. 6. Illustration of the path of the up-over-and-down process.

To identify (40) as an up-over-and-down process, it is important to show how the different terms have functional dependencies that are characteristic to different portions of the process. For example, it will be shown first that the 'up' term of (40) represents near field vertical propagation of magnetic field from an HED in a homogeneous medium and second, why this term would be expected to be a magnetic field rather than an electric field.

To begin, it is helpful to understand how a quasi-static field in the air can be excited by the buried HED. This can be done by recognizing that the HED generates tangential electric and magnetic fields just above the air-water interface and that these fields can be treated as equivalent magnetic and electric current sources respectively in the air region [7]. If, further, the water is replaced by a perfect magnetic conductor (PMC), then the only remaining source is the electric field sources that originate in the incident magnetic field and are doubled in value by the imaging effect [7]. The use of image theory allows the calculations of fields to be done in a homogeneous air medium. These fields will be quasi-static since $k_0\rho << 1$. The original case for HED buried in PMC is shown on the left side of Fig. 7. The tangential magnetic field generated by the HED just above the air-water interface only has an x component, $\bar{H}_{inc,x}^0$. The fields in the air region can be obtained by the equivalent electric surface current source, $\bar{J}_s$ (A/m), which is shown on the right side of Fig. 7.
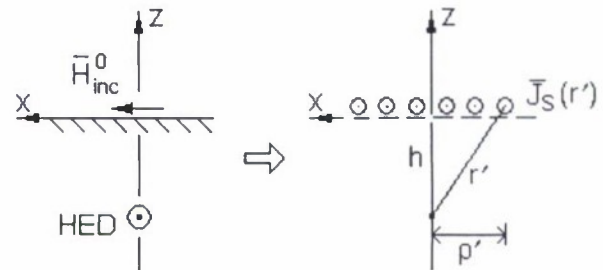

Fig. 7. Equivalent surface current source for the HED buried in PMC.

$\bar{J}_s$ on the interface $(z = 0)$ can be determined by

$$\bar{J}_s = 2\hat{n} \times \bar{H}_{inc}^0 = 2\hat{a}_y \bar{H}_{inc,x}^0 \quad (41)$$

where

$$H_{inc,x}^0(r') \approx T_{up,Hx} \cdot \frac{Idl \cdot h}{4\pi} \frac{e^{-jk_1 r'}}{(r')^3}$$

The primed variable r' represents the distance from the dipole to a point on the source surface and $r' = \sqrt{(\rho')^2 + h^2}$. $T_{up,Hx}$ is the transmission coefficient for x component of the magnetic field.

$$T_{up,Hx} = H_{inc,x}^1 / H_{xs}^1 \tag{42}$$

Integrating the source current over the entire surface gives

$$\bar{Q}_s = \int_0^{2\pi} \int_0^\infty \bar{J}_s \rho' d\rho' d\phi' \tag{43}$$

where $\bar{Q}_s$ has the same dimension as a electric dipole moment (A-m). Therefore, it can be treated as an equivalent dipole moment to replace the original HED if ρ is much larger than the size of the source. This can be understood as follows. The HED is first replaced by the surface current $\bar{J}_s$ on the interface, then the distributed surface current is integrated into a new horizontal (y orientation) electric dipole just above the interface. It is equivalent to say that the original HED is shifted onto the air-water interface with a change in magnitude. The new equivalent HED magnitude can be determined by using (41) in the integration in (43).

$$\bar{Q}_s = \hat{a}_y Idl \cdot e^{-jk_1 h} T_{up,Hx} \tag{44}$$

The exponential term in (44) is obtained by assuming that $k_1 r'$ varies little over the source area and

$$e^{-jk_1 r'} \approx e^{-jk_1 h}. \tag{45}$$

As shown in (41), $\bar{J}_s$ is dependent on the depth of the HED, h. It is proportional to $1/h^2$ when near to the origin. Beyond several multiples of h from the origin, the current becomes very small and negligible. This makes the approximation in (45) reasonable because within several multiples of h the assumption that $k_1 r'$ varies little is valid. Fig. 8 shows the magnitude distribution of $\bar{J}_s$.
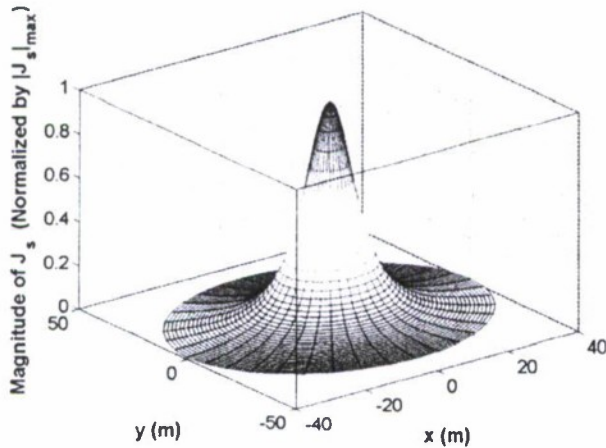

Fig. 8. Normalized magnitude distribution of the surface current (all the magnitudes are normalized by the maximum of the current).

The magnitudes in the figure are normalized by the magnitude of the current at the origin (i.e., the maximum of the current). It can be shown that there is an effective area beyond which the effect of the source current can be ignored. The effective area is proportional to h^2. Since the current decays vertically as $1/h^2$ and the effective area grows with h^2, the integral over the surface will be independent of h. Thus the new dipole moment as shown in (44) is independent of h except for the exponential term. The process shown by (41) to (45) describes the 'up' (Part I in Fig. 6) part of the propagation.

Given the new equivalent HED, the field in the air region can be determined by treating the new HED as a dipole in free space. The x component of the electric field in air on $z = 0$ plane is

$$E_{x,u}^0(\rho,\phi,0) = -\frac{3j\eta_0 Q_s}{4k_0} \cdot \frac{e^{-jk_0\rho}}{\rho^3} \sin\phi\cos\phi$$

where Q_s is the new dipole moment and the subscript 'u' stands for the field obtained by the up-over-and-down interpretation. Replacing Q_s by (44) results in

$$E_{x,u}^0(\rho,\phi,0) = -\frac{3j\eta_0 Idl \cdot e^{-jk_1 h} e^{-jk_0\rho} T_{up,Hx}}{4k_0\rho^3} \sin\phi\cos\phi \tag{46}$$

This is a field propagating, in air, over the air-water interface and the 'over' (Part II in Fig. 6) part of the propagation.

The field shown in (46) travels from the interface down to the observation point P in the same way a plane wave does. This is valid because $|k_0\rho| \ll 1$. An exponential term, $e^{jk_1 z}$, indicating the propagating pattern of a plane wave in the '-z' direction is then added in the expression of the field at P to represent the 'down' (Part III in Fig. 6) part of the propagation. Finally, the expression of electric field component E_x at the observation point is

$$E_{x,u}^1(\rho,\phi,0) =$$
$$-\frac{3j\eta_0 Idl \cdot e^{-jk_1 h} T_{up,Hx}}{4k_0} \frac{e^{-jk_0\rho}}{\rho^3} \sin\phi\cos\phi \cdot T_{down,Ex} \cdot e^{jk_1 z} \tag{47}$$

which shows a complete process of the up-over-and-down propagation. The transmission coefficient $T_{down,Ex}$ in (47) is for the x component of E field when it travels down and crosses the interface. Since there is no reflected wave in the upper region and the tangential fields are continuous across the boundary,

$$T_{down,Ex} = 1.$$

Comparing (47) to (40), there is a constant difference between the two expressions that

$$E_{x,u}^1(\rho,\phi,z) = -2\frac{\eta_0}{k_0}\frac{k_1}{\eta_1} T_{up,Hx} \cdot E_x^1(\rho,\phi,z)$$

The reason why the difference appears is still not identified at this point. But if $T_{up,Hx}$ is selected as

$$T_{up,Hx} = 2\frac{k_0}{\eta_0}\frac{\eta_1}{k_1} = \frac{2\varepsilon_0'}{\varepsilon_1'} \tag{48}$$

then the simple model based on the physical interpretation of the propagation process matches the derived expression.

VIII. CONCLUSIONS

A method to simplify the Sommerfeld integration is proposed in this paper. Using this method a non-integral, far field approximation of the E & H field due to a horizontal electric dipole buried in a conducting half space is obtained. Then it is tested that this approximation works very well when $h, z \ll \rho$, $|k_1| \gg |k_0|$ and $|k_1\rho| \gg 1$ and the error is less than 10%.

This approximation reveals the up-over-and-down behavior of the electromagnetic wave when propagating in the conducting half space. Finally an interpretation based on the surface equivalence theorem to the up-over-and-down process of the wave propagation is introduced.

REFERENCES

[1] A. Baños, *Dipole radiatian in the presence of a canducting half-space*. New York: Pergamon, 1966.

[2] P. R. Bannister, "Extension of finitely conducting earth-image-theory results to any range", Naval Underwater Systems Center, New London, CT, Tech. Rep., Jan. 1984.

[3] J. R. Wait and L. L. Campbell, "The fields of an oscillating magnetic dipole immersed in a semi-infinite conducting medium", *J. Geophys. Res.*, vol. 58, no. 2, pp. 167-178, 1953.

[4] A. K. Sinha and P. K. Bhattacharya, "Vertical magnetic dipole buried inside a homogeneous earth", *Radio Sci.*, vol. 1, no. 3, pp. 379-395, 1966.

[5] T. Tamir, "Radio wave propagation along mixed paths in forest environments", *IEEE Trans. Antennas Prapagat.*, vol. 25, no. 4, pp. 471-477, Jul. 1977.

[6] J. R. Wait, "The electromagnetic fields of a horizontal dipole in the presence of a conducting half-space", *Can. J. Phys.*, vol. 39, no. 7, pp. 1017-1028, 1961.

[7] C. A. Balanis, *Advanced Engineering Electromagnetics*. NJ : John Wiley & Sons, Inc., 1989.

[8] I. S. Gradshtcyn and I. M. Ryzhik, *Table af integrals series and products*. New York: Academic Press, 1965.

[9] C. R. Paul, *Introduction to Electromagnetic Compatibility*. NJ: John Wiley & Sons, Inc., 1992.

Dual Problem Space FDTD Simulation for Underwater ELF Applications

Yang Xia, Dennis M. Sullivan, Zhi Li, and Robert Olsen

Abstract—The finite-difference time-domain (FDTD) method is being used to simulate extremely low frequencies underwater. In order to expand the potential problem space without reducing the resolution at which the source is modeled, a near-to-far-field transformation method has been developed.

Index Terms—Equivalent sources, finite-difference time-domain (FDTD) methods.

I. INTRODUCTION

U NDERWATER mines pose the greatest threat to surface ships [1]. These mines are no longer restricted to direct contact, but can detect the electromagnetic (EM) signature of a ship and launch a torpedo from hundreds of meters away [2]. The EM radiation of a surface ship tends to be in the extremely low frequency (ELF) range and can propagate underwater over long distances. For this reason, simulation is being used to study underwater EM radiation.

One of the most common methods used in EM simulation is the finite-difference time-domain (FDTD) method [3], [4]. It has recently been shown to be effective at ELF frequencies [5]. However, because it employs a uniform grid, one is always left with the problem of choosing a cell size that is small enough to accurately model the radiating source, but large enough to model an extensive far field. In order to overcome this, a three-dimensional near-to-far-field transformation has been developed. This method involves two separate FDTD simulations. The simulation space in the near-field models the source, whether it is a ship's hull or an antenna, with relatively high resolution; a second simulation space models the far-field with larger cells in order to model propagation hundreds of meters from the source. The transition between near- and far-field is accomplished by applying the equivalence principle [6].

This letter is arranged as follows. The use of the equivalence principle to make the near-to-far-field transition is described in Section II. In Section III, we verify the accuracy of the method by comparison with an analytic method based on Sommerfeld's
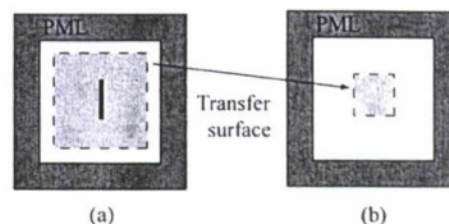
Fig. 1. Two problem spaces are used in the FDTD simulation. (a) The radiating source is modeled in the near-field, and the tangential H-field on the three-dimensional surface are calculated. (b) Using the tangential H-fields, a three-dimensional source is impressed in the far-field. (a) Near-field problem space. (b) Far-field problem space.

half-space method [7]–[9]. In Section IV, a more realistic example of the simulation of a loop antenna in a lake bed is presented. Section V summarizes the letter.

II. THE NEAR-TO-FAR-FIELD TRANSFORMATION

Two three-dimensional FDTD problem spaces are utilized to implement the near-to-far-field transformation (Fig. 1). A problem space with a relatively small cell size (1 m^3) is used to model the source [Fig. 1(a)]. Another problem space with larger cells (13 m^3) is used to model the far-field [Fig. 1(b)]. The ratio of 13 to 1 between far- and near-field cell sizes resulted in near- and far-field problem spaces of about the same size, which seemed to be the optimum case. Each problem space is surrounded by a perfectly matched layer (PML) [10]. (A new PML for ELF frequencies and lossy media has been developed and will be the subject of a future paper.) Each problem space contains a three-dimensional transfer surface where the equivalence principle [6] is implemented. On a surface, the source is uniquely specified by either the tangential E- or H-fields. We use the H-fields. The tangential fields calculated on the transfer surface in the near-field are impressed on the transfer surface in the far-field to form the far-field source. Since the far-field cells are 13 times larger than the new field cells, only one value out of 13 in the near-field is needed in the far-field. This method is effective even when the medium is inhomogeneous, as will be demonstrated in the next section. There is no coupling from the far-field back to the near-field. This is illustrated in Fig. 2.

III. VERIFICATION OF THE ACCURACY

In this section, the results of the near-to-far-field transformation are compared to analytic results calculated using Sommerfeld's half-space (SHS) problem. SHS problem calculates the resulting fields from an oscillating dipole near a plane interface separating two homogeneous half-space regions, as illustrated in Fig. 3. This method is well described in the literature [7]–[9]
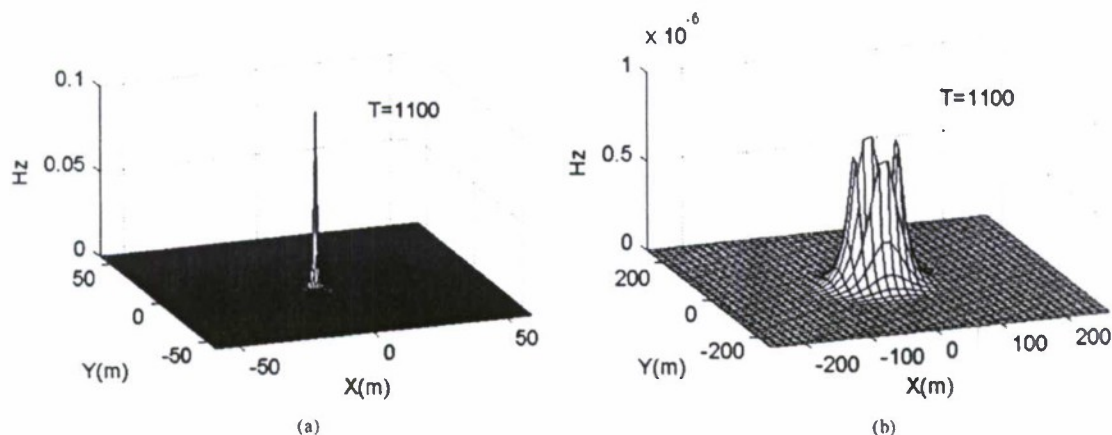
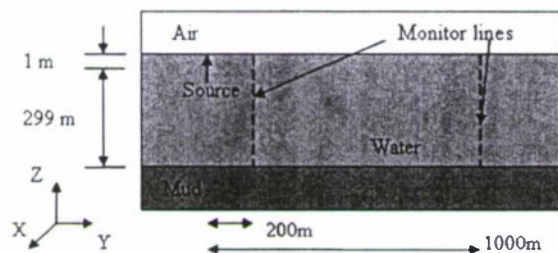Fig. 2. (a) Near-field mesh plot. (b) Far-field mesh plot.

Fig. 3. Diagram of the three-dimensional far-field used in the comparison between the FDTD near-to-far-field transformation and the SHS method. The x-direction (not shown) is 1500 m. The source is a magnetic dipole 1 m below the air-water interface and was generated in the near-field (not shown).

TABLE I
PROPERTIES OF THE MATERIALS USED IN THE SIMULATIONS DESCRIBED
IN THIS LETTER [5]

Material	ε_r	$\sigma\ (S/m)$
Air	1	0
Lake water	80	0.018
Mud	40	0.002

and will not be repeated here. In Fig. 3, the upper layer is air, the middle layer is water, and the lower level is mud. The water layer in the middle is 300 m thick. The dielectric properties for water, mud, and air are given in Table I. The dipole is formed by specifiying the H_z-field in one 1-m³ cell in the near-field problem space. The monitor lines represent the places where comparisons between the methods will be made. Note that the FDTD simulations are all three-dimensional.

Comparisons at 200 and 1000 m are shown in Fig. 4(a) and (b), respectively. The simulation required 30 000 time-steps. The amplitudes in each figure are calculated by the method of two equations, two unknowns [11]. The horizontal coordinate is the distance to the air/water surface, and the vertical coordinate is the magnitude of the field. The discrete symbols represent the FDTD calculations, and the solid lines represent the calculations by SHS method. Clearly, the results of the comparisons are very good in all cases.
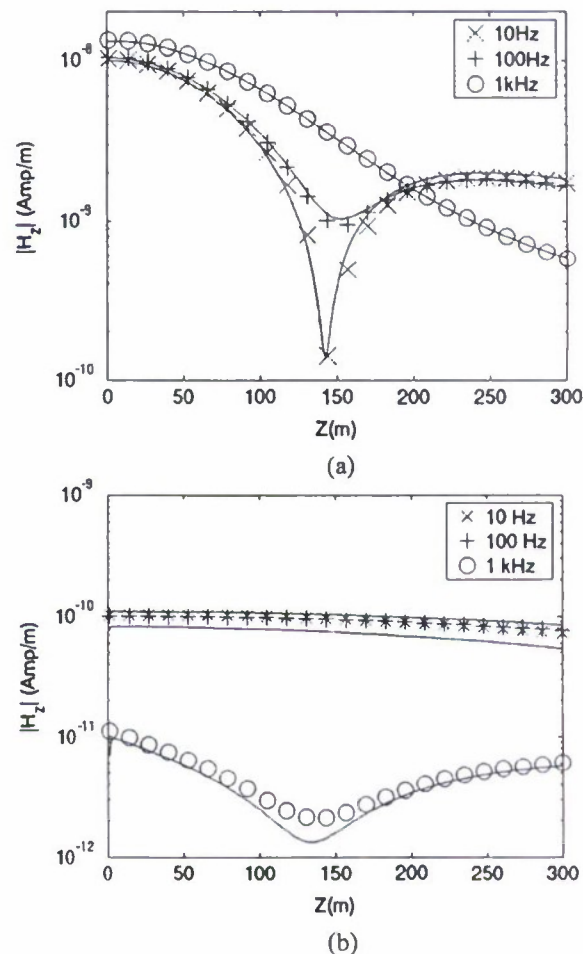

Fig. 4. Comparisons of the FDTD simulations (the symbols) and the SHS calculations (the lines) for the cell size ratio of 13. The source is near the upper surface of the water layer. The comparisons are made at (a) 200 and (b) 1000 m. Z represents the distance from the surface. (a) Comparison at 200 m. (b) Comparison at 1000 m.

IV. EXAMPLE

This section illustrates the use of FDTD with a near-field, far-field transformation in simulating a more realistic case. One of the goals of the simulation is to verify the accuracy of the
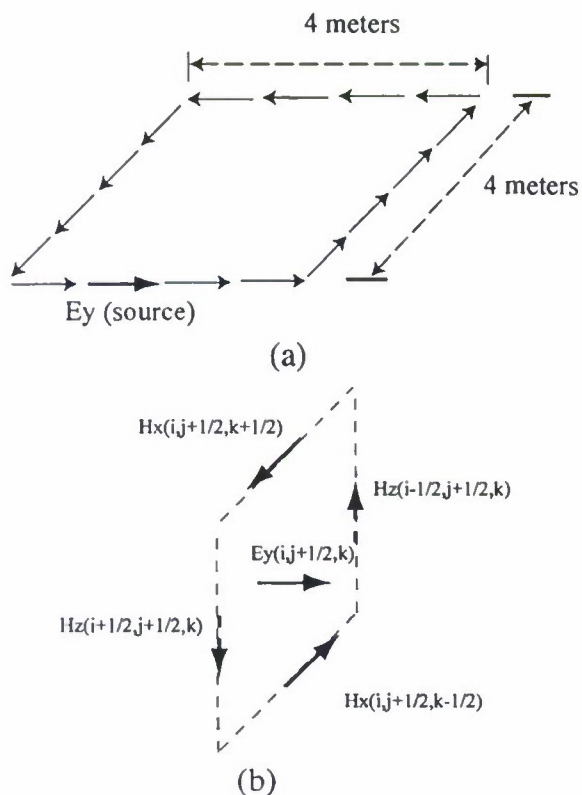
(a)

(b)

Fig. 5. The simulation of a 4 m × 4 m current loop in FDTD as generated in the near-field. (a) Setting the group of cells at the respective E-field points in the grid simulates a metal loop. (b) Current is simulated by setting an E_y-field to a value. This couples to the surrounding H-fields.

modeling with measured data that can be made in a lake. Because the lake bed is not flat, analytical approaches cannot be used to solve the problem.

The antennas that will be used in the transmission are 4 m × 4 m rectangular current loops. Fig. 5(a) illustrates how this is simulated in the XY-plane in the FDTD space. Metal can be simulated by ensuring that an E-field is zero at a particular point in the space. Therefore, using cells that are 1 m^3, the metal loop antenna is simulated at the corresponding E_x or E_y positions, as shown in Fig. 5(a). Since the radius of the wire of the antennas is considerably less than the 1-m cell size, the thin rod approximation [12] is used to model the wire at these positions

In FDTD, a current cannot be simulated directly, but it can be simulated indirectly by using Ampere's circuit law [13] and specifying the surrounding H-fields

$$I = \oint \frac{1}{\mu_0} \mathbf{H} \cdot d\mathbf{l}. \tag{1}$$

By impressing a hard source on one of the E_y-fields, a value is induced on the surrounding H-fields, as shown in Fig. 5(b). This results in a current via (1).

A model of the lake bed is created for the far-field domain (Fig. 6). The cells are 13 m^3. The shape of the lower surface of the water layer shows a complex geometry structure similar to a real lake bed.
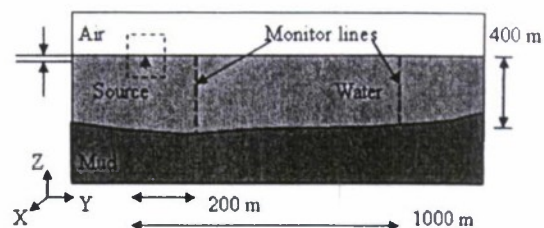

Fig. 6. The lake bed that is simulated in the far-field. The cells in the far-field are 13 m^3. The near-field (the enclosed dashed area) contains a current loop located 1 m below the surface of the water.
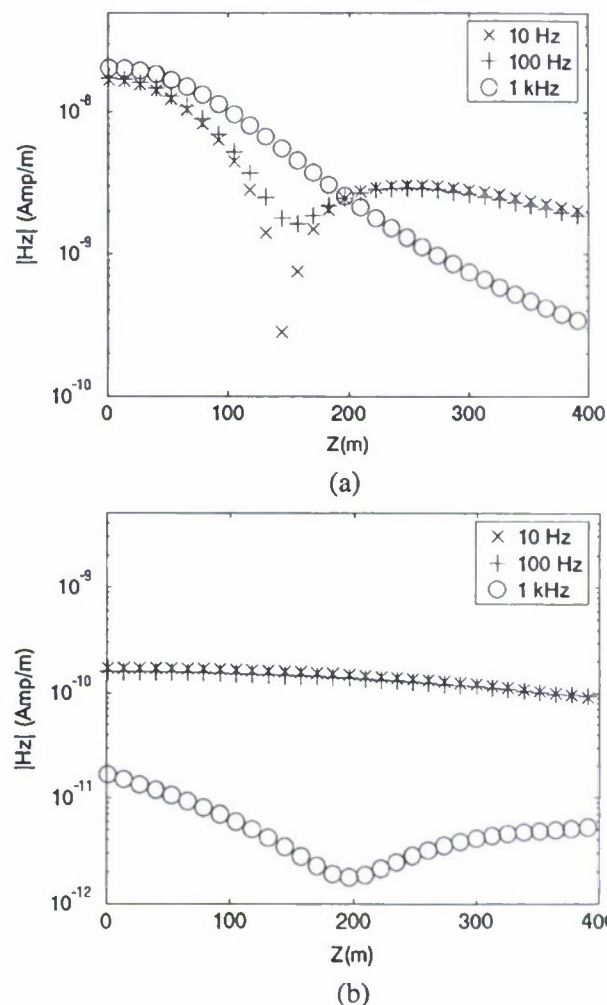

(a)

(b)

Fig. 7. Results of the simulation illustrated in Fig. 6. Z represents the distance from the surface. (a) The results at 200 m. (b) The results at 1000 m.

Fig. 7(a) and (b) shows the results of the near-to-far-field simulation using the current loop source in the near-field and the lake bed in the far-field at 200 and 1000 m from the source and at three different frequencies, 10, 100, and 1000 Hz. These simulations were done on an HP DL140 GE Quad Core and required about 6 h. Both the near- and far-field problem spaces were 120 cells cubed.

V. SUMMARY

A near-to-far-field transformation utilizing the equivalence principle in conjunction with the FDTD method has been pre-

sented. The accuracy of this method was confirmed by comparisons with analytic results based on Sommerfeld's half-space method. An example illustrating the flexibility of the method in simulating a realistic problem has also been presented.

The method presented in this letter substantially extends the range of FDTD simulations at ELF frequencies for the purpose of determining the vulnerability of surface ships to electromagnetically detonated mines. Accuracy at 1 km has already been confirmed, and it is hoped that the development of a new underwater PML will extend this range to 3 km.

REFERENCES

[1] R. H. Wilkens and M. D. Richardson, "Mine burial prediction: A short history and introduction," *IEEE J. Ocean. Eng.*, vol. 32, no. 1, pp. 3–9, Jan. 2007.

[2] J. J. Holmes, *Exploitation of a Ship's Magnetic Field Signatures*. New York: Morgan and Claypool, 2006.

[3] K. S. Yee, "Numerical solution of initial boundary value problems involving Maxwell's equations in isotropic media," *IEEE Trans. Antennas Propag.*, vol. 14, pp. 302–307, 1966.

[4] D. M. Sullivan, *Electromagnetic Simulation Using the FDTD Method*. New York: IEEE, 2000.

[5] Y. Xia and D. M. Sullivan, "Underwater FDTD simulation at extremely low frequencies," *IEEE Antennas Wireless Propag. Lett.*, vol. 7, pp. 661–664, 2008.

[6] R. Harrington, *Time-Harmonic Electromagnetic Fields*. New York: McGraw-Hill, 1961.

[7] J. R. Wait, *Electromagnetic Wave Theory*. New York: Harper and Row, 1985.

[8] W. C. Chew, *Waves and Fields in Inhomogeneous Media*. New York: Van Nostrand Rheinhold, 1990.

[9] L. B. Felsen and N. Narcuvitz, *Radiation and Scattering of Waves*. New York: IEEE, 1994.

[10] J. P. Berenger, "A perfectly matched layer for the absorption of electromagnetic waves," *J. Comp. Phys.*, vol. 114, pp. 185–200, 1994.

[11] C. M. Furse, "Faster than Fourier—Ultra-efficient time-to-frequency domain conversions for FDTD simulations," *IEEE Antennas Propag. Mag.*, vol. 42, no. 6, pp. 24–34, 2000.

[12] J. Nadobny, R. Pontalti, D. M. Sullivan, W. Wladarczk, A. Vaccari, P. Deuflhard, and P. Wust, "A thin-rod approximation for the improved modeling of bare and insulated cylindrical antennas using the FDTD method," *IEEE Trans. Antennas Propag.*, vol. 51, no. 8, pp. 1780–1796, Aug. 2003.

[13] D. K. Chen, *Field and Wave Electromagnetics*, 2nd ed. New York: Addison-Wesley, 1989.